Crustal Fault Zones as geothermal power systems. Contribution of numerical modelling and comparison with natural systems

Hugo Duwiquet

BRGM/ ISTO/ TLS-Geothermics/ Université d'Orléans

ÉNERGIE, MATÉRIAUX, SCIENCES DE LA TERRE ET DE L'UNIVERS

THÈSE présentée par :

Hugo DUWIQUET

Soutenue le : **27 janvier 2022**

Pour obtenir le grade de : **Docteur de l'Université d'Orléans**

Discipline / Spécialité : Sciences de la Terre et de l'Univers / Géoressources

Les Zones de Failles Crustales comme systèmes géothermiques électrogènes
Apport des modélisations numériques et confrontation aux systèmes naturels

THÈSE dirigée et encadrée par :

GUILLOU-FROTTIER Laurent	Ingénieur-Chercheur, HDR, BRGM
ARBARET Laurent	Maître de Conférences, HDR, ISTO
BELLANGER Mathieu	Géologue, PhD, TLS-Geothermics

RAPPORTEURS :

LEDRU Patrick	Professeur, Université de Lorraine
DONZÉ Frédéric	Professeur, Université de Grenoble-Alpes

PRÉSIDENT DU JURY :

GAILLARD Fabrice	Directeur de Recherche, ISTO

JURY :

HORNE Roland	Professeur, Stanford University
GENTER Albert	Directeur Général Adjoint, PhD, ES-Géothermie
SOUQUE Christine	Ingénieure de Recherche, PhD, IFPEN
MAGRI Fabien	Professeur, Freie Universität Berlin

REMERCIEMENTS

Après un peu moins de 3 ans de travail, plus de 49 000 km parcourus sur différents continents, différents pays (maintenant je dois faire gaffe au CO_2). Après des cours donnés à des étudiants perplexes, des sueurs provoquées par des présentations complexes. Après des discussions sans fin sur des missions de terrain. Après une pandémie. Après des nuits écourtées, ou finalement et simplement, après la rédaction de ce manuscrit de thèse… Après tout, il est temps de remercier l'ensemble des personnes qui par leurs contributions pratiques, leur soutien sans réserve ou simplement (mais efficacement) leur bonne humeur, ont contribué à rendre cette expérience de thèse CIFRE véritablement « extra »ordinaire.

Le vrai patron est quelqu'un qui se mêle passionnément de votre travail, qui le fait avec vous, par vous (Jules Romains). Si cette thèse a été une expérience incroyable c'est grâce à mes deux patrons, mes deux directeurs de thèse.

Laurent Guillou-Frottier, un immense merci, pour tout. Je garde en tête, le moment où, dans ton bureau, en te montrant le manuscrit de ma première publication, j'ai reçu la confirmation par email que la thèse CIFRE allait se lancer. Ma réaction s'est alors manifestée par un « oh p***** YES ! ». A ce moment, j'ai peut-être un peu oublié que j'avais à côté de moi un directeur de thèse exceptionnel, les mots sont pesés. Merci pour ta pédagogie. Merci pour la rigueur enseignée. Merci pour ton soutien et ta confiance. Merci de m'avoir laissé une liberté de travail quasi-totale. J'en oublie sans doute... merci pour tout !

Laurent Arbaret, également un immense merci. Tôt, tu m'as parlé de cette aventure de thèse CIFRE. Tu connaissais ma volonté et tes conseils m'ont été, me sont, et me seront toujours très précieux. Merci pour le temps passé à faire en sorte que cette aventure puisse exister et perdurer. Les discussions sur le terrain, tes suggestions, tes remarques ont su évidemment me faire avancer dans toutes les étapes constitutives de ce travail.

Et au-delà même de ces mots, je vous adresse Laurent et Laurent (choisissez l'ordre que vous voulez) une reconnaissance, une affection et un respect immense.

C’était trop cool. Je recommencerai, (presque) demain. Disons après-demain. Après un jour de vacance imposé.

Cette thèse CIFRE a été co-financée par TLS GEOTHERMICS, que je remercie pour ça. Je garde d’excellents souvenirs du stage effectué et de la thèse dans sa globalité. Cette aventure a commencé par un important travail de démolition. La référence est évidemment faite aux nouveaux locaux, pour lesquels j’ai appris à poser du béton sur les fenêtres, au tout début. Je remercie sincèrement Mathieu Bellanger. Merci pour ta disponibilité et de m’avoir, toi aussi transmis cette passion du terrain et de la modélisation numérique. Je remercie également Mathieu Auxiètre pour la confiance accordée par ce co-fiancement et Emilie Bessagnet pour l’aide administrative apportée. Une pensée à Yohann Quaireau. On ne s’est pas beaucoup croisés mais le peu de fois, on a bien rigolé. De façon générale, je pense qu’on aurait bien pu se marrer.

Je remercie les rapporteurs Patrick Ledru, et Frédéric Donzé pour avoir évalué le fruit de ce travail. Mes remerciements s’adressent également à tous les membres du jury pour leur participation, les discussions et leurs suggestions.

Dans l’Avenir d’une illusion (1927), Freud dit *Nous devrions suivre l’exemple des géologues.* Je pense ici à toute l’équ**i**pe DGR/GEM du BRGM. Si ces tr**o**is années ont été mémorables, vous n’y êtes pas pour rien. Et cela a forcément influencé (en bien et/ou en mal) les résultats détaillés dans ce manuscrit. Merci à Laurent Bailly (entre autres, la *Bytownite*), Blandine G**o**urcerol (***suivre***), Maxime Picot (*homéophatie ! et tant de cartons à soulever, de Pokémons très rares).* Merci à Matthieu Chevillard pour les parties de volley et pade**l**. Merci à Sébastien Colin pour les tomates ananas. Merci à Nicolas Charles, j’ai quelques va**g**ues souvenirs de la RST Lyon, 2021… sacré tatouage ! Je remercie é**g**alement chaleureusement Anne-Sophie Serrand, Eric Gloaguen, Guillaume Bertrand, Guillaume Vic, Eric Fournier, Anthony Pochon, Léo Chabot, Isabelle Duhamel-Achin, Thomas Fullgraf

et Lucile Esnee. Finalement, quand je repense aux moments passés, je me demande, en écrivant ces lignes, si Freud avait réellement raison…….. Un immense merci à tous pour votre accueil, j'ai vraiment adoré travailler ainsi !

Au-delà de cette équipe, d'autres personnes du BRGM m'ont beaucoup apporté. Un grand merci à Théophile Guillon pour la pédagogie dont tu as fait preuve lors de mes innombrables questionnements géomécaniques. A travers toi, je remercie également Antoine Armandine Les Landes ainsi que Arnold Blaisonneau. Merci également à Séverine Caritg, Simon Lopez et Jeremie Melleton pour vos conseils et vos encouragements. Je tiens également à remercier chaleureusement Frédéric Simien, Frédéric Moreira, Amanda Hoffbourg, Cyril Boucley et Alex Vella. Je pense ici aux moments passés à Lyon, avec Nicolas et Alexane entre bouchons lyonnais, les routes à sens unique et les cargaisons illégales, voire louches, dans le coffre, ou dans un sac de voyage…

A l'ISTO merci à toute la bande des thésards et post-doc pour cette bonne ambiance et les BBQ organisés ! Un grand merci à Alexane Legeay et Arnaud Isch, que ce soit au Georges (*yeeeeees*) ou sur un terrain de bad (*c'est qui le meilleur ?!?!*), je garderai d'excellents souvenirs de tous nos moments !

Merci à Michael Heap, Alexandra Kushnir et Lucille Carbillet pour votre accueil à Strasbourg et pour les moments passés au Local !

Un grand merci Fabien Magri, pour tous tes conseils et tes suggestions. J'ai beaucoup appris lors de nos discussions.

Évidemment, je n'oublie pas Emmy Penhoët et Florent Foucher. Vous avez dû supporter ma pédagogie, que je n'espère pas trop douteuse. Une pensée particulière à cheval de feux, chien de la forêt et surtout la grande chèvre boiteuse de ce gite, dans le Malzieu…

Je remercie chaleureusement l'association de « La route de Mines » de Pontgibaud ainsi que la Comtesse Gabriel de Germiny pour m'avoir ouvert les portes de Château Dauphin ainsi que leur fabuleux musée !

Quand un arbre tombe, on l'entend ; quand la forêt pousse, pas un bruit (proverbe Africain). Des arbres, vous en avez plantés. J'ai une pensée ici particulière aux parents Duwiquet et Lochet. Cette curiosité pour toutes choses, ce goût prononcé pour l'étranger, l'inconnu, ces sources diverses de motivation… Le travail présenté ici est aussi le résultat de cette transmission, et par-delà même ce travail, la personne.

Un immense merci à Karl et Karine (que j'ai peut-être trop souvent nommé Tic et Tac, Simon and Garfunkel, Bernard et Bianca, et dans un excès d'humour douteux, il y en a sans doute eu d'autres). Si en rédigeant ces lignes, vous pouvez voir mon sourire, vous savez ce qu'il retranscrit. Depuis des parties tellement interminables de rumy, jusqu'aux marches dans des tempêtes de neige, en passant par un ensablement royal dans le désert Omanais, vous avez été à l'écoute des différentes avancées de ce travail et je suis aujourd'hui convaincu que vous avez tout compris (faux !). A Ben & Nut's (je ne crois pas l'avoir déjà faite celle-là…) sincèrement merci pour votre accompagnement, vos encouragements et votre soutien.

Un grand merci à Julien et Caroline ! Merci pour votre accueil lors de mes passages à Toulouse. Cette thèse a commencé à peu près au même moment qu'un bel événement. Et avec cet événement, quelques souvenirs d'un passage à Bordeaux… (héhé).

Merci aussi à Martine, Didier, Célia et Benjamin pour vos encouragements ou par la curiosité dont vous avez fait preuve lorsque j'expliquais mon travail et ses perspectives.

Une pensée aussi particulière à Josette. A l'écoute depuis les débuts. Une immense merci pour tous tes encouragements.

Alors pour terminer définitivement cette thèse et clore ce chapitre, un immense

merci à Tiffany. Les mots ne seraient pas forcément les plus justes, pour te dire à quel point ton soutien a été fondamental dans l'élaboration de ce travail, et je le sais, bien au-delà.

C'est l'histoire d'un têtard [thésard], il croyait qu'il était tôt, mais en fait il était tard.

A ma famille,

Pour Pierrot,

We don't read and write poetry because it's cute. We read and write poetry because we are members of the human race. And the human race is filled with passion. And medicine, law, business, engineering, these are noble pursuits and necessary to sustain life. But poetry, beauty, romance, love, these are what we stay alive for. To quote Whitman, "O me ! O life ! Of the questions of these recurring; of the endless trains of the faithless… of cities filled with the foolish; what good amid these, O me, O life ? Answer. That you are here – that life exists, and identity; that the powerful play goes on and you may contribute a verse." That the powerful play goes on and you may contribute a verse

Peter Weir, *Dead Poets Society*, 1989
Walter Whitman, *Leaves of grass*, 1855

On lit et on écrit de la poésie non pas parce que c'est joli. On lit et on écrit de la poésie parce que l'on fait partie de l'humanité, et que l'humanité est faite de passions. La médecine, le droit, le commerce et l'industrie sont de nobles poursuites, et elles sont nécessaires pour assurer la vie. Mais la poésie, la beauté, l'amour, l'aventure, c'est en fait pour cela qu'on vit. Pour citer Whitman : "Ô moi ! Ô la vie ! Tant de questions qui m'assaillent sans cesse, ces interminables cortèges d'incroyants, ces cités peuplées de sots. Qu'y a-t-il de beau en cela ? Ô moi ! Ô la vie ! Réponse : que tu es ici, que la vie existe, et l'identité. Que le prodigieux spectacle continue et que tu peux y apporter ta rime." Que le prodigieux spectacle continue et que tu peux y apporter ta rime.

Peter Weir, *Le cercle des poètes disparus*, 1989
Walter Whitman, *Feuilles d'herbe*, 1855

TABLE DES MATIÈRES / TABLE OF CONTENTS

LISTE DES FIGURES / FIGURES LIST

Introduction Générale (version française)

“Geothermal energy, potentially the largest – and presently most misunderstood- source of energy”

Our Choice – A plan to solve the Climat Crisis, Al Gore, 2009

1 Évolution des concepts

Du grec *géo* “la Terre”, et *thermós* “la chaleur”, la géothermie désigne une ressource énergétique et l’étude de phénomènes thermiques internes à la Terre. Depuis 400 ans, la compréhension des processus géothermaux s’est largement développée (voir Fig 1).

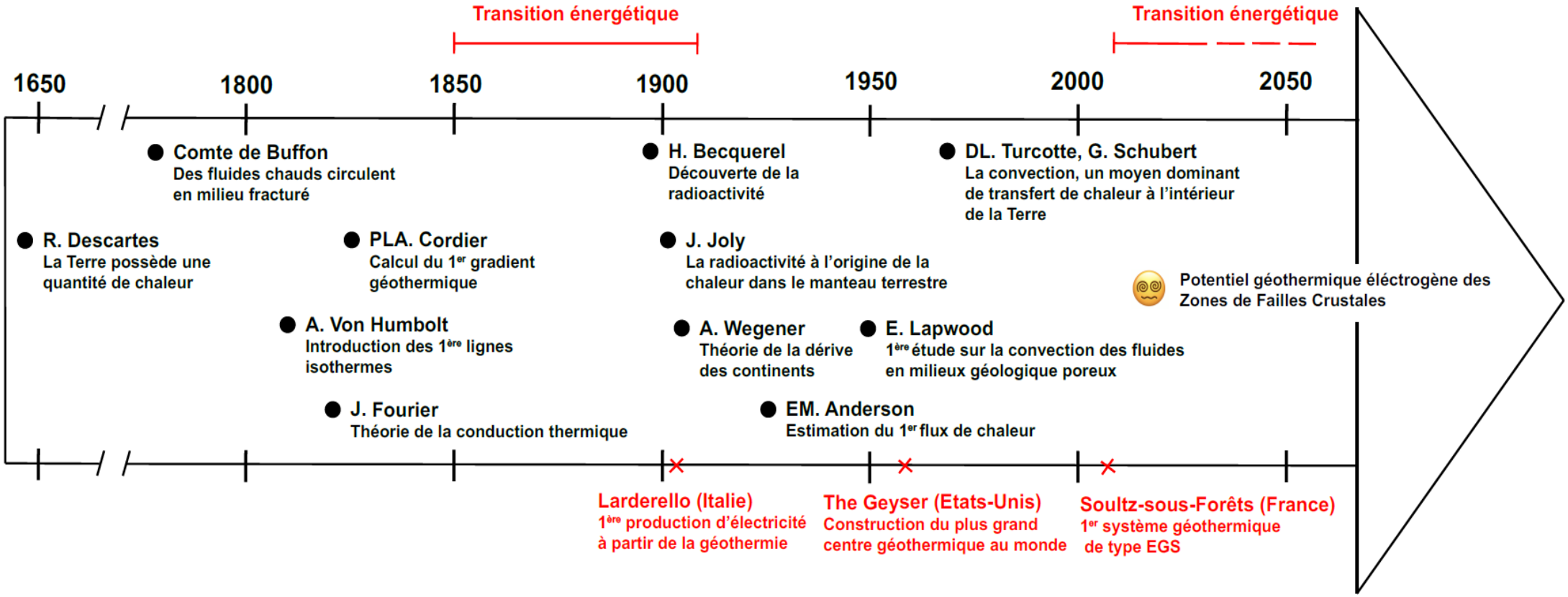

Figure 1 : Positionnement de cette étude dans la succession chronologique des découvertes majeures de phénomènes thermiques internes à la Terre.

En 1644, Descartes émet l'hypothèse qu'à l'origine la Terre est une étoile. Elle possède une certaine quantité de chaleur, se dissipant avec le temps. Dans son ouvrage « *Histoire naturelle, générale et particulière, contenant les époques de la nature* » Buffon (1778) propose que des fluides, réchauffés par cette chaleur interne, peuvent circuler dans un milieu fracturé (Extrait 1) :

> *« [...] mines de sel, de celle de fer en grains, de pyrites & de toutes les autres substances dans la composition desquelles il entre des acides, & dont la première formation n'a pu s'opérer qu'après la chûte des eaux ; ces matières auront été entraînées & déposées dans les lieux bas et dans les fentes de la roche du globe, où trouvant déjà les substances minérales sublimées par la grande chaleur de la Terre, elles auront formé le premier fond de l'aliment des volcans à venir [...]»*

Extrait 1 : Extrait de Histoire naturelle, générale et particulière, contenant les époques de la nature p. 192, de Georges-Louis Leclerc, Comte de Buffon, 1778. Suggérant que dans des fractures (e.i. « les fentes de la roche ») des fluides réchauffés par « la grande chaleur de la Terre » peuvent circuler.

Les premières mesures de température en profondeur ont permis de définir le gradient géothermique et marquent ainsi une étape cruciale dans l'évolution de la géothermie. Ces premières mesures auraient été effectuées en France, dans les mines d'Alsace par De Gensanne (Buffon, 1778). A la fin du XVIII^{e} siècle, dans la mine de sel de Bex (canton de Vaud, Suisse) de Saussure enregistre à 37 mètres de profondeur, une augmentation de la température de 1°C par rapport à la surface (Radau, 1880). Cordier (1827) est le premier scientifique à calculer un gradient géothermique. A cette époque, ces résultats montrent que la température peut augmenter avec la profondeur à raison de 1°C tous les 20-25 mètres. Mais, à Grenelle (Ouest de Paris, France), les mesures effectuées dans un puit par Arago et Walferdin (Walferdin, 1837) donnent une augmentation de 1°C tous les 32.3 mètres. Finalement, ce gradient géothermique est assez proche de la valeur moyenne, communément admise, pour la

croûte continentale européenne, de 1°C tous les 33 mètres (ou 30°C/km) (Turcotte et Schubert, 2002).

L'évolution de la géothermie a aussi été marquée par trois autres avancées scientifiques. La première est l'utilisation des lignes isothermes par Von Humbolt en 1817. La deuxième est le fondement mathématique de la conduction thermique par Fourier en 1824. Il aurait également été le premier scientifique à suggérer que les gaz présents dans l'atmosphère sont susceptibles de provoquer une augmentation de la température à la surface de la Terre. Enfin, la troisième est l'enregistrement des valeurs de flux thermiques. Anderson, en 1934, a effectué les premières estimations du flux de chaleur, en Angleterre, à partir de gradients géothermiques mesurés en profondeur et de la conductivité thermique des roches. Toutes ces avancées montrent qu'avant même la découverte de la radioactivité la communauté scientifique avaient déjà une bonne image des caractéristiques thermiques des couches géologiques de sub-surface.

En 1896, Becquerel découvre la radioactivité. Il découvre alors la principale source de chaleur interne de la Terre. Joly (1909) propose que la désintégration d'éléments radioactifs conduit au réchauffement du manteau terrestre et engendre le processus de convection thermique. Dans les années 1960, la sortie des publications de Tozer (1965), Turcotte et al. (1973), Schubert et al. (1979) a permis de considérer l'idée que la convection thermique est le principal mode de transfert de chaleur à l'intérieur de la Terre. En 1912, Wegener jette les fondations de la théorie de la dérive des continents, mais sans en expliquer le moteur. Holmes (1930, 1931) propose que la convection est l'une des forces susceptibles d'être à l'origine des mouvements horizontaux de la surface terrestre.

La convection naturelle des fluides dans des milieux géologiques poreux et homogènes a été étudiée pour la première fois par Lapwood (1948). En 1979, Murphy développe la première étude sur la circulation des fluides au sein de zones faillées.

En proposant une approche théorique du nombre de Rayleigh, il met en avant des instabilités thermiques verticales liées à des cellules de convection. Ce transfert de chaleur par un mouvement de matière permet de concentrer des anomalies thermiques positives et négatives au sein de zones faillées. Le concept de circulation convective a ensuite été utilisé pour expliquer des conditions thermiques anormales dans des régions où le flux de chaleur ne peut être expliqué par des modèles purement conductifs (Elder, 1965; Palmason, 1967; Williams et al. 1974), où le transfert de chaleur s'effectue sans mouvement de matière.

Par exemple, en Islande, des mesures de gradients géothermaux ont été effectuées sur des forages localisés au sein des fractures sub-verticales. En surface, les gradients géothermaux sont supérieurs à 100°C/km (Fig 2). Puis, jusqu'à 3 kilomètres de profondeur, la température augmente que légèrement (Bodvarson, 1982; Axelsson, 1985; Arnórsson, 1995). De tels profils ne peuvent pas être décrits simplement par un transfert de chaleur purement conductif. La convection thermique serait davantage en mesure d'expliquer ces évolutions de température avec la profondeur. Dans le cas présent, ce mode de transfert de chaleur concentre des températures de l'ordre 100°C à moins de 200 mètres de profondeur. Alors qu'avec un transfert de chaleur purement conductif, et considérant un gradient géothermique moyen pour la croûte continentale européenne, la température est de 15°C à 200 mètres de profondeur.

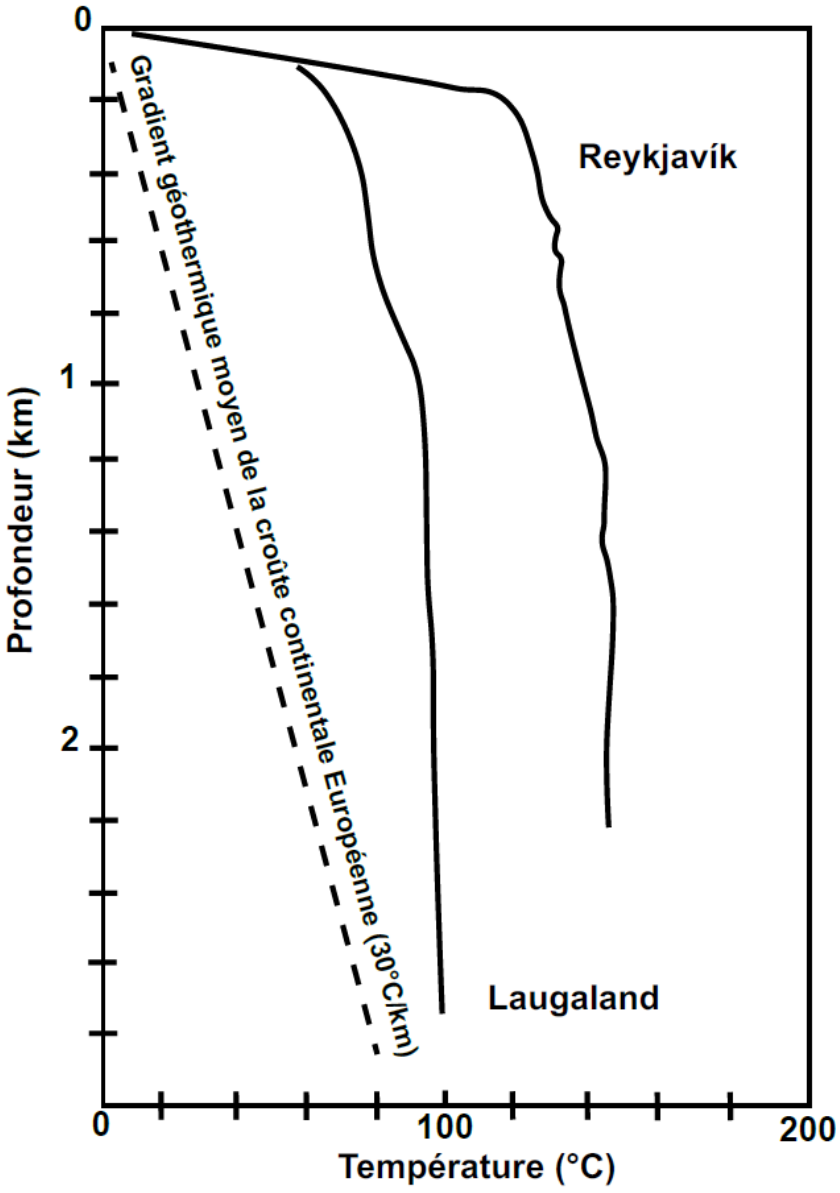

Figure 2 : Mesures de l'évolution de la température avec la profondeur au sein de milieux fracturés, en Islande (Bodvarsson, 1982; Axelsson, 1985, modifié), et comparaison avec le gradient géothermique moyen de la croûte continentale Européenne (30°C/km).

2 L'énergie géothermique dans une transition énergétique écologique

2.1 Depuis une transition énergétique économique

Une *transition énergétique* décrit des changements dans les sources d'approvisionnement en énergie primaire. L'exemple universellement vécu de ce type de changement a été la transition entre des combustibles traditionnels issus de la biomasse (bois, résidu de culture), et des combustibles fossiles (pétrole, gaz naturel, charbon). La figure 3 montre que cette transition énergétique s'est effectuée sur plusieurs décennies. Elle donne un aperçu du temps pouvant être nécessaire à la mise en place d'une telle transition.

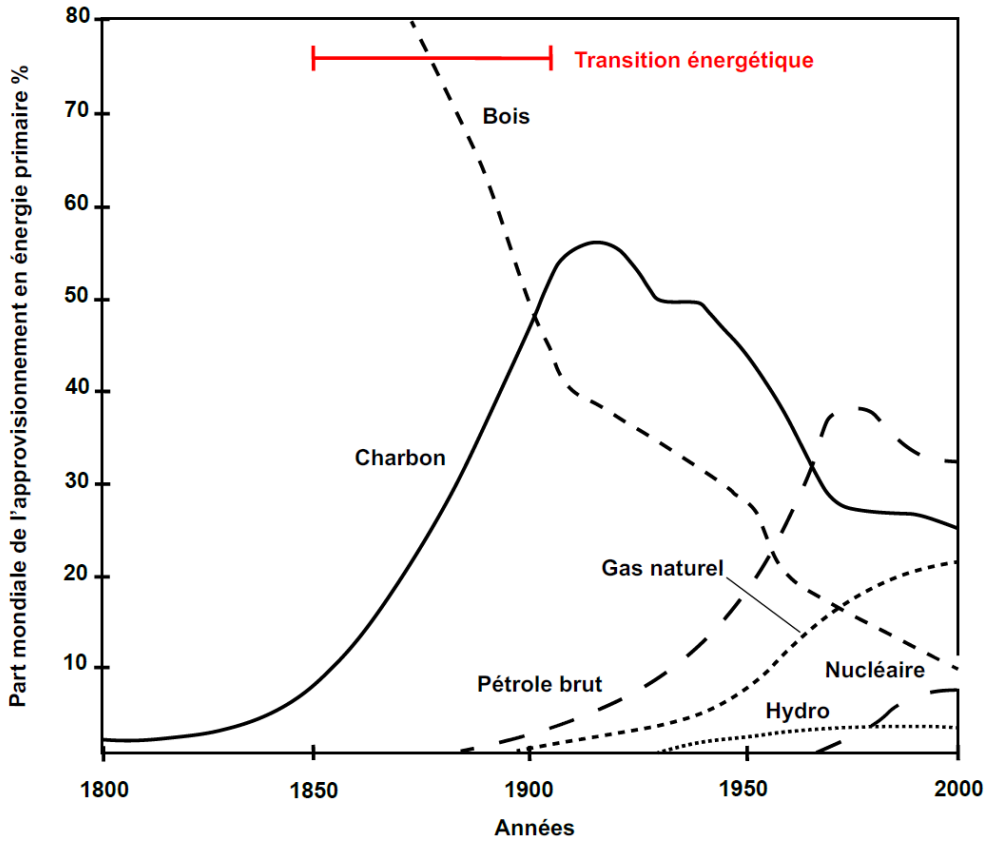

Figure 3 : Parts de la consommation mondiale d'énergie primaire entre 1800 et 2000. La transition énergétique entre des combustibles de biomasse et des combustibles fossiles s'est effectuée sur une période de 50 ans. Modifié d'après Smil (2016).

La découverte de combustibles fossiles, tel que le charbon ou le pétrole brut, a rendu leurs utilisations attrayantes car la quantité d'énergie fournie par unité de masse est beaucoup plus importante que la plupart des ressources de biomasse (Tableau 1).

Tableau 1 : Exemples de quantité d'énergie par unité de masse d'aliments, de combustibles issus de la biomasse et de combustibles fossiles (Merrill and Watt, (1973); Jenkins (1993); USDA (2011), Smil (2016)

	Quantité d'énergie par unité de masse (MJ/kg)
Fruits et légumes	0.8 - 2.5
Tourbes et graminées	5 - 10
Charbon de bois	28 - 32
Pétrole brut	40 - 44

Lorsque les combustibles fossiles sont disponibles et que la densité de population est relativement faible, la croissance économique n'est pas alors limitée par le manque de ressource énergétique. Cependant, ces dernières années, une croissance démographique accrue et une augmentation de la consommation moyenne d'énergie ont modifié ces conditions.

2.2 Vers une transition énergétique écologique

Entre 1850 et 2010, la population est passée de 1.3 milliards d'habitants à 6.9 milliards (Fig 4). La population mondiale va continuer de croître, à un rythme rapide. Selon les estimations actuelles, entre les années 2000 et 2050, la population passera de 6.1 milliards à 9.6 milliards. A cela s'ajoute une augmentation importante de la consommation d'énergie par habitant et par an. En effet, aujourd'hui, cette consommation d'énergie est 15 fois plus importante qu'en 1850 (voir Fig 4).

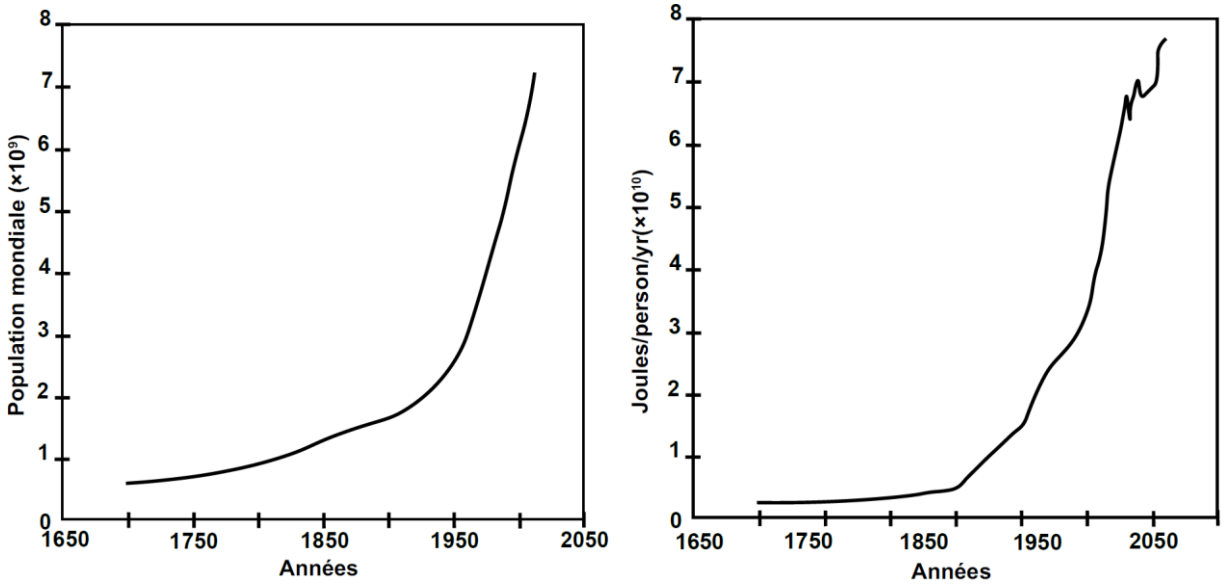

Figure 4: Évolution de la population et consommation d'énergie par personne et par an depuis 1700 (Grübler, 1998; Häfele et Sassin, 1977; www.census.gov/ipc/www/idb/informationGatewaye.php).

Cette croissance démographique et l'augmentation de la consommation d'énergie nécessitent une exploitation accrue des ressources de la Terre, dont les combustibles fossiles. Les émissions de gaz à effet de serre, liées aux exploitations de combustibles fossiles, sont aujourd'hui devenues une préoccupation majeure.

L'analyse de bulles d'air conservées dans des glaciers de l'Antarctique et du Groenland montre que 5,000 ans avant la civilisation préindustrielle les concentrations atmosphériques de CO_2 ont fluctué entre 250 et 290 partie par million (ppm). Aujourd'hui, la concentration de CO_2 dans l'atmosphère est surveillée en permanence à l'observatoire de Mauna Loa (Hawaï). Depuis 1950, une nette augmentation est observable. La moyenne annuelle mondiale est passée de 316 ppm à 400 ppm (Fig 5).

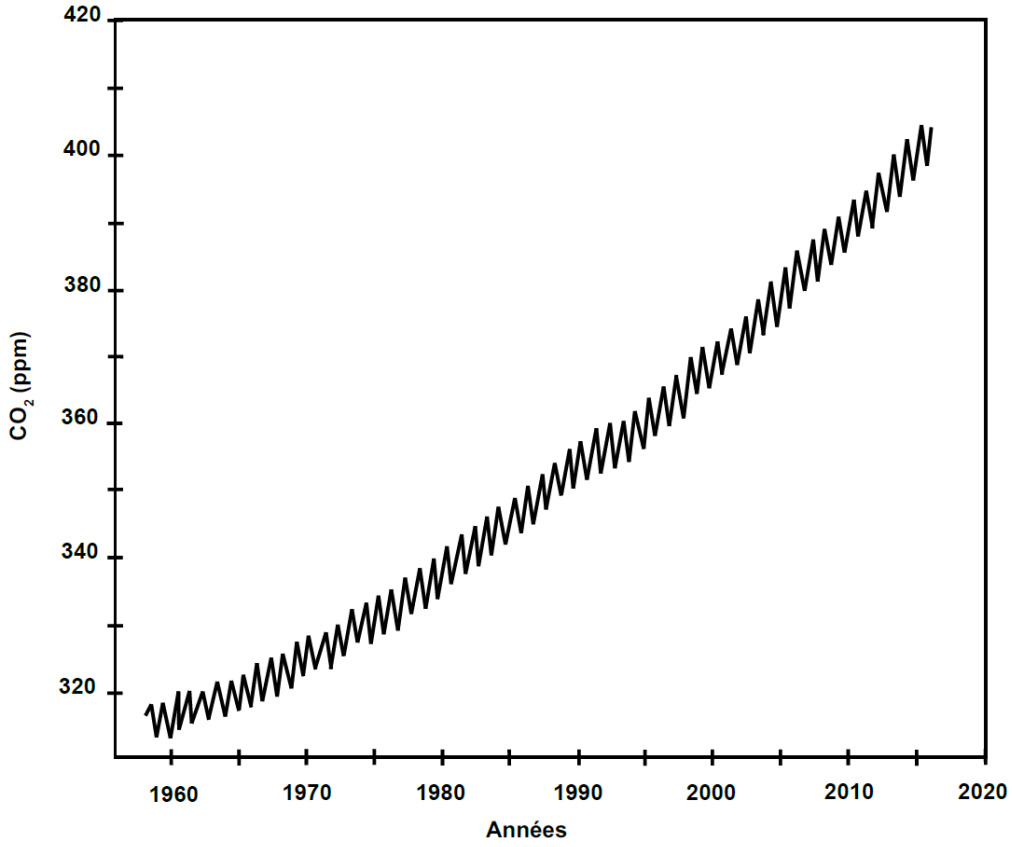

Figure 5 : Mesures des concentrations de CO_2 atmosphérique au Mauna Loa (Hawaï) depuis 1958. Les variations saisonnières annuelles sont représentées par la courbe en dents de scie (extrait des données du CDIAC (2016) et NOAA (2016)- http://www.esrl.noaa.gov/gmd/obop/mlo/.).

En 1988, dans le but de synthétiser des études scientifiques sur le climat, l'ONU forme le Groupe d'experts Intergouvernemental sur l'Evolution du Climat (GIEC). En 2007, le GIEC affirme que le réchauffement climatique depuis 1950 est « très probablement » dû à l'augmentation des gaz à effet de serre d'origine anthropique. En 2014, le degré de certitude est passé à « extrêmement probable ». En 2021, le GIEC évoque une responsabilité « sans équivoque » de l'Homme dans les changements climatiques. Ce dérèglement climatique accélère donc les ambitions de développer des énergies renouvelables avec des programmes comme le *European Green Deal* (https://ec.europa.eu/info/strategy/priorities-2019-2024/european-

green-deal_fr), ou le *Sustainable Energy for All* (https://www.seforall.org/). Marquant ainsi une volonté de tendre vers des énergies bas carbone, ces choix politiques dessinent une nouvelle transition énergétique, écologique. Cette volonté est accentuée lorsque des événements naturels montrent à la civilisation moderne sa vulnérabilité. Même si l'effet direct du déclin des émissions de CO_2 par la pandémie du SRAS-CoV-2 est négligeable (Forster et al. 2020), ces événements permettraient d'accélérer la transition énergétique de certains pays. Alors qu'en 1850 la transition énergétique a été motivée par de meilleurs rendements économiques, aujourd'hui, cette nouvelle transition énergétique est motivée par la nécessité de limiter nos émissions de CO_2, et donc par l'utilisation de ressources bas-carbone.

2.3 Une transition énergétique écologique

2.3.1 Quelques énergies bas-carbone

Parmi les ressources énergétiques bas-carbone, le nucléaire est mentionné comme étant une alternative majeure aux combustibles fossiles. L'énergie produite par la fission d'atomes n'émet pas de CO_2, mais elle nécessite des installations très lourdes. Le principal risque de l'utilisation de l'énergie nucléaire est le *Maximum Credible Accident (MCA).* Même si les scientifiques et les ingénieurs tentent de minimiser ce risque, les accidents de Three Mile Island (États-Unis), en 1979, de Tchernobyl (Ukraine), en 1986, et de Fukushima (Japon), en 2011, ont mis en évidence des conséquences désastreuses sur l'Homme et l'environnement.

L'autre problème majeur de l'utilisation de l'énergie nucléaire est la gestion des déchets radioactifs. En 2013, EDF estime qu'après 40 ans d'exploitation du parc nucléaire français, le volume de déchet de vie longue (concentrant 99.9% de la radioactivité) est de 6,700 m^3. A titre de comparaison, un gymnase municipal de taille moyenne (34 m de long, 28 m de large, 8 m de hauteur) a un volume de 7,616

m^3. Si après 40 ans d'exploitation, le volume de déchet les plus radioactifs paraît faible par rapport à l'énergie produite, à ce jour, les problèmes liés à la gestion de ces déchets ne sont pas résolus.

Dans ce contexte, l'énergie solaire et l'énergie éolienne peuvent être des énergies alternatives. Bien que dans la production d'énergie, la quantité de CO_2 relâchée dans l'atmosphère soit nulle, ce sont des énergies assujetties aux conditions climatiques et météorologiques (Goldenberg, 2000; Tester et al. 2006), et dont l'emprise au sol est importante. Par exemple, le complexe de Noor Ouarzazate (Maroc) s'étend sur 30,000 m^2 (voir Fig 6). Même si la production d'électricité est différente, à titre de comparaison, une centrale géothermique équipée d'aérocondenseurs, de puits, et d'un bassin, a une superficie globale 10 fois moins importante. En sus d'avoir une faible emprise au sol, l'énergie géothermique ne dépend pas des conditions climatiques et météorologiques.

De plus, la quantité d'énergie présente dans la croûte terrestre est plus que suffisante pour satisfaire au besoin énergétique mondial. En effet, considérant toutes activités humaines confondues, l'Agence Internationale de l'Énergie estime à 0.432 EJ (1 EJ = 10^{18} J) la consommation mondiale d'énergie. Dickson and Fanelli (2013) estiment que la quantité d'énergie géothermique dans la croûte terrestre est de 5.4 $\times$ 10^9 EJ.

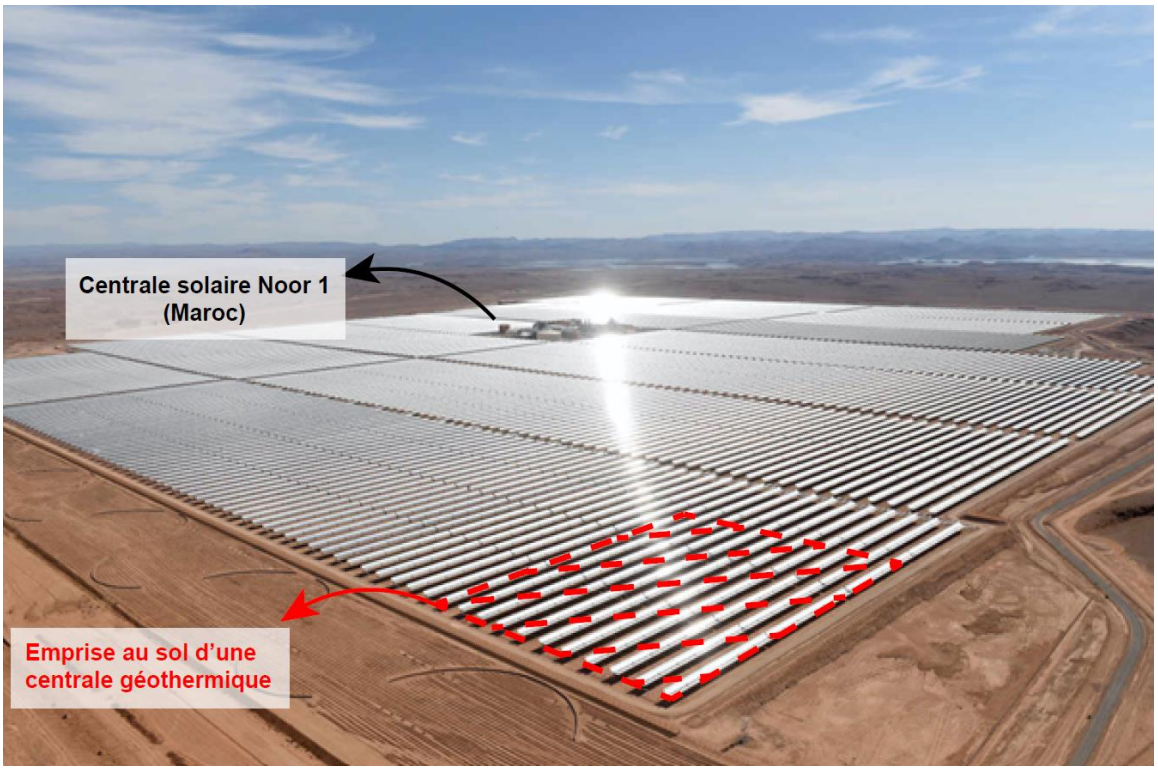

Figure 6 : Emprise au sol de la Central Solaire Noor 1 à 20 km de Ouarzazate (Maroc), comparée à l'emprise au sol d'une centrale géothermique composée d'aérocondenseurs, d'un doublet, et d'un bassin (image source : AFP, modifié).

3 L'énergie géothermique

En tant que ressource énergétique, l'utilisation de la géothermie est ancienne. Il y a 2000 ans les habitants de Pompéi l'utilisaient pour chauffer des habitations. En 1332, la ville de Chaudes-Aigues (France, Massif central) a développé le premier système de chauffage urbain alimenté par des eaux chaudes de 82°C. En 1904, P. G. Conti lance la première production d'électricité à partir de la géothermie, à Larderello (Italie, Toscane). Par la suite, hormis quelques exceptions,

l'énergie géothermique n'a pas joué un rôle important dans la production d'électricité avant la seconde moitié du XX^{e} siècle. En quelques exemples, la centrale de Wairakei en Nouvelle-Zélande a été mise en service en 1958. En 1960, le centre The Geysers, dont la capacité est aujourd'hui de 1517 MW, est ouvert aux États-Unis, au Nord de San Francisco. Celle de Cerro Prieto, au Mexique, ouvre en 1970, et a aujourd'hui une capacité de 820 MW. En comparaison avec l'énergie nucléaire, en France, plus de la moitié des réacteurs nucléaires ont une puissance d'environ 900 MW (www.edf.fr).

Aujourd'hui, l'énergie géothermique est utilisée comme ressource énergétique renouvelable dans plus de 90 pays (Lund et al. 2020). Dans le monde, la capacité installée pour la production d'électricité est de 16.0 GWe, correspondant à une production annuelle d'électricité de 95 GWh (Huttrer, 2020; Lund et al. 2020, www.thinkgeoenergy.com). L'énergie géothermique peut être utilisée pour produire de l'électricité, mais également pour l'utilisation de la chaleur. Des classifications permettent de séparer les différents types de géothermie.

3.1 Classification de l'énergie géothermique

En se basant sur la température, les systèmes géothermaux sont classés en quatre catégories :

- La géothermie Très Basse Température (T < 30°C). Ce type de géothermie est utilisé pour le chauffage individuel, ou le collectif réduit.

- La géothermie de Basse Température (30°C < T < 90°C). Ce type de gisement se trouve à quelques centaines de mètres de profondeur et jusqu'à 2500 m. On en retrouve dans des bassins sédimentaires, riches en roches

poreuses (des grès ou des sables), permettant aux fluides de circuler librement. La géothermie BT est utilisée en pisciculture, en chauffage collectif ou individuel.

- La géothermie Moyenne Température (90°C < T < 150°C). Ce type de gisement se trouve à moins de 1 km de profondeur dans des zones volcaniques, ou entre 2 km et 4 km de profondeur dans des bassins sédimentaires. La géothermie MT est utilisée dans un cadre industriel, ou dans le séchage de produits agricoles.

- La géothermie Haute Température (T > 150°C). Habituellement, ces gisements se situent entre 1 km et 3 km de profondeur, au niveau des zones volcaniques, ou des limites de plaques tectoniques. La géothermie HT est principalement utilisée pour la production d'électricité. Cette étude se place dans cette dernière catégorie. Nous allons nous intéresser à des cibles géologiques hébergeant potentiellement des gisements géothermaux de HT. Ces cibles peuvent se retrouver au niveau des zones volcaniques, en limite de plaques, mais également dans d'autres contextes géologiques. Avant cela, regardons à grande échelle, les contextes géologiques et géodynamiques aujourd'hui reconnus comme étant favorables à l'émergence de ces réservoirs.

4 Contrôle géodynamique et structural des systèmes géothermaux de Haute Température

4.1 Contrôle géodynamique

En première approche les sources d'eaux chaudes et les fumerolles sont des indices géologiques de surface pour l'exploration de systèmes géothermaux de HT. A l'échelle du globe, la répartition de ces indices de surface va dépendre du contexte géodynamique. La classification de Moeck (2014), reprise par Jolie et al. (2020), définit un ensemble de contextes géodynamiques et de modes de transfert de chaleur favorables au développement des systèmes géothermaux de HT (Fig 7).

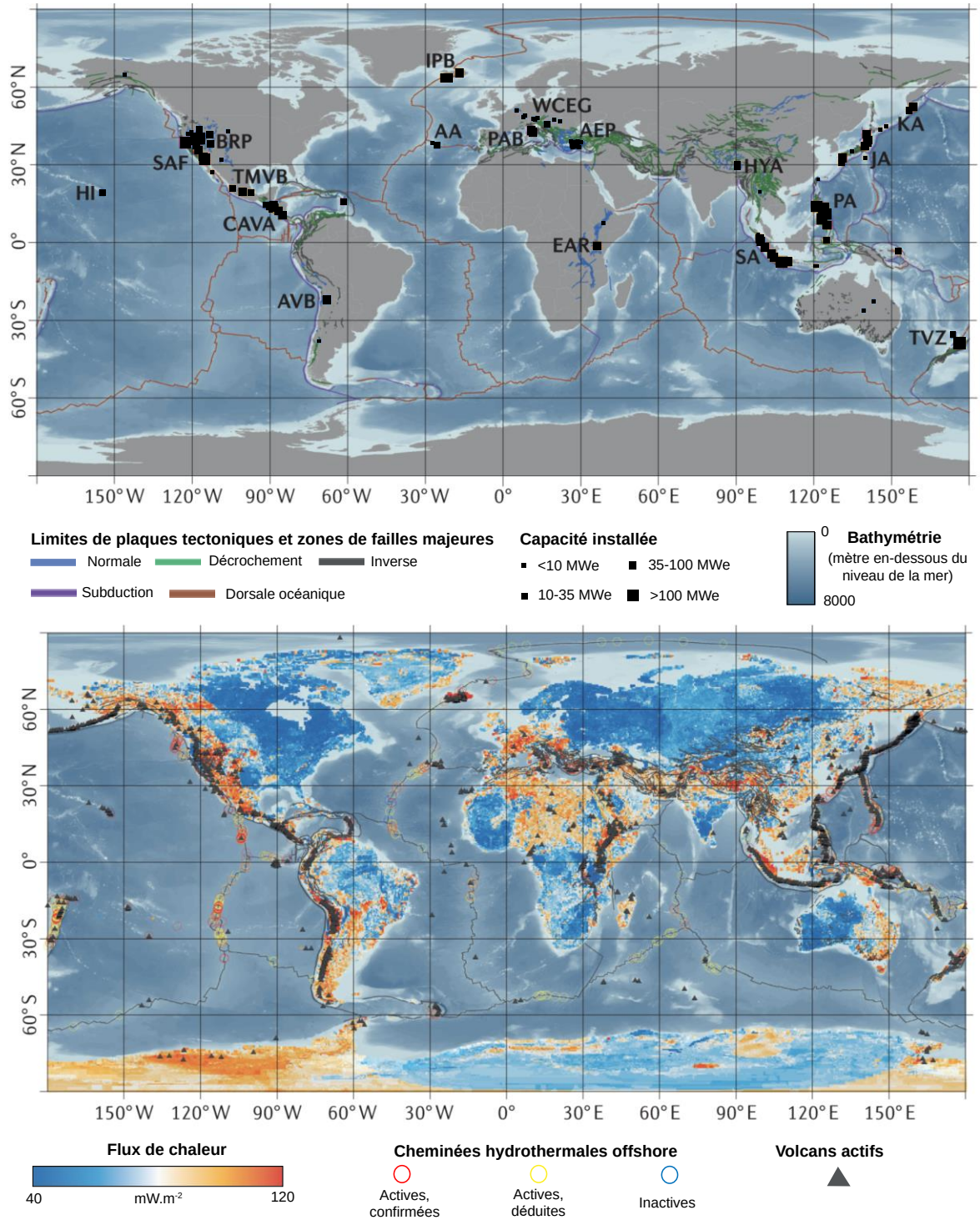

Figure 7 : Localisation de centrales géothermiques dans différents contextes géodynamiques. Actuellement, les réservoirs géothermaux de HT sont principalement localisés proches des zones volcaniques et/ou des régions d'amincissement crustale. Les acronymes suivants sont traduits de l'anglais : AA, Archipel des Açores; AEP, Province d'Extension Égéenne; AVB, Ceinture Volcanique Andine; BRP, Province du Basin & Range; CAVA, Arc Volcanique d'Amérique Centrale; EAR, Rift Est Africain; HI, Archipel d'Hawaï; HYA, Himalaya; IPB, Frontière de Plaque d'Islande; JA, Système d'Arc Japonais; KA, Arc des Kouriles; PA, Arc Philippin; PAB, Ceinture Pré-Appenine; SA, Arc de la Sonde; SAF, Zone de Failles de San Andreas; TMVB, Ceinture Volcanique Trans-Mexicaine; TVZ, Zone Volcanique de Taupo; WCEG, Système Géothermique d'Europe de l'Ouest et d'Europe Centrale. (Après Moeck, 2014; Jolie et al. 2020, modifié. Données : Lucazeau, 2019; Beaulieu et Szafranski, 2020; Styron, 2019; American Geological Institute; GEBCO Compilation Group).

Les systèmes géothermaux de HT, aujourd'hui connus, se trouvent principalement au niveau des arcs magmatiques, au niveau des zones de subduction (Zone Volcanique de Taupo, Ceinture Volcanique Andine, Arc de la Sonde ou l'Arc Philippin), au niveau de zones de failles transformantes (la Zone de Failles de San Andreas), en contexte intracontinental (Rift Est Africain) et aux niveaux de points chauds (Yellowstone, La Réunion, l'Islande ou Hawaï). On en retrouve également dans des bassins en pull-apart (Salton Trough), ainsi que dans des rifts magmatiques et amagmatiques (Rift Est Africain, Basin and Range, Islande).

Les systèmes géothermaux particulièrement productifs, présent notamment en Islande ou en Nouvelle-Zélande, correspondent à des contextes géologiques magmatiques avec extension crustale (Arnórsson, 1995; Wilson et Rowland, 2016). Des contextes géologiques extensifs amagmatiques abritent également de grandes provinces géothermiques comme la province du Basin and Range (Etats-Unis), ou la province Egéenne de l'Ouest de la Turquie. En se basant sur des études de terrain dans cette même zone, Roche et al. (2019) ont suggéré que l'intersection entre différentes familles de faille représente un facteur de contrôle de premier ordre sur des systèmes géothermaux. Quelques années auparavant, un inventaire effectué dans le district de Great Basin (province du Basin & Range, USA) montre une forte corrélation entre la distribution des centrales géothermiques et la présence de failles ; des structures tectoniques potentiellement perméables (Faulds et Hinz, 2015) (Fig 8). Ces éléments mettent donc en lumière un contrôle structural sur les systèmes géothermaux.

4.2 Contrôle structural

Pour les systèmes géothermaux de HT, les environnements structuraux les plus propices sont les terminaisons de faille (Fig 8C), les chevauchements (Fig 8D), les intersections de failles (Fig 8E), les zones d'accommodations (Fig 8F), les zones

de transfert au niveau de système en décrochement (Fig 8G) ainsi que les bassins pull-apart (Fig 8G) (Faulds et al. 2006, 2011; Faulds et Hinz, 2015).

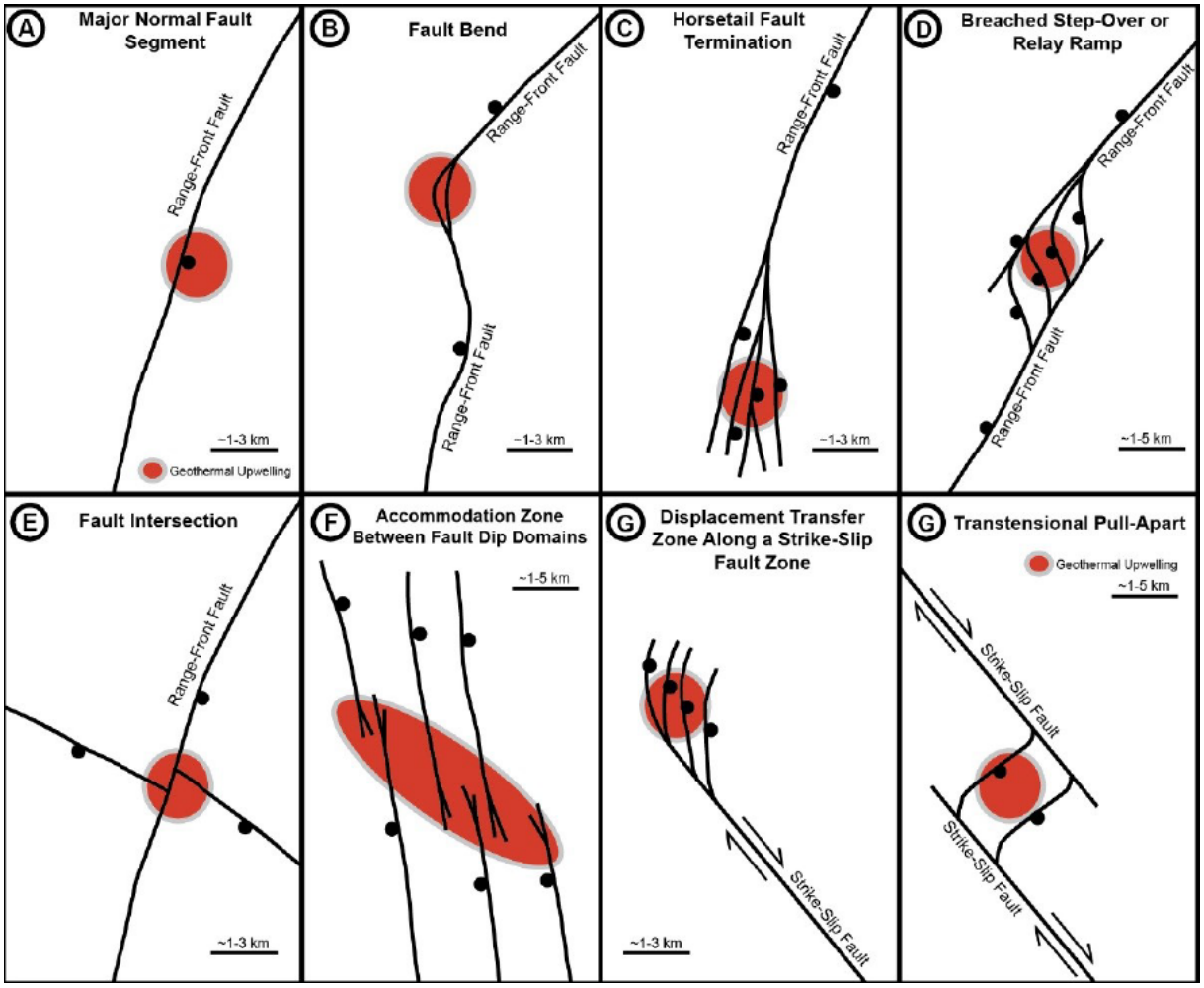

Figure 8 : Exemples de caractéristiques structurales favorables aux systèmes géothermaux du district de Great Basin (province du Basin and Range, USA) (Faulds et Hinz, 2015). Les zones rouges marquent les localisations approximatives de réservoirs géothermaux hypothétiques A. Faille normale majeure;; B. Faille normale coudée; C. Terminaison de faille en queue de cheval; D. Chevauchement ou zone de relais; E. Intersection de failles; F. Zone d'accomodation; G. Zone de transfert au niveau de système décrochant; G. Système en transtension, ouverture en pull-apart.

L'ensemble de ces objets géologiques présentent une forte densité de failles et d'interconnexions de fractures. Ces caractéristiques confèrent au milieu une capacité naturelle à laisser circuler les fluides (Faulds et al. 2006; Coolbaugh et al. 2007;

Lechler et Coolbaugh 2007; Dezayes et al. 2010; Jolie et al. 2015; Siler et al. 2018; Souque et al. 2019), ce qui définit la perméabilité.

La perméabilité est un facteur de premier ordre sur le contrôle de la circulation des fluides (Darcy, 1856) et par conséquent un paramètre de contrôle sur la localisation des réservoirs géothermaux (Gleeson and Ingebritsen, 2016). Les ressources géothermiques conventionnelles désignent des systèmes géothermaux présents dans des roches à forte porosité et perméabilité. Elles se dissocient des ressources géothermiques non-conventionnelles qui se situent dans des roches à faible porosité et perméabilité. Afin de favoriser le développement de la géothermie dans des systèmes non-conventionnels, des réservoirs artificiels peuvent être créés. Pour ce faire, la technologie des Enhanced (ou Engineered) Geothermal System (EGS) est utilisée.

5 Les Enhanced (ou Engineered) Geothermal System

La technologie des EGS consiste à stimuler des réservoirs potentiels dans le but de pouvoir extraire l'énergie présente dans le milieu faiblement perméable. Les EGS augmentent la perméabilité du système par différentes phases d'injection de fluides. La pression de fluide va augmenter, provoquant des processus d'hydro-fracturing et/ou d'hydro-shearing. L'application de la méthode des EGS (voir Fig 9) a été démontrée sur le projet géothermique de Soultz-sous-Forêts, (Alsace, France) (Genter et al. 2010) ou Fenton Hill, (Nouveau-Mexique, États-Unis) (Brown et al. 2012).

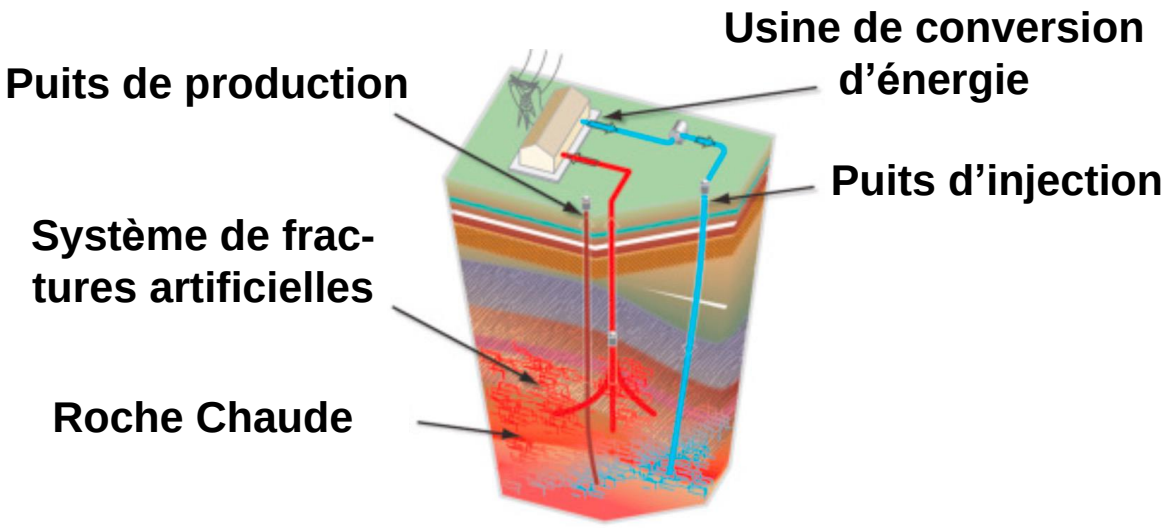

Figure 9 : Représentation schématique du fonctionnement d'une centrale géothermique de type EGS (Olasolo et al. 2016).

Cependant, la sismicité induite par les phases d'injection a mis en péril plusieurs projets géothermiques. A la suite d'une série d'événements sismiques induits, le projet géothermique de Bâle (Suisse) a été abandonné (Deichmann and Giardini, 2009; Terakawa et al. 2012; Gaucher et al. 2015), engendrant des pertes financières estimées à hauteur de 60 millions de dollars.

Plus récemment, en France, les phases d'injection du projet GEOVEN (GEOthermie à VENdenheim), en Alsace (France), ont provoqué une série d'événements sismiques induits (Schmittbuhl et al. 2021). Un séisme de magnitude M = 3 a ainsi été enregistré le 12 novembre 2019, un autre de M = 3.6 est survenu le 4 décembre 2020, enfin un séisme de magnitude M = 3.9 a été enregistré le 26 juin 2021. Ces événements ont provoqué l'arrêt définitif du projet et des interrogations au sein de l'opinion publique sur d'autres cibles potentielles (Fig 10).

Le Parisien

Environnement

La géothermie coulée à Strasbourg pour cause de séisme

Alors que la préfecture du Bas-Rhin interdit l'exploitation de la centrale géothermique de Vendenheim suite à un séisme important, l'avenir de cette énergie est en question dans l'agglomération strasbourgeoise.

08/12/2020

LA MONTAGNE À LA UNE VIE LOCALE SPORTS LOISIRS ÉCONOMIE

Energie

Cinq questions pour comprendre le projet de centrale de géothermie profonde à Saint-Pierre-Roche (Puy-de-Dôme)

SAINT-PIERRE-ROCHE ÉCONOMIE BTP - INDUSTRIE ENVIRONNEMENT PUY-DE-DÔME

Publié le 15/02/2021 à 11h53

*Figure 10 : Article de presse d'un hebdomadaire national (*Le Parisien*) faisant suite aux séismes induits ressentis dans l'agglomération de Strasbourg (Alsace, France). Comme le montre l'article de presse d'un quotidien régional (*La Montagne*), ces événements provoquent des interrogations sur d'autres cibles potentielles.*

Afin de faciliter le développement de cette énergie, verte, durable, qui ne dépend ni du climat, ni de la météo, il sera ici étudié des cibles géologiques en domaine purement crustal, dont la perméabilité naturellement présente serait suffisante pour permettre aux fluides de circuler et de localiser des anomalies positives de température à des profondeurs potentiellement exploitables. Dans ces conditions, il apparaîtrait que la présence d'une source de chaleur externe (présence d'une chambre magmatique, ou contexte d'amincissement crustal) ne serait plus une condition *sine qua non* pour une exploitation géothermique électrogène. Si, à l'échelle d'un pays ou d'une région, il est habituel de cibler des zones anormale-

ment chaudes pour la géothermie de Haute Température, il pourrait alors être envisageable de cibler des zones anormalement perméables au sein de la croûte terrestre. Si ce potentiel est avéré, cela pourrait augmenter considérablement le nombre de cibles pour la géothermique électrogène et cette géoressource pourrait alors jouer un rôle décisif dans la nouvelle transition énergétique, écologique.

6 Les Zones de Failles Crustales (ZFC) comme systèmes géothermiques électrogènes

Si les failles sont reconnues depuis longtemps comme des zones préférentielles de drainage pour les fluides (Caine et al. 1996; Faulkner et al. 2010; Bense et al. 2013; Haines et al. 2016), il n'en reste pas moins que le concept de ZFC n'a jamais été annoncé comme de potentielles ressources renouvelables et économiques. Par conséquent, elles demeurent largement inexplorées et donc inexploitées. Les ZFC sont de larges structures géologiques d'échelle crustale, localisant la déformation (Ben-Zion and Rovelli, 2014; Chester and Logan, 1986; Schulz and Evans, 1998; Sammis et al. 2009) et modifiant les propriétés mécaniques de la croûte jusqu'à la Transition Ductile-Fragile (350-400°C). En domaine continental, les ZFC sont largement répandues. On en retrouve en Allemagne, au Chili, au Canada, en Chine, en Suède, en Russie, en Espagne,… (respectivement Achtziger-Zupančič et al. 2017; Lahsen et al. 2010; Duan et al. 2017; Yang et al. 2016; Duan et al. 2017; Juhlin et Sandstedt, 1989; Lund and Zoback, 1999; Faulkner et al. 2003). Ces occurrences multiples nécessitent de considérer un ensemble de paramètres géologiques et physiques susceptibles de contrôler et/ou de limiter la présence d'un réservoir géothermal HT au sein de ces systèmes naturellement perméables.

Des traces de circulations de fluides jusque dans la croûte moyenne (10-20 km de profondeur) ont été observées dans différents contextes géologiques. Des fractures remplies de fluides ont par exemple été observées au sein du forage profond SG3 de la péninsule de Kola (Russie) (Kozlovsky, 1984) et du forage profond KTB, en Allemagne (Grawinkel and Stöckhert, 1997; Ito and Zoback, 2000). Par ailleurs, Famin et al. (2004) suggère une infiltration massive de fluide météorique jusqu'à 10-15 km de profondeur au sein d'une zone de cisaillement sur l'île de Tinos (Grèce). De même, Siebenaller et al. (2013) ont démontré que l'infiltration d'eau météorique peut s'effectuer jusqu'à la Transition-Ductile-Fragile (TDF) (aux alentours de 8 km de profondeur) au sein du détachement de Naxos (Grèce). Au-delà de la TDF, la déformation du granite entraîne une réduction de la porosité et vraisemblablement de la perméabilité (Violay et al. 2017). Cependant, ces auteurs notent également que les microfissures peuvent rester ouvertes dans le granite à haute température (900°C) et haute pression (100 MPa), entraînant ainsi une perméabilité de la matrice supérieure à celle du matériau intact. La possibilité d'extraire de l'énergie depuis un fluide chaud, drainé par un système fracturé, va dépendre essentiellement de la distribution de la perméabilité au sein de ces conduits. Ainsi, une Zone de Faille Crustale, naturellement perméable, pourrait correspondre à un nouveau type de système géothermique de haute-température, où des fluides chauds et profonds, s'écoulent depuis la Transition Ductile Fragile (350-400°C) jusqu'à la surface.

Dans ce contexte, la société TLS-Geothermics, acteur de la prospection de gisements géothermiques français, souhaite améliorer la connaissance de son Permis Exclusif de Recherche (PER) de "La Sioule" (Puy de Dôme, Massif Central français). Ce PER abrite une zone de faille minéralisée de 3 km de large et 30 km de long (la zone de faille de Pontgibaud) située à proximité d'un corps granite (le granite de Gelle; Négroni, 1981) où des resurgences thermominérales riches en CO_2 sont présentes. Dans la zone de Pontgibaud, le gradient géothermique proche de la surface, est de 37-41°C/km (International Heat Flow Commission database).

Pontgibaud est donc considéré comme un premier cas d'étude ideal pour l'exploration du potentiel géothermique Haute Température des Zones de Failles Crustales.

7 Objectifs et méthodologies

Cette étude vise à comprendre le potentiel géothermique électrogène de nouvelles cibles géologiques pour la géothermie HT : les Zones de Failles Crustales. Cette thèse a donc pour principal objectif la compréhension générale de la dynamique des fluides hydrothermaux dans les ZFC. La corrélation entre études de terrain, données pétrophysiques et modélisations numériques devrait permettre d'améliorer la phase d'exploration géothermique des ZFC. Ce travail vise donc à déterminer :

Comment s'organise un système hydrothermal associé à des Zones de Failles Crustales, et quels en sont les facteurs de contrôle ?

Pour ce faire, une première approche consistera à faire une revue des paramètres susceptibles d'impacter la circulation des fluides dans un système fracturé en domaine de socle. Cette première étape permettra d'isoler certains facteurs dont les effets sur la circulation des fluides et la thermicité d'un milieu fracturé sont encore aujourd'hui inconnus. L'utilisation de la modélisation numérique permettra d'isoler des tendances générales, applicables sur le terrain, et pouvant servir de guide pour l'exploration de ces nouvelles cibles potentielles. Cette revue de la littérature permettra également de mettre en avant les méthodes employées dans l'exploration pour la géothermie Haute Température. Une deuxième approche favorisera ainsi une méthodologie multidisciplinaire (terrain, laboratoire, modélisations numériques grande échelle) sur le PER "La Sioule" de TLS-Geothermics. En outre, cette deu-

xième approche permettra de contraindre qualitativement et quantitativement certains paramètres clefs (structures géologiques, porosités, perméabilités), essentiels à la compréhension d'un système géothermique en 2D et 3D. Ces éléments seront intégrés dans des modélisations numériques de grande échelle. Les résultats de ces modélisations numériques seront comparés avec d'autres données de terrain (géophysiques, températures, flux de chaleur). Il sera ainsi possible d'estimer la profondeur et l'intensité de l'anomalie de température au sein du système hydrothermal de Pontgibaud. Enfin une discussion générale sera portée sur les limites de la méthodologie employée ainsi que des outils utilisés, et plus largement sur le potentiel géothermique des Zones de Failles Crustales avec certains risques associés.

General Introduction (english version)

"*Geothermal energy, potentially the largest – and presently most misunderstood-source of energy"*

Our Choice – A plan to solve the Climat Crisis, Al Gore, 2009

1 Evolution of geothermal concepts

From the Greek *geo* "the Earth", and *thermós* "heat", geothermal energy both refers to a resource and the study of Earth's internal thermal phenomena. Over the past 400 years, the comprehension of geothermal processes has been considerably developed (see Fig 1).

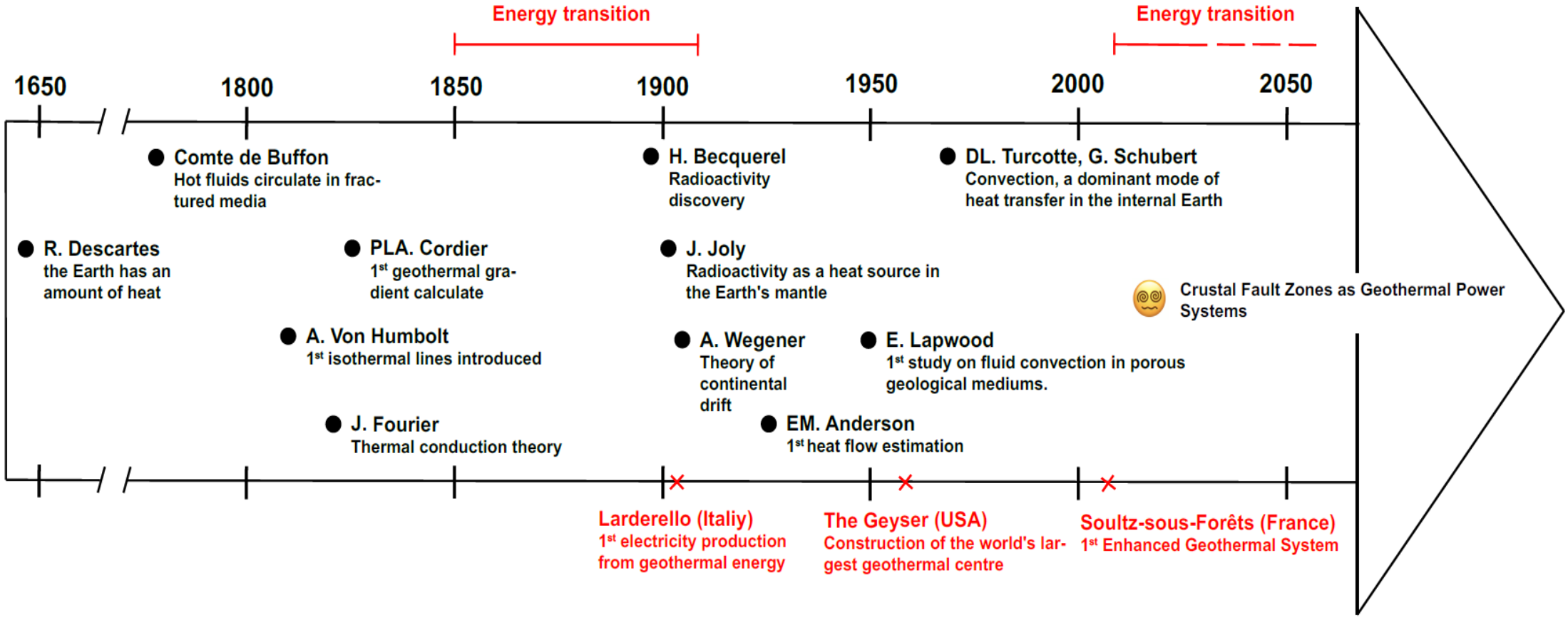

Figure 1 : Setting of this study in the chronological succession of major discoveries of internal thermal phenomena on Earth.

Initially, in 1644, Descartes speculated that the Earth was originally a star. It has a quantity of heat, which dissipates over time. In his work "*Histoire naturelle, générale et particulière, contenant les époques de la nature*" Buffon (1778) suggests that fluids, heated by this internal heat, can circulate in a fractured medium (Extract 1):

> *« [...] mines de sel, de celle de fer en grains, de pyrites & de toutes les autres substances dans la composition desquelles il entre des acides, & dont la première formation n'a pu s'opérer qu'après la chûte des eaux ; ces matières auront été entraînées & déposées dans les lieux bas et dans les fentes de la roche du globe, où trouvant déjà les substances minérales sublimées par la grande chaleur de la Terre, elles auront formé le premier fond de l'aliment des volcans à venir [...]»*

Extract 1 : From Histoire naturelle, générale et particulière, contenant les époques de la nature p. 192, Georges-Louis Leclerc, Comte de Buffon, 1778. Suggesting that in fractures (i.e. « les fentes de la roche ») fluids heated by the internal Earth heat can circulate.

The first measurements of temperature at depth were used to define the geothermal gradient, and thereby constitute a crucial step in the evolution of geothermal concept. These first measurements were made in France, in the mines of Alsace by De Gensanne (Buffon, 1778).

At the end of the 18th century, in the Bex salt mine (canton of Vaud, Switzerland) de Saussure recorded at 37 m depth, a temperature increases of 1°C compared to the surface (Radau, 1880). Cordier (1827) was the first scientist to calculate a geothermal gradient. His results showed that the temperature could increase with depth at a rate of 1°C every 20-25 metres. However, at Grenelle (west of Paris, France), measurements made in a well by Arago and Walferdin (Walferdin, 1837) give an increase of 1°C every 32.3 meters. Finally, this geothermal gradient is quite close to the commonly accepted average value for the European continental crust of 1°C every 33 meters (or 30°C/km) (Turcotte and Schubert, 2002).

The geothermal evolution has also been marked by three other scientific achievements. The first is the use of isothermal lines by Von Humbolt in 1817. The second is the mathematical development of thermal conduction by Fourier in 1824. He would have been the first scientist to suggest that gases in the atmosphere can increase the temperature at the Earth's surface. Finally, the third is the recording of heat flux values. Anderson, in 1934, would have been made the first estimates of heat flux in England from geothermal gradients and the thermal conductivity of rocks. All these achievements show that even before the radioactivity discovery, scientists had a clear knowledge of the thermal characteristics of sub-surface geological layers.

In 1896, Becquerel discovered radioactivity. He then discovered the main source of the Earth's internal heat. Joly (1909) proposed that the decay of radioactive elements leads to the heating of the Earth's mantle and generates the process of thermal convection. In the 1960s, the publications of Tozer (1965), Turcotte et al. (1973), Schubert et al. (1979) made it possible to consider the idea that thermal convection is the main mode of heat transfer within the Earth. In 1912, Wegener established the foundations of the theory of continental drift, but without explaining its driving force. Holmes (1930, 1931) proposed that convection is one of the forces that may be responsible for horizontal movement of the Earth's surface.

Natural fluid convection in porous and homogeneous geological medium was first studied by Lapwood (1948). In 1979, Murphy developed the first study of fluid circulation in faulted zones. By proposing a theoretical approach to the Rayleigh number, he highlighted vertical thermal instabilities associated to convection cells. This heat transfer by material movement allows positive and negative thermal anomalies to be concentrated within faulted zones.

The concept of convective circulation has subsequently been used to explain anomalous thermal conditions in regions where the heat flux cannot be explained by purely conductive heat transfer mode (Elder, 1965; Palmason, 1967; Williams et al. 1974).

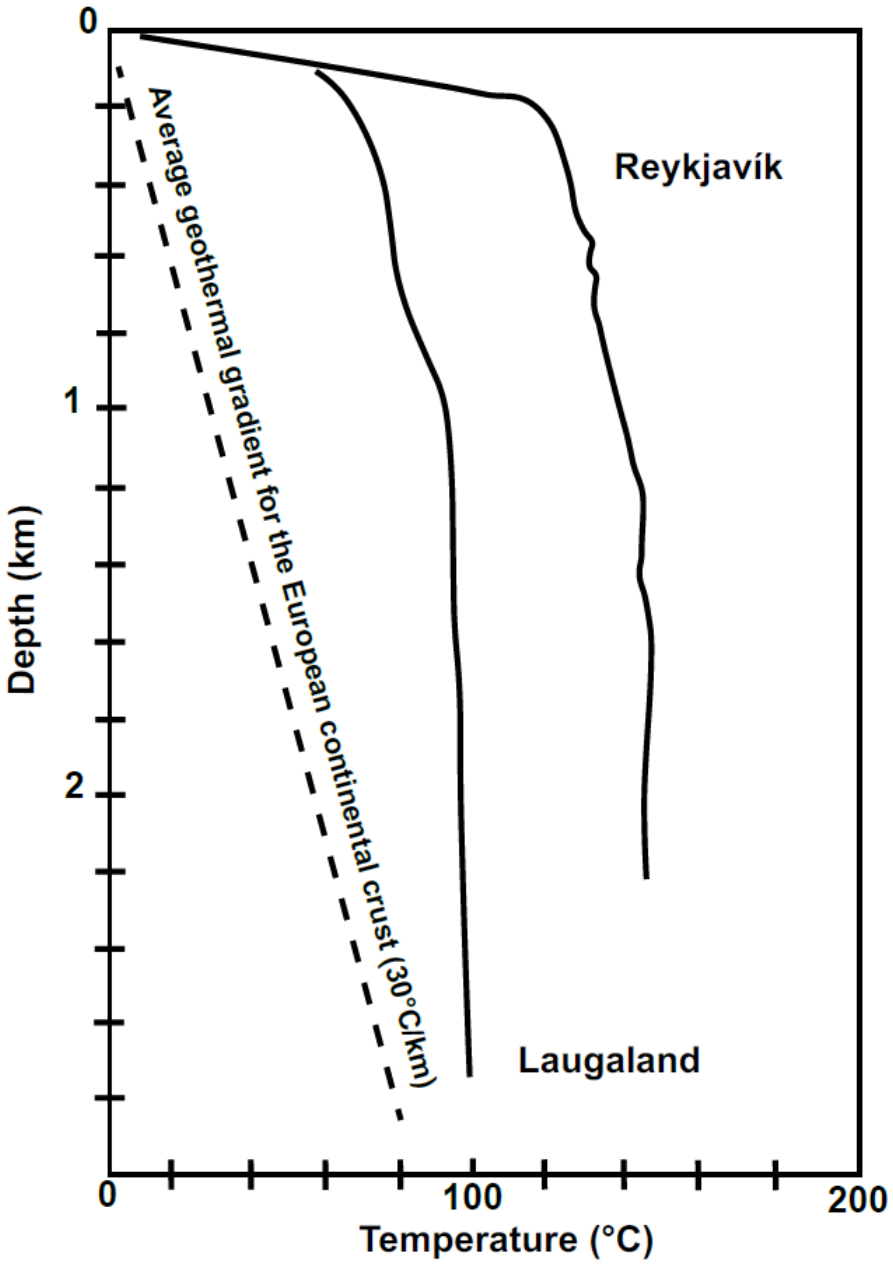

Figure 2 : Measurements of temperature change with depth in fractured media in Iceland (Bodvarsson, 1982; Axelsson, 1985, modified) and comparison with the average geothermal gradient of the European continental crust (30°C/km).

For example, in Iceland, measurements of geothermal gradients have been made on borehole located within sub-vertical fractures and partially sealed dykes. At the surface, geothermal gradients are greater than 100°C/km (Fig 2). Then down to almost 3 km depth, the temperature slightly increases (Bodvarson, 1982; Axelsson, 1985; Arnórsson, 1995). Such profiles cannot be described by purely conductive heat transfer mode. Thermal convection would be better able to explain these temperature evolutions with depth. In this case, the convection heat transfer mode concentrates, temperatures of the order of 100°C at a depth of less than 200 meters. Whereas with purely conductive heat transfer mode, and considering an average geothermal gradient for the European continental crust, the temperature is about 15°C at 200 meters.

2 Geothermal energy in an environmental energy transition

2.1 From an economic energy transition

An *energy transition* describes shifts in the sources of primary energy supply. The best known example of this kind of change has been the transition from traditional biomass fuels (wood, crop residues) to fossil fuels (oil, natural gas, coal). Figure 3 shows that this energy transition took place over several decades. This gives an idea of how long it can take to accomplish such a transition.

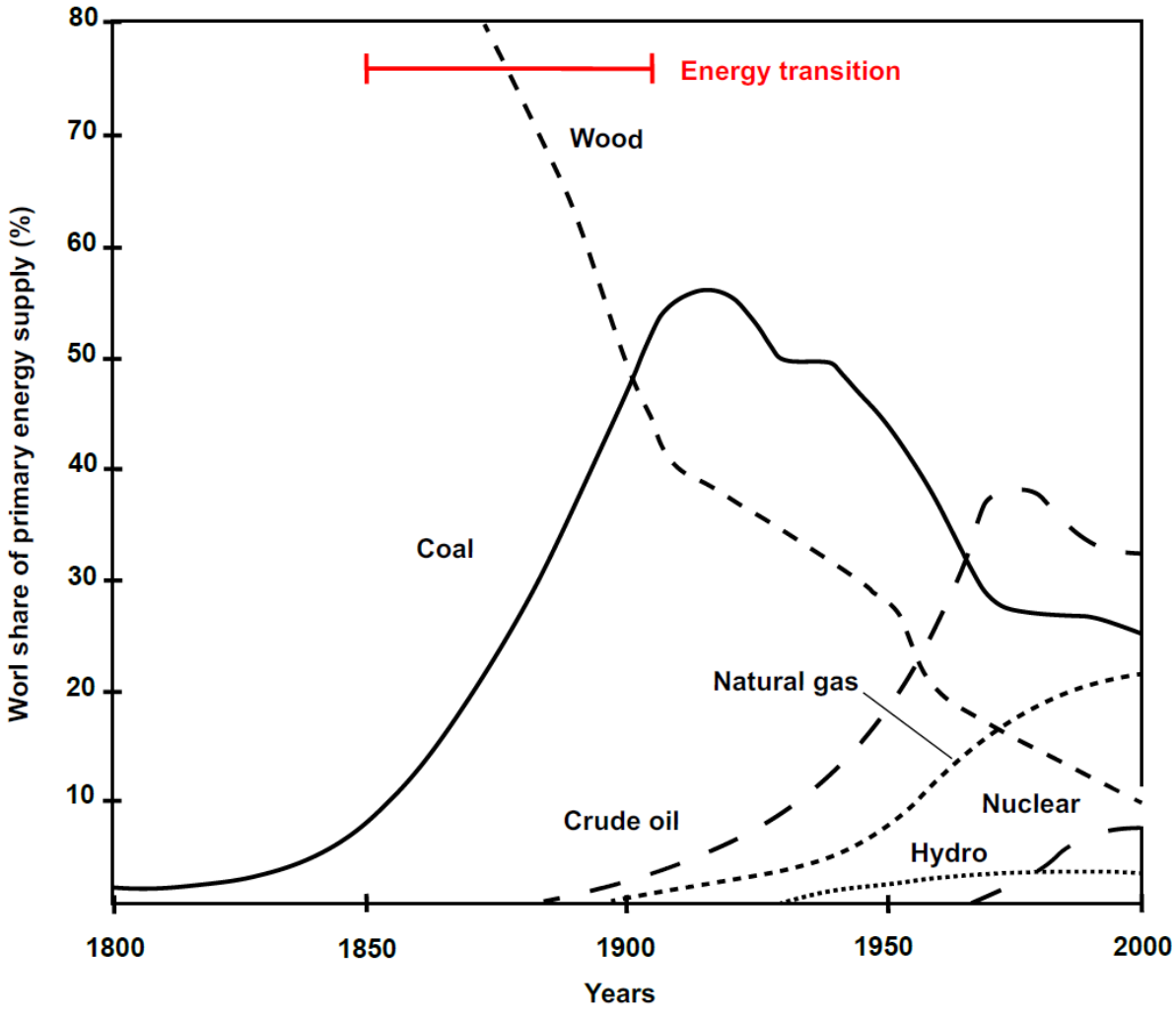

Figure 3 : Global primary energy consumption shares between 1800 and 2000. The energy transition from biomass to fossil fuels took place over a period of 50 years. Modified from Smil (2016).

The discovery of fossil fuels such as coal or crude oil has made their uses attractive because the amount of energy supplied per unit of mass is much greater than most biomass resources (Table 1).

Table 1 : Examples of the amount of energy per unit mass of food, biomass fuels and fossil fuels (Merrill and Watt, 1973; Jenkins, (1993); USDA (2011), Smil (2016).

	Energy quantity per unit of mass (MJ/kg)
Fruits and vegetables	0.8 - 2.5
Peat and grasses	5 - 10
Coal	28 - 32
Crude oil	40 - 44

When fossil fuels are available and the density of population is relatively small, economic growth is not limited by the lack of energy resources. However, the increase in demography and increased average energy consumption have changed these fundamental conditions.

2.2 Towards a green energy transition

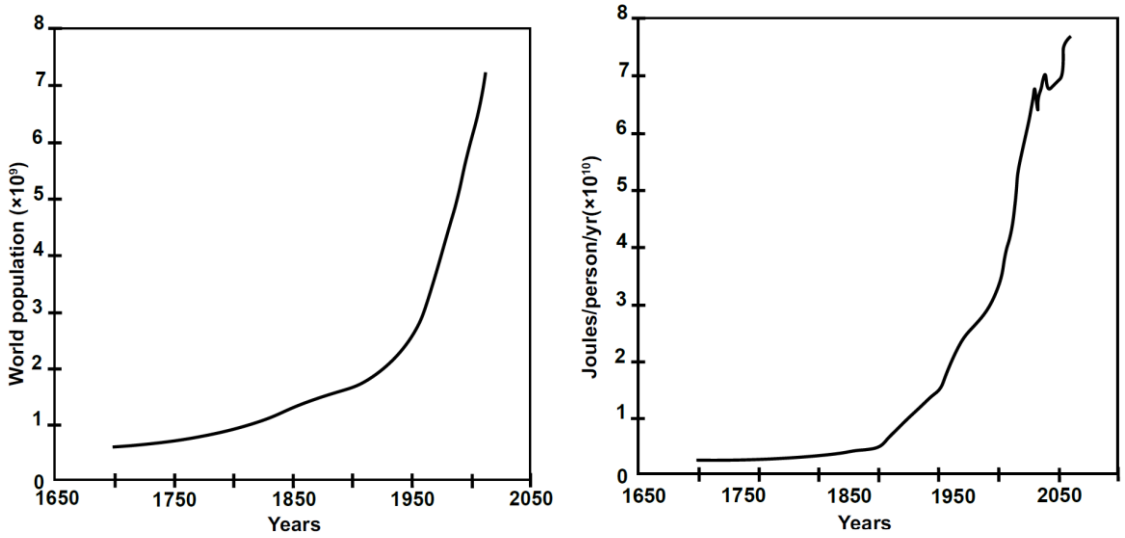

Figure 4 : Population trends and energy consumption per person per year since 1700 (Grübler, 1998; Häfele et Sassin, 1977; www.census.gov/ipc/www/idb/informationGatewaye.php).

Between 1850 and 2010, the population grew from 1.3 billion to 6.9 billion (Fig 4) and the world's population will continue to grow. According to current estimates, between 2000 and 2050, the population will increase from 6.1 billion to 9.6 billion. In addition, there is a significant increase in energy consumption per person and per year. Today, energy consumption is 15 times higher than in 1850 (see Fig 4). This demographic growth and the increase in energy consumption requires an increased exploitation of the Earth's resources, including fossil fuels. Therefore, greenhouse gas emissions from fossil fuel exploitation have become a major concern.

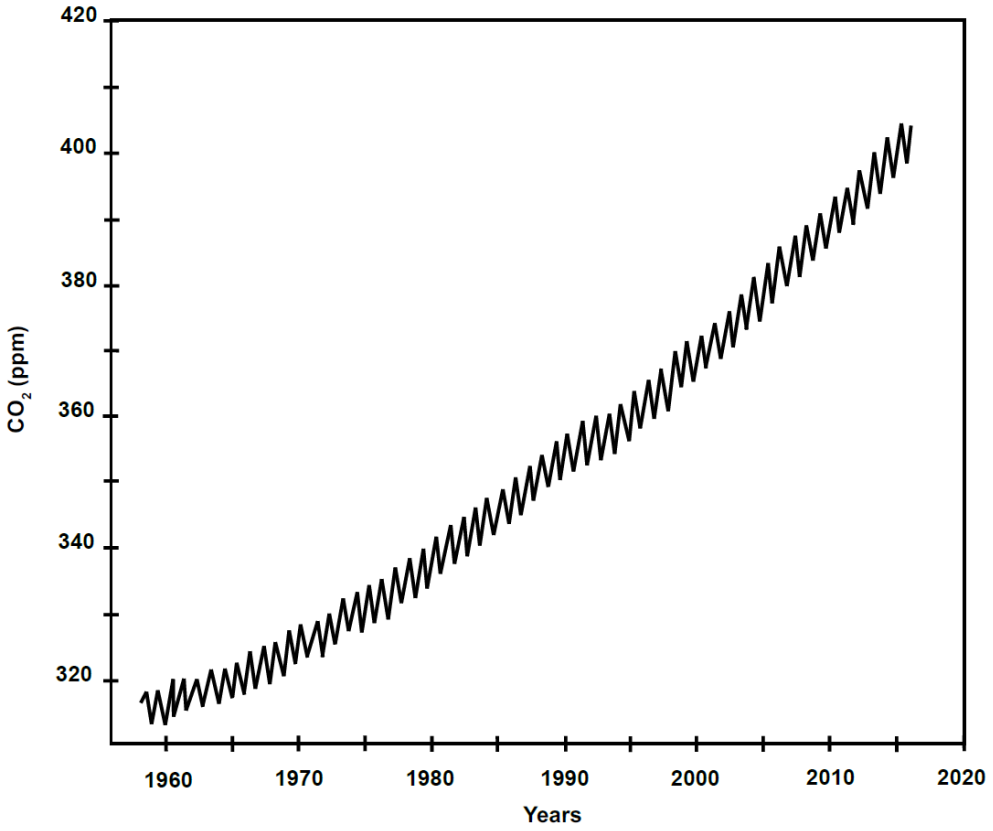

Figure 5 : Measurements of atmospheric CO_2 concentrations at Mauna Loa (Hawaii) since 1958. The annual seasonal variations are represented by the saw-tooth curve (from CDIAC (2016) and NOAA (2016) data). http://www.esrl.noaa.gov/gmd/obop/mlo/.).

Analysis of preserved air bubbles in Antarctic and Greenland glaciers shows that 5,000 years before pre-industrial civilization, atmospheric CO_2 concentrations fluctuated between 250 and 290 ppm. Today, the concentration of CO_2 in the atmosphere is continuously monitored at the Mauna Loa Observatory in Hawaii, and since 1950 a clear increase has been observed. The global annual average has risen from 316 ppm to 400 ppm (Fig 5).

In 1988, the UN formed the Intergovernmental Panel on Climate Change (IPCC) to synthesize scientific studies on climate. In 2007, the IPCC stated that global warming since 1950 is "*most likely*" due to the increase in anthropogenic greenhouse gases. In 2014, the degree of certainty was raised to "*extremely likely*". In 2021, the IPCC states that humans are "*unequivocally responsible*" for climate change. This climate disruption is therefore accelerating the ambitions to develop renewable energies with programs such as the *European Green Deal* (https://ec.europa.eu/info/strategy/priorities-2019-2024/european-green-deal_fr), or *Sustainable Energy for All* (https://www.seforall.org/). These political choices mark the desire to move towards low-carbon energies, and are shaping a new energy transition. This desire is enhanced when natural events show modern civilization its vulnerability. Although the direct effect of the SARS-CoV-2 pandemic's decline in CO_2 emissions would be negligible (Forster et al. 2020), it would accelerate the energy transition of some countries. Whereas in 1850 the energy transition was motivated by better economic returns, nowadays, this new energy transition is motivated by the aim of limiting our CO_2 emissions, and therefore by the use of low-carbon resources.

2.3 Green energy transition

2.3.1 Some low-carbon energies

Among low-carbon energy resources, nuclear power is mentioned as a major alternative to fossil fuels. The energy produced by the fission of atoms does not emit CO_2, but it requires heavy plants. The main hazard of using nuclear energy is the Maximum Credible Accident (MCA). Although scientists and engineers try to minimise this danger, the accidents at Three Mile Island (USA) in 1979, Chernobyl (Ukraine) in 1986 and Fukushima (Japan) in 2011 have shown disastrous consequences for humans and the environment.

The other major issue in the use of nuclear energy is the treatment of radioactive waste. In 2013, EDF (Electricité de France) estimates that after 40 years of the French nuclear power plant operation, the volume of long-lived waste (concentrating 99.9% of radioactivity) is 6,700 m^3. By comparison, an average-sized municipal gymnasium (34 m long, 28 m wide, 8 m high) has a volume of 7,616 m^3. Although after 40 years of operation, the volume of the most radioactive waste seems small in relation to the energy produced, the problems associated with the treatment of this waste have not yet been resolved.

In this context, solar and wind energy can be alternative option. Although in the production of energy, the amount of CO_2 released into the atmosphere is zero, these are energies that will depend on climatic and meteorological conditions (Goldenberg, 2000; Tester et al. 2006), and their land use is important. The Noor Ouarzazate (Morocco) complex covers 30,000 m^2 (see Fig 6). Even if it is for a different amount of energy, in contrast, a geothermal power plant equipped with air-cooled condensers, wells and a basin has a total surface area 10 times smaller. In addition

to having a small footprint, geothermal energy is not dependent on climatic and weather conditions.

Moreover, the amount of energy present in the Earth's crust is more than sufficient to meet the world's energy needs. Indeed, considering all human activities, the International Energy Agency estimates that the world's energy consumption is 0.432 EJ (1 EJ = 10^{18} J). Dickson and Fanelli (2013) estimate that the amount of geothermal energy in the Earth's crust is 5.4×10^{9} EJ.

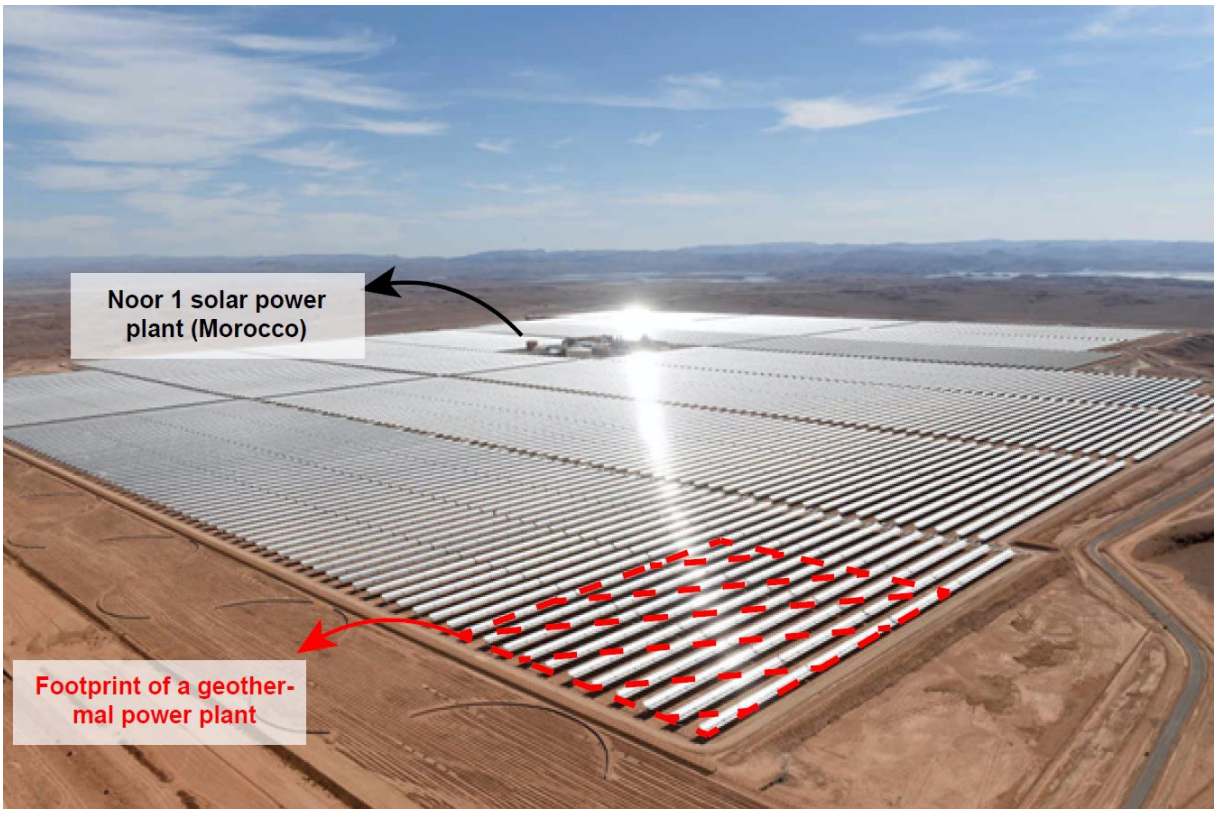

Figure 6 : The footprint of the Noor 1 solar power plant 20 km from Ouarzazate (Morocco), compared to the footprint of a geothermal power plant consisting of an air-condenser, a doublet, and a basin (image source: AFP, modified).

3 Geothermal energy

As an energy resource, the use of geothermal energy is old. Two thousand years ago the residents of Pompeii used it to heat some of their houses. In 1332, the town of Chaudes-Aigues (French Massif Central), developed the first district heating system fed by hot water of 82 °C. In 1904, P. G. Conti launched the first electricity production from geothermal energy in Larderello (Italy, Tuscany). Thereafter, with a few exceptions, geothermal energy did not play an important role in electricity generation until the second half of the 20th century. In some examples, the Wairakei power station in New Zealand was operational, in 1958. In 1960, The Geysers, which now has a capacity of 1517 MW, was opened in the United States of America (north of San Francisco). The Cerro Prieto power plant in Mexico opened in 1970, and has a current capacity of 820 MW. By comparison with the nuclear energy, in France, more than half of the nuclear reactors have a power of around 900 MW (www.edf.fr).

Today, geothermal energy is used as a renewable energy resource in over 90 countries (Lund et al. 2020). Worldwide, the installed capacity for electricity generation is 16.0 GWe, corresponding to an annual electricity production of 95 GWh (Huttrer, 2020; Lund et al. 2020, www.thinkgeoenergy.com). Geothermal energy can be used for electricity generation, but also for heat use in different applications. Classifications are used to separate the different kinds of geothermal energy.

3.1 Classification of geothermal energy

Based on temperature criteria, geothermal systems are classified into four categories:

- Very Low Temperature geothermal energy (T < 30°C). This kind of geothermal energy is used for individual or reduced collective heating.

- Low Temperature geothermal energy (30°C < T < 90°C). This kind of deposit is found at a few hundred meters, up to 2500 m depth. It is found in sedimentary basins, rich in porous rock (sandstone or sand), allowing fluids to circulate freely. LT geothermal energy is used in fish farming, collective or individual heating.

- Medium Temperature geothermal energy (90°C < T < 150°C). This kind of deposit is found at a depth of less than 1 km in volcanic areas, or between 2 km and 4 km in sedimentary basins. MT geothermal energy is used for industrial purposes, or for drying agricultural and industrial products.

- High Temperature geothermal energy (T > 150°C). Usually, these deposits are located between 1 km and 3 km deep, in volcanic zones, or at the boundaries of tectonic plates. HT geothermal energy is mainly used for electricity generation.
The present study will focus on this category. We will focus on geological targets with potential HT geothermal deposits. These targets can be found in volcanic zones, on plate boundaries, but also in other geological contexts. Before that, we shall look at the large-scale geological and geodynamic contexts that are currently recognized as being favourable for the emergence of these reservoirs.

4 Geodynamic and structural control of HT geothermal systems

4.1 Geodynamic control

Hot springs and fumaroles are recognized as surface geological clues for the exploration of HT geothermal systems. On a global scale, the distribution of these clues depends on the geodynamic context. The classification of Moeck (2014), re-used by Jolie et al. 2020, defines a set of geodynamic contexts and heat transfer modes favorable for the development of HT geothermal systems (Fig 7).

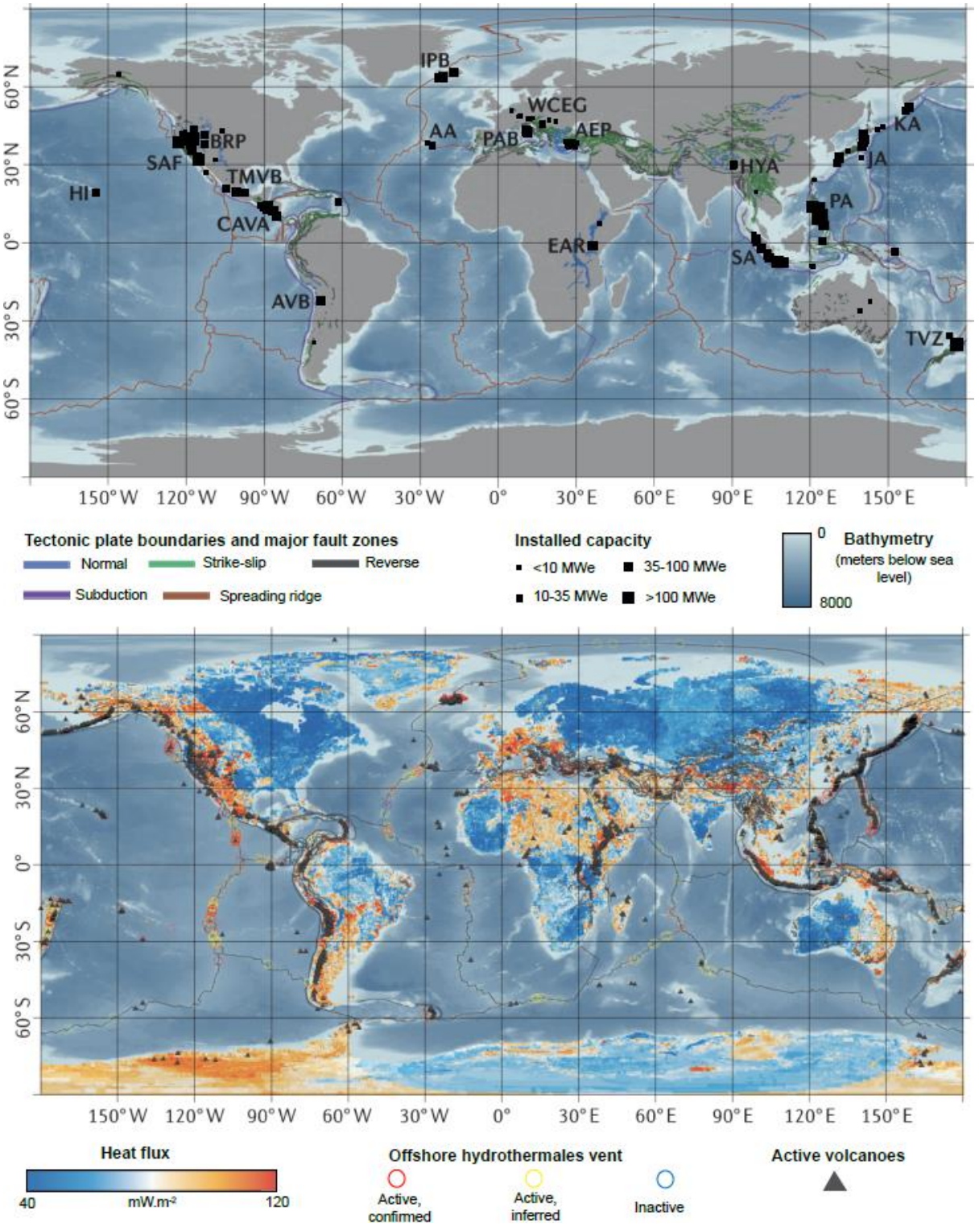

Figure 7 : Global distribution of geothermal power plants in different geodynamic contextes. Currently, HT geothermal reservoirs are mainly located near volcanic areas and/or crustal thinning regions. AA, Azores archipelago; AEP, Aegean extensional province; AVB, Andean Volcanic Belt; BRP, Basin and Range Province; CAVA, Central American Volcanic Arc; EAR, East African Rift; HI, Hawaï archipelago ; HYA, Himalaya; IPB, Iceland plate boundary; JA, Japanese arc system; KA, Kuril Arc; PA, Philippine Arc; PAB, Pre-Apennine Belt ; SA, Sunda Arc; SAF, San Adreas Fault Zone; TMVB, Trans-Mexican Volcanic Belt; TVZ, Taupo Volcanic Zone; WCEG, Western/Central European Geothermal System. (After Moeck, 2014; Jolie et al. 2020, modified. Data : Lucazeau, 2019; Beaulieu et Szafranski, 2020; Styron, 2019; American Geological Institute; GEBCO Compilation Group)

HT geothermal systems are mainly found in magmatic arcs, in subduction zones (Taupo Volcanic Zone, Andean Volcanic Belt, Sunda Arc or Philippine Arc), in transform fault zones (San Andreas Fault Zone), in intracontinental contexts (East African Rift) and in hot spots (Yellowstone, Reunion, Iceland or Hawaii). They are also found in pull-apart basins (Salton Trough), as well as in magmatic and amagmatic rifts (East African Rift, Basin and Range, Iceland).

Highly productive geothermal systems, such as those found in Iceland or New Zealand, correspond to magmatic geological contexts, with crustal extension (Arnórsson, 1995; Wilson and Rowland, 2016). Extensive amagmatic geological contexts also host large geothermal provinces such as the Basin and Range Province (USA) and the Aegean Province of western Turkey. Based on field studies in the same area, Roche et al. (2019) suggested that the intersection between different fault families represents a first order control factor on geothermal systems. A few years earlier, an inventory made in the Great Basin district (Basin & Range province, USA) shows a strong correlation between the distribution of geothermal power plants, and the presence of faults (Faulds and Hinz, 2015) (Fig 8). This clearly suggests a structural control on geothermal systems.

4.2 Structural control

For HT geothermal systems, the most favorable structural environments are fault termination (Fig 8C), thrusts (Fig 8D), fault intersections (Fig 8E), accommodation zones (Fig 8F), transfer zones (Fig 8G) as well as pull-apart basins (Fig 8G) (Faulds et al. 2006, 2011; Faulds and Hinz, 2015).

All of these geological structures are composed of high fault density and fracture interconnections. These features result in a high natural capacity for fluid flow uides (Faulds et al. 2006; Coolbaugh et al. 2007; Lechler et Coolbaugh 2007; Dezayes et

al. 2010; Jolie et al. 2015a, b; Siler et al. 2018; Souque et al. 2019), which describes the permeability.

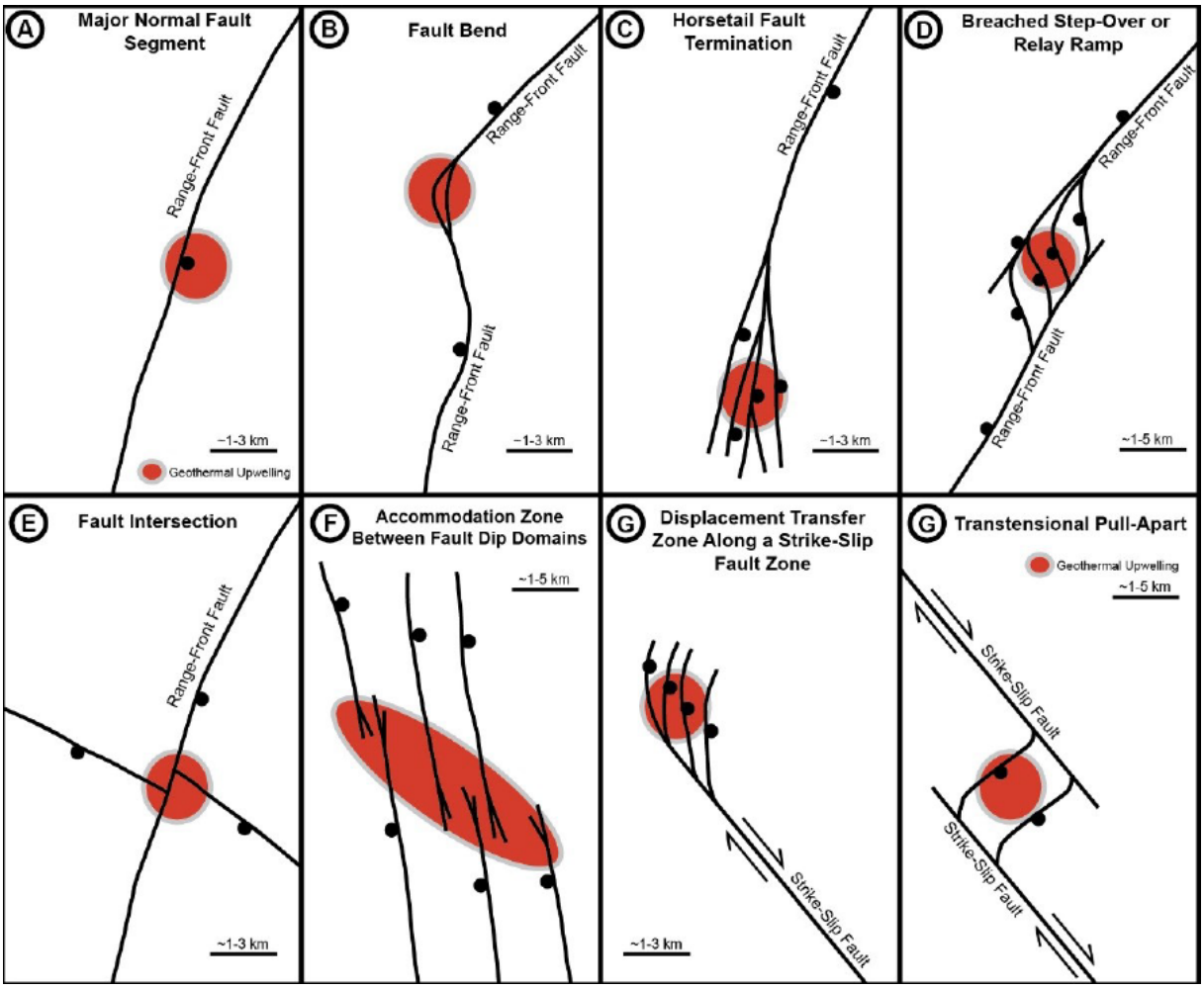

Figure 8 : Examples of favorable structural features for geothermal systems in Great Basin District (USA). Red areas indicate approximate locations of geothermal reservoirs (Faulds et Hinz, 2015).

Permeability is a first order factor in controlling fluid flow (Darcy, 1856, 1857) and therefore a controlling parameter in locating geothermal reservoirs (Gleeson and Ingebritsen, 2016). Conventional geothermal resources refer to geothermal systems in rocks with high porosity and permeability. They are different from uncon-

ventional geothermal resources, which are found in rocks with low porosity and permeability. To promote the development of geothermal energy in non-conventional systems, artificial reservoirs can be created. For this, Enhanced (or Engineered) Geothermal System (EGS) technology is required.

5 The Enhanced (or Engineered) Geothermal System

The EGS technology consists in stimulating potential reservoirs in a way to extract the energy present in the low permeability medium (Fig 9). EGS increase the permeability through different fluid injection phases. The fluid pressure will increase, causing hydrofracturing and/or hydro-shearing processes. The application of the EGS method has been demonstrated on the Soultz-sous-Forêt geothermal

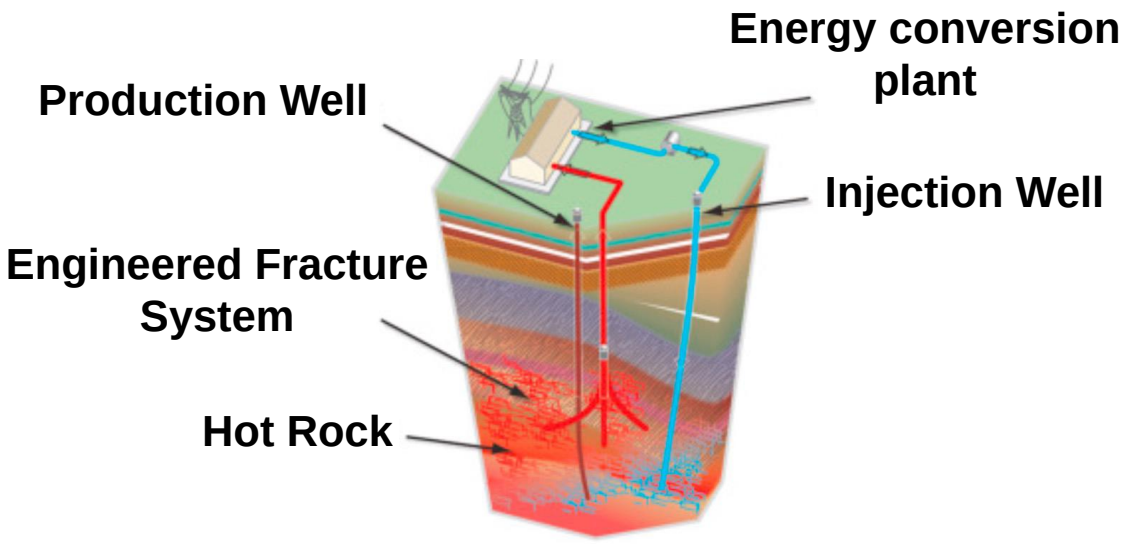

Figure 9 : Schematic representation of the operation of an EGS (modified after Olasolo et al. 2016).

project, (Alsace, France) (Genter et al. 2010) or Fenton Hill, (New Mexico, USA) (Brown et al. 2012).

However, seismicity induced by the injection phases has jeopardized several geothermal projects. Following a series of induced seismic events, the Bâle (Switzerland) geothermal project was abandoned (Deichmann and Giardini, 2009; Terakawa et al. 2012; Gaucher et al. 2015). Financial losses were estimated at $60 million.

Recently, in France, the injection phases of the GEOVEN project (GEOthermie in VENdenheim), in Alsace (France), have caused a series of induced seismic events (Schmittbuhl et al. 2021). An earthquake of magnitude M = 3 was recorded on 12 November 2019, another of magnitude M = 3.6 was recorded on 4 December 2020, then an earthquake of magnitude M = 3.9 was recorded on 26 June 2021. These events have led to the shutdown of the project and provoke public debate on other potential targets (Fig 10).

Le Parisien

Environnement

La géothermie coulée à Strasbourg pour cause de séisme

Alors que la préfecture du Bas-Rhin interdit l'exploitation de la centrale géothermique de Vendenheim suite à un séisme important, l'avenir de cette énergie est en question dans l'agglomération strasbourgeoise.

08/12/2020

LA MONTAGNE À LA UNE VIE LOCALE SPORTS LOISIRS ÉCONOMIE

Energie

Cinq questions pour comprendre le projet de centrale de géothermie profonde à Saint-Pierre-Roche (Puy-de-Dôme)

SAINT-PIERRE-ROCHE ÉCONOMIE BTP - INDUSTRIE ENVIRONNEMENT PUY-DE-DÔME

Publié le 15/02/2021 à 11h53

*Figure 10 : Press article from a national weekly newspaper (*Le Parisien*) following the induced earthquakes felt in the Strasbourg agglomeration (*Alsace, France*). As shown in the press article of a regional daily newspaper (*La Montagne*), these events raise questions about other potential targets.*

In order to facilitate the development of this green, sustainable energy, which does not depend on climate or meteorology conditions, geological targets in the purely crustal domain will be studied here, where the permeability naturally present would be sufficient to allow fluids to circulate and localize positive temperature anomalies at potentially exploitable depths. Under these conditions, it would appear that the presence of an external heat source (presence of a magma chamber, or crustal thinning context), would no longer *be a sine qua non* condition for a geothermal power system. If on a country or regional scale it's usual to target abnormally hot zones for High Temperature geothermal energy, it could then be possible to target abnormally permeable zones within the Earth's crust. If this potential is proven, it could considerably increase the number of targets for geothermal power plant. This georesource could then play a decisive role in this new ecological energy transition.

6 Crustal Fault Zones (CFZ) as geothermal power systems

While faults have long been recognized as preferential drainage zones for fluids (Caine et al. 1996; Faulkner et al. 2010; Bense et al. 2013; Haines et al. 2016), the concept of CFZs has never been heralded as potential renewable and economic resources. Consequently, they remain largely unexplored and therefore unexploited. CFZs are crustal-scale geological structures, localizing deformation (Ben-Zion and Rovelli, 2014; Chester and Logan, 1986; Schulz and Evans, 1998; Sammis et al. 2009) and modifying the mechanical properties of the crust up to the Brittle-Ductile Transition (BDT).
In the continental domain, CFZs are widely present. They can be found in Germany, Chile, Canada, China, Sweden, Russia, Spain,... (Achtziger-Zupančič et al. 2017; Lahsen et al. 2010; Duan et al. 2017; Yang et al. 2016; Duan et al. 2017; Juhlin and Sandstedt, 1989; Lund and Zoback, 1999; Faulkner et al. 2003; respectively). These multiple occurrences require consideration of a range of geological and physical parameters that may control and/or limit the presence of a HT geothermal reservoir within these naturally permeable systems.

Traces of fluid flow into the middle crust (10-20 km depth) have been documented in various geological settings. For example, fluid-filled fractures have been observed in the SG3 deep borehole on the Kola Peninsula, Russia (Kozlovsky, 1984), and in the KTB deep borehole, Germany (Grawinkel and Stöckhert, 1997; Ito and Zoback, 2000). Furthermore, Famin et al. (2004) suggest massive meteoric fluid infiltration down to 10-15 km depth within a shear zone on the Tinos Island (Greece). Similarly, Siebenaller et al. (2013) demonstrated that meteoric water in-

filtration can occur down to the BDT (around 8 km depth) within the Naxos detachment (Greece). Beyond the TDF, granite deformation leads to a reduction in porosity and presumably permeability (Violay et al. 2017). However, these authors also note that microcracks can remain open in granite at high temperature (900°C) and high pressure (100 MPa), resulting in a higher permeability of the matrix than the intact material. The ability to extract energy from a hot fluid draining through a fractured system will depend, essentially, on the permeability distribution within these conduits. Thus, a Crustal Fault Zone, naturally permeable could correspond to a new type of high-temperature geothermal system, where deep, hot fluids flow from the BDT (350-400°C) to the surface.

In this framework, TLS-Geothermics, a French geothermal exploration company, is keen to improve the knowledge of its Exclusive Research Permit (PER) of "La Sioule" licence (Puy de Dôme, French Massif Central). This licence hosts a 3 km wide and 30 km long mineralized fault zone (the Pontgibaud fault zone) close to a granite body (the Gelle granite; Négroni, 1981) and where CO_2-rich thermomineral resurgences are present. In the Pontgibaud area, the geothermal gradient near the surface is 37-41 °C/km (International Heat Flow Commission database). Pontgibaud is therefore considered an ideal first case study for the exploration of the high-temperature geothermal potential of the Crustal Fault Zones.

7 Objectives and methodologies

The present study aims to understand the potential of a new and novel types of geothermal play system for high temperature and electricity production: Crustal Fault Zone. The main goal of this thesis is therefore to understand the hydrothermal fluid dynamics in CFZs. The correlation between field studies, petrophysical data and numerical modelling should allow the improvement of the geothermal exploration phase of CFZs. This work aims to determine:

How is a hydrothermal system associated with Crustal Fault Zones organised, and what are the controlling factors?

For this purpose, a first approach will consist of a review of the parameters that can affect the fluid circulation in a fractured-basement domain. This first step will allow to isolate some factors whose effects on the fluid circulation and the thermicity of a fractured medium are still unknown. The use of numerical modelling will make it possible to isolate general trends, applicable in the field, which can be used as a guide for the exploration of these new potential targets.

This literature review will also highlight the methods used in exploration for high temperature geothermal energy. Thus, a second approach will favor a multidisciplinary methodology (field, laboratory, large-scale numerical modelling) on the "La Sioule" PER of TLS-Geothermics. In addition, this second approach will allow to qualitatively and quantitatively constrain some key and essential parameters (geological structures, porosities, permeabilities) to understand a geothermal system, in 2D and 3D.

These elements will be integrated into large-scale numerical modelling. The results of these numerical models will be compared with other field data (geophysical, temperature, heat flux). Thus, it will be possible to estimate the depth and intensity of the temperature anomaly within the Pontgibaud hydrothermal system. Finally, a general discussion will be held on the limits of the methodology employed, the tools used, and more broadly on the geothermal potential of the Crustal Fault Zones with some associated risks.

Chapter II : Geodynamics and geothermal system

1 The Earth, a thermal engine

Earth is a thermal engine. Different processes (inner-core crystallisation, chemical separation of the inner core, radioactive element decay) produce an estimated 4 to 12 TW of heat (Jaupart et al. 2007). Plate tectonics, and overall activity at plate margins, is controlled by thermal processes responsible for density contrasts and rheological changes. Geodynamics studies these changes in the Earth's crust. It therefore appears that knowledge of internal thermal processes contributes to understanding the Earth's general dynamics.

Plate tectonics is a model that divides the Earth's crust into a number of rigid plates (Fig 11). They are made up of relatively cold rocks with an average thickness of 100 km. These plates are in relative motion with respect to each other. These speeds are of the order of tens of millimetres per year. Oceanic ridges, subduction zones and transform faults define the plate boundaries. The boundaries of these plates concentrate the main volcanic eruptions, a large proportion of earthquakes, and the formation of mountain ranges.

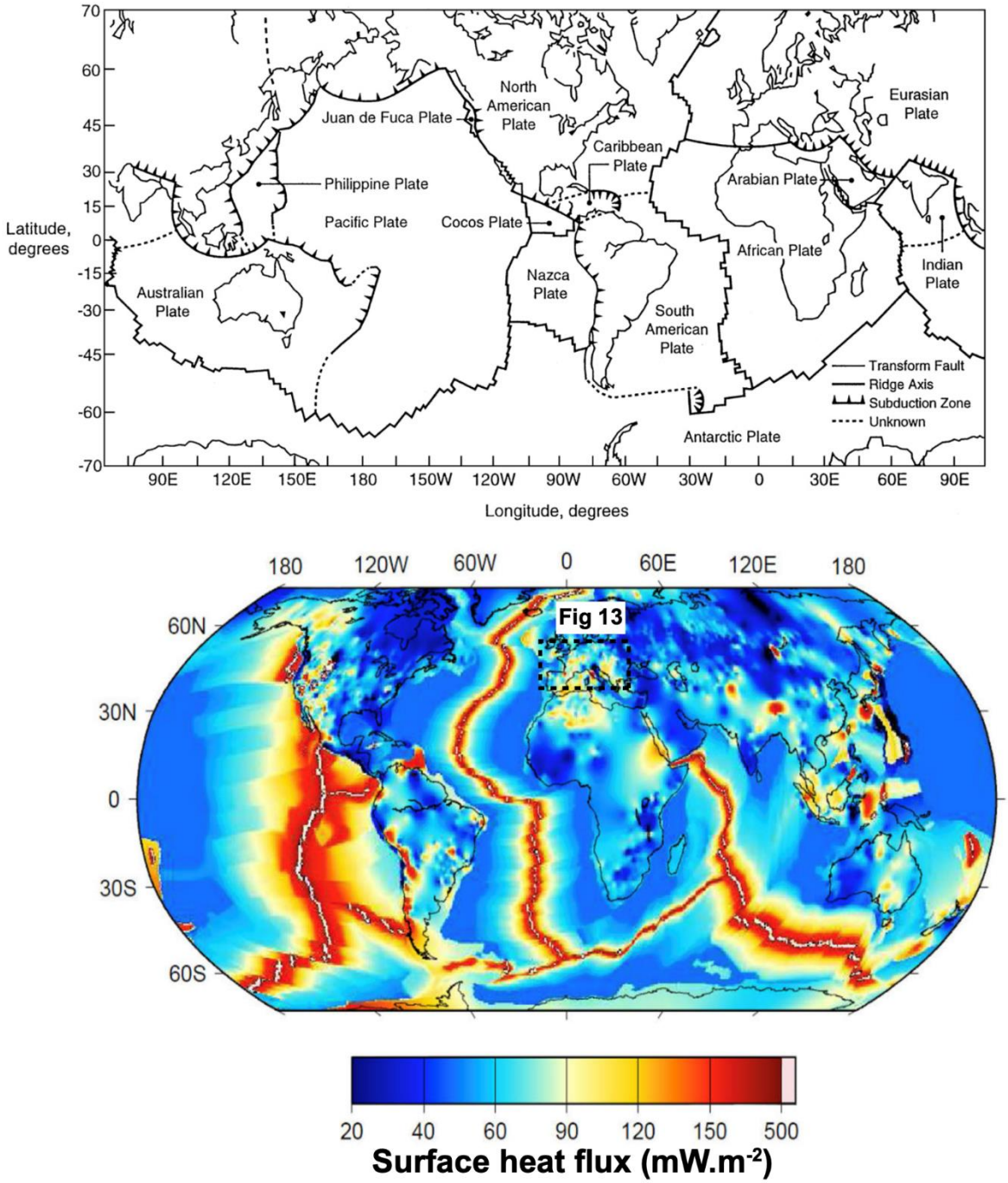

Figure 11 : Maps of tectonic plate distribution and global heat flux. Oceanic ridges concentrate the highest heat fluxes (above 500 mW.m^{-2}). Other areas, such as back-arc basins, concentrate high fluxes (western Mariana Islands). The heat flux map is based on heat flux observations over the continents and their margins, but for the oceans, the surface heat flux is calculated from a model of energy loss through the oceanic lithosphere (Turcotte and Schubert, 2002; Jaupart et al. 2007).

One of the most tangible pieces of information about the thermal properties of the Earth is obtained from the surface heat flux. This heat flux provides important information about the amount of heat produced on the Earth and the temperature distribution within it. The simplest way to determine the heat transferred in the crust is to measure several values of temperature and thermal conductivity *K* ($W.m^{-1}.K^{-1}$) of rocks in boreholes. The heat flux *f* ($W.m^{-2}$), geothermal gradient *dT/dz* ($K.km^{-1}$) and conductivity are related by the following expression:

$$f = \frac{KdT}{dz} \qquad \text{Eq 1}$$

Thousands of heat flux measurements have been made on the continents and in the oceans. The average heat flux for all continents is 65 +/- 1.6 $mW.m^{-2}$. The average heat flux for the oceans is 101 +/- 2.2 $mW.m^{-2}$. In the continental domain, the regions with the highest heat flux are concentrated in volcanic areas, for example the Andes. However, their sizes are relatively small, so these systems do not contribute significantly to the average heat flux. In the oceanic domain, at the level of ridges, mantle upwelling occurs in areas where the plates diverge. The mantle rock, behaves fluidly due to solid-state creep processes. This upwelling of the mantle at the ridges explains the highest heat flux values recorded on Earth.
In general, due to its basaltic composition, the heat production by decay of radioactive elements is negligible in the oceanic crust, so the heat flux through the ocean floor corresponds to the heat flux from the mantle to the bottom of the oceanic lithosphere (Fig 12). While values of 300 $mW.m^{-2}$ (locally close to 500 $mW.m^{-2}$) are observed at the ridges (Fig 12), this flux is about 50 $mW.m^{-2}$ over the 80 million year old oceanic lithosphere (Lister et al. 1990).

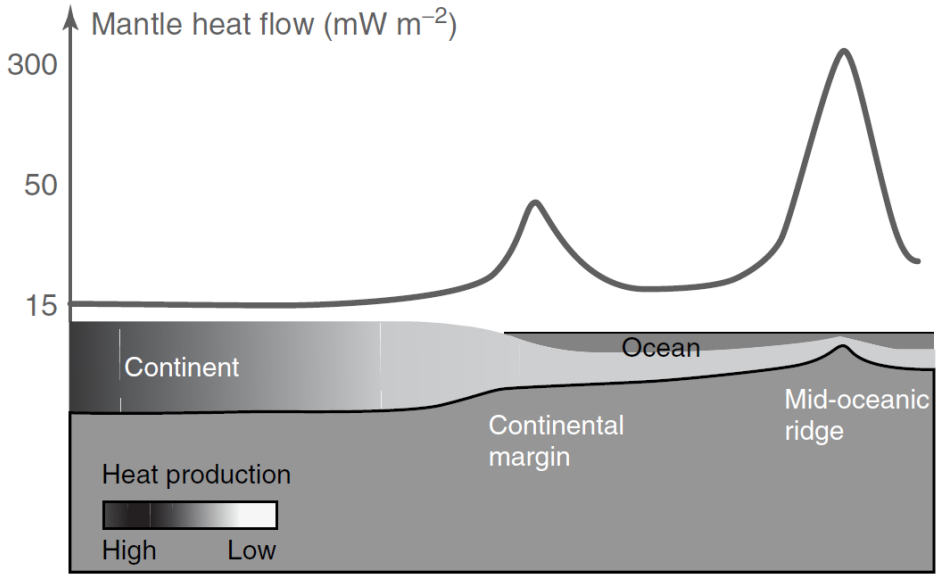

Figure 12 : Schematic variation of mantle heat flux from the continents to the mid-ocean ridge (from Ledru and Guillou-Frottier, 2011)

On the continents, variations in heat flux (between 18 and 200 mW.m^{-2}) can be explained by crustal heat production (by decay of radioactive elements) and crustal thickness. Measurements of the surface heat flux over the continents and estimates of the associated heat production rates have shown that the mantle heat flux values under thermally stable continental areas (older than about 500 million years) would be low, around 15 ± 3 mW m^{-2} (Pinet et al., 1991; Guillou et al., 1994; Kukkonen and Peltonen, 1999; Mareschal et al., 2000). On the contrary, the mantle heat flux would be significantly enhanced under the continental margins (Goutorbe et al. 2007; Lucazeau et al. 2008) where crustal thickness and heat production rates decrease. Older central parts of the continents would be associated with low heat flux from the sub-continental mantle while younger continental margins would receive more heat from the mantle.

Finally, two regions can be distinguished:

(1) Areas where the heat flux is between 18 and 200 mW.m^{-2}. These zones cover the vast majority of the Earth's surface.

(2) Areas where the heat flux can be higher than 300 mW.m^{-2}, which are much less represented.

Overall, on the Earth's surface, there is a net outward flow of heat everywhere. Heat is continuously supplied to the Earth's surface from the interior to the exterior. In the continental domain, the heat flux varies between18 and 200 mW.m^{-2}. Mareschal and Jaupart (2004) observed that heat flux variations <500 km are related to local crustal scale structures, while heat flux variations >500 km are generally related to large scale events (see below). As we shall see, on a European scale, the heat flux varies between 70 to 150 mW.m^{-2}. If locally significant differences can exist, larger scale anomalies can also be found in some regions. This suggests both local and large-scale control.

2 Heat fluxes in Europe and France

In the north-eastern part of Europe, the heat flux varies between 30 and 60 mW.m^{-2} (Fig 13). These values are close to the average flux values for Precambrian cratons (Nyblade and Pollack, 1993; Sandiford and McLaren, 2006; Mareschal and Jaupart, 2004; Jaupart et al. 2007). These zones are considered to be in thermal equilibrium and have not been tectonically reactive since their formation.
The heat flux in Western and Central Europe varies from 50 to 80 mW.m^{-2} (Fig 13). The origin of these values is thinning of the lithosphere and a thermal disequilibrium formed by the proximity of the Precambrian basement to the north (Cermak, 1993, Cloetingh et al. 2010).

In the northern part of the Bohemian Massif, the surface heat flux varies between 61 and 108 mW.m^{-2}. These values are correlated with the presence of late Variscan granite, enriched in radioactive elements (Förster and Förster, 2000).

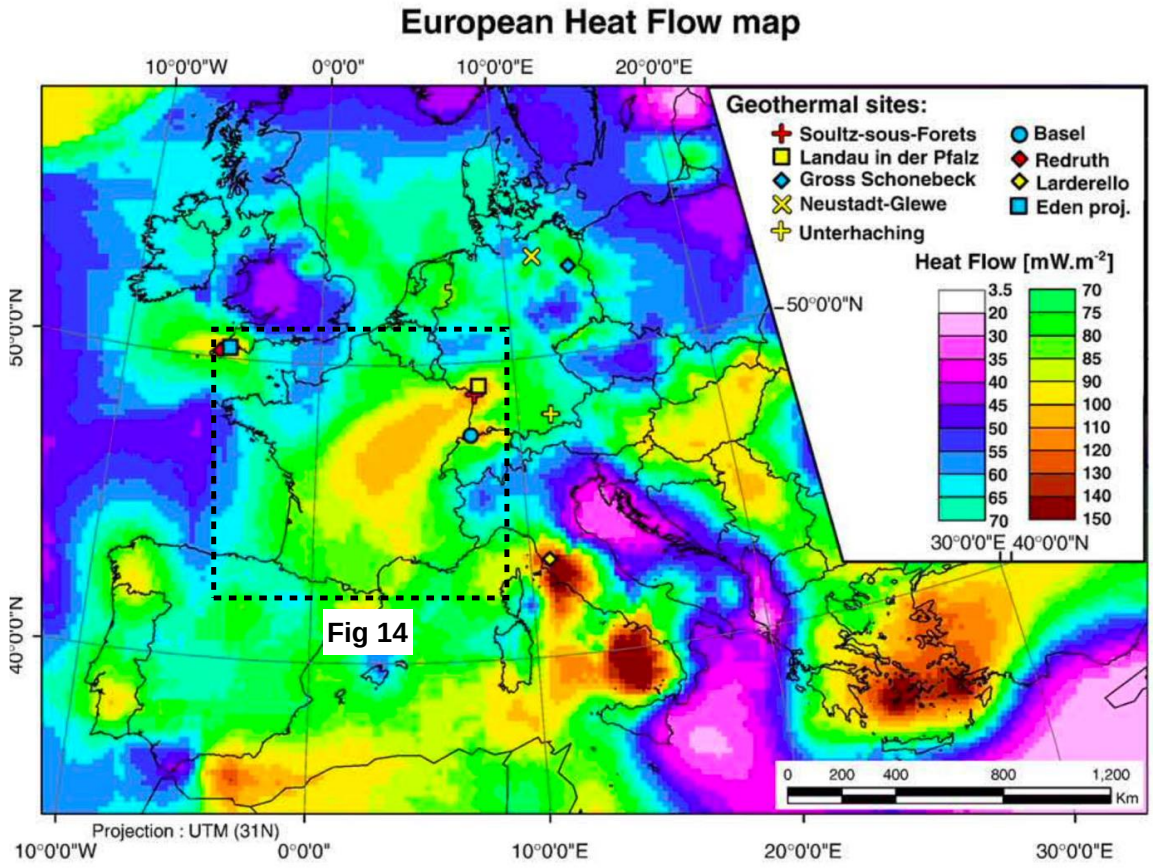

Figure 13 : European heat flux map and location of geothermal power plants - excluding Turkey's geothermal power plant - (Haenel et al. 1988; Hurtig et al. 1992; Hurter & Haenel, 2002; Cloetingh et al. 2010).

In Central and Eastern Europe, the Pannonian Basin has been characterized since the Middle Miocene by upwelling of the asthenosphere and thinning of the lithosphere, responsible for coexisting rifting in the basin and compression in the adjacent Carpathian and Dinaric belts (Huismans et al. 2001).

On a European scale (Fig 13), the highest heat fluxes (>100 $mW.m^{-2}$) are found in Turkey, France (especially in Alsace and the French Massif Central) and Italy. In Italy, since the Miocene, the crust has been thinned, heated and intruded by mafic magmas. In Tuscany, this evolution is at the origin of a granitic complex that was emplaced between 3.8 and 1.3 Ma. Hydrothermal activity is marked by the Larderello geothermal field (Fig 13) (Dini et al. 2004). In Turkey, most of the geothermal activity is concentrated along fault-detachments systems (Roche, 2018), mostly associated with E-W oriented grabens (Sengör et al.1985; Ercan, 2002). The collision between the Arabian and Eurasian plates causes the Anatolian block to thrust westwards, which is accommodated by the Anatolian Fault.

In France (Fig 13, Fig 14), values of 110 $mW.m^{-2}$ are found in the Massif Central and in the Rhine graben. These values could be linked to thermal events that have been effective since 30 Myrs (Guillou-Frottier et al. 2013). Indeed, over the last 30 Myrs, thermal and mechanical events have affected the deformation of the European lithosphere.

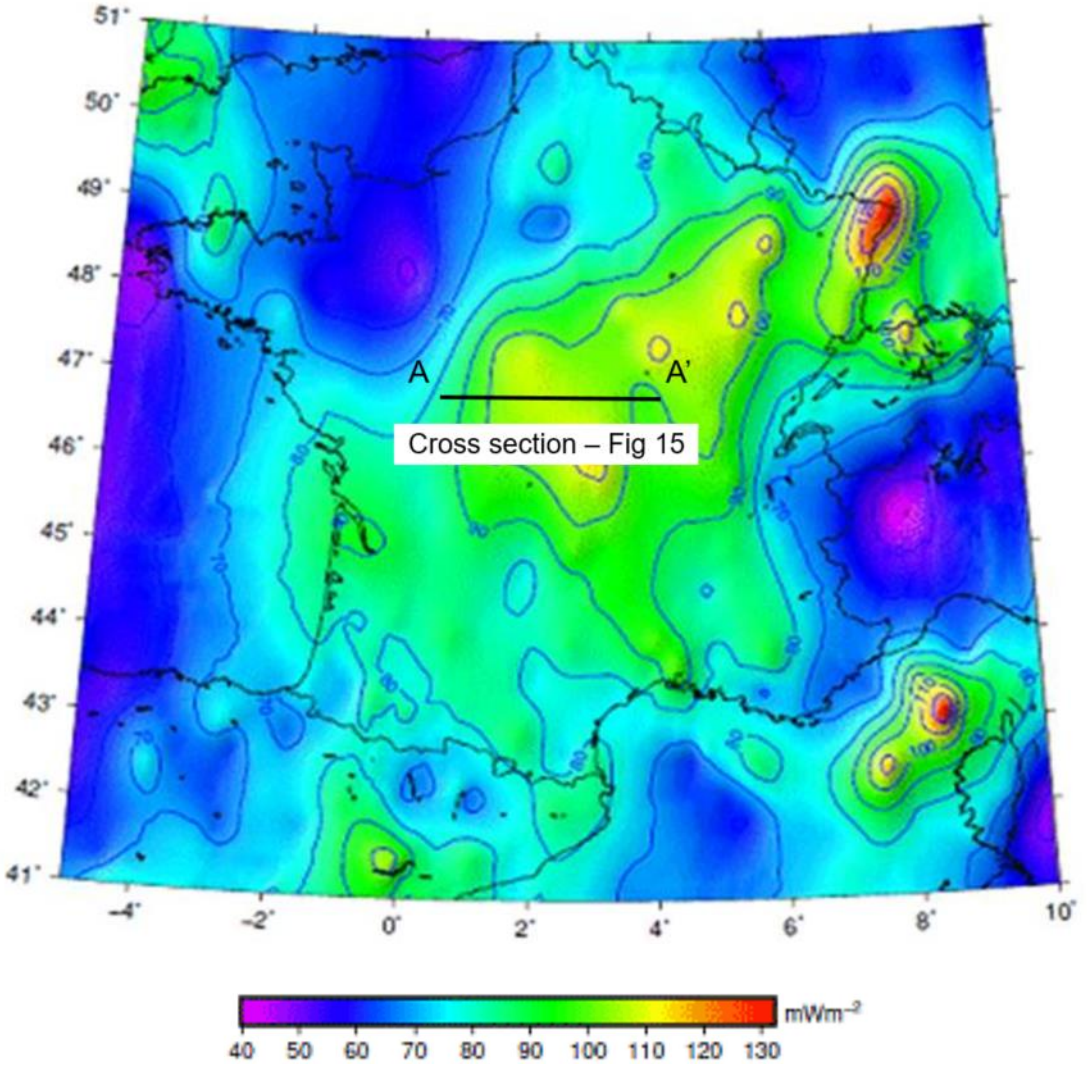

Figure 14 : Heat flux map of France (Lucazeau and Vasseur, 1989). The map shows a strong heat flux anomaly in the northern Rhine graben, as well as a fairly high heat flux zone (over 110 mW.m^{-2}) over a large portion of the territory extending from the centre of the Massif Central to the Vosges.

The Alpine and Pyrenean compressional phases would be at the origin of the Moho undulation (Lefort and Agarwal, 2002). This mantle flow anomaly, higher than the average continental flow (65 mW.m^{-2}, see part 1) (Lucazeau et al. 1984; Lucazeau and Vasseur 1989) (Fig 15), may be linked to large-scale phenomena: may either be due to an asthenospheric upwelling driven by a mantle plume (Granet et al.

1995); or by past subduction-induced mantle flow (as in western Anatolia, Roche et al. 2018).

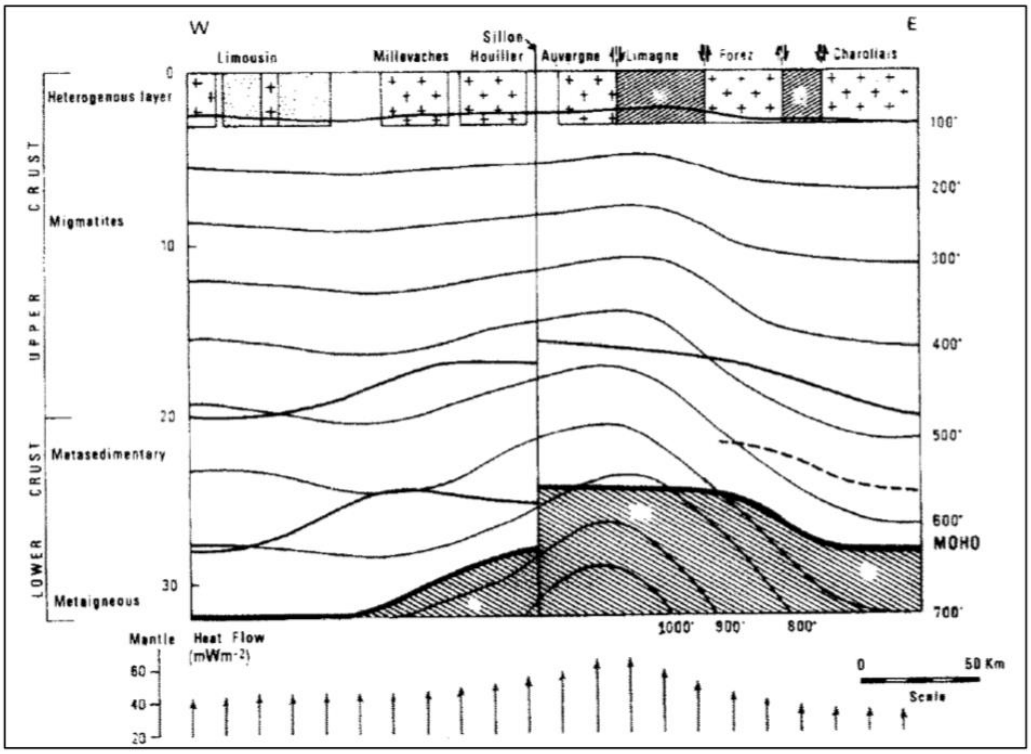

Figure 15 : E-W cross section evaluated mantle heat flux with crustal heat production (Lucazeau et al. 1984).

Large-scale European geodynamic events (mantle plume, past subduction) could have a role on the establishment of anomalously high mantle heat flux. Retreat of the subduction trenches during the Oligocene and Miocene involved more than 800 km of Southeastward displacement, which have been accomodated during opening of the back-arc basin at an average velocity around 10 cm/yr. This major geodynamic event has thus displaced the asthenospheric mantle on considerable distances and this must have thermal and mechanical consequences below the French Massif Central, and possibly below the entire European Cenozoic Rift System (Cloetingh et al. 2010). In particular, one may expect to predict the location of

weakness zones, which could be localized upwelling of hydrothermal fluids, as recently suggested by Roche et al. (2018) for high-temperature geothermal systems in western Anatolia.

This study focuses on the high temperature geothermal potential of new geological targets: deep naturally permeable zones in basement areas. The geological heritage is essential for understanding and approaching deformed zone, which may localize abnormally permeable areas. At this step, it seems necessary to remind that variations in heat fluxes over short lengths can also be linked to local structural objects. These aspects will be detailed later, when we focus on our study area. But first, we shall examine the general geological setting of the French Massif Central.

3 Geological setting of the French Massif Central

The French Massif Central (FMC) (Fig 16) as well as the Armorican Massif, Galicia, the Ardennes, the Vosges-Black Forest and Bohemia are remnants of the Variscan orogeny. This took place from the Devonian (450 Ma) to the Permian (280 Ma). Throughout this period, the Massif Central underwent one or more thickening phases and then a general extension. This complex evolution led to the formation of large structural units limited by major tectonic faults. The French Massif Central is the largest Variscan basement outcrop in France.

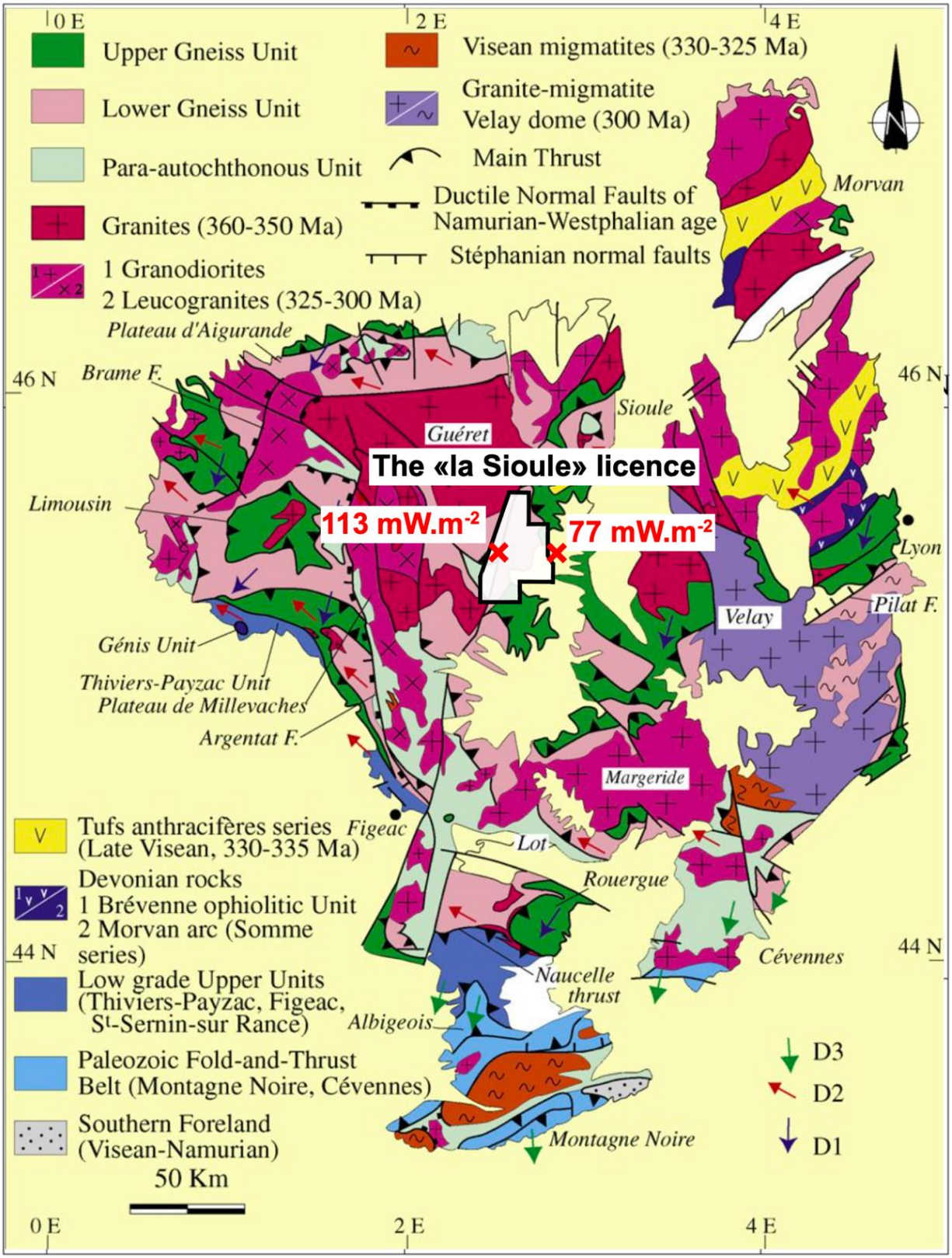

Figure 16 : Structural scheme of the French Massif Central (Faure et al. 2009). Location of the "La Sioule" licence, owned by TLS-Geothermics. Within 50 km, two different heat flux values exist (red crosses, Lucazeau and Vasseur, 1989; Vasseur et al. 1991), suggesting that local structures could be at the impetus of these differences.

3.1 Variscan history

The Variscan Chain is developed in the Paleozoic period. From the East to the West, it extends from Czech Republic, Germany, SW England, France, Morocco to South America. The formation of this chain took place in several cycles and is considered to be poly orogenic.This Variscan orogen is the result of a continuous orogenic cycle with the formation of two collision chains. The Caledonides, in the North, resulted from the meeting of the Laurentia block in the West with Baltica in the East, with the Avalonia microplate between the two blocks. This episode causes the rising of the Laurussia super continent. Then continental extension, leading to the detachment of the Armorica microplate from the northern margin of Gondwana. The formation of the Variscan chain starts with the subduction of Laurussia under Armorica and ends with a collision. The same pattern is repeated by Armorica subducted under Gondwana.

Four orogenic periods have been defined by Ledru et al. (1989), however the system is not perfectly cylindrical and this evolution can be shifted from one area of the chain to another depending on the different blocks and crustal features in the collisional system:

(i) The Eo-Variscan period (450-400 Ma) marked by subduction.

(ii) The Medio-Variscan period (400-340 Ma) marked by continental collision with nappes setting up.

(iii) The Neo-Variscan period (340-330 Ma): corresponds to the intracontinental evolution still in a domain of convergence with southeastward kinematics.

(iv) Tardi-Variscan period (325-280 Ma) marked by crustal thickening.

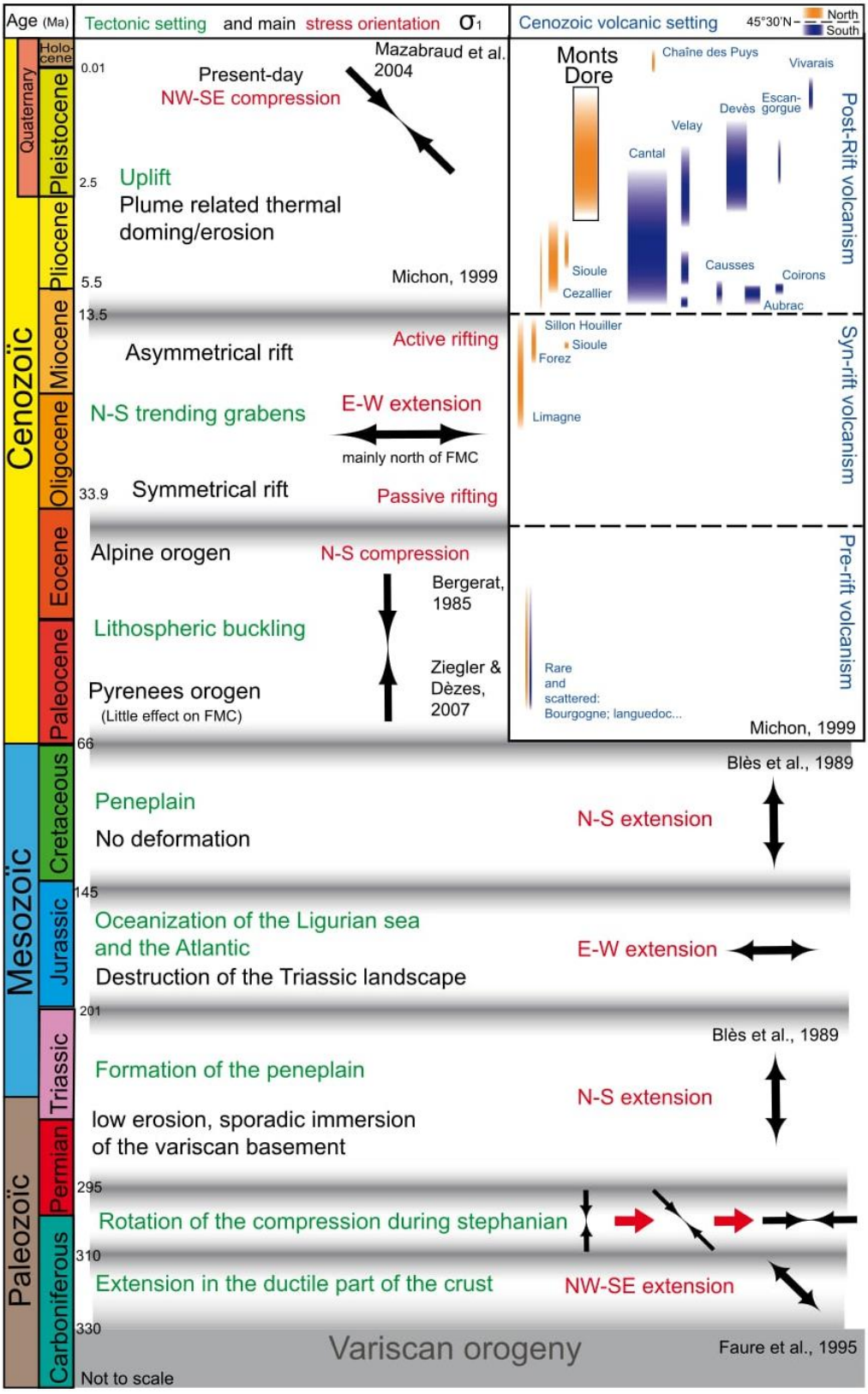

Figure 17 : Synthesis of the paleo stress direction in the French Massif Central, from the Paleozoïc to the present day. (Penhoët (2021), modified after Daffos (2018)). In our case study, the stress orientation from the end of the Oligocene to the present day will be further detailed, in relation to the structures present within the "La Sioule" licence.

For this Variscan heritage, two successive phases can be differentiated across the FMC and are detailed below:

(i) An extensive syn-collisional phase of Middle Carboniferous age (330-310 Ma) with a NW-SE direction (Fig 17). This NW-SE extension corresponds to an extension in the ductile part of the crust (Faure, 1995). The brittle part was eroded at the end of the Paleozoic with the outcrop of the ductile granite-gneiss part (Fig 17). This extension was well recorded by these structural, metamorphic and plutonic effects in the deep crust.

(ii) An extensive phase from the Upper Carboniferous to the Lower Permian (307-295 Ma) with NE-SW direction. During the Lower and Middle Stephanian, the N-S compression generated a fracture system consisting of dextral conjugate faults N140°-170°E and sinistral faults N10°-50°E and reverse faults N80°-120°E. This episode is responsible for the sinistral NNE-SSW fault of the "Sillon houiller" and the N-S fault of the Loir-et-Cher. Local extension in the transfer zones between the strike-slip faults or in the transtension zones produces a series of small carbonaceous basins. During the transition from Middle to Upper Stephanian, the rotational axis of the compression changes from N-S to NW-SE, activating or reactivating dextral N120°E and sinistral N160-180°E conjugate faults. This compression affects the basement and the sedimentary filling of the basins and controls the geometry of the basins along the Sillon Houiller. During the Upper Stephanian, the compression becomes E-W, resulting in strong folding of the coal deposits in the Decazeville basin and along the Sillon Houiller.

This Stephanian/Permian phase has a significant amount of extension as it controls the development of deep sedimentary basins. The Variscan heritage is therefore

characterized by the development of intense fracturing of the basement linked to the succession of compressive, transpressive and transtensional contexts (Fig 18).

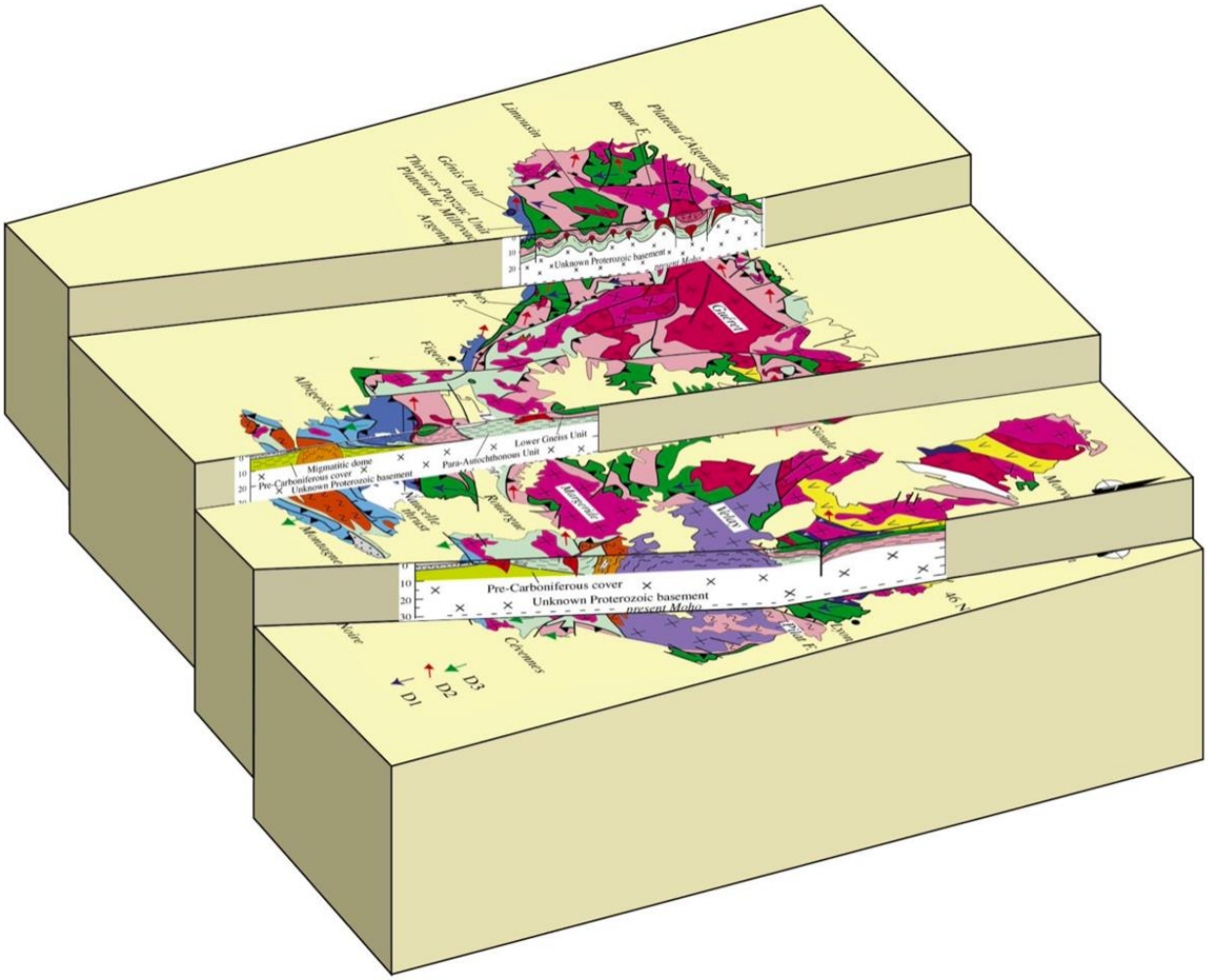

Figure 18 : Map and cross-section of the French Massif Central (from TLS-Geothermics, modified after Faure et al. 2009). The legend is the same as in the figure 16.

After the Stephanian compression and up to the Autunian (Lower Permian), a new period began during which new intracontinental basins were formed. The thickness and extent of the basins differ from those formed during the Stephanian. The Permian basins are much narrower and have deposits several thousand metres thick.

This Variscan event ends with the creation of a peneplain which is related to the chain erosion (325-250 Ma).

3.2 Mesozoïc history

Following the Stephanian compression, a Permo-Triassic extension oriented N-S then NE-SW begins (Santouil, 1980). This is represented in the basement and in the sedimentary basins by normal faults, tension cracks, veins and seams (Blès, 1989). In some places, such as at the Cévennes border, this N-S extension persisted and exploited NW-SE directions inherited from the Stephanian, forming NE trending faults (Blès, 1989).

The Jurassic-Cretaceous period corresponds mainly to the opening of the Ligurian-Provençal Ocean and then the Atlantic. The beginning of the Jurassic is characterized by a radical change in the direction of extension. Indeed, the extensive stresses previously mentioned lose their intensity with the increasing distance of the plate boundaries, the deformations are then of smaller magnitude. The beginning of the E-W phase is accompanied by significant thermal and metallogenic phenomena. This period is characterized by the formation of a large number of veins and stratiform deposits of barite and sphalerite dated at 194 Ma (Baubron et al. 1980).

In the Upper Jurassic, the extensive dynamics once again took on a north-south direction, and this was to continue until the Cretaceous. This new period of stress rotation significantly modifies the morphology of the sedimentary basins but does not seem to be accompanied by new metallogenic events (Blès, 1989). The weak erosion and/or sporadic immersion of the basement indicate that the topographic surface was always close to the base level (Michon, 1999). Variscan peneplanation continued and became more pronounced, and the reliefs disappeared.

In the Upper Cretaceous and Paleocene, a phase of intraplate compression took place, involving buckling of the lithosphere (FMC and Vosges-Forêt Noire) and re-activation of pre-existing crustal discontinuities. The deformation of Mesozoic basin sediments and the surrection of basement blocks (Bohemian Massif) caused a deep truncation of the Mesozoic platform sediments and the development of a regional erosional unconformity.

3.3 Cenozoïc history

The Cenozoic in Europe is characterized by the establishment of a rift system: the European Cenozoic Rift System (ECRIS). This system is about 1100 km long and consists of the North Sea Rift in the North and the Northwest Mediterranean Rift in the South. The ECRIS is associated with a set of faults that cross the entire Variscan Massif in the Alpine foreland. It was activated during the Eocene in the Pyrenean foreland on the one hand and in the Alpine foreland on the other in response to the accumulation of intraplate stress (Dèzes et al. 2004).

During the Upper Eocene and Oligocene, the region experienced a major E-W divergent phase. However, this Eo-Oligocene extension had relatively little effect on the Variscan basement apart from the major N-S grabens in the Bresse, Roanne-Montbrison and Limagne regions. These grabens are located all around the Alpine arc, so the graben of the Bohemian massif is oriented rather NE-SW. The fracture network of the FMC is essentially a heritage of Paleozoic history. The impact of Cenozoic events on the Paleozoic evolution remains weak, only the crust will undergo these deformations (Michon and Merle, 2001). This E-W extension essentially affects the northern part of the FMC, and is also accompanied towards the end of the Oligocene by monogenic volcanic activity: syn-rift volcanism (Michon, 1999).

From the Upper Oligocene to the Lower Miocene, the extension became asymmetrical and concentrated at the Limagne graben (Michon, 1999). This evolution is contemporary with the development of a volcanic phase localised in this basin and in line with the crustal thinning zones. This syn-rift volcanism is the result of asthenospheric upwelling leading to partial melting of the mantle responsible for crustal thinning. This magmatic activity stops in the Lower Miocene, which could suggest a stop in extension phase. All these features are consistent with a passive rift. Geophysical data show that this rifting phase did not significantly affect the southern part of the French Massif Central, which would explain the absence of volcanism at this time.

As can be seen in Figure 16 and detailed in section 4.2 (next part), the heat flux values are above the average continental heat flux values. However, the scale of lateral variations in surface heat flux values (a few kilometres) is much smaller than the crustal scale of thermal events leading to continental rifting (several tens of kilometres). Therefore, it is likely that anomalously high temperature gradients in the subsurface are best explained by local geological features. Deformation zones, such as Crustal Fault Zones, could locally modify the thermal distribution of the medium. Since 2014, TLS-Geothermics, a French company involved in geothermal exploration has been keen to demonstrate the viability of CFZ as a geothermal exploration play for economic power generation. The demonstration of the potential of CFZ is underway at a site in the French Massif Central (FMC) using an exploration licence named “La Sioule” (see location Fig 16). Several geological observation and geophysical data, which are detailed below represent good indicators for high-temperature geothermal exploitation.

4 Geothermal setting of the “La Sioule” licence

4.1 Spring and magma chamber

Present-day fluid flow occurs within the Pontgibaud fault zone (the Pranal spring in Fig 19). In addition, at the time of Pb-Zn mining activities, the galleries were regularly flooded (Lebocey, 2013). Due to cessation of mining activities in the 20th century, the mining wells were abandoned. Some wells, such as the one at Sainte-Barbe in Barbecot (4 km north of Pontgibaud), are marked by ion-rich and extremely CO_2-charged flows. In addition, the Pranal spring (see Fig 19) comes from a deep reservoir with estimated temperatures between 150°C and 175°C (estimated using Na/K geothermometer; Verney, (2005)).

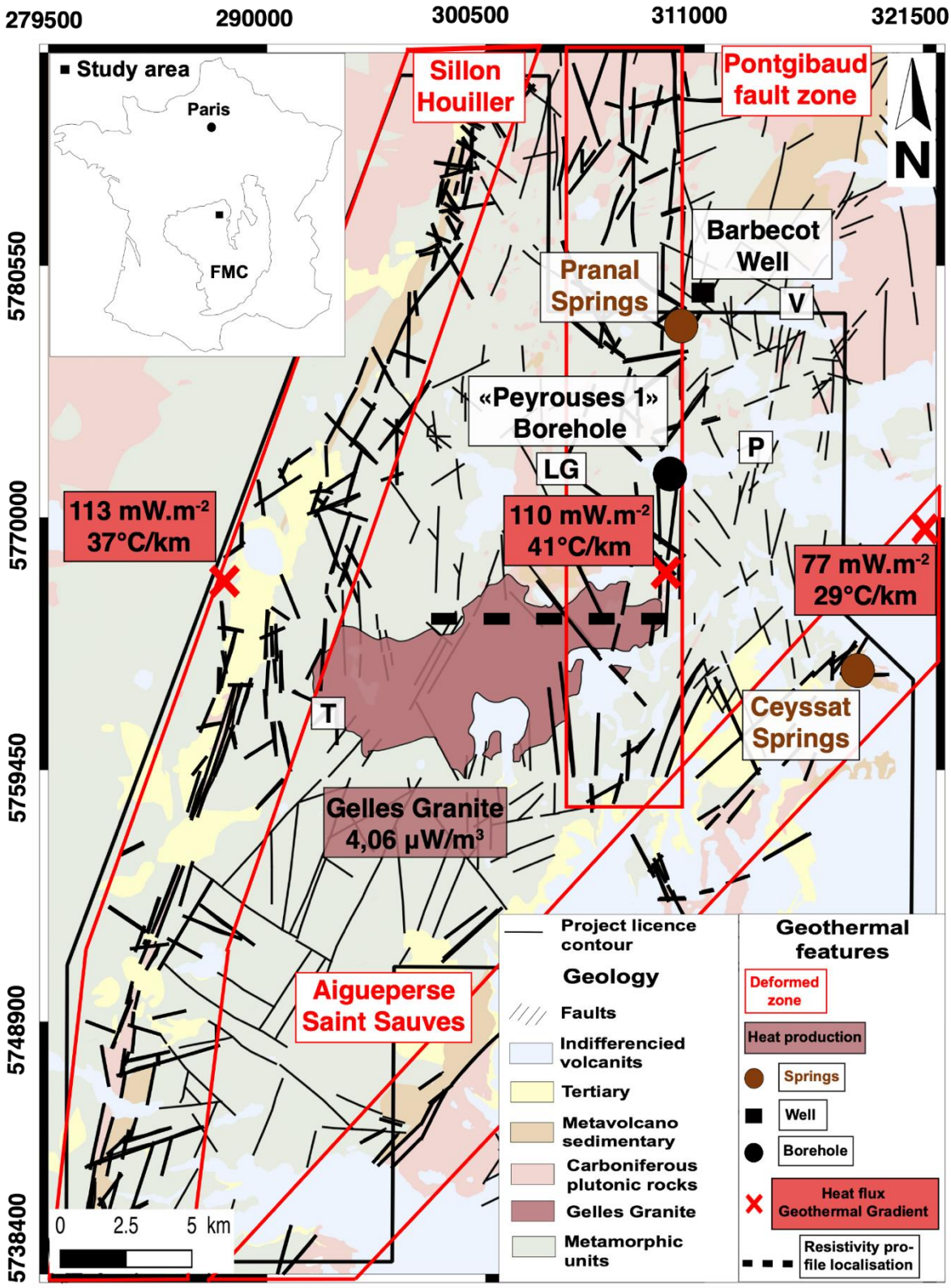

Figure 19 : Geological and geothermal features in the "La Sioule" licence area (black contour). FMC: French Massif Central. Heat flux and geothermal gradient (red crosses (Lucazeau and Vasseur, 1989; Vasseur et al. 1991), International Heat Flow Commission). Heat production (Lucazeau, 1981) and resistivity profile (black dashed line (Ars et al. 2019)). P: Pontgibaud; LG: La Goutelle; V: Villelongue; T: Tortebesse. Coordinate system: WGS84 Pseudo-Mercator EPSG:3857 (after the 1/50,000th geological map published by BRGM (Hottin et al. 2000)).

At a deeper level, thermo-barometric experiments on the CdP trachytes estimated the storage pressure and temperature conditions of magmas (Martel et al. 2013). For temperatures ranging from 700°C to 825°C, the results of Martel et al. (2013) indicate pressures between 3 and 3.5 kbar (i.e., between 11 and 13 km deep, respectively). The thermal relaxation time calculated for these reservoirs indicate that cooling started about 15,000 years ago (Martel et al. 2013). This means that they are still hot (500–600°C), if not partially melted.

4.2 Surface heat flux and heat production

Part of the Pontgibaud fault zone was intersected by core drilling undertaken by the BRGM (French Geological Survey) in the 1970s. The purpose of these drillings was to characterize the mining potential of these structures. As part of this study, one of these boreholes (Peyrouses 1, location in Fig 19) remains accessible and has been used in this study. In the past, temperature measurements have been carried out between 55 and 120 m. From these measurements, a geothermal gradient of 41°C.km^{-1} has been inferred and a heat flux of 110 mW.m^{-2} was estimated (IHFC database; http://www.datapages.com/gis-map-publishing-program/gis-open-files/global-framework/global-heat-flow-database).

This relatively high heat flux value can be explained by an elevated mantle heat flow and/or a large crustal heat production. The analysis of 660 rock samples taken from granitic units in the FMC (Lucazeau, 1981) revealed an average heat production of 4.06 µW.m^{-3}. Considering an average granite thickness of 7 km (Vigneresse et al. 1999), the heat production of this granitic upper crust can only explain 26% of the heat flux measured in the Pontgibaud fault zone. The analysis of 112 samples taken from metamorphic units revealed an average heat production of 2.27 µW.m^{-3}. If this average value is representative for the remaining 22 km of crust (considering the crustal thickness in this area is 29 km, Zeyen et al. 1997), the mantle heat flux

would be close to 32 mW.m^{-2}, twice as large as for a thermally stable Archean crust.

4.3 Magnetotelluric data

Magnetotelluric (MT) campaigns were carried out in the Pontgibaud fault zone area by TLS-Geothermics and IMAGIR between 2015 and 2017 (Ars et al. 2019). From their 3D model of electrical resistivity produced in 2016 by IMAGIR, the profile corresponding to our geological cross-section was extracted (Fig 20). The interest of this passive electromagnetic method is its sensitivity to geometries and its ability to image conductive objects in three dimensions. Results show that the obtained conductive bodies in the upper crust could be related to the Pontgibaud fault zone.

Mining work on the Pontgibaud fault zone has highlighted structures with a dip of 70° E (Bouladon et al. 1961), but more recent data favors dips of ~ 60°, as detailed later. This steep dip is consistent with the structures that are visible on the MT image (Fig 20). The obtained resistivity model makes it possible to identify highly conductive bodies, one of which is located between a depth of 10 and 20 km (Fig 20). Petrological observations on trachytes suggest that the conductivity anomaly located at a depth between 10 and 20 km could reflect the presence of silicate melt (Martel et al. 2013). At these depths it seems unlikely that the origin of this anomaly could be linked to the presence of clay. However, hydrothermal fluids could be present at the BDT, but here, the volume imaged by the anomaly allows to reject this assumption, contrary to the two other anomalies.

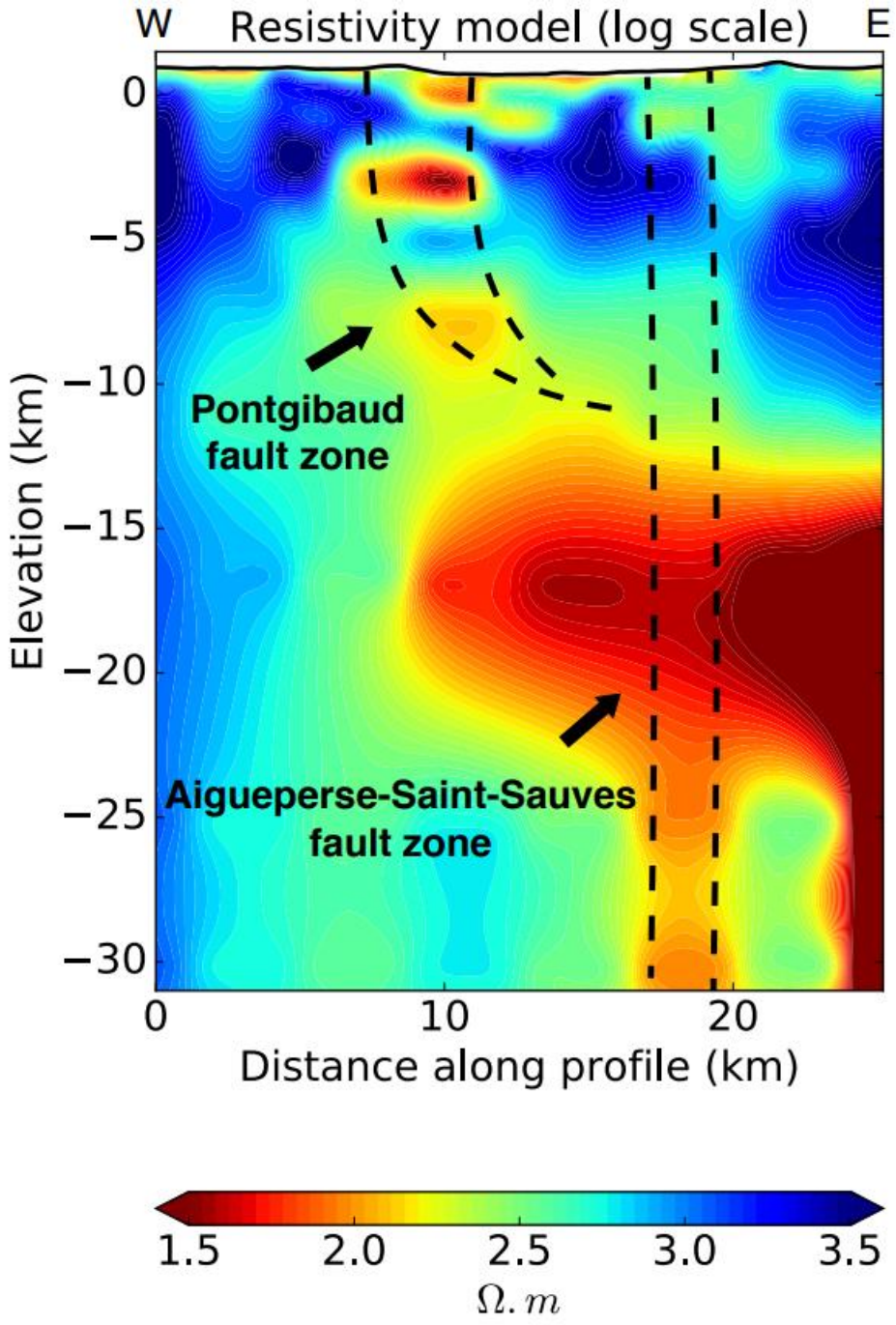

Figure 20 : 2D resistivity profile. The dashed lines represent the hypothetical tracing of the deep structures, constrained by surface signatures (fault orientation and dips). Modified after Ars et al. (2019).

At a depth of 8 and 3 km, two other anomalies located in the brittle crust could be linked to the presence of magmas, clays (smectites) and/or hydrothermal fluids. Whatever their nature, these two anomalies appear to be related to the Pontgibaud fault zone. This fault zone, which could be interpreted as a listric fault zone, seems to join the Aigueperse–Saint-Sauves fault system at a depth of 10 to 15 km (Ars et al. 2019). In order to constrain the general geometry of the Pontgibaud Crustal Fault Zone it would be interesting to coupled gravimetric, magnetotelluric and magnetic methods. Isotopic analyses of CO_2 from the Ceyssat and Pranal resurgences at $\delta^{13}C$ (Fig 20) indicate a mantle origin (Verney, 2005), which is in agreement with isotopical results from the whole French Massif Central (Brauer et al. 2017). Indeed, the presence of CO_2 at the surface could be explained and consistent with a connectivity of the Pontgibaud and Aigueperse–Saint-Sauves structures to magmatic activity. It also highlights that these two fault zones could serve as pathways for hydrothermal fluid flow.

Such data-rich context offers a rare opportunity to test *a priori* 3D geological models including the distribution of lithological units and main tectonic contacts inherited from the Variscan history. Apart from the evidence of the geothermal potential of the area, the geological details and a calendar of the paleostress on the licence-scale will be detailed when we focus on this case study. In general, integration of geophysical data should result in a well-constrained geological model (Calcagno et al. 2008; Guillen et al. 2008), which can then be used to simulate fluid circulation and heat transfer in such Crustal Fault Zones. This fully integrated approach (geophysical data constraining a geological model in 3D, then used to simulate hydrothermal processes) coresponds to a scientifc and technological challenge, yet recently achieved for a simpler case (Taillefer et al. 2018). However, fluid flow and heat transfer in hydrothermal systems depend on a many factors. Approaching a general understanding of these limiting and/or controlling elements could be essential for a geothermal exploration phase.

Chapter III : Hydrothermal circulation in crystalline basement: critical parameters, driving forces and large-scales numerical modelling

1 The permeability

1.1 Permeability, a control parameter for fluid flow and heat transfer within the Earth's crust

1.1.1 Fluid flow control

Since the first works of Darcy (1856, 1857), the permeability characterization is at the center of many scientific issues in the Earth Sciences, since the 1990s (Fig 21), with direct applications in energy resources (geothermal, oil, gas, CO_2 storage) and minerals (uranium, lithium, tin, tungsten...). This parameter is inherently linked to two rock properties.

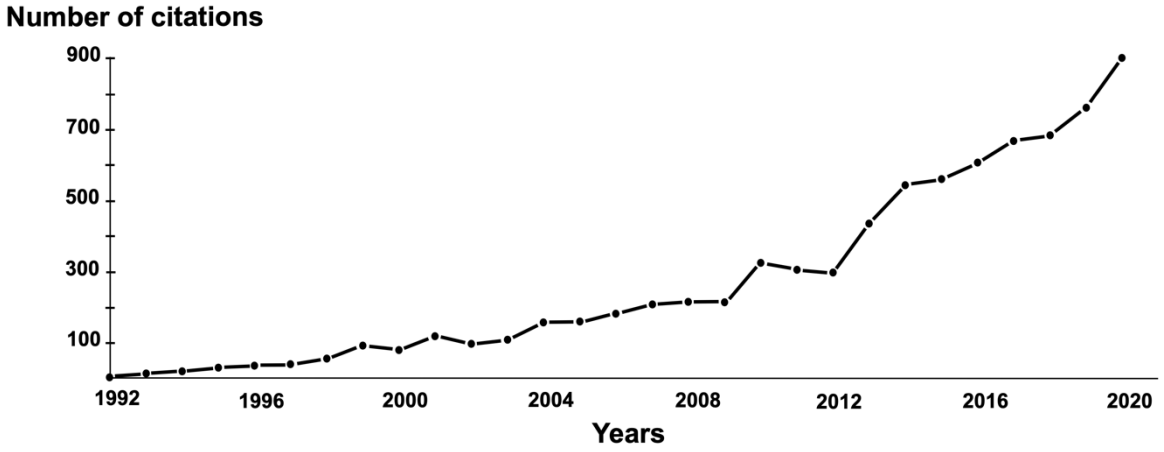

Figure 21 : Sum of annual citations on the crustal permeability topic since 1990 (citation of scientific and book publications, all disciplines considered -without abstract-).

-The porosity defines the ratio between the pore volume and the total volume. There are two different porosities, matrix porosity and fracture porosity. In natural formations both types of porosity are present.

-Permeability is the ability of the system to let fluids flow. The permeability is directly correlated to the porosity. These parameters are related to the internal structure of the rocks: their nature, their size, as well as the geological processes they have been exposed to (e.g. compaction, diagenesis). Primary permeability is associated with the pore spaces naturally present in rocks and is preserved after being buried (Fig 22).

Sedimentary rocks such as sandstones, conglomerates, are generally porous and can store large fluids amount. Their porosities vary from 1 to 40% and their permeability from 4×10^{-17} to 7×10^{-10} m^2 (Fig 22). They can represent natural reservoirs in the earth's crust for all kinds of fluids. Intact crystalline rocks have a porosity that varies from 0.1 to 13% and a permeability varies from 10^{-18} to 5×10^{-15} m^2 (Fig 22). Without other geological processes, the capacity of these systems to store and/or circulate fluids is very low. Physical and/or chemical rocks alterations are processes that can increase the permeability. These processes result in secondary permeability. Secondary permeability, or fracture permeability is related to the rock discontinuities along which fluid flow is facilitated. The porosity varies from 0.1 to 8% and the permeability from 9×10^{-15} to 7×10^{-10} m^2 (Fig 22). Thus, the presence of a secondary permeability increases the capacity of the crystalline basement to store and/or let the fluids flow (Caine et al. 1996; Faulkner et al. 2010).

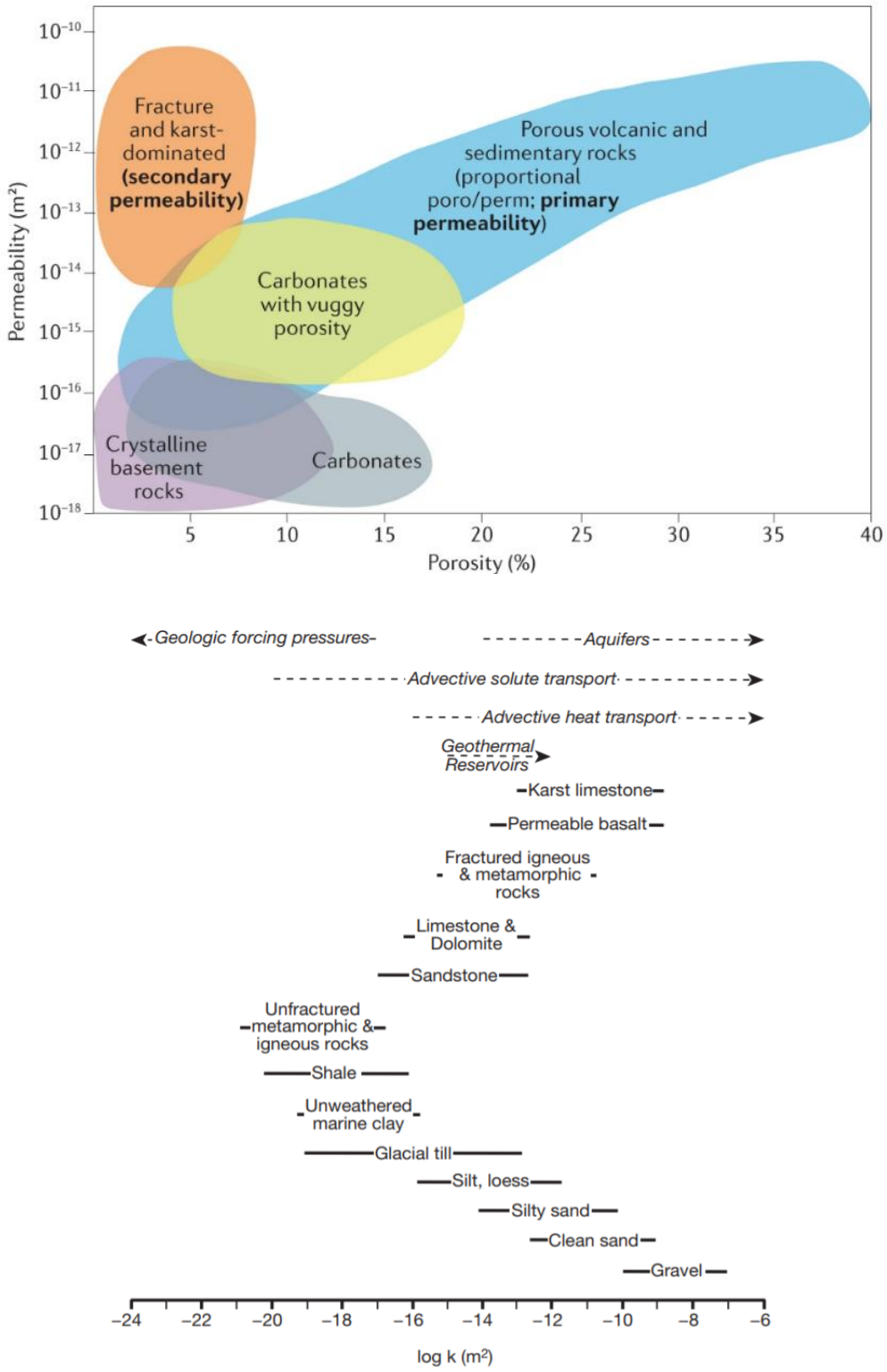

Figure 22 : Permeability/porosity relationship in different geothermal reservoirs and range of permeabilities measured within major crustal rocks (Manning and Ingebritsen, 1999; Ingebritsen and Appold, 2012; Moeck, 2014; Lamur et al. 2017; Cant et al. 2018; Eggertsson et al. 2020; Bohnsack et al. 2020; Jolie et al. 2021). Generally, unconventional geothermal resources have permeabilities below 10^{-15} m^2, conventional geothermal resources have permeabilities greater than 10^{-15} m^2.

1.1.2 Heat transfer control

1.1.21 In a homogeneous porous medium

Turcotte and Schubert (1982) looked at the thermal conditions necessary for convection to take place in a porous medium. This minimum geothermal gradient is given by:

$$\frac{dT}{dz} = \frac{4.2 \times 10^{-10}}{kb^2} \qquad \text{Eq 2}$$

Where k is the permeability and b is the length scale for convection flow. With a geothermal gradient greater than 20°C/km and for consistent values of the coefficient of thermal expansion, the authors predict that convection in porous media occurs over length scales greater than several kilometers when permeability are greater than 10^{-15} m^2.

1.1.22 In a fractured medium

Fluid circulation within the crust controls the mode of heat transfer. Within vertical fractured media, López and Smith, (1995) investigate the effects of basement and fault permeability and also basal heat flux on temperature variations of hydrothermal springs (Fig 23). Depending on this permeability ratio, the authors distinguish three different modes:

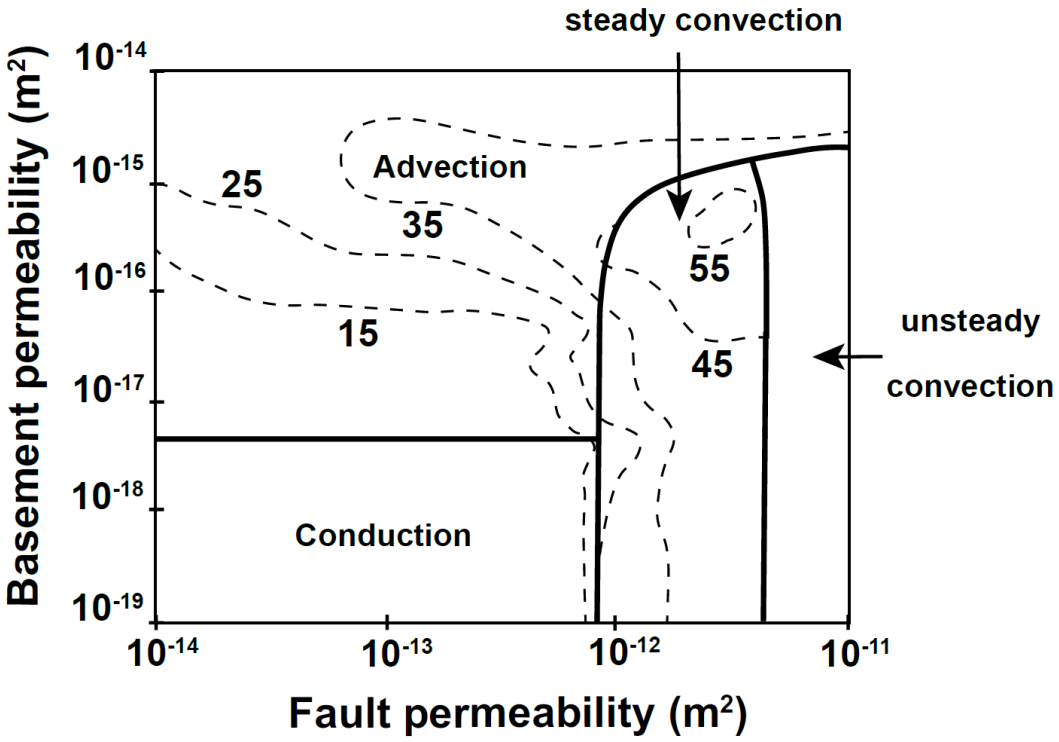

Figure 23 : Different heat transfer modes depending on the permeability of the vertical fault and the basement. The dotted lines indicate the maximum temperatures recorded. The warmest temperatures are associated with the convective heat transfer mode (López and Smith, 1995 - modified).

-For fault permeability values between 10^{-14} to 10^{-12} m^2 and basement permeability values between 10^{-19} to 10^{-18} m^2 (Fig 23), heat transfer occurs by conduction. No springs source seems to develop for these permeability values.

- For fault permeability values of 10^{-12} and 10^{-11} m^2 and for basement permeability values between 10^{-19} and 2×10^{-15} m^2 (Fig 23), heat transfer occurs by free convection. This heat transfer is associated with a matter motion, the fluids. The driving force involved in this fluid flow is described in Part 2. According to the authors, this mode of heat transfer would result in the highest spring's temperatures, 55°C.

- For fault permeability values between 10^{-14} and 10^{-11} m^2, and for basement permeability values between 3×10^{-18} and 10^{-14} m^2 (Fig 23), heat transfer occurs by forced convection. This heat transfer is also associated by matter motion, but the flow comes from an external forcing condition (e.g. a topographic gradient, see Part 2). This heat transfer could concentrate springs temperatures between 15 and 45°C.

Thus, in order to better define the heat transfer modes present in a fault/basement system, it will be necessary to consider the permeability values of these two entities. In a fault/basement system, convective heat transfer concentrates the most important temperatures. This different heat transfer mode has been described by López and Smith (1995) by considering a vertical fracture zone. However, in natural fracture system, the dip, which describes the plane orientation with respect to horizontal can vary from 0° to 90°, not only vertical. It would then be interesting to consider the dip of the structures as a variable parameter, and to see the possible effects on the medium thermicity.

1.1.221 The Rayleigh number

The possibility for thermal convection to occur within permeable area was often tested with the calculation of the Rayleigh number (Turcotte and Schubert, 2002). The Rayleigh number expresses the ratio between the driving forces (e.g. gravity) that promote fluid circulation and the resistant forces (e.g. viscous resistance) that prevent circulation. It is expressed in the form:

$$Ra = \frac{KL\alpha\Delta Tg}{D\,\nu} \qquad \text{Eq 3}$$

where K (m^2) is the medium permeability, L (m) is the thickness of the system, α ($°C^{-1}$) is the thermal expansion coefficient, ΔT (°C) is the temperature difference

between the upper and lower limits, *g* is the acceleration due to gravity (m.s^{-2}) and ν is the kinematic fluid viscosity (m².s^{-1}). *D* is the thermodispersion tensor (m².s^{-1}) (e.g. Magri et al. 2016) as defined by:

$$D = \frac{\Phi\lambda f + (1-\Phi)\lambda s}{\rho f Cpf} \quad \text{Eq 4}$$

where *Φ* corresponds to the porosity, *Cpf* (J.kg^{-1}.K^{-1}) to the fluid thermal capacity, *λf* and *λs*, respectively, to the fluid and solid thermal conductivity (W.m^{-1}.K^{-1}).
In 2020, Guillou-Frottier et al. explained how the critical Rayleigh number differs according to physical conditions: *"The critical Rayleigh number is the value above which heat is evacuated through convective circulation. This dimensionless number depends on the imposed temperature gradient, the considered geometry (thickness and depth), and fluid and rock properties. If the Rayleigh number exceeds a critical value, then thermal convection occurs. The critical value of $4\pi^2$ (Lapwood, 1948) was determined by linear stability analysis for an infinitely long homogeneous porous medium, whereby fixed temperature conditions are applied on both horizontal boundaries, and for a constant viscosity fluid. For different (and more realistic) boundary conditions (e.g., fixed heat flow at depth and fixed pressure at the surface) the critical Rayleigh number is decreased (see Jaupart and Mareschal, 2011). When temperature-dependent viscosity is accounted for, Lin et al. (2003) demonstrated that the critical Rayleigh number is also decreased when compared to the constant viscosity case. In other words, when realistic boundary conditions are considered and when appropriate fluid properties are taken into account, the critical permeability for which free convection would occur is not as high as previously thought"*

For 3D vertical faults with a permeable top, and in the case of a constant fluid viscosity (not temperature-dependent), Malkovsky and Pek (2004) provided an analytical relationship to calculate the critical Rayleigh number (Rcf). This relationship depends only on the fault aspect ratio Δ:

$$Rcf = \left[\left(\frac{6.428}{\Delta}\right)^{1.165} + (27.1)^{1.165}\right]^{0.8584} \quad \text{Eq 5}$$

where $\Delta = \frac{d}{2H}$, where *d* is the thickness of the fault zone (m) and *H* its depth (m). Other numerical and analytical simulations have shown that, for a temperature-dependent fluid viscosity, the critical permeability above which convection begins is lower than the case where the fluid viscosity is considered constant (Malkovsky and Magri, 2016). According to the calculations of Malkovsky and Magri (2016), the critical fault permeability Kfc from which convection is likely to be initiated in the faults is calculated using $Rcf/4$.

Nevertheless, the permeability of fractured systems is recognized as a discontinuous parameter whose geometric complexity and spatial variation are difficult to assess. These spatial heterogeneities could have an impact on the heat transfer mode, and consequently on the geothermal potential of the system.

1.2 Spatial variation of permeability

1.2.1 Permeability variation with depth

Porosity and permeability decrease with depth (Fig 24). The lithostatic stress increases with depth, causing pore closure and thus a decrease in primary and secondary permeability. Between 10 and 15 km depth, the Brittle-Ductile Transition (BDT) is a mechanical geological limit, where the physical laws of fracture and creep intersect. In terms of fluid infiltration, this is a crustal decoupling zone marking the limit at which meteoric fluids can flow (Famin et al. 2004).

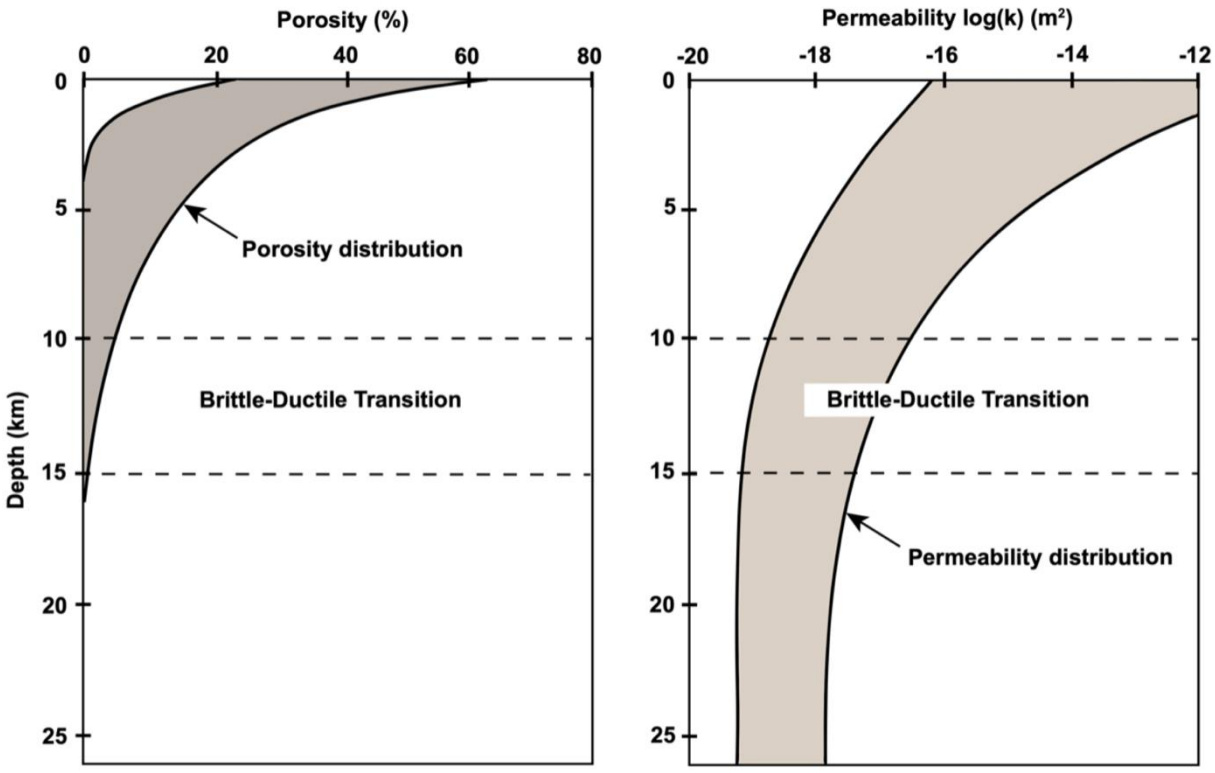

Figure 24 : Evolution of porosity and permeability with depth (after Manning and Ingebritsen, 1999; Moore and Saffer, 2001; Saar and Manga, 2004; Ranjram et al. 2015).

Therefore, geothermal reservoirs are more likely to be developed in the upper part of the Earth's crust, where permeability varies between 8×10^{-16} and 10^{-11} m^2, than in the lower part of the crust, where permeability varies between 10^{-20} and 10^{-18} m^2. This decrease in permeability with depth, whatever the lithology, follows exponential laws which can be integrated into numerical modelling (Manning and Ingebritsen, 1999; Garibaldi et al. 2010; Guillou-Frottier et al. 2013).

1.2.2 Permeability variation within a fault zone

Geological structures (fractures and faults) are heterogeneous, multi-scale systems, and play a major role on the focus of secondary permeability. Field studies of exhumed fault zones reveal different architectures, varying according to lithologies and the amount of deformation accommodated. The Punchbowl Fault (a component of the San Andreas Fault System, California, USA), accommodates a slip of about 30 km. It cuts through predominantly quartzo-feldspathic rocks, and is characterized by a mineralized fault core and a fractured damage zone (Chester et al. 1993; Chester and Chester, 1998). Based on this study, the conceptual model of a "uni-core" fault was established (Fig 25A).

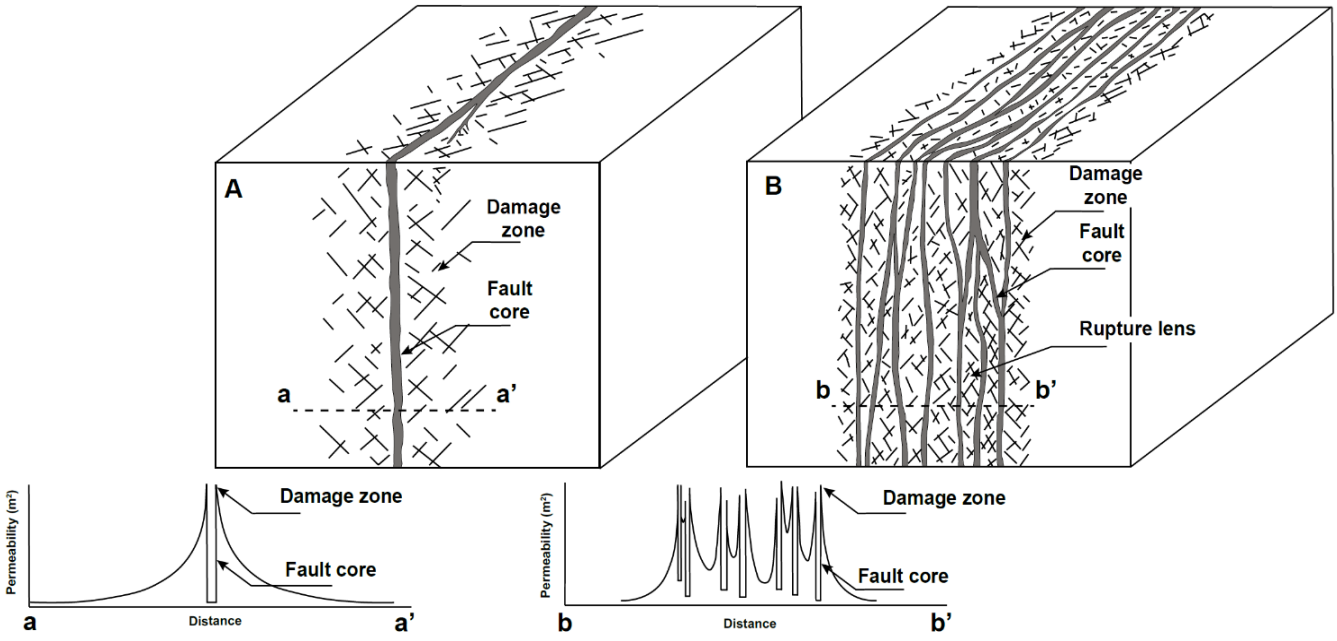

Figure 25 : Conceptual fault model and associated permeability variation. A. Schematic 3D block of the Punchbowl Fault Zone, California (USA) and associated permeability variation. (After Chester and Logan, 1986) B. Schematic 3D block of the exhumed Carboneras crustal fault, Andalusia (Spain) and associated permeability variation (after Faulkner et al. 2003; 2010). Block A corresponds to the conceptual model of a "uni-core" fault. Block B corresponds to the conceptual model of a "multi-core" fault. These two conceptual models are representative of deformation occurring at various scales.

This conceptual model of a fault zone implies some permeability variation. The permeability of this zone increases progressively from the intact, less permeable basement, to the fractured permeable damage zone before reaching the mineralized, sealed, impermeable fault core (Chester and Logan, 1986) (see Fig 25A).
In damaged zones, permeability can vary between 5×10^{-10} and 10^{-17} m^2 (Manning and Ingebritsen, 1999; Ingebritsen and Appold, 2012; Noda and Shimamoto, 2005). At the core of the fault zone, the presence of mineral deposit, cataclasites, clays, and/or gouges, seal the system. This core zone has a low permeability, ranging from 10^{-17} to 10^{-21} m^2 (Caine et al. 1996; Evans et al. 1997; Noda and Shimamoto, 2005; Ballas et al. 2012).

Another example of fault architecture has been studied on the Carboneras Fault Zone (Andalusia, Spain). This fault zone accommodates a displacement of 40 km and is characterized by a set of ramified and anastomozing faults and fractures, at different scales, and linking intact blocks between these fault (Faulkner et al. 2003). Based on this field case, Faulkner et al. (2003; 2010) developed the conceptual "multi-core" fault model (Fig 25B). This model is characterized by a successive lateral variation of damage zone and fault core. The permeability follows this same lateral variation in the same orders of magnitude as the "uni-core" model. However, in the case of the Carboneras fault zone, this variation occurs over a thickness of one kilometer (Faulkner et al. 2003).

Localizing the deformation and defined by a complex geometry of fault and fracture intersection, the permeability variation of CFZ should be more similar to the conceptual multiple fault core models than to the uni-core models. However, permeability variations are very different from one site to another (Scibeck, 2020). This requires a case-by-case study. Therefore, this aspect will be considered in our case study. All these fractures are distributed at different scales. Various works on flow in fractured porous media focus on the characteristics of fracture networks as well as pore size distribution (Juliusson and Horne, 2010; Alaskar et al. 2010; Zhao et

al. 2013; Ghanbarian et al. 2014; Cai et al. 2015; Guo et al. 2015; Zhang et al. 2016; Zhang et al. 2020). Particular geometries can be found at different scales in natural systems and can impact fluid flow.

1.2.3 Spatial variation of permeability within fault zones at different scales of observations, from the fractal to the constructal theory

The scale invariance of structures, in which permeability varies, and more broadly of geological phenomena, is a fundamental problem faced by petroleum geologists. It is also one of the first concepts taught in geology. A coin, a pen, a hammer must define the scale of a photographed geological feature, otherwise it is difficult to say whether the photograph covers 10 cm, 10 m or 10 km. For petroleum geologists, data are obtained from rock samples, laboratory measurements, thin-section (2D) and X-ray micro-tomography (3D) observations, drill core, well logging, outcrop observations and geophysical acquisition. From these data their objective is to reconstruct the geology of reservoirs, sedimentary basins and/or fractured systems using, among other things, dynamic numerical modelling.

To follow a fractal distribution, the frequency-size distribution of fragments of, faults or fractures must depend on a power law (Bertrand, 2016). These elements were outlined by Mandlebrot, 1982, and Korvin 1992 reviewed numerous applications of this mathematical theory of fractals in the Earth sciences. This theory suggests that the model is complex, and that this complexity extends infinitely in nature. However, by definition a model should be simple.

Based on a thermodynamic physical approach, Bejan (2000) was able to show that in any system subject to flow, macrostructures can be formed from thermodynamically optimized microstructures. The constructal theory states: "*For a finite-size flow*

system to persist in time (to live) it must evolve such that it provides greater and greater access to the currents that flow through it" (Bejan, 1997; Bejan and Lorente; 2008). This means that the configuration of the flow system evolves in time in a predictable way by forming optimal geometries. With the knowledge of the parameters of the system under study, this geometry will be able to facilitate the efficiency of the fluid flow. This requires special attention to the geometry of structures at different scales and as for the permeability values, its geometry requires a case-by-case study. Therefore, particular attention should be dedicated to the geometry of the permeability. Field and laboratory observations can give us insights into how permeability propagates in 2D and 3D space.

1.3 The dynamic permeability

Permeability is recognized as a dynamic parameter dependent on different geological processes such as deformation, fracturing, dewatering, fluid production, seismicity, hydrothermal alteration (Sibson et al. 1974; Walder and Nur, 1984, Yardley, 1986; Hanson, 1995; Connoloy 1997; Manning and Ingebritsen, 1999; Ingebritsen and Appold, 2012; Ingebritson and Gleeson, 2014). Field and petrological observations (Jamtveit et al. 2009; Faulkner et al. 2010; Stober and Bucher, 2015), as well as numerical models and laboratory experiments (Tenthorey and Cox, 2003; Tenthorey and Fitzgerald, 2006; Coelho et al, 2015; Ingebritsen and Gleeson, 2015; Mezri et al., 2015; Weis, 2015; Launay et al., 2019) help explain how initially impermeable systems can evolve into permeable and favorable fluid flow systems.

In a few examples, using the isotopic composition and age of sinter in the former Beowawe geyser field (Nevada, USA), Howald et al. (2015) deduce two hydrothermal discharge events of 5,000 years duration. A gradual permeability increase in a fault damage zone has been suggested by Louis et al. (2019) to explain this temporal evolution. However, depending on the hydrogeologic and tectonic setting, a

sudden increase or decrease in permeability could also happen and should significantly affect the fluid flow conditions.

On an active fault localized within a subduction zone, Saffer (2015) shows transient permeability values between 10^{-13} and 10^{-12} m^2, which is 10^6 times higher than permeability of these sedimentary rocks estimated at 5 km depth. The effects of dynamic permeability have also been studied around magmatic intrusions (e.g., Gerdes et al., 1998; Weis et al., 2012; Scott and Driesner, 2018; Launay, 2018). However, to our knowledge, these effects have not yet been studied on CFZ. We propose to look at the effects of a dynamic and adapted permeability to fractured media, on the fluid circulation (see Chap IV, part 5).

The evolution of permeability and porosity is a widely debated topic within the scientific community (Anovitz and Cole, 2015; Clavaud et al. 2008; Yokoyama and Takeuchi, 2009; Wright et al. 2009). For systems describing laminar flow within conduits, the Kozeny-Carman relationship (Kozeny, 1927; Carman, 1937, 1956; Gueguen and Dienes, 1989) is often used to describe a non-linear increase in permeability as a function of porosity for a wide range of rocks (Loaiza et al. 2012).

In this formulation, the permeability is proportional to the cube of the porosity ($k \propto n^3$). This equation describes the evolution of the permeability/porosity coupling by considering the geometry of the conduit allowing the fluids to flow. This geometry can be tabular (connected pores) or planar (cracks) (Bernabé et al. 2010; Kushnir et al. 2016). Experimental studies on explosive volcanic rock have proposed the existence of a percolation threshold (~30% porosity), below which rocks are considered impermeable (Klug and Cashman, 1996; Mueller et al. 2005). Though other percolation thresholds for media have been mathematically modelled at 59% in 2D (Sukop et al. 2002), and at 31 % in 3D (Stauffer and Aharony, 2018).

However, in the presence of fractures and vesicles, studies have shown that fluid flow is possible at lower porosity (Mueller et al. 2005; Lavallée et al. 2013; Gaunt et al. 2014; Ashwell et al. 2015; Dobson et al. 2003; Kendrick et al. 2016; Heap and Kennedy 2016). This raises questions about the use of a percolation threshold when describing the relationship between porosity and permeability, and thus the difficulty in capturing fluid flow behavior in hydrothermal/geothermal systems channeled by complex, heterogeneous, and connected structures at different scales (Sibson, 1994; Lee et al. 2001; Mourzenko et al. 2011; Wannamaker, 2005).

Rather than percolation thresholds, Lamur et al. (2017) and Parisio et al. (2019) proposed to use Kozeny coefficients in the presence of bubbles and fractures to characterize the evolution of permeability and porosity during different processes, notably fracturing (Kendrick et al. 2013; Laumonier et al. 2011; Lavallée et al. 2012) or shearing (Ashwell et al. 2015; Okumura et al. 2010; Shields et al. 2014).
The study by Lamur et al. (2019), empirically related the permeability of fully fractured rock k_f and intact rock k_i to the porosity *n*. This relationship is written as:

$$\log k = (1-\omega)\log k_i + \omega log k_f$$
$$k_i = 4.979 \times 10^{-11}\, n^{3.11} \qquad \text{Eq 6}$$
$$k_f = 1.143 \times 10^{-11}\, n^{0.64}$$

Where ω representing the degree of rock fracturing, $\omega = 1$ for fully fractured rock, and $\omega = 0$ for fully intact rock. Here we take $\omega = 0.8$ corresponding to the significant fracturing degree of the fault zone, interspersed with intact zones, n represents the initial porosity. Considering the effect of mechanical parameters on this initial porosity n, will allow to consider the effect of a dynamic permeability associated with mechanical processes and to account for the geothermal potential of naturally fractured zones. These points are detailed in chapter IV, part 5.

2 The driving forces involved in the fluid flow within a fault zone

In shallow permeable zones, at the scale of kilometer-size reservoir two main processes can induce fluid circulation: buoyancy forces, and variations in pression gradient. Depending on the process, induced convection can be forced, free, or both.

2.1 The buoyancy forces

For fluids with non-uniform density, the terms $\rho_f g$ of the Darcy's law provide a driving force for buoyancy-driven effects associated with spatial variations in fluid density in a porous medium (Murphy, 1979). Hydrothermal convection is induced by changes in the density of the fluid phase which affect buoyancy forces causing the sinking of colder, denser fluids and the upwelling of hotter, less dense fluids. Buoyancy forces can therefore cause convection within permeable structures, and are dependent on pressure and temperature conditions, and salinity. Convection caused by buoyancy forces is said to be "free".

2.2 The pressure gradients

2.2.1 Topography effects

Hydraulic gradients, which govern the flow of fluids under pressure, can be generated in different ways: metamorphic devolatilization, magmatic fluid production and/or topographic elevation (Forster and Smith, 1989; Nur and Walder, 1990). In the superficial parts of the earth's crust (typically a few kilometers deep) the effects

of topography can cause lateral variations in fluid pressure that will guide fluid flow (Forster and Smith, 1990; López and Smith, 1995; Ehlers, 1999, Cox, 2005; 2015; Bucher et Stober, 2010). For instance, infiltrating cold fluids could dominate and prevent hot fluids from rising to the surface, except in a few locations (see the clusters of thermal springs in the Pyrenees in Taillefer et al. 2018). The role of topography in the location of thermal springs in the Jordan rift valley has also been investigated by Magri et al. (2015), who illustrated the coexistence of topography-driven and buoyancy-driven flow. Topography-driven flow can predominate and modify the convective patterns.

The role of topography has been studied on fault systems typical of the 'uni-core' conceptual model of Chester and Logan, (López and Smith, 1995; Taillefer et al. 2017). However, to our knowledge, this role has not been studied on large deformation zones typical of multiple faut cores, which may correspond to a larger lateral permeability variation. We will discuss the influence of topography on the fluid flow within a large deformation zone in Chap VI (Part 3).

2.2.2 Tectonic stresses

On large-scale, tectonic stresses has been considered as driving forces that influence fluid flow in different geological contexts (Ord and Oliver, 1997a, 1997b; Cox, 1999; Rowland and Sibson, 2004; Branquet et al. 2019; Armandine Les Landes et al. 2019). Bethke, (1985), shows that compressive environments can lead to increased fluid pressure and favor upward movement. Sibson (1987) links overpressure and upward movement to fault valve activity. On compressive systems, the degree of shortening has a control on fluid flow (Li et al. 2017). In extensional environments, the generated under-pressure appears to cause downward fluid migration (McLellan et al. 2004). Cui et al. (2012) used simplified 2D models with a fault zone to show that with degrees of shortening exceeding 1% the fluid flow is then different. In 3D, Eldursi et al. (2020) suggest that during tectonically active periods, the decrease in pore pressure can reorient fluid flow in fractured zones.

On a small-scale, pore volume changes associated with elastic deformation of intergranular pores or cracks generate hydraulic gradients. Poroelastic effects may be significant around active fault zones where stress changes occur (Muir-Wood and King 1993). Poroelasticity-induced flow is likely to be most prevalent where large changes in normal stress occur around zones of high fracture density, such as in the shallow crust (Cox et al. 2005). Furthermore, seismic rupture is not essential for an increase in permeability. As a matter of fact, favorably oriented tectonic stresses may be enough to sustain sufficient permeability for fluid flow (Barton et al. 1995; Brown and Bruhn, 1998; Ito and Zoback, 2000), particularly in localized deformation zone (Curewitz and Karson, 1997). These effects have been demonstrated in inter-seismic phases, where stresses re-equilibrate at fractures, and faults begin to load again under regional tectonic stresses. Without seismic events, hydrothermal systems eventually reach a state of equilibrium that can be sustained as long as the permeability of faults and fractures remains sufficient for fluid flow (Sibson, 1994).

The fluid flow within the crust depends on many factors. Using numerical models constrained by a multidisciplinary approach can integrate a number of the factors detailed above. In addition, some of these numerical models have given consistent results with other field data, and are now used as a predictive tool for different exploration context, such as oil, gas, uranium ou geothermal exploration.

3 Large-scale numerical modelling of fault zones constrained by a multidisciplinary approach

The first models of fluids circulation in faulted zones allowed to understand the formation of convection cells and the influence of some key parameters on their

geometries. The critical Rayleigh number is the value at which convection starts to form (Zhao et al. 2004; Malkovsky & Pek, 2004). The geometry of the cells depends on the boundary conditions imposed on the models, and thus on the geological knowledge of the environment.

One way to understand hydrothermal systems could rely on the possibility to numerically simulate heat and mass transfer through a 3D geological model that incorporates realistic physical properties, as well as appropriate thermal flow, and mechanical boundary conditions (Jupp and Schultz, 2000; Harcouët-Menou et al. 2009; Guillou-Frottier et al. 2013; Weis 2015; Magri et al. 2016). By using Comsol Multiphysics^{TM} Taillefer et al. (2018) recently used 3D numerical models to understanding hydrothermal regimes (temperature and velocity fields, convective patterns) within the Têt fault hydrothermal system (Pyrenees, France) (Fig 26).

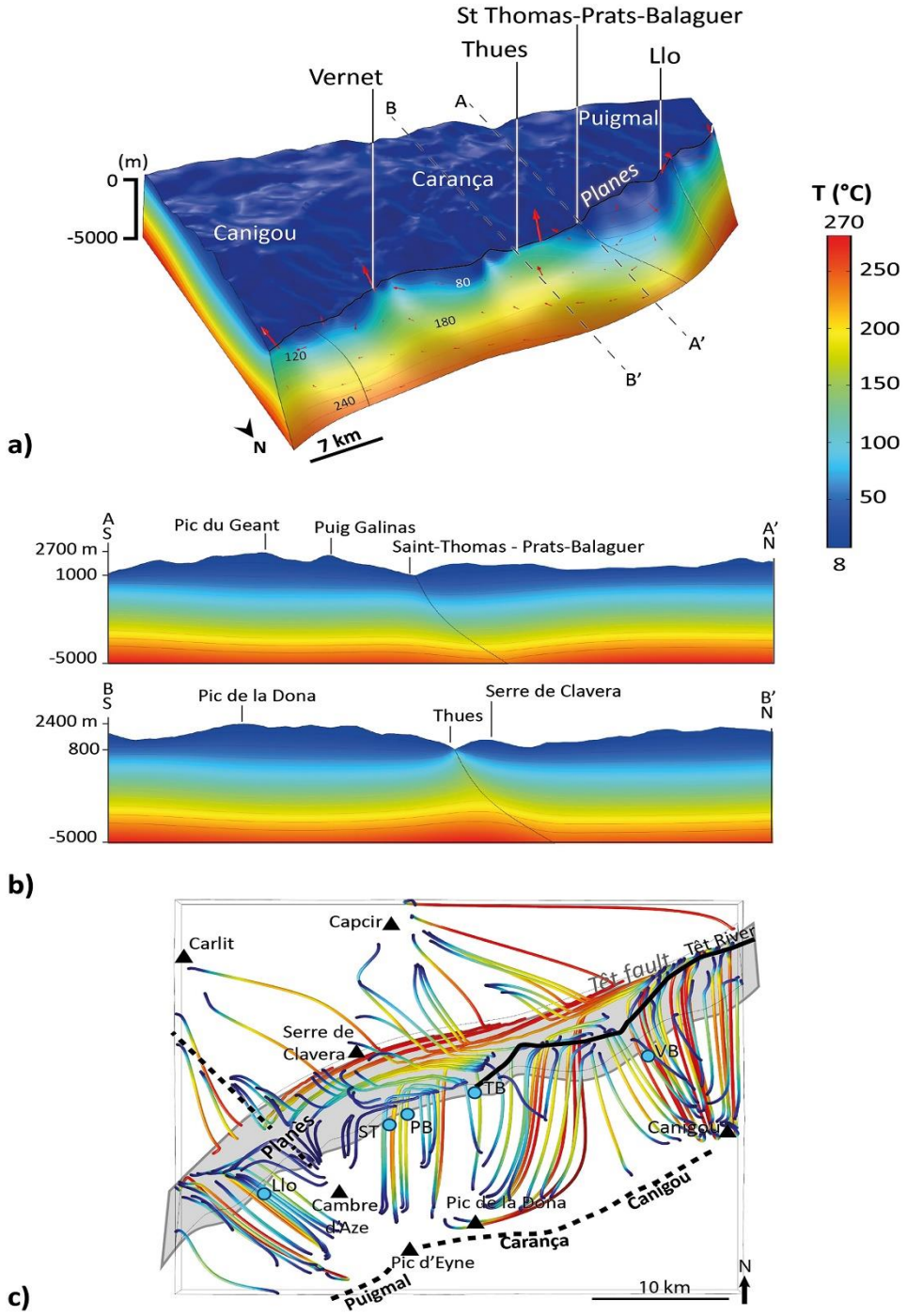

Figure 26 : (a) Distribution of thermal anomalies for large-scale 3D single-fault model of the Têt fault hydrothermal system, (Pyrenees, France). Temperature scale is the same for all figures. (b) N-S cross sections (c) Vertical view, with the hot spring locations, of the flow lines inside the model colored according to temperature (for more details see Taillefer et al. 2018).

While fault zones often host hydrothermal systems (Faulds et al. 2010), the permeability of these networks depends on a multitude of parameters. The relationships between (i) fault geometry and stress field (Barton et al. 1995); (ii) fractures and their connectivity, and (iii) alteration, dissolution and precipitation, are all processes, that can cause faults to behave as conduits for (Caine et al. 1996; Mazurek, 2000, Gudmundsson, 2000; Grasby and Hutcheon 2001; Brogi and Fulignati, 2012; Belgrano et al. 2016, Patterson et al. 2018a; 2018b; 2021) or barriers to (Bense et al.

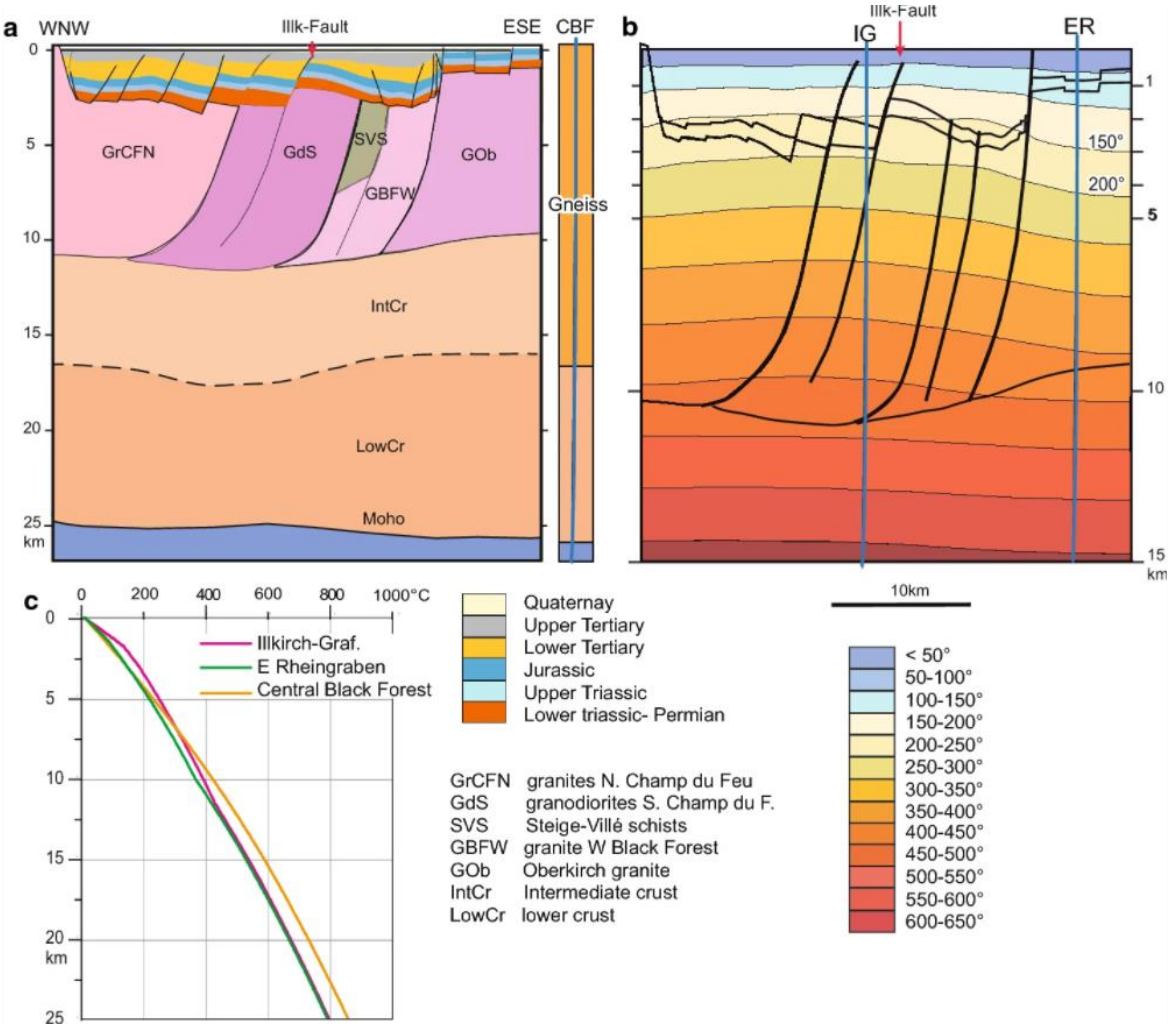

Figure 27 : (a) Crustal section based on the EU GEORG section of the sedimentary infill of the Rhinegraben and on the ECORS_DEKORP seismic section down to the Moho (Brun et al. 1991; Edel and Schulmann, 2009). The NW-SSE profile passes through the Illkirch area. (b) Temperature model result, estimating the depth of 150 °C isotherm at 2.5 km (for more technical detail see Edel et al. (2018)). (c) Log of temperatures in the Illkirch project area (IG), the eastermost Rhinegraben (ER) and the Central Black Forest (CBF). From Edel et al. 2018.

2008; Bertrand, 2016) fluid flow. Consequently, it is worth using a multidisciplinary approach to strongly constrain fluid flow models in hydrothermal systems (Oda, 1986; Caine et al. 1996; Bense and Person, 2006; Micarelli et al. 2006; Faulkner et al. 2010; Bense et al. 2013). As an example, the recent study by Edel et al. (2018) predicts, using a combination of magnetic, gravity, seismic and geological data, a temperature of 150°C at a depth of 2,500 m in the northern Vosges area (France) (Fig 27). In addition, with an improved numerical modelling approach, Guillou-Frottier et al. (2013) reproducted and predicted temperatures at geothermal sites of Soultz-sous-Forêts and Rittershoffen (Fig 28).

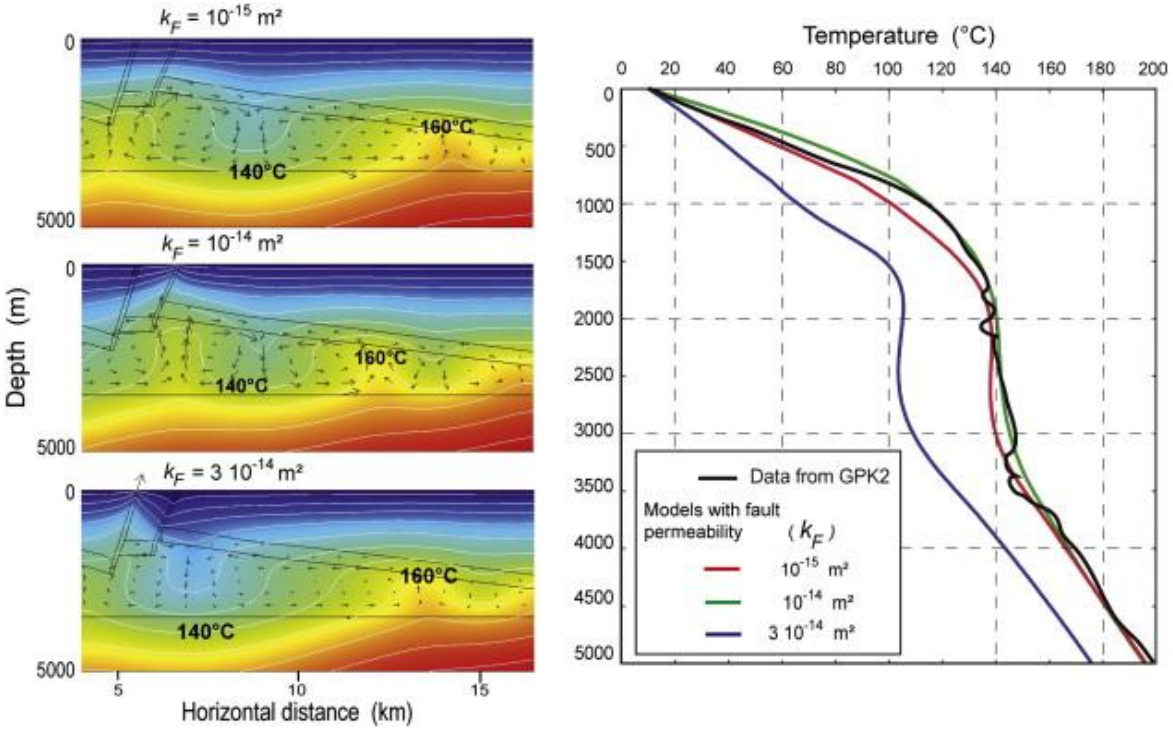

Figure 28 : Models at basin-scale with a varying permeability for two main faults. Thermal and velocity fields are shown on the left. The associated temperature profiles at GPK2 location are shown on the right. (For more details see Guillou-Frottier et al. (2013).

The above studies integrate a multidisciplinary approach in large-scale numerical modelling and retrieve different field data. Crustal scale numerical modelling also allows to define how fluids are likely to flow, depending on different parameters. For

example, the study by Magri et al. 2016, models on a large-scale the Lower Yarmouk Gorge (LYG) (Fig 29). Helicoïdal fluid flows within fault systems, which can sometimes be caused by the transition from a low-permeability interface (basement) to a high-permeability zone (fault zone). The general geometry of the modelled system will influence the convective patterns, as will the permeability imposed on each domain. In order to define the way fluids can circulate within such a system, it is therefore essential to describe the natural system in its structural and lithological settings, as well as to characterize quantitatively and qualitatively the capacity of the system to let fluids circulate.

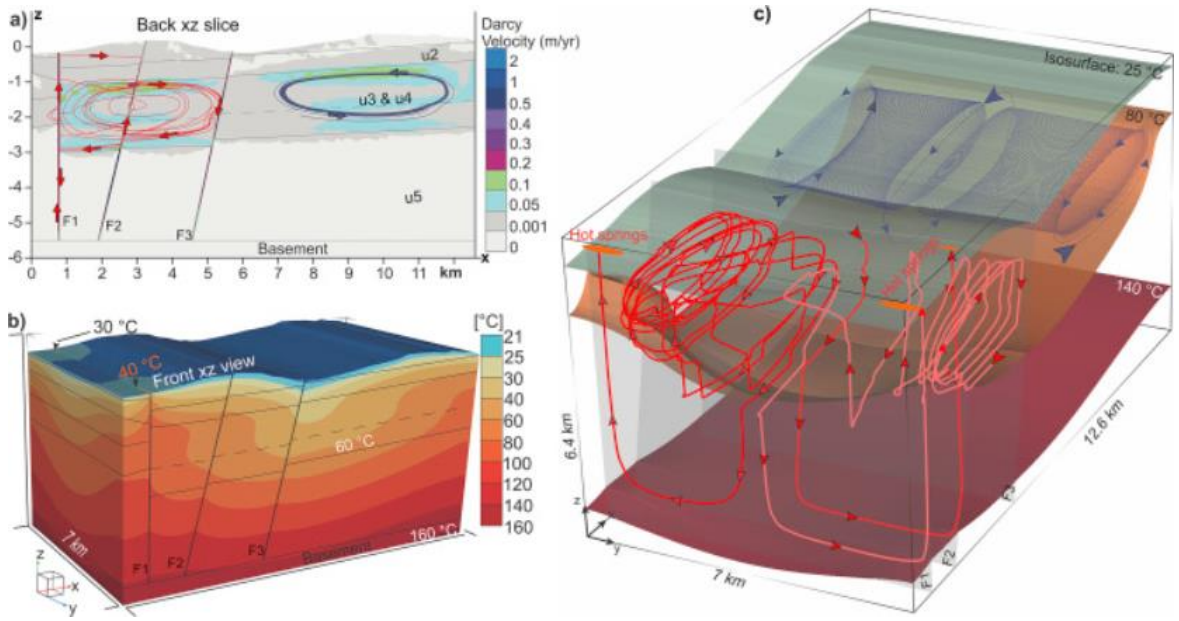

Figure 29 : Results of large-scale numerical modelling of the Lower Yarmuk Gorge (Magri et al. 2016). Fluid circulations can follow helicoïdal movements that have direct consequences on the thermicity of the modelled system. These fluid circulations depend on the integrated physical properties, the general geometry of the system.

Indeed, the way in which fluids are circulated have a direct impact on the geothermal potential. Integrating geophysical data, borehole information and numerical modelling, the study of Tong et al (2008) investigates the distribution of isotherms in a structure in Chingshui, Ilan, Taiwan. The results tend to show a rise in isotherms

in the SE part of the reservoir (Fig 30). This upwelling is related to upward fluid movement in this area. The downward movement of fluids would maintain the position of these isotherms at deeper depths.

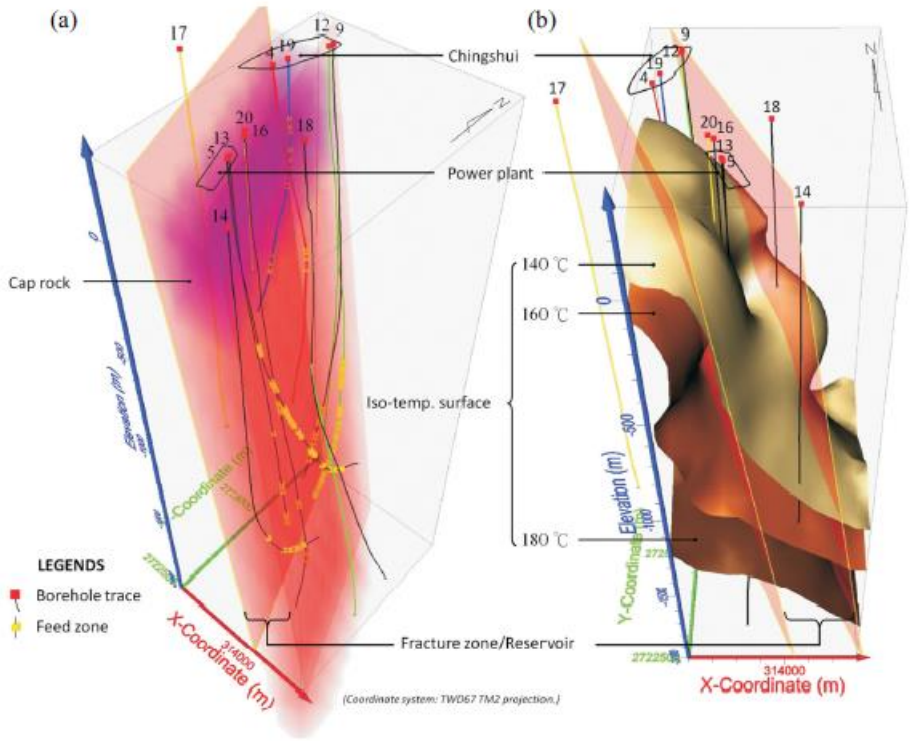

Figure 30 : 3D conceptual model of Chingshui geothermal reservoir (Taiwan). The position of the isotherms shows an upward fluid movement in the SE part and a downward fluid movement in the NW part. The characterization of the fluid flow within a hydrothermal system appears to be essential to define the geothermal potential of a study area (from Lun-Tao et al. 2008).

Whether it is to find the resurgence position, or to retrieve temperature data, large-scale numerical modelling, integrating a multidisciplinary approach, also allows to characterize the way fluids can circulate within a faulted hydrothermal system. For each case, some surprising dynamical features were discovered. The characterization of these fluid circulations has direct consequences on the thermicity of the medium. The final volume of the reservoir potential may largely depend on the fluid circulation pattern.

With the available geophysical database, additional geological field measurements, and core sampling from a 250 m deep borehole, the numerical approach dedicated to the understanding for the Pontgibaud hydrothermal system will be relevant as previous study. However, we can see that the use of numerical modelling constrained by multidisciplinary approaches has only been applied to single fault zone models. In this study, we will adopt a multidisciplinary approach to constrain numerical modelling of larger deformation zones than a single fault zone. While this kind of approach allows to combine and understand a set of elements, this approach also has limitations. Some of these limitations are discussed in Chapter VI (Part 1).

As mentioned earlier, fluid flow within the crust depends on many factors. The permeability ratio between the fault and the basement, the static permeability, the dynamic permeability, the buoyancy forces, the pressure gradients, are parameters that have been widely studied in the past. However, the effects of these parameters on the fluid circulation in the purely crustal domain, within an abnormally permeable zone, and especially their consequences on the temperature anomalies, are, to our knowledge, not widely documented in the literature.

This is why, before looking at a natural case, we propose to focus at the effect of some unknown parameters on fluid circulation within a CFZ. For this purpose, numerical modelling is an ideal tool for testing the effect of unconstrained parameters. Afterwards, these results can then be compared with a field study. In this context, we have seen in the previous sections that the hydrothermal system of Pontgibaud represents an interesting example for the understanding of a hydrothermal system in a deep fractured basement zone.

Chapter IV : Some controlling and limiting factors on fluid flow, within a Crustal Fault Zone, in a basement domain

“It is very nice that the computer understands the problem. But, I would like to understand it too.”

Eugene Wigner (Nobel Laureate in Physics, 1963).

In order to quantify the effect of unconstrained parameters, on the fluid flow, and its consequences on the temperature anomalies a series of numerical simulations using Comsol Multiphysics™ software are performed. Considering simplified geometries, but realistic physical properties we present different parametric studies. This numerical approach is organized in four stages. The first stage corresponds to the calibration of the modelling tool with previously published numerical modelling results. Benchmark tests are performed in order to reproduce the already published results by Magri et al. (2017) and Guillou-Frottier et al. (2020). The second stage is focused on the influence of fault dip and permeability ratio on fluid flow. The third stage is dedicated to the demonstration of the effects of stress intensity and stress direction on fluid flow and thermal regime within the CFZ. The fourth stage is focused on the tectonic regime as control factor for Crustal Fault Zone geothermal reservoir. After benchmarking test, the last three stages were performed in order to understand the effect of some parameters on the fluid flow of CFZ. We will also look at the consequences that these parameters can have on intensity and depth of temperature anomalies. If certain trends could be identified, such as dips more or less favorable for geothermal exploration, stress intensities and orientations, or tectonic regimes, a comparison of these results with a natural case study will then be performed.

1 Equation and benchmarking

Originally developed with MATLAB, Comsol Multiphysics™ (previously called FEMLAB) software is based on the Finite Element Method (FEM) and can, among other various physical processes, model fluid flow, heat transfer and elastic deformation of materials in 1D, 2D and 3D geometry. The FEM is designed to represent analytically the dynamic behavior of some physical systems (behavior of a fluid, mechanical behavior of a system, etc.). Another dynamic numerical approach is the Discrete Element Method (DEM). This method represents the material as a

set of grains that can interact with each other. This numerical approach is particularly suitable for simulating the mechanical behavior of granular materials (such as soil, aggregate, rock) (Donzé et al. 2009; Scholtès and Donzé, 2012). In this study, we will base the development of the numerical approach on the FEM. When the objective of the numerical approach is to integrate field observations and laboratory data into realistic numerical models (as can be done in Chap V), a discretization of the different domains will be necessary, and we will then try to reconcile the numerical imperatives and the geological requirements. The Comsol Multiphysics™ software allows the user to define the geometry, material properties, mesh, choose the physics, solve and display the results on a single interface. Comsol Multiphysics™ is a well-known tool offering a complete access to the solution of partial differential equations. The user of Comsol Multiphysics™ can define his own systems of partial differential equations. The complete user guide is available at https://www.comsol.fr

1.1 Governing equations

1.1.1 Equations used in the Thermal and Hydraulic (TH) models

Physically, fluid flow in fractured and/or porous media can be described by the Darcy law (1856, 1857). Darcy's law is an expression of the conservation of mass momentum that describes fluid flows as a function of pressure gradient and permeability of the medium:

$$\vec{v} = -\frac{k}{\mu_f}(\overrightarrow{\nabla P} - \rho_f \vec{g}) \qquad \text{Eq 7}$$

Where $\vec{q}$ (m.s^{-1}) is the Darcy velocity, k (m^2) is the permeability of the medium, μ_f (Pa.s) dynamic viscosity of the fluid, ρ_f (kg.m^{-3}) is the density of the fluid and $\vec{g}$ (9.81 m^2.s^{-1}) the gravitational acceleration. Darcy's law states that laminar flow ap-

plies to fractured and porous rocks. The limits of Darcy's law are discussed in Chapter VI (Part 4). Coupling Darcy's law with other physical equations permits the simulation of fluid flow in the crystalline basement. The coupling with the heat equation is written as:

$$\rho C_p \frac{\partial T}{\partial t} = \nabla\left(\lambda \cdot \vec{\nabla}\mathrm{T}\right) - \rho_L C_L \vec{v} \cdot \vec{\nabla}\mathrm{T} \qquad \text{Eq 8}$$

Where T (°C) is temperature, t is time and $\vec{v}$ (m.s^{-1}) the Darcy law. ρ (kg.m^{-3}) is the rock density, C_p (J/kg.K) is the specific heat, λ (W/m.K) is the thermal conductivity. ρ_L and C_L are fluid density and fluid specific heat, respectively. Properties of the satured fractured medium obey to a simple mixing rule between the fluid (L) and the solid (S):

$$\rho C_p = \varphi\left(\rho C_p\right)_L + (1-\varphi)\left(\rho C_p\right)_S \qquad \text{Eq 9}$$

$$\lambda = \varphi(\lambda_L) + (1-\varphi)\lambda_S \qquad \text{Eq 10}$$

Where φ is porosity. Fluid is supposed incompressible and mass conservation equation writes:

$$\nabla \cdot \vec{v} = 0 \qquad \text{Eq 11}$$

For fractured medium, fluid motion is driven by pressure gradient and buoyancy, and fluid filtration velocity obeys Darcy's law:

$$\vec{v} = -\frac{k}{\mu}(\vec{\nabla}\mathrm{p} - \rho_L \vec{g}) \qquad \text{Eq 12}$$

Where k (m^2) is the permeability of the medium, μ (Pa.s) is the fluid dynamic viscosity, p (Pa) is pressure and $\vec{g}$ ($m.s^{-2}$) is gravity acceleration. Hence, coupling between heat transfer and fluid motion occurs through the velocity field, which appears in Eqs 8, 11, and 12. The fluid density corresponds to fitting experimental data for pure water and for temperature and pressure ranges of 0-1000°C and 0-500 Mpa, respectively (NIST Chemistry WebBook; Linstrom and Mallard, 2001; Launay, 2018):

$$\rho_L(T,P) = 1006 + (7.424\ 10^{-7} \times P) + (-0.3922 \times T) + (-4.441\ 10^{-15} \times P^2)\ ) + (4.547\ 10^{-9} \times P \times T) + (-0.003774 \times T^2) + (1.451\ 10^{-23} \times P^3) + (-1.793\ 10^{-17} \times P^2 \times T) + (7.485\ 10^{-12} \times P \times T^2) + (2.955\ 10^{-6} \times T^3) + (-1.463\ 10^{-32} \times P^4) + (1.361\ 10^{-26} \times P^3 \times T) + (4.018\ 10^{-21} \times P^2 \times T^2) + 7.372\ 10^{-15} \times P \times T^3) + (5.698\ 10^{-11} \times T^4) \quad \text{Eq 13}$$

Where T is the temperature (°C) and P is the pressure (Pa). The dynamic viscosity of the fluid is function of temperature T (°C), such that Smith and Chapman, (1983), Rabinowicz et al. (1998):

$$\mu_f(\mathrm{T}) = 2.414.10^{-5}.\exp\left(\frac{570}{T+133}\right) \quad \text{Eq 14}$$

Some rock and fluid properties are set as constant for the parametric study and in the large-scale numerical modelling of the Pontgibaud system (Next chapter). Their values are summarized in Appendix 1, and 4.

Permeability is a critical parameter in the functioning of geothermal systems and will be our main adjustment variable. We will distinguish between the permeability of the basement and the permeability of the fault zone, whose variations will be differentiated. In the basement, and up to the BDT, the permeability will be subject to the lithostatic pressure and will therefore be considered as decreasing with depth. It will be characterized by the following equation Garibaldi et al. (2010):

$$K_b(z) = K_{b_0} \exp\left(\frac{z-800}{\delta}\right) \quad \text{Eq 15}$$

Where $K_{b_0}(z)$ (m^2) is the maximum permeability (present at the surface) taken here at 10^{-16} m^2. z (m) is the depth below sea level, here the depth is negative below sea level. The term "z-800" is applied to the z-axis by removing the altitude from the model. δ (m) defines the decrease in permeability with depth, taken here at 2500 m, following the models of Guillou-Frottier et al. (2013), Garibaldi et al. (2010). Within the fault zone, we considered that the permeability variation with depth varied according to Eq 15. However, multiple fault core area has a very high fracture density. In addition, the lateral variation in permeability will be heterogeneous. Therefore, we consider that the use of Eq 15 is not sufficient. By keeping the decrease in permeability with depth, a first 2D lateral variation can be included, by using the following spatial variation:

$$K_f(x,z) = K_{f_0} \times \left[exp\ \frac{z-800}{\delta}\right] \times \left[101 + 100\ \times sin\left(2 \times \pi \times \frac{(x+z)}{\lambda}\right)\right] \quad \text{Eq 16}$$

Where $K_f(x,z)$ is the space-dependent permeability of the fault and $K_{f_0} \times 201$ being the maximum permeability value at the surface. The last term on the right side of Eq 16 makes the permeability alternate along a sinusoid applied to the vertical and horizontal axes of the numerical model. The term λ corresponds to the wavelength of the sinusoid. To reproduce rather fine alternations of high and low permeability, as suggested by multiple fault core a low value of λ was chosen. Finally, the choice of constants 100 and 101 makes it possible to vary the permeability over two orders of magnitude. This function is illustrated in Figure 32.

1.1.2 Equations used in the Thermal Hydraulic and Mechanical (THM) models

The poroelasticity interface of Comsol Multiphysics™ combines the regular fluid flow formulation with linear elastic solid mechanics of the porous medium matrix. Poroelasticity coupling means that the deformation of the porous medium affects fluid flow, while changes in volumetric stress will in turn affect the amount of motion and heat transport. This interface includes an expression of the stress tensor as a function of the strain tensor and of the Biot-Willis coefficient (Zhou et al. 2018).
Mixing mass conservation of the fluid and momentum balance yields that the poro-elastic model is governed by the following relation:

$$\rho_f S \frac{\partial pf}{\partial t} + \nabla \cdot \left(\rho_f \vec{v}\right) = Q_m - \rho_f \alpha_B \frac{\partial}{\partial t} \varepsilon_{vol} \qquad \text{Eq 17}$$

Where ρ_f is the fluid density (kg.m^{-3}), S is the poroelastic storage coefficients (Pa^{-1}) see Eq 24, pf is the fluid pressure (Pa), t is time (s), $\vec{v}$ is velocity (m.s^{-1}), Q_m is the fluid source term (kg.m^{-3}.s^{-1}), α_B is the Biot-Willis coefficient (-), and ε_{vol} is the volumetric strain of the porous matrix (-). Darcy's law sets that $\vec{v}$ is equal to:

$$\vec{v} = -\frac{k}{\mu_f}\left(\nabla pf - \rho_f \vec{g}\right) \qquad \text{Eq 18}$$

Where k (m^2) is the permeability of the medium, μ_f is the fluid dynamic viscosity (Pa.s), and g is acceleration due to gravity (m.s^{-2}). The governing equation for the momentum balance model is:

$$-\nabla . \sigma = \rho g \qquad \text{Eq 19}$$

Here σ (Pa) is the stress tensor and ρ (kg.m^{-3}) is the total density. Notice that negative compression convention is considered. The components of the strain tensor

depend on the displacement vector $\vec{u}$ (m). Under the small strains assumption, we have:

$$\varepsilon = \frac{\nabla\vec{u} + {}^{\mathrm{T}}\nabla\vec{u}}{2} \quad \text{Eq 20}$$

The stress-strain relationship for linear materials relates the stress tensor and the strain tensor ε through Hooke's law. Accounting for the hydromechanical coupling, we have for isotropic materials:

$$\sigma = 2\mu\varepsilon + 3\lambda\varepsilon_V\delta - \alpha_B p f \delta \quad \text{Eq 21}$$

Here, δ, is the second order identity tensor (-) $\varepsilon_V = Tr(\varepsilon)/3$ is the volumetric strain (-) μ and λ are Lamé's parameters (Pa) and are function of Young's modulus *E* (Pa) and Poisson's ratio ν (-) by the following relationship:

$$\lambda = \frac{\mathrm{E}\nu}{(1+\nu)(1-2\nu)} \quad \text{Eq 22}$$

and

$$\mu = \frac{\mathrm{E}}{2(1+\nu)} \quad \text{Eq 23}$$

The storage coefficient *S* (in Eq15) depends on the porosity ε_p (-), Biot coefficient α_B (-), fluid compressibility χ_f fixed at 4.8×10^{-10} Pa^{-1} (Saar and Manga, 2004) and matrix compressibility χ_m (Pa^{-1}):

$$S = \varepsilon_p\chi_f + \chi_m(\alpha_B - \varepsilon_p)(1 - \alpha_B) \quad \text{Eq 24}$$

The matrix compressibility is fixed with Young's modulus and the Poisson's coefficient by the following relationship:

$$\chi_m = \frac{\frac{E}{3}}{1-(2\times \nu)} \quad \text{Eq 25}$$

Consequences of Eq 24 and 25 on numerical values of *S* are the following: the coefficient is time-dependent through porosity variations; the obtained values vary between 10^{-11} and 10^{-10} Pa^{-1}. These values are consistent with the compressibility values provided by Freeze and Cherry, 1979. Some rock and fluid properties are set as constant for the parametric study and in the large-scale numerical modelling of the Pontgibaud system (Next chapter). Their values are summarized in Appendix 2, 3 and 4 (see Appendice).

The poroelastic material model obey Eq 19, which describes changes in the stress tensor σ and porous matrix deformation due to boundary conditions and changes in pore pressure. Eq 19 defines a state of static equilibrium because the changes in the solid equilibrate quickly, implying that there are no time-dependent terms. Still the time rate of change in strain $\frac{\partial}{\partial t}\varepsilon_{vol}$ appears as a coupling term in Eq 17 because the solids equation becomes transient when solved simultaneously with a time-dependent flow model. However, in these studies, we did not investigate the mathematical theory of the fluids redistribution in poroelastic media, as a function of time. The complexity of this approach has been detailed in the studies of Rice and Cleary, (1976) and Rudnicki and Hsu, (1988).

In 3D, the permeability function is similar to that already used in Eq 16, where the permeability varies in 2D along the z and x axes with a decrease in permeability in 3D, we add a “y” coordinate to the Eq 16, and we obtain:

$$K_f(x,y,z) = K_{f_0} \times \left[exp\ \frac{z-800}{\delta}\right] \times \left[101 + 100\ \times sin\left(2 \times \pi \times \frac{(x+y+z)}{\lambda}\right)\right] \quad \text{Eq 26}$$

Where $K_f(x,y,z)$ is the fault permeability dependent on the three space directions and $\mathrm{K_{f_0}} \times 201$ will be the maximum permeability at the surface. The choice of 100 and 101 means that the permeability will vary over two orders of magnitude.
The permeability here will vary according to a sinusoid applied to the three directions $x + y + z$. This function is illustrated in Figure 61 and 62. Details of the coupling equations between Darcy's law and Fourier's law can be found in the previous section, as well as the fluid density and the dynamic viscosity.

1.2 Benchmarking

The calibration of our numerical experiments, with Comsol Multiphysics™ version. 5.5 is performed based on results from Comsol Multiphysics™ version 3.5a (Guillou-Frottier et al. 2020) as well as the OpenGeoSys numerical code (Magri et al. 2017). These models consider a 40 m wide vertical fault in an impermeable casing (a 5.5*5.5*5.5 km side cube). The fluid properties are identical for all three results. A linear dependence of temperature with water density, and an exponential decrease of viscosity with temperature. This result is shown for a time $t_0 + 10^{13}$ s. The imposed permeability value is 5×10^{-15} m^2. The obtained fluid flow velocity is 2.03×10^{-9} $m.s^{-1}$.

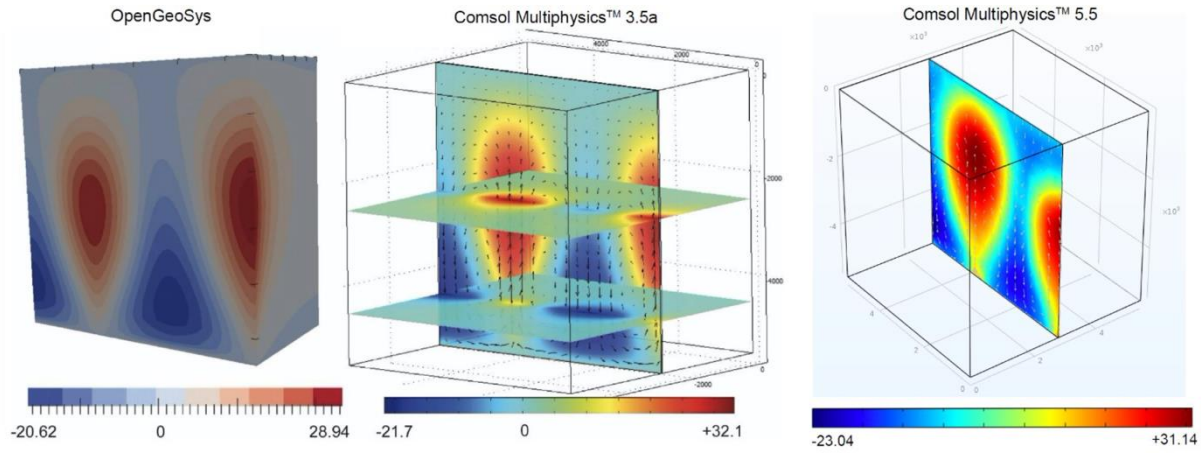

Figure 31 : Benchmarking (Comsol Multiphysics™ .5.5) with the OpenGeoSys Code (Magri et al. 2017) and Comsol Multiphysics™ 3.5a (Guillou-Frottier et al. 2020).

The fluid flow velocity is slightly higher than that described by Guillou-Frottier et al. (2020), who record a velocity of 1.4×10^{-9} m.s^{-1}. The convective patterns are similar. Fluid velocity increases along the permeable fault and exhibits upward movement due to the thermal gradient and buoyancy forces related to lower water density at depth. The thermal perturbations are also similar to those of previous studies with -22.04°C and +31.14 °C. The numerical experiments of Magri et al. (2017) and Guillou-Frottier et al. (2020) used Darcy's law coupled with the heat equation. The following numerical experiments couple the equations of heat and mass transfer with the modulus of poroelasticity. The poroelasticity interface of Comsol Multiphysics™ combines Darcy's law with the linear elastic behavior of porous media. Poroelastic coupling allows boundary stresses to be imposed, which can be recorded as fluid pressure. In Figure 22 (right), no stress or other mechanical conditions are applied. Consequently, this experiment corresponds to an identical coupling as in the previous studies (Fig 22, left and middle cases).

2 Dip and permeabilty effects of CFZ on fluid flow

2.1 Geometry boundary conditions and meshing

An idealized geometry is considered (Fig 32). The average temperature at the surface is fixed at 10°C. A constant heat flux of 70 $mW.m^{-2}$ is imposed at the base of the model. The lateral borders of the model were thermally insulated.

The initial conditions of the model were defined from the stationary state obtained for the pure water conduction regime. At $t=0$, the permeabilities were assigned to the different compartments, and the fluid flow is initiated. The results are shown in steady-state regime. For Darcy's law, a no flow condition is imposed at the bottom and on both sides of the model, a surface pressure equivalent to atmospheric pressure ($P=10^5\ Pa$) is imposed at the surface and a positive pressure evolution with depth is adopted as the initial condition. The use of such boundary conditions will be discussed in Chapter VI (Part 2).

For the models of the theoretical fault zone (Fig 32), the mesh consisted of 61,211 triangles with a size not larger than 5 m in the high-permeability zones and not smaller than 150 m in the low-permeability zones. The mesh is also refined at the intersections of the fault planes. Preliminary convergence tests have shown that a finer mesh size gives the same results.

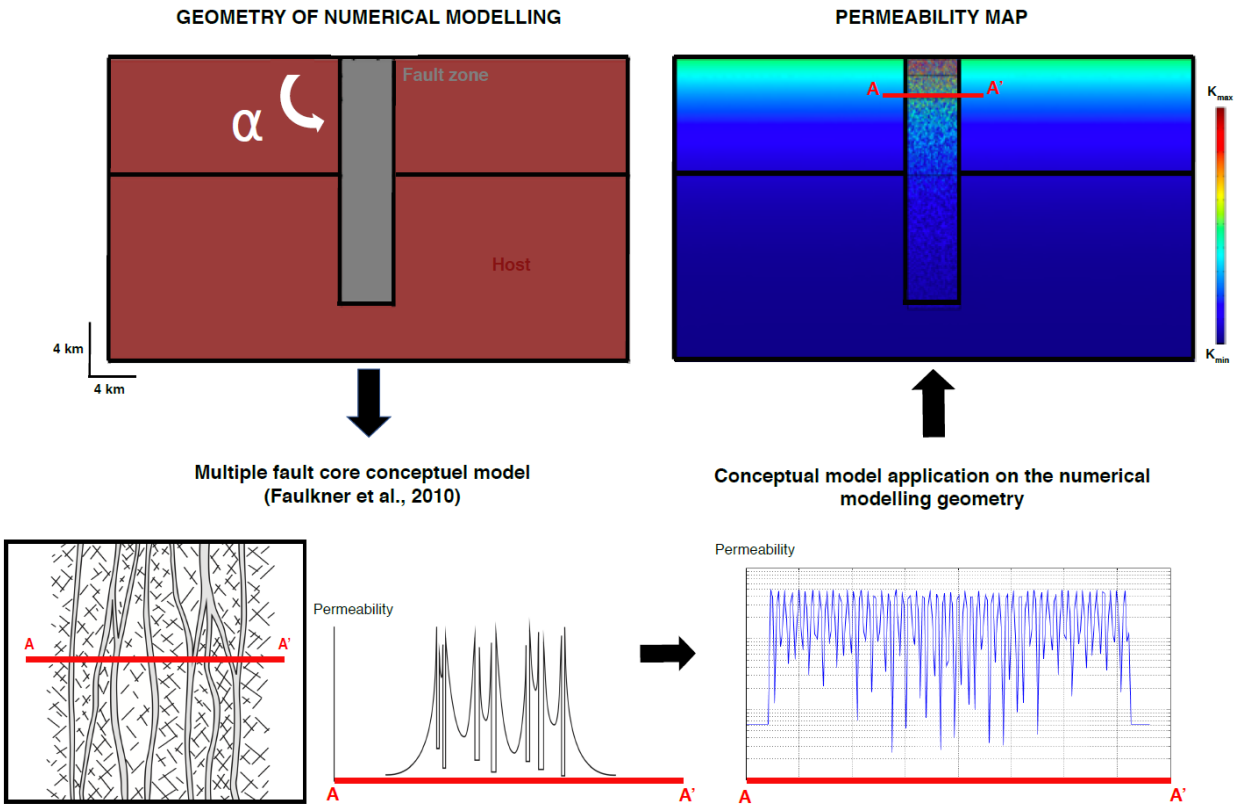

Figure 32 : Permeability imposed in the numerical models of the parametric study. The alpha angle corresponds to the dip of the fault zone (here α = 90°). The permeability of the basement and fault will decrease with depth according to Eq 15 (Garibaldi et al. 2010). Within the fault zone, permeability will also vary laterally (Eq 16) according to the multiple fault core conceptual model (see Fig 25).

In order to see the effects of geometry and permeability, the physical properties on either side of the fault zone were identical and fixed (Fig 32). During the various simulations, the dip of the fault zone is tested at angles ranging from 10 to 90°. The assigned permeability to the basement and fault zone varied according to equations 15 and 16. The K_{f_0} value varied from 1 × 10^{-18} to 2 × 10^{-16} m^2, thus giving a maximum permeability value ($K_{f_{max}}$) of 4 × 10^{-14} m^2. For the basement, the K_{b_0} value is 10^{-16} m^2 and decreased down to 1 × 10^{-20} m^2 at depth.

2.1 Results

More than 200 simulations were performed, with the numerical set-up of Figure 32. The results are summarized in Figure 33.

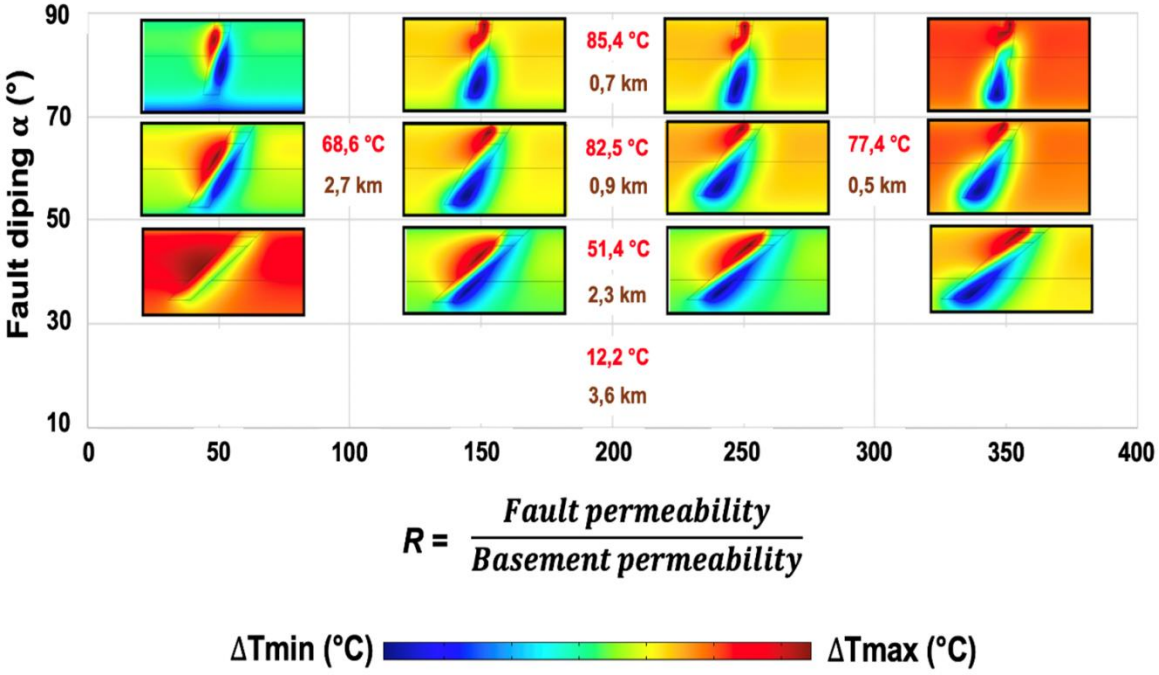

Figure 33 : Graphical representation of all numerical models of temperature anomalies on the theoretical fault zone performed (n= 216). The values of positive thermal anomalies are shown in red. Their depths are represented in brown.

The images in Figure 33 represent temperature anomalies (ΔT), corresponding to abnormally hot and abnormally cold temperatures compared to an undisturbed (conductive) thermal regime. The amplitude of the temperature anomalies are different for each case, but numerical values are indicated for some of them. In order to account for both the permeability of the fault and of the basement rock, the *R* ratio is defined by:

$$R = \frac{K_{f\,max}}{K_{b_0}} \qquad \text{Eq 27}$$

This ratio compares the maximum permeability of the fault ($K_{f_{max}}$) and of the basement (the permeability K_{b_0} being set at 10^{-16} m^2). Other K_{b_0} values have been tested, but higher values are not realistic and lower values do not change the results detailed below. Moreover, this value is compatible with the permeability values extracted from laws of permeability decrease proposed by Ingebritsen and Appold (2010, 2012).

As it can be seen in Figure 33, for *R* = 200, as the dip of the fault zone increases from 10 to 90°, the temperature values increase from 12 to 85.4°C (red numbers in Fig 33). Thus, for a fixed R ratio, the highest thermal anomaly value will be for a vertical fault zone.

The depth of the thermal anomaly also varies as a function of fault dip. By increasing the fault dip from 10 to 90°, the depth of the thermal anomaly (brown numbers in Fig 33) decreases from 3.6 to 0.7 km. Thus, for a fixed R value, vertical structures will result in the largest thermal anomalies at the shallowest depths.

By observing the variations in the temperature anomalies, we can see that when R increases for a fixed angle of 60°, the values of the thermal anomalies are 68.6°C, 82.5 °C and 77.4°C. Indeed, an increase in the R ratio does not show a significant increase in the temperature anomaly. However, the depth of these same anomalies decreases from 2.7 to 0.5 km. So for a fixed dip, when R ratio is high, the thermal anomaly will be at a maximum at a shallower depth. Therefore, a fault zone with a high dip and a high R ratio will result in the largest thermal anomalies at the shallowest depths.

While this representation characterizes the distribution and intensity of positive thermal anomalies, it does not characterize the processes at their origin. Based on the results of these same numerical simulations, Figure 34 graphically summarizes the

morphology of the numerically-obtained isotherms as a function of fault dip angle, value of positive thermal anomaly and the R ratio. Three main zones can be described:

(i)- For R values between 1.9 and 250 (blue area in Fig 34) the morphology of isotherms is slightly deformed. This low deformation occurs at dip values below 50°. The value of the resultant thermal anomaly will be lower than 65°C. These results are consistent with Figure 34 since the lower the dip of the structure and the lower the R ratio, the lower the thermal anomaly produced. The black arrows show that the fluids circulation is controlled by a single long-wavelength convection cell. This domain will be called the “unicellular weak type convection zone”.

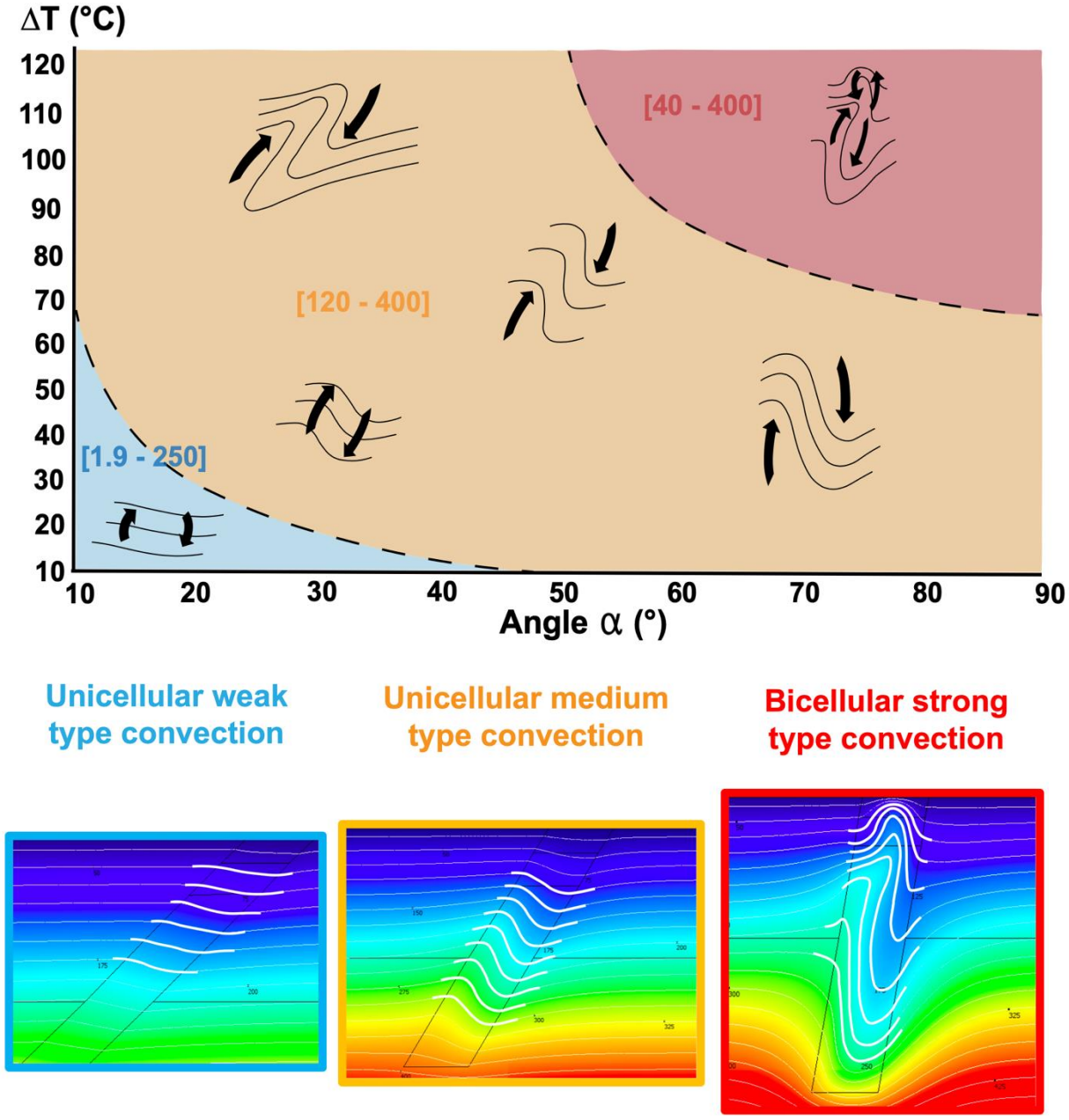

Figure 34 : Diagram of convective regimes, with three results examples of the parametric study. Grey lines represents isotherm morphology. The dashed black line separate three area. In blue, the area of unicellular weak type convection zone. In orange the area of unicellular medium type convection zone. In red the area of bicellular strong type convection zone.

(ii)- For R values between 120 and 400 with a dip value between 10 and 90° (orange area in Fig 34), the isotherms show moderate deformation. The range of values of the thermal anomalies produced is between 10 and 120°C. In the same way, the arrows show that fluid circulation is controlled by moderate-wavelength convection cells. This domain will be called the “unicellular medium type convection zone”.

(iii)- Finally, for R values between 120 and 400 and dips greater than 50° (red area in Fig 34) the isotherms are significantly deformed. The value of the thermal anomaly is higher than 67°C. These results also show consistency with Figure 34 since the higher the dip and R ratio, the greater the thermal anomaly at shallow depth produced. The black arrows show that the circulation of fluids is controlled by two small-wavelength convection cells. This domain will be called the “bicellular strong type convection zone”.

The results of this parametric study should be applicable to hydrothermal systems in a crustal context. To sum up, for unicellular convection, the values of the thermal anomalies produced are between 10 and 120°C. For bicellular convection, the values of the thermal anomalies produced are between 70 and 120°C. However, the fluid circulation can take place in the three dimensions (Magri et al. 2016, Patterson et al. 2018a). Moreover, tectonic deformation has been considered as driving force that influence fluid flow in different geological contexts (Ord and Oliver, 1997b; Cox, 1999; Rowland and Sibson, 2004). Thus, one could assume that the stress orientation and stress intensity could also have an influence on the fuids circulation in the three dimensions of space (Fig 35).

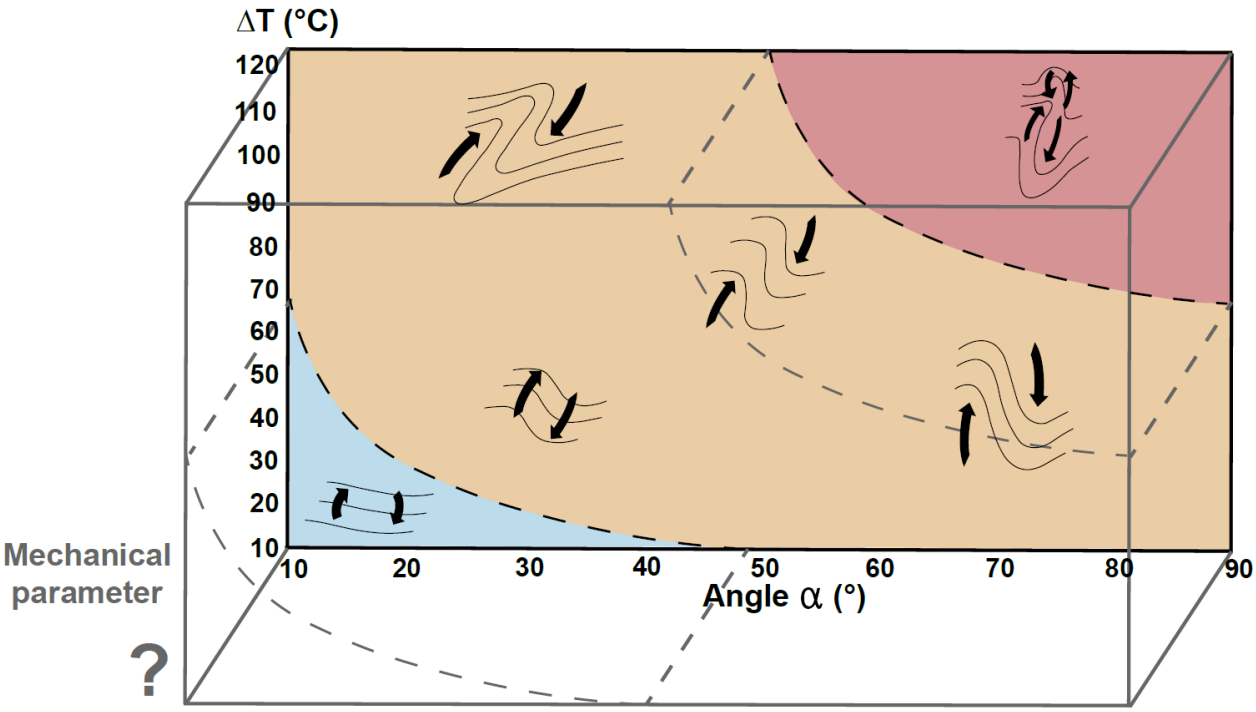

Figure 35 : Could a mechanical parameter modify the circulation of fluids and have consequences on the intensity and depth of temperature anomalies? Parts 3, 4 and 5 of this chapter will focus of this important issue.

3 Stress direction, stress intensity, and permeability effects on fluid flow within CFZ

To account for the mechanical aspect, we have performed a preliminary 3D THM model where hypotheses are simple with the aim to focus on one single but important issue: could mechanical stresses affect the hydrothermal convective regimes? To our knowledge THM models are generally applied to purely pressure-driven flow, where fluid density is constant and thus with no buoyancy-driven components (see however Wang et al. 2019; Shi et al. 2019). However, Vallier et al. (2020), used a similar approach as ours but with another objective being the study of mechanical effects on gravity anomalies, so that no information on the coupling between fluid flow and mechanical effects can be retrieved. Thus in this part, we explore by numerical modelling the effect of stress intensity, stress direction on fluid flow, and temperature anomalies.

3.1 Geometry, boundary conditions and meshing

Taking into account the 3D aspects, the geometry of this parametric study remains idealized. The mesh consists of 175,789 tetrahedra, with a maximum size of 200 m for low permeability values and a maximum size of 20 m for high permeability values. Preliminary convergence tests have shown that a finer mesh size gives the same results. The stress is applied on the red side (see Fig 36); the other three lateral borders have roller conditions (no perpendicular displacement). At the base of the model, an embedding condition (no displacement) and a heat flow of 80 $mW.m^{-2}$ are applied. The vertical sides are thermally and hydraulically insulated, and at the surface, a temperature and pressure of 10°C and 10^5 Pa are imposed,

respectively. A positive pressure evolution with depth is imposed as an initial condition. In the same way as for the previous parametric study, the use of this kind of boundary conditions will be discussed in Chapter VI (Part 2).

The initial thermal conditions of these models are defined from the stationary state obtained for a pure conductive regime. At *t=0,* values of permeability are assigned to the different compartments and the fluid flow is initiated.

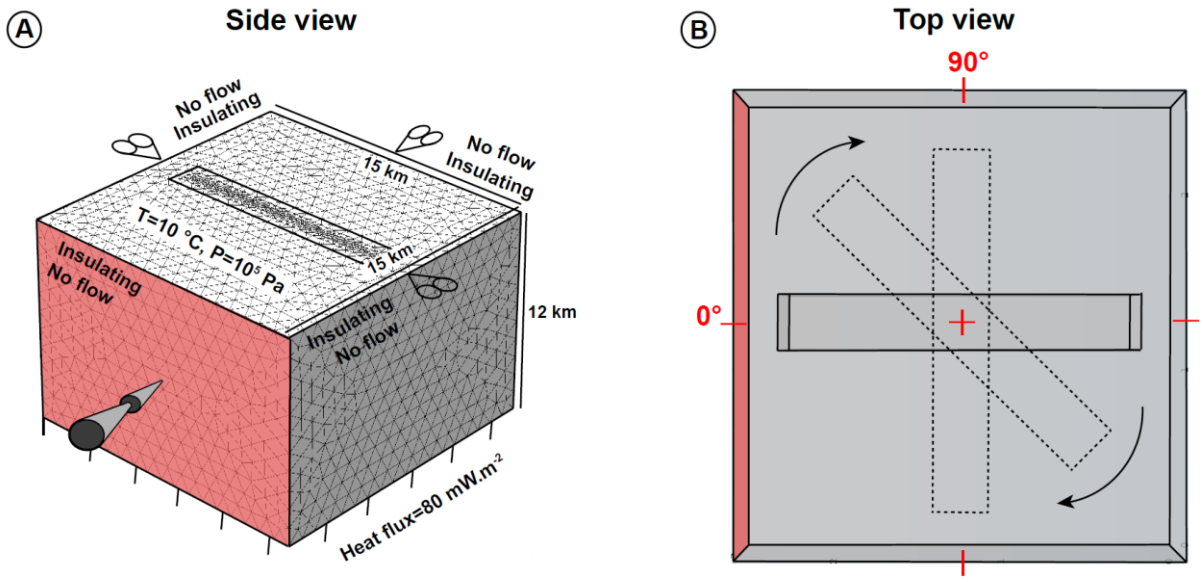

Figure 36 : Geometry, meshing and boundary conditions of the parametric study. Numerical set-up is detailed in the text.

The first stage consists of investigating the effects of the fault direction, permeability, and stress value on the fluid flow, on the intensity of the temperature anomaly and on its depth. To do this, the runs were established along directions of the deformation zone that vary from 0° to 90° (with a 10° step). Represented by the arrow; stress values that vary from 0 to 100 MPa (with a 10 MPa step) is applied, and permeability values that vary from 1×10^{-16} to 4×10^{-14} m^2 (with a 10^{-16} m^2 step) is tested (Fig 36).

3.2 Results

More than 2,500 numerical simulations were run to understand the effects of fault direction, stress intensity, and permeability on the intensity and depth of the positive temperature anomaly. Fig 37 synthetizes these results. This figure presents the value of the positive temperature anomalies, as well as their depths, as a function of the stress intensity (x-axis), the angle with respect to the stress direction (y-axis) and the permeability ratio between the fault and the basement defined as Eq 27.
In the same way as in the previous parametric study, this permeability ratio compares the maximum value of the permeability of the fault ($K_{f_{max}}$) with that of the basement (K_{b_0}), here fixed at 10^{-16} m^2. Other (K_{b_0}) values were tested, but higher values do not correspond to the field date, and lower values of permeability do not change the results.

By considering all the directions of the deformation zone and all the stress values, we can see that the largest temperature anomalies and the smallest depths will be concentrated for values of [50-200] and [200-400] (Fig 37A). By varying the direction of the deformation zone with respect to the stress, for permeability ratios [50-400], the higher temperature anomalies and the smallest depths will be concentrated in directions of 30 and 70°.

This tendency is, however, less visible for [1-50]. By varying the stress, we notice that for [1-50], the intensity of the stress does not significantly influence the value of the positive temperature anomaly as well as its depth. However, trends seem to emerge for stresses of 30 and 90 MPa. These stress values seem to concentrate the highest temperature anomalies for the directions of 30° and 70° relative to the stress as well as for [200-400].

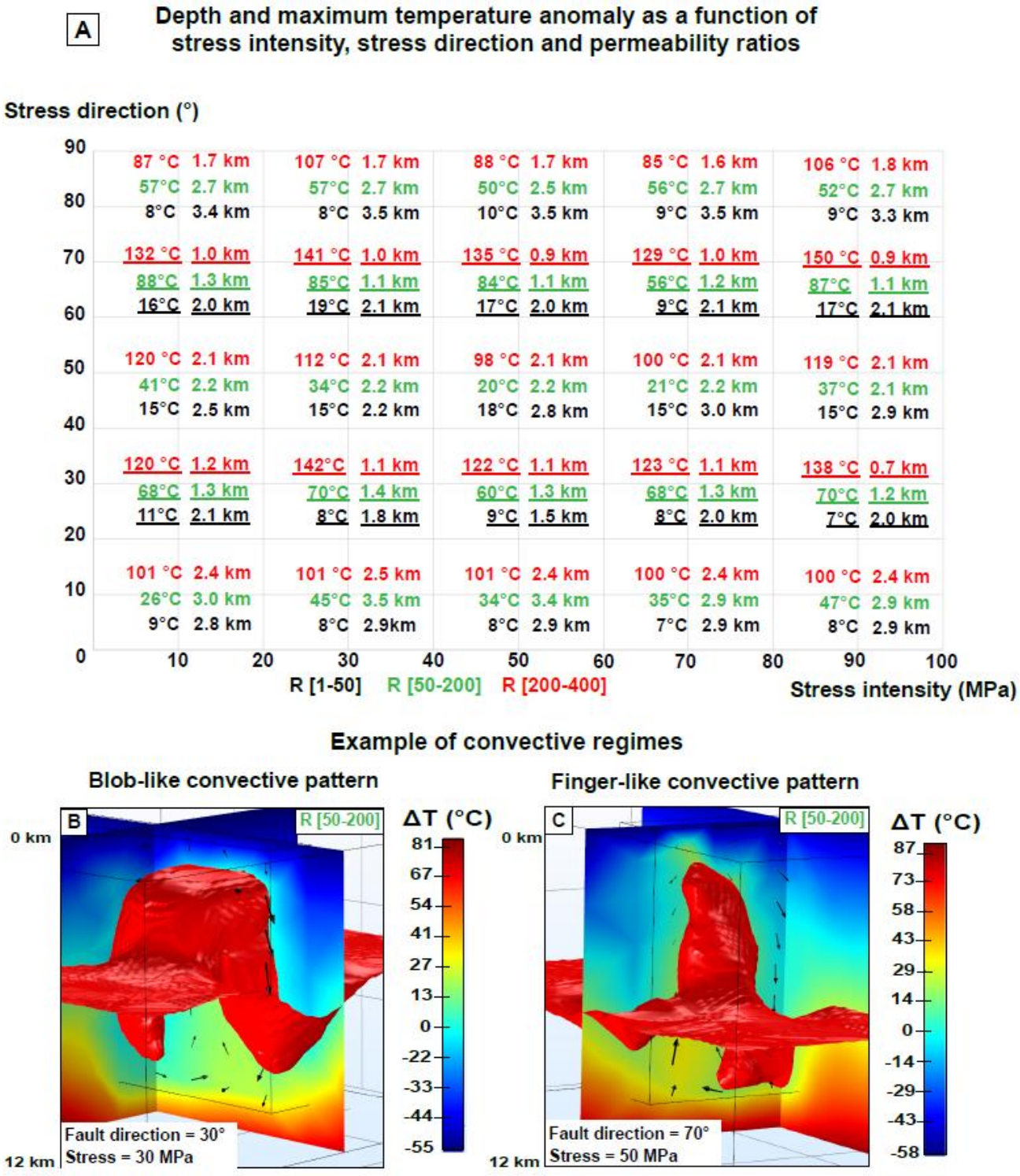

Figure 37 : (A) Positive temperature anomalies and their depth for different permeability ratios (black, green, and red) as a function of fault direction (vertical axis) and stress intensity (horizontal axis). The underlined values show the trends of temperature anomalies and their depths for fault direction of 30 and 70° and for different stress values. (B, C) Show the fluid flow for the same ratio (green), but for different fault direction and stress. Red surface illustrates the morphology of the 70°C isotherm. (B) Shows a "blob-like" pattern. (C) Shows a "finger-like" pattern.

For values of [50-200], we do not observe significant effects of stress on the depth and intensity of the temperature anomaly.
Finally, for [50-400], the deformation zone directions of 30° and 70° relative to stress will concentrate the highest temperature anomalies at the shallowest depths. For these directions, stresses of 30-90 MPa will have the highest temperature anomalies.
Figures 37B and 37C, show the fluid flow for [50-200]. For Figure 37B the direction of the deformation zone is oriented at 30° to the stress, which is 30 MPa. The fluid flow (marked by the black arrows) is defined by an upward movement in the center and downward movements at both ends.

The bulging of the 70°C isotherm (shown in red in Figure 37B) is the consequence of this fluid circulation, which follows a “blob-like” pattern. For Figure 37C, the fault direction is 70° with respect to the stress, which is 50 MPa. Fluid flow is also defined by an upward movement in the center and downward movements at both ends. However, compared to Figure 37B, the downward movements are more concentrated around the upward movement. The morphology of the 70°C isotherm (shown in red in Figure 37C) is the consequence of this fluid circulation which follows a “finger-like” pattern. As can be seen, there seems to be different types of convection patterns for different stress and fault direction values. Note that the irregular morphology of the red surfaces may be due either to the 3D heterogeneity of the permeability or to the effects of stress direction and/or intensity. To solve for this important issue, convective patterns have been systematically observed for all experiments.

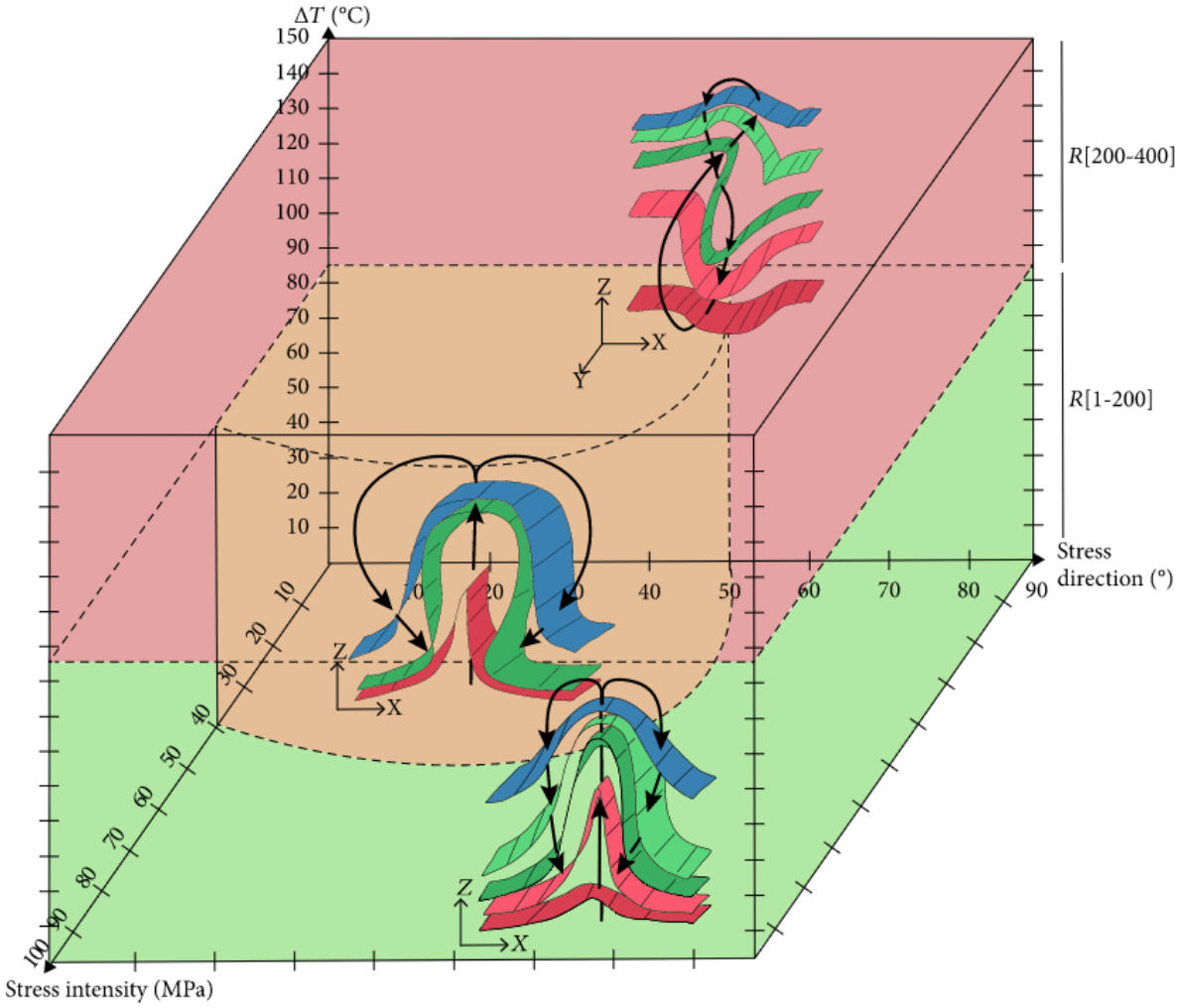

Figure 38 : Diagram of convective regimes. The distorted planes represent the isotherms. The arrows represent the fluids circulation. In the brown area are the blob-like convection patterns. In the green zone are the finger-like convection patterns. In the red zone are the double-convective patterns.

Observations of the convective figures from the numerical simulations make it possible to distinguish three zones as a function of the stress intensity, fault direction, and the value of the temperature anomaly (Fig 38). The brown zone and the green zone correspond to a ratio R [1-200]. The red zone corresponds to a ratio R [200-400]. For this permeability ratio, the temperature anomalies will be between 88 and

150°C. For the lowest permeability ratio (R [1-200]), temperature anomalies are between 7 and 88°C. For these values, two convective regimes are observable. Firstly, for stress values below 40 MPa and for a fault direction below 50°, the blob-like pattern described in Figure 38 is found. This convective regime occurs along two dimensions of the space (along the z and x axes). Secondly, for stresses greater than 40 MPa and for a fault direction greater than 50°, the finger-like pattern described in Figure 38 is preferred. This convective regime is expressed along two dimensions of the space (along the z and x axes). For the highest permeability ratios (R [200-400]), we find a continuous upward and downward motion in all three dimensions of space. Circulation of warmest fluids is along the z and y axes, while the circulation of the coldest fluid is along the z and x axes. This circulation of fluids occurs according to a “double-like” pattern.

By considering a simple geometry and idealized hypotheses, it can be seen that the stress direction, the stress intensity, and the permeability ratio between the fault and the basement are parameters that have an influence on fluid flow and consequently on the intensity and depth of the temperature anomalies.

4 Discussion

4.1 Dip and permeability effects on fluid flow within CFZ

Putative structures sufficiently permeable to allow fluid circulation are commonly described for hydrothermal systems (Forster and Evans,1991; Bruhn et al. 1994; Belgrano et al. 2016) and are used in many numerical models (Forster and Smith, 1989; Mckenna and Blackwell, 2004; Garibaldi et al. 2010; Guillou-Frottier et al. 2013; Magri et al. 2016; Taillefer et al. 2017, 2018). 2D numerical modelling with a TH coupling, has made it possible to test the effect of the fault dip and permeability on the intensity and depth of positive temperature anomalies of a fault zone, and also to characterize the deformation of the resultant isotherms.

The results of the parametric study presented herein, show that when the fault zone is vertical, the value of thermal anomaly will be high and at shallow depth. This depth is also controlled by the ratio between the fault and its basement permeability: when the R ratio is high, thermal anomaly will be at a shallower depth. Although we did not consider the present-day stress field, the value of the thermal anomalies and their depths are the result of convective heat transfer processes. In addition to the result of López and Smith (1995), in which the *R* ratio was studied, we have explored here the effect of the dip angle of the fault zone on fluid circulation.

4.2 Stress direction, stress intensity, and permeability effects on fluid flow within CFZ

Multiple parameters can influence fluid flow, and the 3D behavior of convective cells can be complex (Horne, 1979). López and Smith (1995) showed that temperature anomalies can be directly influenced by the permeability ratio between the fault and the basement. Previous 2D modelling based on TH coupling has shown the influence of this permeability ratio on the morphology of the temperature anomalies. Our parametric study (Fig 37 and 38) made it possible to approach three factors influencing fluid flow: stress intensity, stress direction, and the permeability ratio between the fault and the basement.

(i) For the simplified used boundary conditions, vertical deformation zones, having an angle of 30° and 70° with respect to the boundary stress, will concentrate the highest temperature anomalies, at the lowest depths.

(ii) Different convective patterns could exist: finger-like convective patterns, blob-like convective patterns, and double-like convective patterns. These three convective regimes depend on parameters such as the intensity and direction of the stress, the permeability ratio between the basement and the deformation zone.

For high permeability ratios between R [200-400], the poroelastic effects due to stress state variation have no significant effect on fluid flow pattern. However, for lower permeability ratios R [1-200], changes in the fluid flow pattern can be observed depending on the stress direction and stress intensity.

The simplified and idealized model illustrate the impact of mechanics with one boundary stress only. The effects are expected to be greatly emphasized under anisotropic boundary conditions because of the shearing conditions they introduce.

Permeability is widely recognized as a central parameter in the understanding of a geothermal system. It is also a factor that evolves in space and time. Stresses, fluid overpressures, thermal cracking mineral dissolution, and precipitation are just a handful of examples that can affect the permeability of a geothermally system (Manning and Ingebritsen, 1999; Ingebritsen and Appold, 2012; Ingebritson and Gleeson; 2014; Kolditz et al. 2016; Cox, 2005). All of these phenomena evolve into a geothermal reservoir potential over time. Thus, a way to improve the 3D models would be to consider permeability as dynamic parameter that varies in response to different geological processes, including varying tectonic regime. It would then be possible to identify a mechanical process(es) that could impact the fluid flow.

5 Tectonic regimes as a control factor for crustal fault zone geothermal reservoir in an amagmatic system

(*Manuscript to be submitted*)

Tectonic regime as a control factor for Crustal Fault Zone (CFZ) geothermal reservoir in an amagmatic system

H. Duwiquet, F. Magri, S. Lopez, T. Guillon, L. Arbaret, M. Bellanger, L. Guillou-*Frottier*

Abstract

The Crustal Fault Zones provides an interesting geological target for high temperature geothermal energy source in naturally deep-fractured basement areas. Field and laboratory studies have already shown the ability of these systems to let fluid flow down to Brittle-Ductile-Transition. However, several key questions about exploration still exist, in particular the fundamental effect of tectonic regimes on fluid flow in fractured basement domains. Based on poroelasticity assumption, we considered an idealized 3D geometry and realistic physical properties. We examined a model with no tectonic regime (benchmark experiment) and a model with different tectonic regimes applied. Compared to the benchmark experiment, the results suggest that different tectonic regimes cause pressure changes in the fault/basement system. The tectonic-induced pressure changes affect fluid patterns, onset of convection as well as the spatial extent of thermal plumes and the intensity of the temperature anomalies.

1 – Introduction

Usually, the formation of a geothermal resource requires the presence of fluid, a drain and a heat source. Permeable faults are natural drains for fluids circulation and have a rising scientific and economic interest for mineral (e.g. lithium) and geothermal resources (Saevarsdottir et al. 2014; Liang et al. 2018, Guillou-Frottier et al. 2020). Crustal Fault Zones (CFZ) are geological structures that localize deformation (Ben-Zion and Rovelli, 2014) and modify the petrophysical properties of the crust above Brittle-Ductile-Transition (BDT). CFZ are defined by faults network and interconnected fractures which extension vary from of a few meters to several kilometers. Field and laboratory observations show a succession of damage zones and fault cores corresponding to the multiple fault core conceptual model of Faulkner et al. (2003). Within the interconnected fracture networks of the Pontgibaud Crustal Fault Zone, the presence of pores at different scales (from 2.5 µm to 2 mm) facilitates fluid flow (Duwiquet et al. 2021). CFZ are widely present around the globe. They are found in Chile - Atacame Fault System - (Mitchell and Faulkner, 2009), Germany - Badenweiler-Lenzkirch Sutur – (Brockamp et al. 2015), or Finland - Pasmajärvi Fault Zone - (Ojala et al. 2019). These geological structures can be located in different geological settings (magmatic or amagmatic) and different tectonic stress regimes. This paper investigates the role of the tectonic regime on geothermal reservoirs within and around CFZ, in amagmatic systems.

Although CFZ provide potential renewable and economic geothermal resources, they remain largely unexplored and undeveloped. Thus, full understanding of the processes that impact fluid flow in CFZ is a prerequisite for successful exploration. Recent work has shown that pressure and temperature conditions can induce fluid flow near the BDT (Violay et al. 2017; Watanabe et al. 2017; 2021). Fluid-filled fractures have been observed down to mid-crustal depths, as shown by the deep boreholes of the Kola Peninsula (Kozlovsky, 1984), and the German KTB continental deep drill hole (Grawinkel and Stöckhert, 1997; Ito and Zoback 2000). Additionally,

Famin et al. 2004 suggested that massive infiltration of surface-derived fluids occurred in a detachment shear zone of Tinos Island (Greece), down to a depth of 10-15 km. Similarly, Siebenaller et al. (2013) demonstrated that meteoric fluid infiltration occurs down to the BDT (around a depth of 8 km) in the Naxos detachment fault (Greece).

Convection around geothermal wells is mandatory to reach production power that leverage the high drilling cost of deep borehole. When the permeability is too low, the strategies developed by the Enhanced Geothermal System (EGS) technique increase the permeability by different injection phases, among which hydraulic stimulations aim at causing hydro-shearing and/or hydro-fracturing. These methods have allowed the development of many geothermal power plants, such as Soultz-sous-Forêts, Upper Rhine Graben, France (Genter et al. 2010). However, the seismicity induced by these injection phases have jeopardized several geothermal projects (Deichmann and Giardini 2009, Evans et al. 2005). Between 2020 and 2021 in Alsace (France) a series of induced earthquakes of magnitude M=3, M=3.6, M=3.9 caused the definitive shutdown of the geothermal project and raised doubts in the population. Since 2020, the United Downs Deep Geothermal Project (UDDGP) is attempting to target a naturally fractured reservoir in the heat-producing Cornish granite (Ledingham et al. 2019; Paulillo et al. 2020). Drilling through the sub-vertical, strike-slip Porthtowan fault zone has induced an earthquake of magnitude M = 1.5 (www.inducedearthquakes.org), too small to be felt by local population. Through their permeable nature, fractured zones in purely basement domain can then be areas where the risk of induced seismicity is limited.

The complex nature of the interactions between Thermal (T), Hydraulical (H), Mechanical (M) and Chemical (C) couplings affect the behavior of the geothermal reservoir under natural conditions. Numerical modelling has been used since 1945 to understand the controlling factors of fluid circulations (Horton and Rogers, 1945; Katto & Masuoka, 1967; Horne, 1979; Forster & Smith, 1989; López & Smith, 1995;

O'Sullivan et al. 2001; Magri et al. 2016; Guillou-Frottier et al. 2020). Tectonic deformation has been considered as driving forces that influence fluid flow in different geological contexts (Ord and Oliver, 1997b; Cox, 1999; Rowland and Sibson, 2004). Bethke (1985) shows that compressive environments can lead to increased fluid pressure and favor upward movement. Sibson (1987) links overpressure and upward movement to fault valve activity. In extensional environments, the generated under-pressure appears to cause downward fluid migration (McLellan et al. 2004). Nevertheless, none of them have looked at the effect of tectonic regime on fluid flow, and the consequences on the temperature anomalies in CFZ. Cui et al. (2012) used simplified 2D models with a fault zone to show that with degrees of shortening exceeding 1% the fluid flows whose driving force was buoyancy forces is then different. In 3D models, Eldursi et al. (2020) suggest that during tectonically active periods, the decrease in pore pressure can reorient fluid flow in fractured zones.

Fluid flow velocities, and thus efficiency of heat transport by convection through the crust, are directly controlled by the permeability of the rocks. Permeability is a dynamic and variable parameter that can change during different geological processes (Gleeson and Ingebritsen, 2016). The relationship between permeability and porosity is widely debated. Although adapted to porous media, the Kozeny-Carman relationship does not seem appropriate for fractured media (Lamur et al. 2017; Parisio et al. 2019).

In CFZs, fluid circulation driven by buoyancy forces occurs through upward and downward movement localizing positive temperature anomalies at shallow depths (Duwiquet et al. 2019; Guillou-Frottier et al. 2020). These 2D and 3D TH numerical modelling studies have shown that vertical or subvertical deep deformation zones could concentrate the most important temperature anomalies at the lowest depths. However, these results do not consider poroelastic effects on fluid flow. Poroelastic

models describe the interaction between fluids and deformation in the porous medium. The fluids in a reservoir are affected by stresses whether on their pressure (undrained conditions in low-permeable media with, e.g., increase in pressure under compressive stress state), or on their circulation (drained conditions in permeable media with, e.g., convection from more to less compressed regions). Our previous study, which includes poroelasticity, suggested that vertical deformation zones oriented at 30° and 70° to a maximum horizontal stress could correspond to potential targets for high temperature geothermal energy (Duwiquet et al. 2021). Thus, the stress orientation has an effect on the fluid flow. In anisotropic boundary conditions, these effects are expected to be strongly accentuated. Indeed, they introduce shearing conditions favorable to dilation. These aspects could be treated in mechanical terms, which would allow the calculation of slip tendency, defined by the ratio of shear stress and effective normal stress (Morris et al. 1996).

Here, we investigate, the role of tectonic regimes on the formation of an amagmatic geothermal reservoir (i.e. the only heat is the natural geothermal flux) within a CFZ and without any other heat source than the natural geothermal flux (amagmatic system). We propose a faulted 3D THM numerical model with a simplified geometry. The physical properties are realistic and the hydraulic permeability is adapted to the fractured environment. In order to understand the role of tectonic regimes, we first considered a benchmark experiment that neglects tectonic stress. This result is compared to several numerical experiments where tectonic stresses are implemented.

The effect of the poroelasticity-driven force on fluid flow will differ from one tectonic regime to another and impact the formation of a HT geothermal reservoir in fractured environment. The observed differences can be mainly explained by different lateral fluid pressure variation. This paper highlights the importance of mechanical effects in geothermal processes. The tectonic induced pressure changes affect fluid

patterns, onset of convection, the spatial extent of thermal plumes and the intensity of the temperature anomalies.

2 - Results

2.1 - Formation of a high temperature geothermal reservoir within a vertical fault zone with no tectonic stresses, the benchmark experiment.

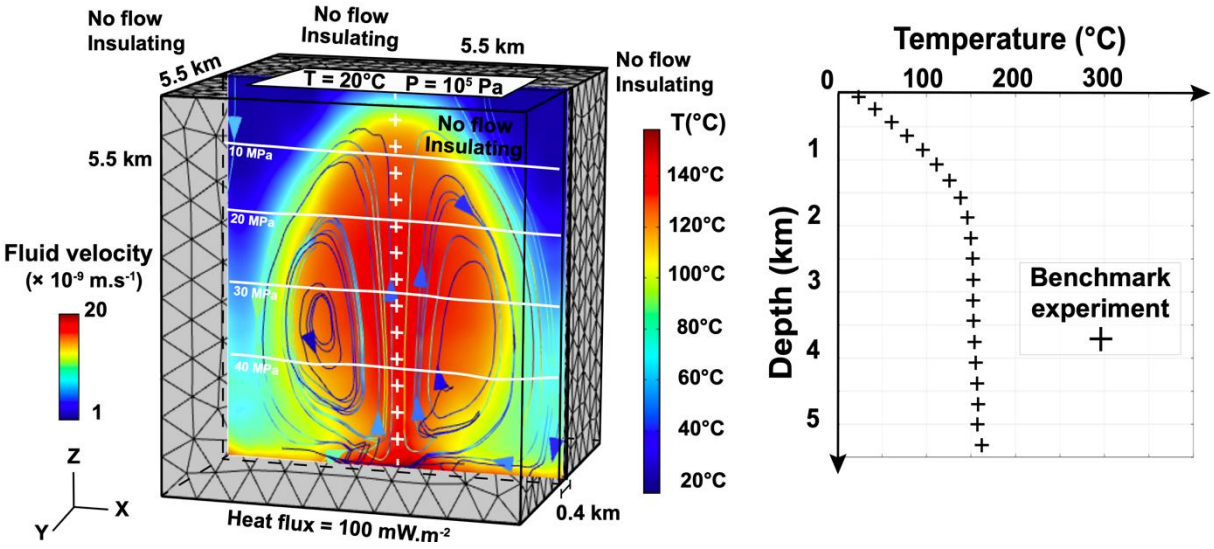

Figure 1 : Model setup, initial condition and results of the benchmark experiment (+) -without stress application-. Pressure (white contour), temperature (color patterns) and flow field (vectors) are displayed. The temperature profile is plotted against depth (right chart, dotted line). When free convection is established, the 150°C isotherm is located at 1.8 km depth. The benchmark experiment reaches the steady-state regime at 65 kyrs.

The numerical simulation without stress application shows an upward circulation at the fault center and two downward circulations at the fault ends (Fig 1). As illustrated by colored streamlines in Figure 1, these fluid circulations transfer heat by convection. Thermally induced force is buoyancy are driving the flow. In a classical natural convection pattern, the hot fluid, less dense, goes up to the surface, cools down, and its density increases, bringing back the fluid down deeper in the fault.

Considering realistic physical conditions, no external heat source except a basal heat flux, and no mechanical stress, this free convection generates a thermal disturbance of the environment and localized the 150°C isotherm at 1.8 km depth, at the center of the fault. By comparison, in a purely diffusive setting, we would reach 150°C at 5 km depth. Fluid velocities are of the order of 1×10^{-9} m.s^{-1} at the center of the fault and 20×10^{-9} m.s^{-1} at the ends of the fault. The higher fluid velocities at the bottom center of the fault are responsible for slight increase in pressure (white lines). This trend is already observed in other numerical TH modelling (Scott et al. 2017). The temperature gradient at the center of the model is similar to typical temperature gradient in geothermal reservoirs such as Soultz-sous-Forêts (Genter et al. 2010).

2.2 – Application of tectonic stresses

Figure 2 (with tectonic regimes written in red) corresponds to the high stress intensity application (see the definition of high stress intensity in the method section, Eq 1). Figure 3 (with tectonic regimes written in green) corresponds to the low stress intensity application (see the definition of low stress intensity in the method section, Eq 2). Results are shown on vertical cross sections in the fault, and on horizontal cross sections, at 2 km depth. For each tectonic regime that is considered, the results show the temperature anomalies, the fluid flow pattern and the fluid velocities. The results are different from the benchmark experiment (Fig. 2 and 3)

2.2.1 Different Temperature Anomalies

Regardless of the considered tectonic regime, positive and negative temperature anomalies are observed. They differ by their number, intensity and lateral extension.

2.2.1.1 In extensional tectonic regime, two positive temperature anomalies are found (Fig. 2 and 3). They are +55 °C in high stress intensity and +47 °C in low stress intensity. For both stress intensities, the second temperature anomalies are less intense, + 10°C in high stress intensity, and +7 °C in low stress intensity. For both stress intensities, a negative temperature anomaly at the center of the fault is found. This anomaly is -60°C for the high stress intensity and -57°C for the low stress intensity. For a high stress intensity, at 2 km depth, the horizontal cross-section shows a negative temperature anomaly that reaches a maximum of -30°C. This anomaly covers a large surface area of the fault. The positive temperature anomaly of +45°C occupies the remaining space, but extends further into the basement. In the basement and up to the edge of the model, we find a positive temperature anomaly of +20°C. For a low stress intensity, at 2 km depth, two positive temperature anomalies and one negative anomaly are observed. The first positive anomaly is +41 °C, the second has a value of +20 °C. This +20 °C anomaly spreads more widely in the system whilst the +41 °C anomaly remains localized on the fault. The negative anomaly located at the center of the fault is -37 °C and extends into the basement in the same way as the positive +41 °C anomaly.

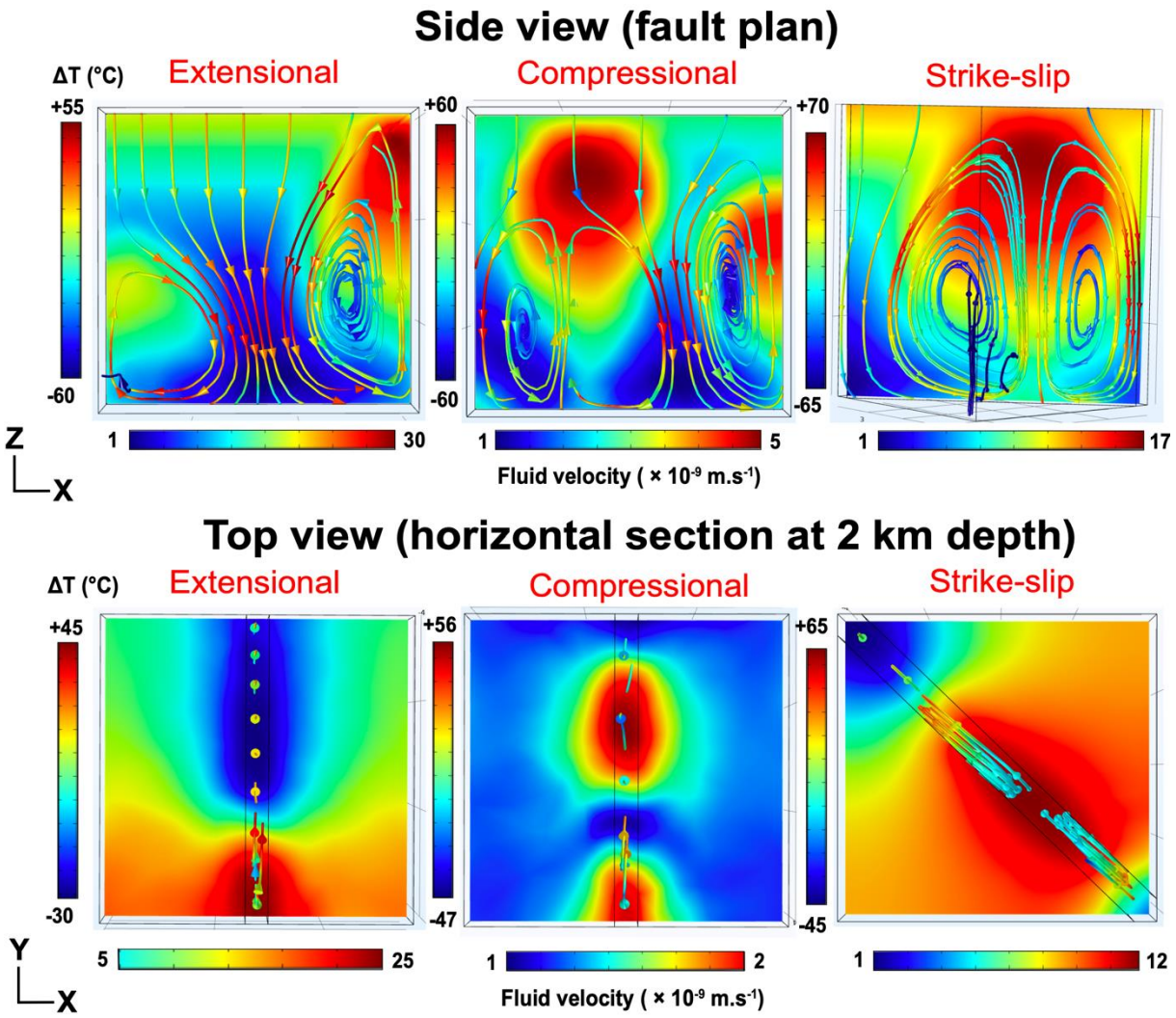

Figure 2 : Results of numerical modelling after high stress intensity stresses application (in red, see Eq 2). The results are shown in vertical section (Side View, located in the middle of the fault) and in horizontal section, (Top view, located at 2 km depth). The scale of temperature anomalies and fluid flow velocities is different according to the tectonic regimes. For each regime, the maximum and minimum values of temperatures and fluid flow velocities are indicated. Positive temperature anomalies are colored red, negative temperature anomalies are colored blue. Fluid circulation is marked by the lines, the direction by the arrows. The color of the lines corresponds to the fluid velocity. In red the velocity is the highest, in blue the velocity is the lowest.

2.2.1.2 In compressional tectonic regime, independently from the stress intensity, we find two positive temperature anomalies. The value of the maximum temperature anomaly in high stress intensity is +60 °C and in low intensity it is +51 °C.

Depending on the stress intensity, these two maximum values are spatially slightly shifted (Fig.2 and 3). The amplitudes of the second temperature anomaly are +35°C and +40°C for low and high stress intensity, respectively. In the horizontal cross-section, the two temperature anomalies are found for each intensity. In high stress intensity the values of these two temperature anomalies are +56 °C and +47°C. In low stress intensity the values are +47 °C and +35 °C. The lateral extension of these temperature anomalies is limited. They are surrounded by negative temperature anomalies that locally reach -47°C in high intensity and -42°C in low intensity. At a depth of 2 km, the positive temperature anomalies are much less extended than in extensional tectonic or strike-slip regimes (see below).

2.2.1.3 In strike-slip regimes and regardless of stress intensity applied (Fig 2 and 3), positive temperature anomaly extends widely along the length of the fault, from the surface to 4.5 km deep. The maximum positive temperature anomaly value is +70°C for the high stress intensity (Fig 2), and +62°C for the low stress intensity (Fig 3). In horizontal cross-section, these temperature anomalies spread largely beyond the fault. Temperature anomalies of + 25°C are found in the basement, suggesting that in a strike-slip system, the positive temperature anomaly, and independently from the stress intensity, represents an important volume. This heat propagation is done by thermal diffusion from the fault center, where the temperature anomaly is the most intense. Indeed, the larger the convection cell inside the fault, the wider the extent of the diffusive perturbation. At 2 km depth, the maximum value of the temperature anomaly is +65 °C for the high stress intensity, and +61 °C for the low stress intensity. Negative temperature anomalies are present and localized at the extremities of the fault. They are -45°C for the high stress intensity and -40°C for the low stress intensity

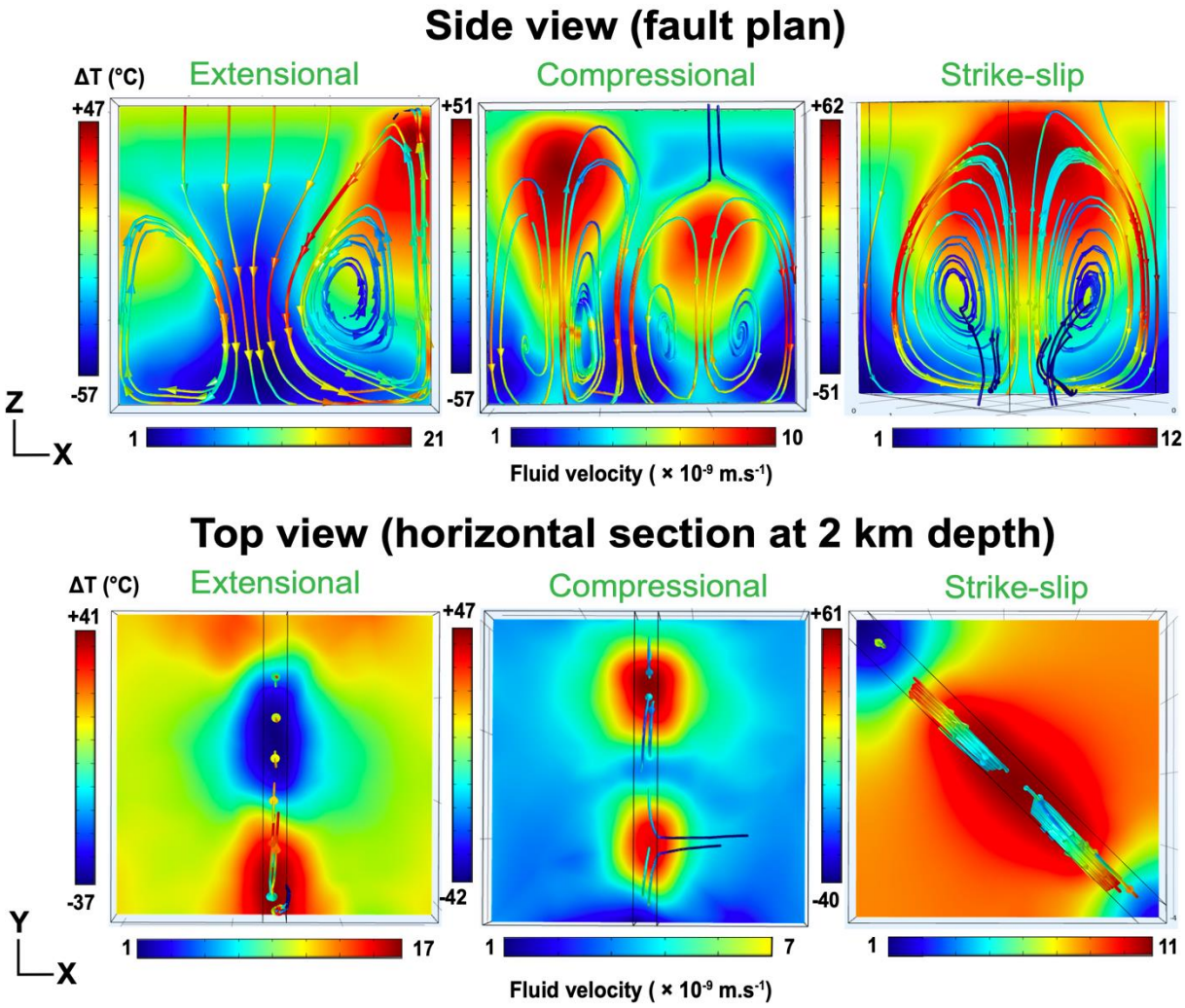

Figure 3 : Results of numerical modelling after low stress intensity application (in green, see Eq 1). The results are shown in vertical section (Side View, located in the middle of the fault) and in horizontal section, (Top view, located at 2 km depth). The scale of temperature anomalies and fluid flow velocities is different according to the tectonic regimes. For each regime, the maximum and minimum values of temperatures and fluid flow velocities are indicated. Positive temperature anomalies are colored red, negative temperature anomalies are colored blue. Fluid circulation is marked by the lines, the direction by the arrows. The color of the lines corresponds to the fluid velocity. In red the velocity is the highest, in blue the velocity is the lowest.

To summarize, tectonic regimes influence the distribution and the amplitude of temperature anomalies. Positive temperature anomalies are most intense in strike-slip, then in compression and extension. The spatial extent of positive temperature anomalies is not identical for each tectonic regime. In strike-slip, these anomalies are largely extended through the basement. This lateral extension is less important

in the extensive tectonic regime. Finally, in compressional regime these anomalies are localized in the near vicinity of the fault. The tectonic regimes have shown to play a key role in temperature, and this is clearly related to the different convective patterns and fluid flow velocity, as described below.

2.2.2 Fluid flow pattern

2.2.2.1 In extensional tectonic regimes, the fluid flow pattern is characterized by a downward movement at the center of the fault and two upward movements at the ends of the fault (Fig. 2 and 3). In high stress intensity the maximum fluid velocity is 30×10^{-9} $m.s^{-1}$, against 21×10^{-9} $m.s^{-1}$ in low stress intensity. The minimum fluid velocities are, for each intensity, 1×10^{-9} $m.s^{-1}$. In horizontal cross-section, at 2 km depth, upward movements are localized at positive temperature anomalies, while downward movements are localized at negative temperature anomalies. In high stress intensity, the maximum fluid velocity is 25×10^{-9} $m.s^{-1}$, compared to 17×10^{-9} $m.s^{-1}$ in low stress intensity. And the minimum fluid velocity is 5×10^{-9} $m.s^{-1}$ in high stress intensity, compared to 1×10^{-9} $m.s^{-1}$ in low stress intensity.

2.2.2.2 In compressional tectonic regimes, for each stress intensity, there is a slightly different convective pattern. In high stress intensity, there are two upward and two downward movements whereas in low stress intensity, there are two upward and three downward movements. The maximum fluid velocity for high stress intensity is 5×10^{-9} $m.s^{-1}$ and 10×10^{-9} $m.s^{-1}$ for low stress intensity. For this tectonic regime the maximum fluid velocity is present when the lowest stress intensity is applied. In horizontal cross-section, at 2 km depth, and for high stress intensity upward movements are localized where temperature anomalies are positive whereas downward movements are localized where temperature anomalies are negative. The fluid velocity is between 1 and 2×10^{-9} $m.s^{-1}$. In low stress intensity, the downward movements are localized at the extremities and at the center of the fault. The

upward movements are localized between each downward movement. The maximum fluid velocity is 10×10^{-9} m.s^{-1} and the minimum is 1×10^{-9} m.s^{-1}. At a depth of 2 km, fluid velocities vary from 1 to 2×10^{-9} m.s^{-1}. Thus, fluid velocity values in compressional regime are the lowest recorded.

2.2.2.3 In the strike-slip tectonic regime, as for the benchmark experiment, the fluid flow pattern is characterized by an upward movement at the center of the fault and two downward movements at the ends of the fault (Fig 2 and Fig 3), as observed in the benchmark experiment. The fluid velocity varies with stress intensity. In low stress intensity, the minimum fluid velocity is 1×10^{-9} m.s^{-1} and the maximum is 12×10^{-9} m.s^{-1} at the downward movements. In high stress intensity, the minimum fluid velocity is 1×10^{-9} m.s^{-1} and the maximum is 17×10^{-9} m.s^{-1}.

With application of tectonic stresses; the fluid flow is different from the benchmark experiment, with consequences on temperature anomalies. In the benchmark experiment, buoyancy is the only driving force for fluid convection. Here, in presence of tectonic stresses, other forces seem to influence the fluid flow.

2.2.3 Lateral fluid pressure variation

After stress application, the fluid pressure is different from the benchmark experiment, where pressure is hydrostatic (Fig. 4). Whatever the stress intensity applied, the experiment with compressional and strike-slip tectonic regimes show fluid pressures higher than those in the benchmark experiment, whereas, the extensional tectonic regime display fluid pressures lower than those in the benchmark experiment. The fluid pressure varies between the basement and the fault. This lateral variation differs according to the stress intensity applied.

In each of these cases, the tectonic regimes and the stress intensity generate lateral fluid pressure variation between the fault and the basement. In high stress intensity,

and for the same horizontal distance, these lateral pressure differences are 1.5 MPa, 0.45 MPa, and 0.97 MPa for compressional, strike-slip, and extensional tectonic regimes, respectively. In low stress intensity the lateral pressure differences are 1.35 MPa, 0.3 MPa and 0.91 MPa for compressional, strike-slip, and extensional tectonic regimes (respectively). These lateral fluid pressure differences drive the fluids from the high-pressure zones (i.e. basement), to the low-pressure zone (i.e. fault).

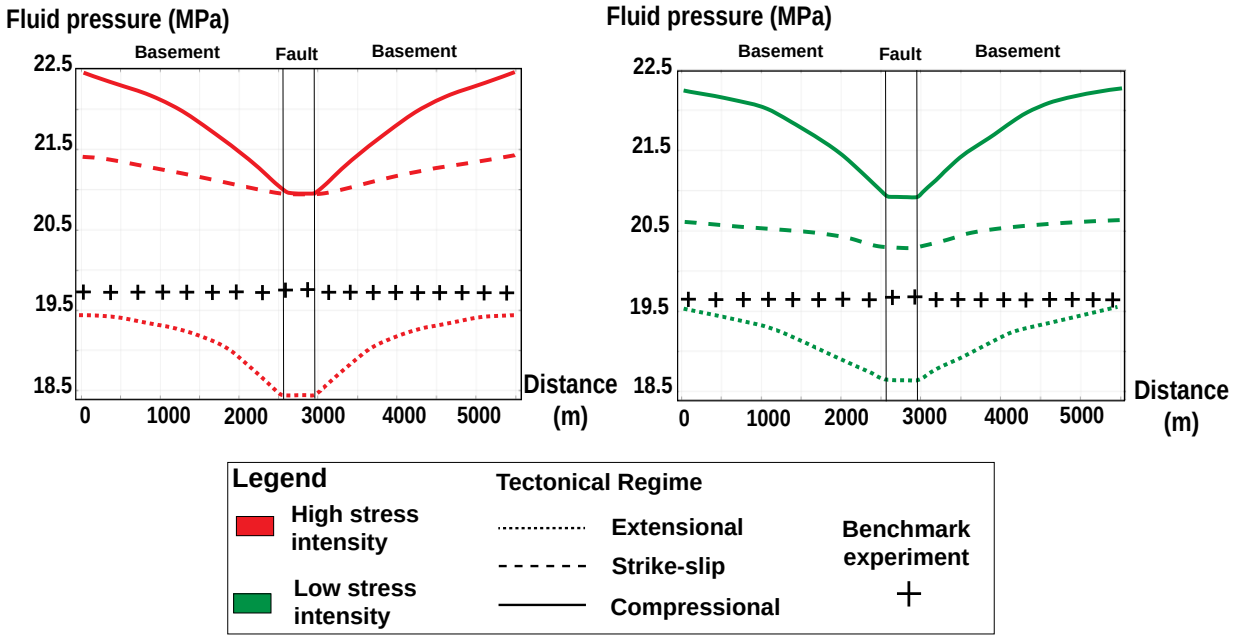

Figure 4 : Graphs representing the lateral fluid pressure in high stress intensity application (in red), and low stress intensity application (in green). The fluid pressure of the benchmark experiment is indicated (+). With stresses application, the fluid pressure is different than the benchmark experiment. The lateral fluid pressure variation depends on the tectonic regime and stress intensity.

2.2.4 What effect(s) on the onset of the positive temperature?

The regional mechanical stresses imposed a pressure distribution that will interact with buoyancy forces responsible for free convection patterns. The lateral fluid pressure differences bring the fluid from the zones of high pressure to those of low

pressure. However, the time needed to set up this temperature anomaly appears to vary, as show in Figure 5.

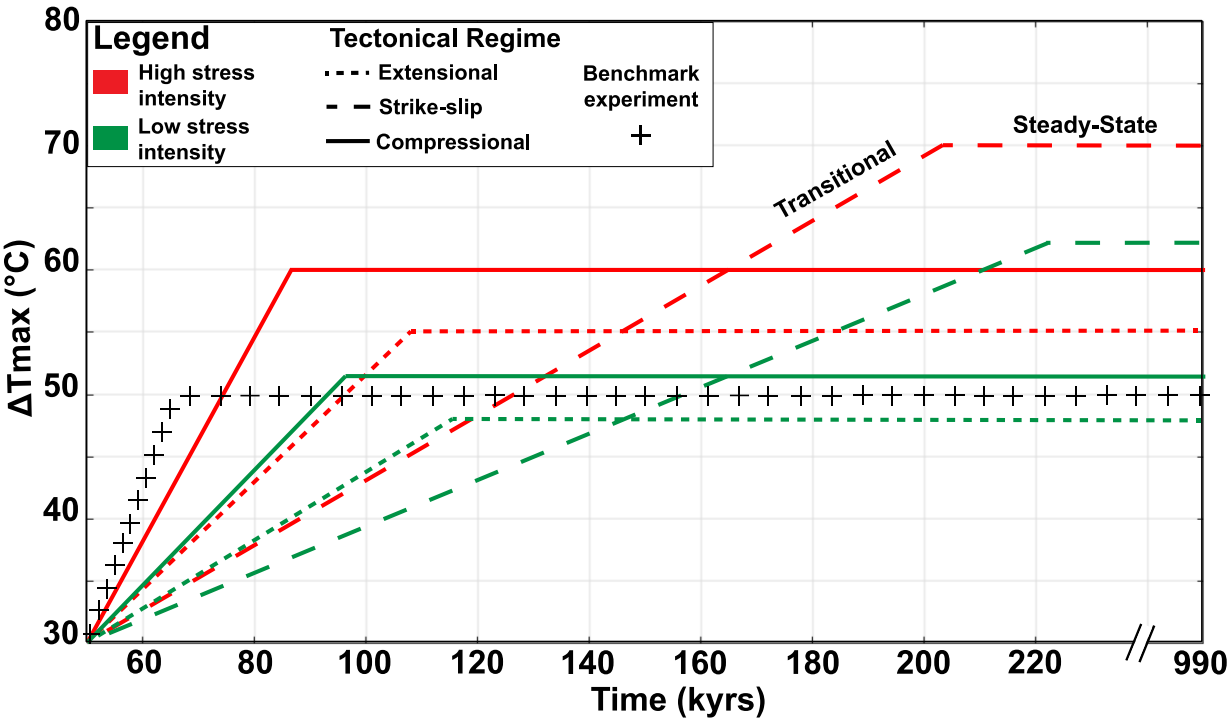

Figure 5 : Time required to reach the steady-state temperature anomalies, depending on the tectonic regimes and the applied stress intensities. The color code and patterns are the same as those used in the previous figures.

Considering the compressional tectonic regime (solid line), the time needed to reach a steady-state regime in high stress intensity is 85 kyrs, while it is 95 kyrs in low stress intensity. This difference is observed for each regime, so that the stress intensity has a role in the setting up convection. The high stress intensity allows bringing the fluid more quickly to the zone of high permeability, and low fluid pressure. In this way, the compressional regime, which has the highest lateral fluid pressure difference, reaches the steady-state more quickly than the other tectonic regimes. The lowest lateral fluid pressure difference is recorded for the strike-slip

regime. The strike-slip regime reaches the steady-state regime at 203 kyrs for high stress intensity and 223 kyrs for low stress intensity.

In a geothermal exploration context, these numerical calculations show that in a strike-slip tectonic regime the temperature anomalies should be more intense than in a compressive or extensive regime, but that the onset is the most delayed with respect to the benchmark case.
The benchmark experiment reaches the steady-state regime as early as 65 kyrs, and finally the additional stress input may increase the time to reach a steady-state *in situ*. The differences observed on the different tectonic regimes is consistent with the differences observed on the lateral fluid pressure between the fault and the basement. However, this does not allow to explain the different fluid velocities observed (Fig. 2 and 3), and the mechanical behavior of the basement-fault system after stress application.

2.2.5 Permeability and slip tendency variation

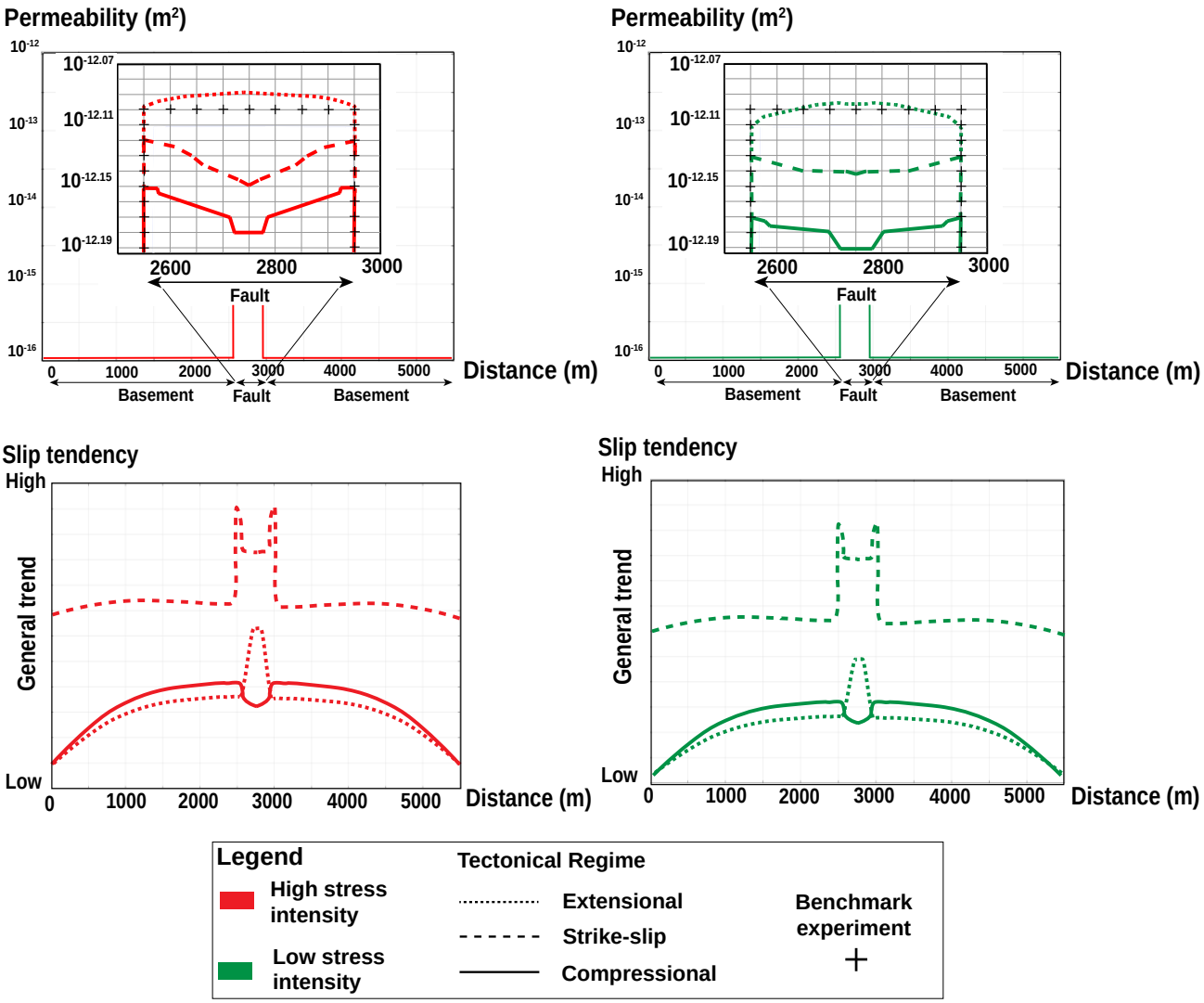

Figure 6 : Graphs representing the permeability and the slip tendency in high stress intensity application (in red), and low stress intensity application (in green). The permeability of the benchmark experiment is indicated (+).

In the fault, very small permeability variations are observed as a function of stress intensity and tectonic regime (Fig. 6). In high stress intensity, the permeability values in the center of the fault are $10^{-12.09}$, $10^{-12.15}$, $10^{-12.18}$ m^2, for extensional, strike-slip and compressional tectonic regimes, respectively. In low stress intensity, the

permeability values are $10^{-12.09}$, $10^{-12.14}$, $10^{-12.19}$ m^2, for extensional, strike-slip and compressional tectonic regimes, respectively. The effect of stress intensity on permeability remains negligible. For example, considering the compressional tectonic regime, the difference between high and low stress intensity is to 2.3 %.
To understand if these small variations in permeability between the tectonic regimes can explain the different convective patterns previously described, runs were performed considering the two extreme values of permeability obtained: $10^{-12.09}$ and $10^{-12.19}$ m^2 (for more details see Appendix 2). The general thermal distribution of the system remains identical.

We note a consistency between the values of fluid velocities and permeability values. Indeed, the fluid velocities are the most important for the highest permeability, and the least important for the lowest permeability. Once the stresses are applied, the permeability are slightly different from the benchmark experiment, and control the fluid velocity.

The slip tendency is calculated and plotted for each tectonic regime and stress intensity applied (Fig. 6). The global general trend is higher in high stress intensity than in low stress intensity applied. The results show a distinctive variation in the fault and in the basement for each tectonic regime. Regardless of the stress intensity applied, the slip tendency in a strike-slip tectonic regime is the highest, since it is more critically stressed. In the strike-slip regime, the slip tendency increases slightly from the edge of the basement to the level of the fault zone. At the edge of the fault, the slip tendency increases significantly. In the middle of the fault, the slip tendency slightly decreases. This evolution is the same independently from the stress intensity applied.

In compressional and extensional regimes, the trend from the edges of the basement to the fault increases similarly. This increase is slightly greater in compression

than in extension. At the edge of the fault the general trend is the same. In compression the slip tendency decreases, and in extension it increases. In extension the middle of the fault is less critically stressed than in compression. Independently from the intensity of the stress this evolution is the same. Of the three tectonic regimes tested, the strike-slip regime is the most critically stressed. The general trend shows that it is at the interface between the basement and the fault that the trend is most important. This result illustrates the heterogeneity of the mechanical parameters incorporated in the numerical model, and also show that the role of the stress intensity on the range of values tested will not drastically change the mechanical response of the basement-fault system.

3- Discussion

The presence of fluids and a sufficiently high permeability are two factors to allow the development of a geothermal resource, from a natural geothermal flux. Considering a simplified geometry, but realistic physical properties (pressure and temperature dependent fluid density, temperature-dependent fluid viscosity), our 3D TH and 3D THM numerical modelling show that in a basement domain, CFZs allow hot fluids to rise to economically viable depths. The comparison of numerical models with and without tectonic stresses highlight the non-negligible role of tectonic regime on the spatial distribution of positive temperature anomalies.

Without stress application, the benchmark experiment shows that an upward movement at the center of the fault and brings a temperature of 150 °C at 1.8 km depth (Fig 1). Two downward movements are located at the ends of the fault. This convective pattern has already been observed in 2D and 3D TH numerical modelling of fault zones in the crustal domain (Wanner et al. 2019; Guillou-Frottier et al. 2020) and was called “bulb-like” convective pattern. This particular shape is favored because hot fluids have less resistance when flowing upwards (viscosity is smaller at high temperature) and can localize temperature anomalies also in the basement. With a flat topography and without metamorphic devolatilization and/or magmatic

fluid production that might change fluid pressure (Nur and Walder, 1990), fluid circulation is only driven by the buoyancy force. With tectonic regimes application, we have seen that other forces are added and modify the fluid circulation.

Considering the experiments where tectonic regimes are accounted for, the obtained results are different from the benchmark experiment (Fig. 2 and Fig. 3). This highlights the key role of the relationship between tectonic settings and fluid flow. In our results, the stress intensity parameter does not change the general dynamics of convective patterns between two identical regimes. Considering a sensitivity study on a large Pontgibaud Crustal Fault Zone (French Massif Central), where the stresses boundary magnitudes are tested while holding their directions, a shift from one convective pattern to another would occur for a variation of approximately 40 MPa in the maximum horizontal stress magnitude (Duwiquet et al. 2021). For this last example and in the light of the observations made in this study, it could be possible that another force than the buoyancy, influences fluid circulation. In this study the stress intensity applied is not a factor influencing the convection pattern. However, the stress intensity has a role in the time to reach the steady-state. Indeed, the steady-state is reached faster when the most intense stresses are applied (Fig. 5), and this was not explored in the Duwiquet et al. 2021 study. Moreover, the role of tectonics on the direction of fluid flow has been highlighted. Considering a numerical approach, studies have shown that in compression, upward fluid movements are favored (Upton, 1998), whereas in extension, downward fluid movements are favored (Cui et al. 2012). Here we could see that the different tectonic regimes will have a role in the onset of convection. This element also explains the final results observed.

These numerical models show that the tested tectonic regimes have an influence on fluid pressure variation. The poroelastic assumption describes the interaction of fluids and deformation in porous media. Compressional, extensional, and strike-slip tectonic regimes induce variable fluid pressures for each case. The incorporation

of heterogeneous mechanical parameters between the fault and the basement (see Table 1) leads to a different mechanical response and thus to a heterogeneous variation of the fluid pressure between the fault and the basement (see Fig 4). This lateral fluid pressure difference drives the fluids from the high-pressure zones to the low-pressure zones. This effect is facilitated by higher permeability values in the fault than in the basement.

This force, which drives fluids from high pressure zones to low pressure zones is similar to the effects of topography on fluid flow (Forster and Smith 1989; Lopez and Smith 1995). This poroelasticity driven force will therefore influence the initial fluid motions (downward and upward movement) and thus the time required for the steady-state temperature anomaly to develop. Considering a TH coupling, the fluid circulation in the benchmark experiment is driven by free convection. Considering three different tectonic regimes with the same TH coupling, the fluid circulation is the result of an interplay between forced and free convection. These changes are not related to boundary conditions, but to the tectonic regimes themselves. Forced convection is referred to as stress induced convection.

After stress applications, the permeability values obtained are consistent with fractured and altered granitic environment (Sardini et al. 1997; Duwiquet et al. 2019; 2021; Gomila et al. 2021). This should be sufficient to allow fluids to flow by buoyancy forces and transfer heat by free convection. However, between tectonic regimes, the difference in permeability cannot explain convective pattern variability results. Nevertheless, these small permeability variations influence the velocities of fluid flow. The fluid velocity decreases with a permeability decrease (see Fig. 2, 3, and 6). Actually, the positive temperature anomalies in the compression and extensional regime model remain centered on the fault compared to the extensional and strike-slip tectonic regimes. Therefore, other processes must limit the development of temperature anomalies in compressional regime. By concentrating the flow of

fluids on limited spaces, the poroelasticity driven force could have the effect of spatially concentrating temperature anomalies when the difference between the fluid pressure of the basement and the fault is large.

For geothermal exploration, slip tendency analyses can be used to target favorable zones for natural fluid flow and future enhancement by fault reactivation (Barton et al. 1995; Morris et al. 1996; Ito and Zoback, 2000). Our results show that the strike-slip regime would be the most favorable to allow fluid flow. The occurrence of geothermal reservoirs in such contexts is already known, Alpine Fault, New Zealand (Boulton et al. 2012), the Geysers (Altmann et al. 2013). In the light of our results, an exploratory phase on the geothermal potential of fault zones could further consider strike-slip faulted as interesting targets for geothermal power system.

If slip tendency can be used as a potential qualitative indicator in purely elastic models, a more accurate interpretation would require incorporating dissipative mechanical behaviors such as, e.g., Mohr-Coulomb elasto-plastic law, which would allow to quantify the variation in slip tendency. By considering irreversible mechanical processes, including dilation (opening under shearing) and fracturing (increase of pore space/fractures), the best favorability of strike-slip regime towards convection is expected to be emphasized.

We used an idealized geometry with single, vertical fault zone. The linear stress boundary conditions hence give rather homogeneous stress ratios and states along the fault. In natural systems, the network of variously oriented and dipping fault zones brings heterogeneous stress states, even along each fault zone taken separately. Still, and recalling that the aim of our study is to better understand the setup conditions of convection cells, the results already allow us to highlight the complex impact of mechanics over convection patterns. Among others, our conclusions tend to show that within a complex fault zone network, fault zones undergoing strike-slip conditions might be the ones to be preferably explored.

These fundamental results are generally applicable in nature to any fracture rock that may contain fluids, gas or oil in its pores, in basement geological context. However, our results do not take into account fundamental aspects such as the consideration of more complex rheology, to start with plastic phenomena. The effects of fault intersections, precipitation and dissolution of mineral phases, and fluid composition were also not taken into account. The dependence of permeability on all of these phenomena should probably generate permeability anisotropy. The development of this anisotropy can cause a change in the intrinsic properties of the geothermal reservoir and induce a change in the heat transfer mode (Sun et al. 2017). In cases where fluid flow is important (i.e. areas of high permeability) the permeability can take a particular geometry minimizing the resistance to flow and then optimizing fluid flow (Bejan and Lorente, 2011). Fluid salinity could also play an important role, but effects would be marked above 400°C (Driesner, 2007), which is beyond our modeled temperatures.

Geothermal energy can become a major asset for the transition to low-carbon energy sources. Its development requires, prior to exploration, comprehensive understanding of limiting and enabling factors controlling fluid flow and the location of temperature anomalies (Jolie et al. 2021). Our numerical results show that the poroelasticity driven force provoked by the tectonic regimes causes lateral fluid pressure variation, allowing for the more or less rapid development of the temperature anomaly, by mixed, free and forced convection. For example, strike-slip tectonic regimes would have the largest temperature anomalies, but would take the longest time to set up.

Overall, this work suggests that anomalously permeable zone, like CFZ, with no external heat source, have significant energy potential. The exploration of the vertical Crustal Fault Zones in strike-slip stress regime, could accelerate the transition to low-carbon, renewable and climate-neutral energy. Studies have already shown

that major strike-slip fault zones localize porosity and permeability even beyond the BDT (Faulkner et al. 2010; Cao and Neubauer, 2016). Our study confirms that this tectonic regime seems to favor higher thermal anomalies than compressional tectonics.

The complex nature of the processes occurring during the development of a geothermal resource within a CFZ makes it an environment that requires a state-of-the-art numerical analysis of the process that can control the fluid circulation. Such fully coupled analysis will help exploration phases and ultimately promote the development of this renewable energy, not only in anomalously hot areas, but in anomalously permeable areas, and thus promote the development of this climate-neutral energy.

4 - Methods

Comsol Multiphysics™ software is based on the Finite Element Method (FEM) and can, among other various physical processes, model fluid flow, heat transfer and elastic deformation of materials in a 3D geometry. Comsol Multiphysics™ is a well-known tool offering a complete access to the solution of partial differential equations. Benchmark tests have already been performed with previous numerical codes (OpenGeoSys, Comsol Multiphysics™ v3.5a, see Guillou-Frottier et al. 2020 and Appendix 1).
We consider an idealized and synthetic model that represents a typical vertical fault zone of 400 m thickness, in the middle of a 5.5 km side cubic volume of homogeneous basement rock. The fault zone, which corresponds to a multiple fault core, is treated like continuous porous medium. At very high fracture density, this assumption seems to be convenient (Zareidarmiyan et al. 2021). The mesh is defined by 15,785 tetrahedra, with mesh sizes of 500 m for low permeability zones and mesh sizes of 170 m for high permeability zones. Preliminary convergence tests have shown that a finer mesh size gives the same results. The transient simulations are

run up to 990 kyrs. The vertical faces of the basement are thermally insulated and fluid circulation is blocked. On the upper horizontal face, a temperature of 20°C and a pressure of 10^5 Pa are imposed (Fig. 1).

The initial thermal regime corresponds to a geothermal gradient of 30°C/km. At the base of the model a heat flux of 100 mW.m^{-2} is imposed. This heat flux can represent the sum of the mantle heat flow and the heat emitted by the decay of radioactive elements in the crust. The fluid is assumed to be pure water, and the fluid density depends on the pressure and temperature conditions (as detailed in Duwiquet et al., 2021). The details of the equations between Darcy's law, Fourier's law and Hooke's law can also be found in Duwiquet et al. 2021. All thermal, hydraulic and mechanical parameters are detailed in Table 1:

*Table 1 : Set of physical parameters used in numerical modelling. *Fault zone permeability is variables and adapted to fractured media (see Eq 3).*

Category	Symbols	Fault zone	Basement	Unit
Porosity	Φ	0.1	0.05	-
Permeability	k	Variable*	10^{-16}	m^2
Thermal conductivity	λ_s	3	2	W/(m.K)
Heat capacity	Cp_s	800	800	J/(kg.K)
Bulk density	ρ_s	2700	2700	kg/m^3
Young's modulus	E	5	60	GPa
Poisson's ratio	v	0.30	0.25	-
Biot-Willis coefficient	α_B	0.8	0.8	-

The Young's moduli imposed in the numerical models are suitable for fault zone and basement (Cappa and Rutqvist, 2011). In the basement, the Poisson's ratio is 0.25, a value generally accepted in the literature. However, in the fault zone we impose a value of 0.30. This value can be explained by two aspects, the first one is that the samples on which the Poisson coefficients are measured are much smaller than the block considered. This change of scale tends to increase the value of the Poisson coefficient (Heap et al. 2020). In addition, weathering and fracturing processes present in fault zones tend to increase the value of the Poisson's ratio (Heap et al. 2020). The physical properties of the fluids are identical to the study by Duwiquet et al. 2021.

In order to investigate the influence of tectonic regimes on fluid flow, we will compare a model with no tectonic stresses applied (which we will call the "benchmark experiment") with models where different tectonic regimes are considered. For these models, we have free boundary condition at the top, and clamping at the bottom (displacement blocked in all three directions). For the four vertical sides of the model, we use mechanical boundary conditions corresponding to the evolution of the stress with depth for different tectonic regimes. For this, we refer to an Andersonian assumption -where the principal stresses are expressed with vertical S_v, maximum horizontal S_{Hmax} and minimum horizontal S_{hmin} components- which is regularly used in geomechanical studies of reservoirs (Anderson, 1905; Zoback et al. 2003):

- Compressional (reverse/thrust faulting), $S_{Hmax} \geq S_{hmin} \geq S_V$
- Extensional (normal faulting) with, $S_V \geq S_{Hmax} \geq S_{hmin}$
- Strike-slip, with, $S_{Hmax} \geq S_V \geq S_{hmin}$

In order to understand the possible effects of stress intensity, stress-depth profiles were collected on two natural systems, one in the French Massif Central, and one near the San Andreas Fault. Two cases are considered, a low stress intensity zone

(e.g. French Massif Central) and a high stress intensity zone (e.g. San Andreas Fault). It should be noted that we assume that regional stresses prevail over local stress variations, which is consistent with our homogeneity assumption. The stress profiles as a function of depth correspond to the following equations (Cornet & Burlet, 1992; Zoback, 1992):

High stress intensity:

$$\begin{aligned} \sigma_3 &= 1 \times 10^6 + (15000 \times (-z)) \\ \sigma_2 &= 4 \times 10^6 + (20000 \times (-z)) \\ \sigma_1 &= 7.5 \times 10^6 + (28667 \times (-z)) \end{aligned} \qquad \text{Eq 1}$$

Low stress intensity:

$$\begin{aligned} \sigma_3 &= 0.1 \times 10^6 + (13975 \times (-z)) \\ \sigma_2 &= 0.1 \times 10^6 + (26225 \times (-z)) \\ \sigma_1 &= 0.1 \times 10^6 + (28725 \times (-z)) \end{aligned} \qquad \text{Eq 2}$$

where σ_1, σ_2, σ_3, are the maximum, intermediate and minimum principal stresses, respectively. z is the vertical upwards axis, and an increase in depth (z <0) brings a more compressive stress (positive compression convention). We assume the constant evolution of the stress with depth. The red color code corresponds to the high stress intensity and green color code corresponds to low stress intensity. Notice that in their natural state, a strike-slip stress regime holds for both regions, i.e., $\sigma_1 = S_{Hmax}$, $\sigma_2 = S_v$, $\sigma_3 = S_{Hmin}$. In the following, we keep the realistic principal stress magnitude given in Eq 1 and Eq 2 but change in our different scenarii the axes along which they operate. This way, we are able to investigate the effect of tectonic regimes while keeping realistic stress ratios. For the understanding of the results, the color code used in Eq. 1 and Eq. 2 is the same throughout the study. In order to allow the convergence of the 3D numerical calculations with this THM coupling, the application of the stresses is applied progressively from t = 0 yrs, until t =

10 yrs. The results are shown in steady-state, at 65 kyrs for the benchmark experiment, at 990 kyrs for the model where stresses are applied. The permeability *k* we will consider has been empirically demonstrated to be appropriate for fractured media (Lamur et al. 2017). It is written as:

$$\log k = (1-\omega) log k_i + \omega log k_f$$
$$k_i = 4.979 \times 10^{-11} n^{3.11} \quad \text{Eq 3}$$
$$k_f = 1.143 \times 10^{-11} n^{0.64}$$

where ω representing the degree of rock fracturing, $\omega = 1$ for fully fractured rock, and $\omega = 0$ for fully intact rock. Here we take $\omega = 0.8$ corresponding to the significant fracturing degree of the CFZ, interspersed with intact zones. n represents the initial porosity. Here n = 0.05 for intact rock, and n = 0.1 for fractured rock. k_i (m^2) the permeability of intact rock, and k_f (m^2) the permeability of fractured rock. The stress state of a fault can be qualitatively defined in terms of slip tendency (Morris et al. 1996). In purely elastic domain and without dissipative phenomena the slip tendency is an indicator (high/low general trend) to assess the stress variation on a fault zone. More specifically, slip tendency indicates how critically stressed fault zones are, and how easily they can be reactivated by, e.g., stimulation methods. Consequently, some preferential flow paths may appear under the action of a given applied tectonic stress (Siler et al. 2019). The slip tendency it is defined by:

$$T_S = \frac{\tau}{\sigma'_n} \quad \text{Eq 4}$$

where τ is the shear stress and σ'_n the effective normal stress.

$$\sigma'_n = \sigma_n - (\alpha_B \times pf) \quad \text{Eq 5}$$

where σ_n is the total normal stress; α_B Biot-Willis coefficient and pf fluid pressure.

Appendix 1

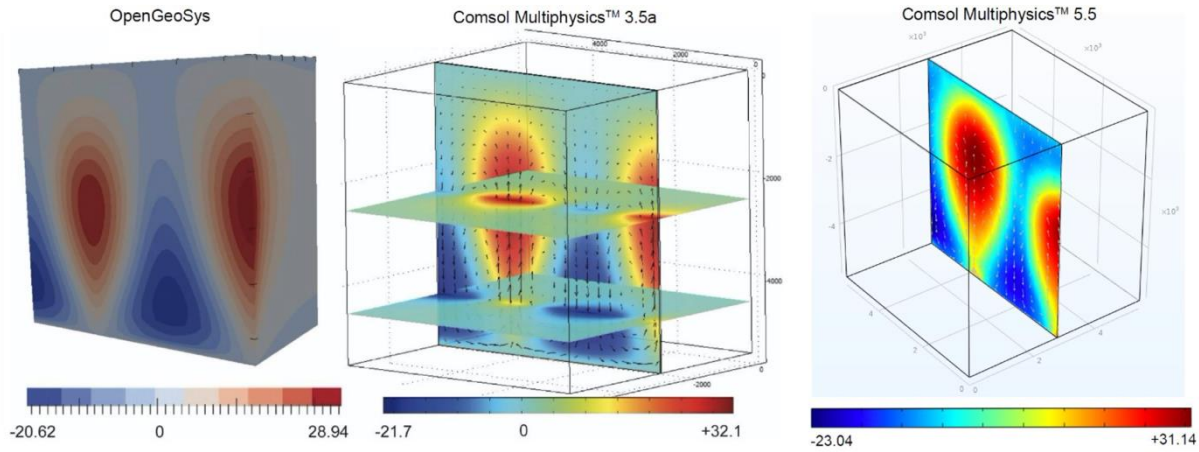

Appendix 1 : Benchmarking of our numerical experiment with the OpenGeoSys Code (Magri et al. 2017) and Comsol Multiphysics™ V3.5a (Guillou-Frottier et al. 2020) (From Duwiquet et al. 2021).

The calibration of our numerical experiments was performed based on results from Comsol Multiphysics™ version 3.5 (Guillou-Frottier et al. 2020) as well as the OpenGeoSys numerical code (Magri et al. 2017). These models consider a 40 m wide vertical fault in an impermeable box (a 5.5*5.5*5.5 km side cube). The fluid properties are identical for all three results with a linear dependence of temperature with water density, and an exponential decrease of viscosity with temperature. This result is shown for a time $t_0 + 10^{13}$ s. The imposed permeability value is 5×10^{-15} m^2. The fluid flow velocity is 2.03×10^{-9} $m.s^{-1}$. The fluid flow velocity is slightly higher than that described by Guillou-Frottier et al. 2020, who record a velocity of 1.4×10^{-9} $m.s^{-1}$.

The convective patterns are similar. Fluid velocity accelerates along the permeable fault and exhibits upward movement due to the thermal gradient and buoyancy forces related to lower water density at depth. The thermal perturbations are also within the orders of magnitude of previous studies with -22.04°C and +31.14 °C.

The numerical experiments of Magri et al. (2017) and Guillou-Frottier et al. (2020) used Darcy's law in conjunction with the equations of heat. The numerical experiments of this study couple the equations of heat and mass transfer with the modulus of poroelasticity. The poroelasticity interface of Comsol Multiphysics^{TM} combines Darcy's law with the linear elastic behavior of porous media (details can be found in Duwiquet et al. 2021). Poroelastic coupling allows boundary stresses to be imposed, which can be recorded as fluid pressure. In Figure 6 (right), no stress or other mechanical conditions are applied. Consequently, this experiment corresponds to an identical coupling as in the previous studies (Fig 6, left and middle cases).

Appendix 2

In order to understand if the permeability variations obtained after the stress application can explain the differences observed between the tectonic regimes, two numerical calculations with only a TH coupling have been performed. The parameters and their geometries are identical, the only difference is the permeability variation. On the left, a permeability of $10^{-12.09}$ m^2 is imposed on the fault, on the right a permeability of $10^{-12.19}$ m^2 is imposed on the fault. The results are similar. The only difference is located at the bottom right of the fault. On the left, the anomaly is -40°C, on the right it is -12°C. This localized difference does not seem to influence the thermal distribution of the overall system.

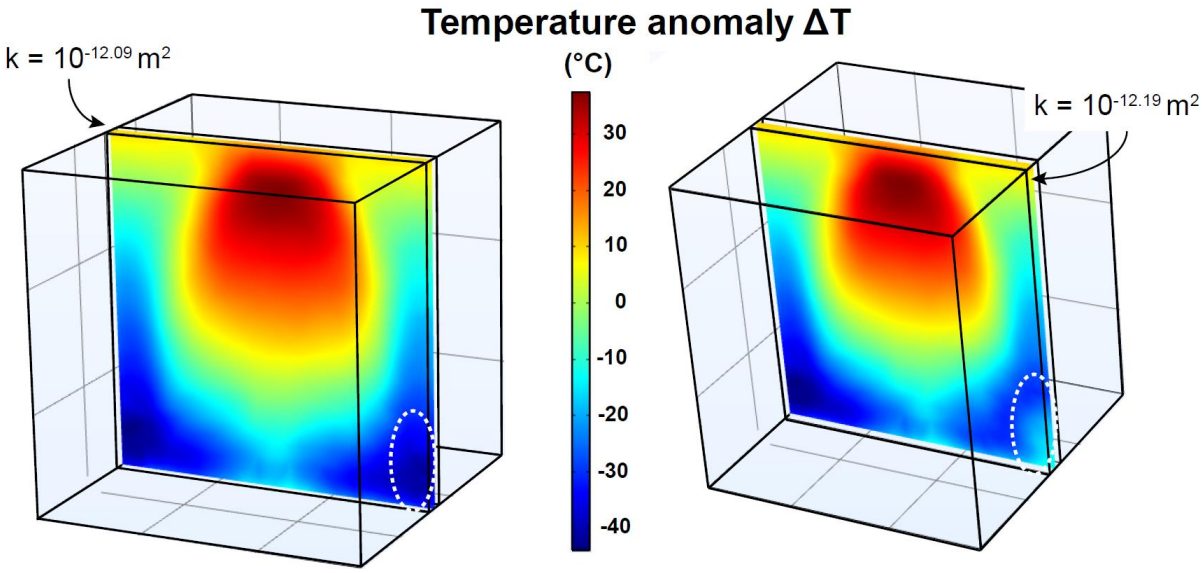

Appendix 2 : Comparison of the numerical results with a TH coupling considering as the only difference, a permeability variation of the order of $10^{-0.10}$ m^2. The results of the numerical calculations show no difference in the calculated values (see color bar). In cross-section, parallel to the fault, the difference is only at the bottom right of the numerical model.

References

Altmann, J. B., Heidbach, O., & Gritto, R. Relative importance of processes leading to stress changes in the Geysers geothermal area. In Proceedings of thirty-eighth workshop on geothermal reservoir engineering, (2013).

Anderson, E. M. The dynamics of faulting. *Transactions of the Edinburgh Geological Society*. **8(3)**, 387- 402 (1905). https://doi.org/10.1144/transed.8.3.387.

Barton, C. A., Zoback, M. D., & Moos, D. Fluid flow along potentially active faults in crystalline rock. *Geology*. **23(8)**, 683-686 (1995). https://doi.org/10.1130/0091-7613(1995)023<0683:FFAPAF>2.3.CO;2

Bejan, A., & Lorente, S. The constructal law and the evolution of design in nature. *Physics of life Reviews*, **8(3)**, 209-240 (2011). https://doi.org/10.1016/j.plrev.2011.05.010.

Bethke, C. M. A numerical model of compaction-driven groundwater flow and heat transfer and its application to the paleohydrology of intracratonic sedimentary basins. *Journal of Geophysical Research: Solid Earth*. **90(B8)**, 6817-6828 (1985). https://doi.org/10.1029/JB090iB08p06817

Ben-Zion, Y., & Rovelli, A. Properties and Processes of Crustal Fault Zones: Volume I. *Pure and Applied Geophysics*. **171(11)**, 2863-2865 (2014). https://doi.org/10.1007/s00024-014-0943-3

Cappa, F., & Rutqvist, J. Impact of CO_2 geological sequestration on the nucleation of earthquakes. *Geophysical Research Letters*. 38(17) (2011). https://doi.org/10.1029/2011GL048487.

Cao, S., & Neubauer, F. Deep crustal expressions of exhumed strike-slip fault systems: Shear zone initiation on rheological boundaries. *Earth-Science Reviews*. **162**, 155-176 (2016). https://doi.org/10.1016/j.earscirev.2016.09.010

Cornet, F. H., & Burlet, D. Stress field determinations in France by hydraulic tests in boreholes. *Journal of Geophysical Research: Solid Earth*. **97(B8)**, 11829-11849 (1992). https://doi.org/10.1029/90JB02638.

Cox, S. F. Coupling between deformation, fluid pressures, and fluid flow in ore-producing hydrothermal systems at depth in the crust. *Economic Geology*. **100**, 39-75 (2005).

Cox, S. F. Deformational controls on the dynamics of fluid flow in mesothermal gold systems. *Geological Society, London, Special Publications*. **155(1)**, 123-140 (1999). https://doi.org/10.1144/GSL.SP.1999.155.01.10

Cui, T., Yang, J., & Samson, I. M. Tectonic deformation and fluid flow: implications for the formation of unconformity-related uranium deposits. *Economic Geology*. **107(1)**, 147-163 (2012). https://doi.org/10.2113/econgeo.107.1.147.

Deichmann, N., and Giardini, D. Earthquakes induced by the stimulation of an enhanced geothermal system below Basel (Switzerland). *Seismological Research Letters*. **80(5)**, 784-798 (2009). https://doi.org/10.1785/gssrl.80.5.784.

Driesner, T. The system H2O–NaCl. Part II: Correlations for molar volume, enthalpy, and isobaric heat capacity from 0 to 1000 C, 1 to 5000 bar, and 0 to 1 XNaCl. *Geochimica et Cosmochimica Acta*. **71(20)**, 4902-4919 (2007). https://doi.org/10.1016/j.gca.2007.05.026.

Duwiquet, H. et *al*. On the geothermal potential of crustal fault zones: a case study from the Pontgibaud area (French Massif Central, France). *Geothermal Energy*. **7(1)**, 1-29 (2019). https://doi.org/10.1186/s40517-019-0150-7.

Duwiquet, H et *al*. Crustal Fault Zones (CFZ) as Geothermal Power Systems: A Preliminary 3D THM Model Constrained by a Multidisciplinary Approach. *Geofluids*. 2021 (2021). https://doi.org/10.1155/2021/8855632.

Duwiquet, H. et *al*. Crustal Fault Zones (CFZ) as Geothermal Power Systems: 3D Variation of Permeability and Related Processes. In Stanford Geothermal Workshop. (2021, February)

Eldursi, K et *al*. New insights from 2-and 3-D numerical modelling on fluid flow mechanisms and geological factors responsible for the formation of the world-class Cigar Lake uranium deposit, eastern Athabasca Basin, Canada. *Mineralium Deposita*. **1-24**, (2020). https://doi.org/10.1007/s00126-020-00979-5.

Evans, K. F. et *al*. Microseismicity and permeability enhancement of hydrogeologic structures during massive fluid injections into granite at 3 km depth at the Soultz HDR site. *Geophysical Journal International*. **160(1)**, 388-412 (2005). https://doi.org/10.1111/j.1365-246X.2004.02474.x.

Famin, V., Philippot, P., Jolivet, L., & Agard, P. Evolution of hydrothermal regime along a crustal shear zone, Tinos Island, Greece. *Tectonics*. **23(5)**, (2004). https://doi.org/10.1029/2003TC001509.

Faulkner, D. R., Lewis, A. C., & Rutter, E. H. (2003). On the internal structure and mechanics of large strike-slip fault zones: field observations of the Carboneras fault in southeastern Spain. *Tectonophysics*, **367(3-4)**, 235-251 (2003). https://doi.org/10.1016/S0040-1951(03)00134-3

Faulkner, D. R. et *al*. A review of recent developments concerning the structure, mechanics and fluid flow properties of fault zones. *Journal of Structural Geology*. **32(11)**, 1557-1575 (2010). https://doi.org/10.1016/j.jsg.2010.06.009

Forster, C., & Smith, L. The influence of groundwater flow on thermal regimes in mountainous terrain: A model study. *Journal of Geophysical Research: Solid Earth*. **94(B7)**, 9439-9451 (1989). https://doi.org/10.1029/JB094iB07p09439.

Gomila, R. et *al*. Quantitative anisotropies of palaeopermeability in a strike-slip fault damage zone: Insights from micro-CT analysis and numerical simulations. *Tectonophysics*, 228873 (2021). https://doi.org/10.1016/j.tecto.2021.228873

Genter, A., Evans, K., Cuenot, N., Fritsch, D., Sanjuan, B. Contribution of the exploration of deep crystalline fractured reservoir of Soultz to the knowledge of enhanced geothermal systems (EGS). *Comptes Rendus Geoscience*. **342(7-8)**, 502-516 (2010). https://doi.org/10.1016/j.crte.2010.01.006

Gleeson, T., & Ingebritsen, S. (Eds.). Crustal permeability. John Wiley & Sons. (2016).

Glover, P. W. J., Matsuki, K., Hikima, R., & Hayashi, K. Fluid flow in synthetic rough fractures and application to the Hachimantai geothermal hot dry rock test site. *Journal of Geophysical Research: Solid Earth*. **103(B5)**, 9621-9635 (1998). https://doi.org/10.1029/97JB01613

Grawinkel, A., & Stöckhert, B. Hydrostatic pore fluid pressure to 9 km depth-Fluid inclusion evidence from the KTB deep drill hole. *Geophysical Research Letters*. **24(24)**, 3273-3276 (1997).
https://doi.org/10.1029/97GL03309

Guillou-Frottier, L., Carrė, C., Bourgine, B., Bouchot, V., & Genter, A. Structure of hydrothermal convection in the Upper Rhine Graben as inferred from corrected temperature data and basin-scale numerical models. *Journal of Volcanology and Geothermal Research*. **256**, 29-49 (2013). https://doi.org/10.1016/j.jvolgeores.2013.02.008

Guillou-Frottier et *al*. On the morphology and amplitude of 2D and 3D thermal anomalies induced by buoyancy-driven flow within and around fault zones. *Solid Earth*. **11(4)**, 1571-1595 (2020). https://doi.org/10.5194/se-11-1571-2020.

Heap, M. J. et *al*. Towards more realistic values of elastic moduli for volcano modelling. *Journal of Volcanology and Geothermal Research*. **390**, 10668 (2020). https://doi.org/10.1016/j.jvolgeores.2019.106684.

Horton, C. W., & Rogers Jr, F. T. Convection currents in a porous medium. *Journal of Applied Physics*. **16(6)**, 367-370 (1945). https://doi.org/10.1063/1.1707601.

Horne, R. N. Three-dimensional natural convection in a confined porous medium heated from below. *Journal of Fluid Mechanics*. **92(4)**, 751-766 (1979).

Ito, T., & Zoback, M. D. Fracture permeability and in situ stress to 7 km depth in the KTB scientific drillhole. *Geophysical Research Letters*. **27(7)**, 1045-1048 (2000). https://doi.org/10.1029/1999GL011068

Katto, Y., & Masuoka, T. Criterion for the onset of convective flow in a fluid in a porous medium. *International Journal of Heat and Mass Transfer*. **10(3)**, 297-309 (1967). https://doi.org/10.1016/0017-9310(67)90147-0.

Kozlovsky, Y. The World's Deepest Well. Scientific American, **251(6)**, 98-105. (1984). from http://www.jstor.org/stable/24969503

Kwiatek, G., et *al*. Microseismicity induced during fluid-injection: A case study from the geothermal site at Groß Schönebeck, North German Basin. Acta Geophysica. **58(6)**, 995-1020 (2010). https://doi.org/10.2478/s11600-010-0032-7

Lamur, A. et *al*. The permeability of fractured rocks in pressurised volcanic and geothermal systems. *Scientific reports*. **7(1)**, 1-9 (2017). https://doi.org/10.1038/s41598-017-05460-4.

Ledingham, P., Cotton, L., & Law, R. The united downs deep geothermal power project. *Proc. 44th Work. Geotherm. Reserv. Eng*, **1-11** (2019).

López, D. L., & Smith, L. Fluid flow in fault zones: analysis of the interplay of convective circulation and topographically driven groundwater flow. *Water resources research*. **31(6)**, 1489-1503 (1995). https://doi.org/10.1029/95WR00422.

Liang, X., Xu, T., Feng, B., & Jiang, Z. Optimization of heat extraction strategies in fault-controlled hydro-geothermal reservoirs. *Energy*. **164**, 853-870 (2018). https://doi.org/10.1016/j.renene.2019.02.070

Magri, F. et *al*. , Cacace, M., Fischer, T., Kolditz, O., Wang, W., & Watanabe, N. Thermal convection of viscous fluids in a faulted system: 3D benchmark for numerical codes. Energy Procedia. **125**, 310-317 (2017). https://doi.org/10.1016/j.egypro.2017.08.204

McLellan, J. G., Oliver, N. H. S., & Schaubs, P. M. Fluid flow in extensional environments; numerical modelling with an application to Hamersley iron ores. *Journal of Structural Geology*. **26(6-7)**, 1157-1171 (2004). https://doi.org/10.1016/j.jsg.2003.11.015

Morris, A., Ferrill, D. A., Henderson, D. B. Slip-tendency analysis and fault reactivation. *Geology*. **24(3)**, 275-278 (1996). https://doi.org/10.1130/0091-7613(1996)024<0275:STAAFR>2.3.CO;2

O'Sullivan, M. J., Pruess, K., & Lippmann, M. J. State of the art of geothermal reservoir simulation. *Geothermics*. **30(4)**, 395-429 (2001). https://doi.org/10.1016/S0375-6505(01)00005-0.

Ord, A., & Oliver, N. H. S. Mechanical controls on fluid flow during regional metamorphism: some numerical models. *Journal of Metamorphic Geology*. **15(3)**, 345-359 (1997). https://doi.org/10.1111/j.1525-1314.1997.00030.x

Parisio, F., Vilarrasa, V., Wang, W., Kolditz, O., Nagel, T. The risks of long-term re-injection in supercritical geothermal systems. *Nature communications*. **10(1)**, 1-11 (2019). https://doi.org/10.1038/s41467-019-12146-0

Paulillo, A., Cotton, L., Law, R., Striolo, A., & Lettieri, P. (2020). Geothermal energy in the UK: The life-cycle environmental impacts of electricity production from the United Downs Deep Geothermal Power project. *Journal of Cleaner Production*, 249, 119410.

Phillips, W. J. Hydraulic fracturing and mineralization. *Journal of the Geological Society*. **128(4)**, 337-359 (1972).

Rowland, J. V., & Sibson, R. H. Structural controls on hydrothermal flow in a segmented rift system, Taupo Volcanic Zone, New Zealand. *Geofluids*. **4(4)**, 259-283 (2004). https://doi.org/10.1111/j.1468-8123.2004.00091.x

Saevarsdottir, G., Tao, P. C., Stefansson, H., & Harvey, W. Potential use of geothermal energy sources for the production of lithium-ion batteries. *Renewable energy*. **61**, 17-22 (2014). https://doi.org/10.1016/j.renene.2012.04.028

Sardini, P., Ledésert, B., & Touchard, G. Quantification of microscopic porous networks by image analysis and measurements of permeability in the Soultz-sous-Forêts granite (Alsace, France). *In Fluid flow and Transport in rocks*. **171-189**, (1997). https://doi.org/10.1007/978-94-009-1533-6_10

Scott, S., Driesner, T., & Weis, P. Boiling and condensation of saline geothermal fluids above magmatic intrusions. *Geophysical Research Letters*. **44(4)**, 1696-1705 (2017). https://doi.org/10.1002/2016GL071891.

Sibson, R. H. Earthquake rupturing as a mineralizing agent in hydrothermal systems. *Geology*. **15(8)**, 701-704 (1987). https://doi.org/10.1130/0091-7613(1987)15<701:ERAAMA>2.0.CO;2

Siebenaller, L. et *al*. Fluid record of rock exhumation across the brittle–ductile transition during formation of a Metamorphic Core Complex (Naxos Island, Cyclades, Greece). *Journal of Metamorphic Geology*. **31(3)**, 313-338 (2013). https://doi.org/10.1111/jmg.12023

Siler, D. L.H et *al*. Three-dimensional geologic mapping to assess geothermal potential: examples from Nevada and Oregon. *Geothermal Energy***. 7(1)**, 1-32 (2019). https://doi.org/10.1186/s40517-018-0117-0.

Sun, Z. X. et *al*. Numerical simulation of the heat extraction in EGS with thermal-hydraulic-mechanical coupling method based on discrete fractures model. *Energy*. **120**, 20-33 (2017). https://doi.org/10.1016/j.energy.2016.10.046.

Violay, M., Heap, M. J., Acosta, M., & Madonna, C. Porosity evolution at the brittle-ductile transition in the continental crust: Implications for deep hydro-geothermal circulation. *Scientific reports*. **7(1)**, 1-10 (2017). https://doi.org/10.1038/s41598-017-08108-5.

Wanner, C., Diamond, L. W., & Alt-Epping, P. Quantification of 3-D thermal anomalies from surface observations of an orogenic geothermal system (Grimsel Pass, Swiss Alps). *Journal of Geophysical Research: Solid Earth*. **124(11)**, 10839-10854 (2019). https://doi.org/10.1029/2019JB018335

Watanabe, N., Egawa, M., Sakaguchi, K., Ishibashi, T., & Tsuchiya, N. Hydraulic fracturing and permeability enhancement in granite from subcritical/brittle to super-critical/ductile conditions. *Geophysical Research Letters*. **44(11)**, 5468-5475 (2017). https://doi.org/10.1002/2017GL073898.

Watanabe, N., Abe, H., Okamoto, A., Nakamura, K., & Komai, T. Formation of amorphous silica nanoparticles and its impact on permeability of fractured granite in superhot geothermal environments. *Scientific reports*. **11(1)**, 1-11 (2021). https://doi.org/10.1038/s41598-021-84744-2

Wilson, M. P. et *al*. HiQuake: The human-induced earthquake database. Seismological Research Letters, 88(6), 1560-1565. Data set https://doi.org/10.1785/0220170112 (2017). https://inducedearthquakes.org

Zareidarmiyan, A., Parisio, F., Makhnenko, R. Y., Salarirad, H., & Vilarrasa, V. How equivalent are equivalent porous media? *Geophysical Research Letters*, e2020GL089163. https://doi.org/10.1029/2020GL089163.

Zoback et *al*. Determination of stress orientation and magnitude in deep wells. *International Journal of Rock Mechanics and Mining Sciences*. **40(7-8)**, 1049-1076 (2003). https://doi.org/10.1016/j.ijrmms.2003.07.001.

Zoback, M. L. Stress field constraints on intraplate seismicity in eastern North America. *Journal of Geophysical Research: Solid Earth*. **97(B8)**, 11761-11782 (1992). https://doi.org/10.1029/92JB00221.

Chapter V : Geothermal potential of the Pontgibaud Crustal Fault Zone (French Massif Central) - a Multidisciplinary Approach

“These waters traverse the body of the Earth with infinite ramifications.”

Leonardo Da Vinci (1452-1519), *Notebooks*.

The Pontgibaud area is located 20 km west of Clermont-Ferrand, at the base of the Chaîne des Puys. Forgotten for nearly a century, the Pontgibaud lead-silver district had a prosperous period in the 19th century. Nearly 50,000 tons of lead and 100 tons of silver were extracted by the “Société des Mines et Usines de Pontgibaud”. Six main deposits are present in this district: les Rosiers, Pranal, Barbecot, la Grange, Roure, la Brousse. These mines have given rise to numerous studies providing information, for example, on the structures observed in the mines, which are now closed. The results presented in this chapter have benefited from these descriptions.

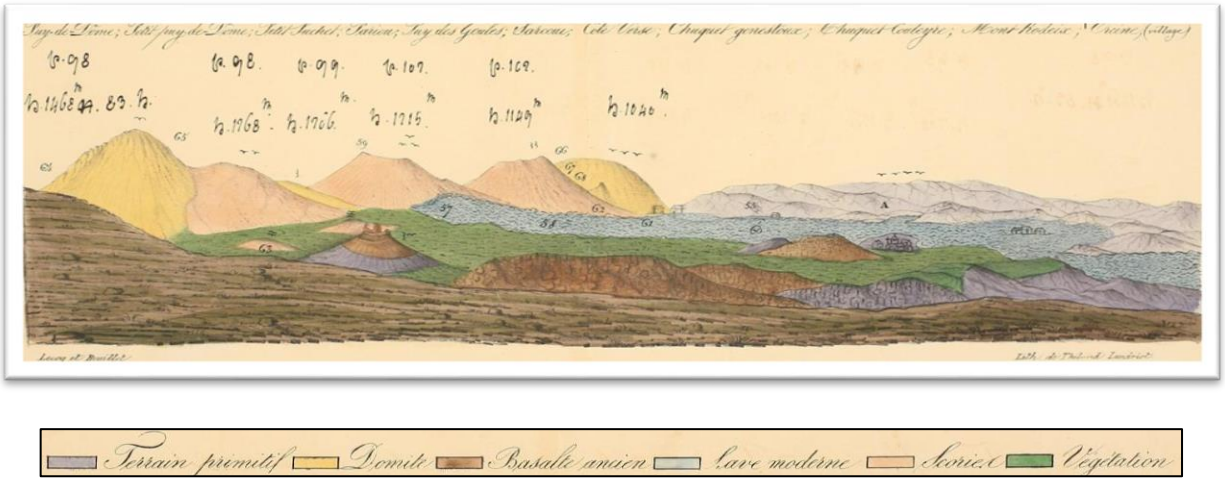

Figure 39 : Panorama from the Puy de Dôme to the Orcine village (Lecoq and Bouillet, 1830)

Since 2014, TLS-Geothermics, a French company involved in geothermal exploration has been keen to demonstrate the viability of CFZ as a geothermal exploration play for economic power generation. The demonstration of the potential of CFZ is underway at a site in the French Massif Central (FMC) using an exploration licence named “La Sioule”. Several geological observations and geophysical data, which are detailed below, represent good indicators for high-temperature geothermal exploitation.

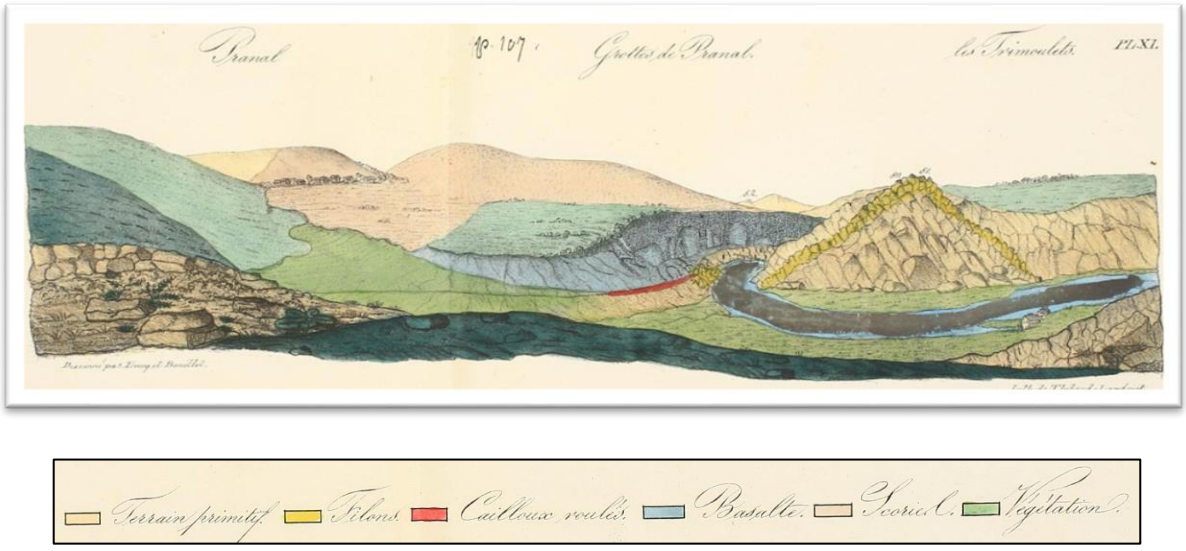

Figure 40 : Panorama of the Sioule valley with view on the Pranal village (Lecoq and Bouillet, 1830)

1 Geological setting

In order to facilitate the understanding of the geological context of the “La Sioule” licence, some parts are taken from chapter I. However, the geological formations, the tectonic calendar as well as the structures favorable to fluid circulation are detailed below.

1.1 Geological formation

Bounded to the east and west by the Aigueperse Saint Sauves fault and the Sillon Houiller fault, the “La Sioule” licence (Fig 41) is largely affected by late Variscan tectonics. Metamorphic formations and the Gelles granite, are the main lithologies present in the field.

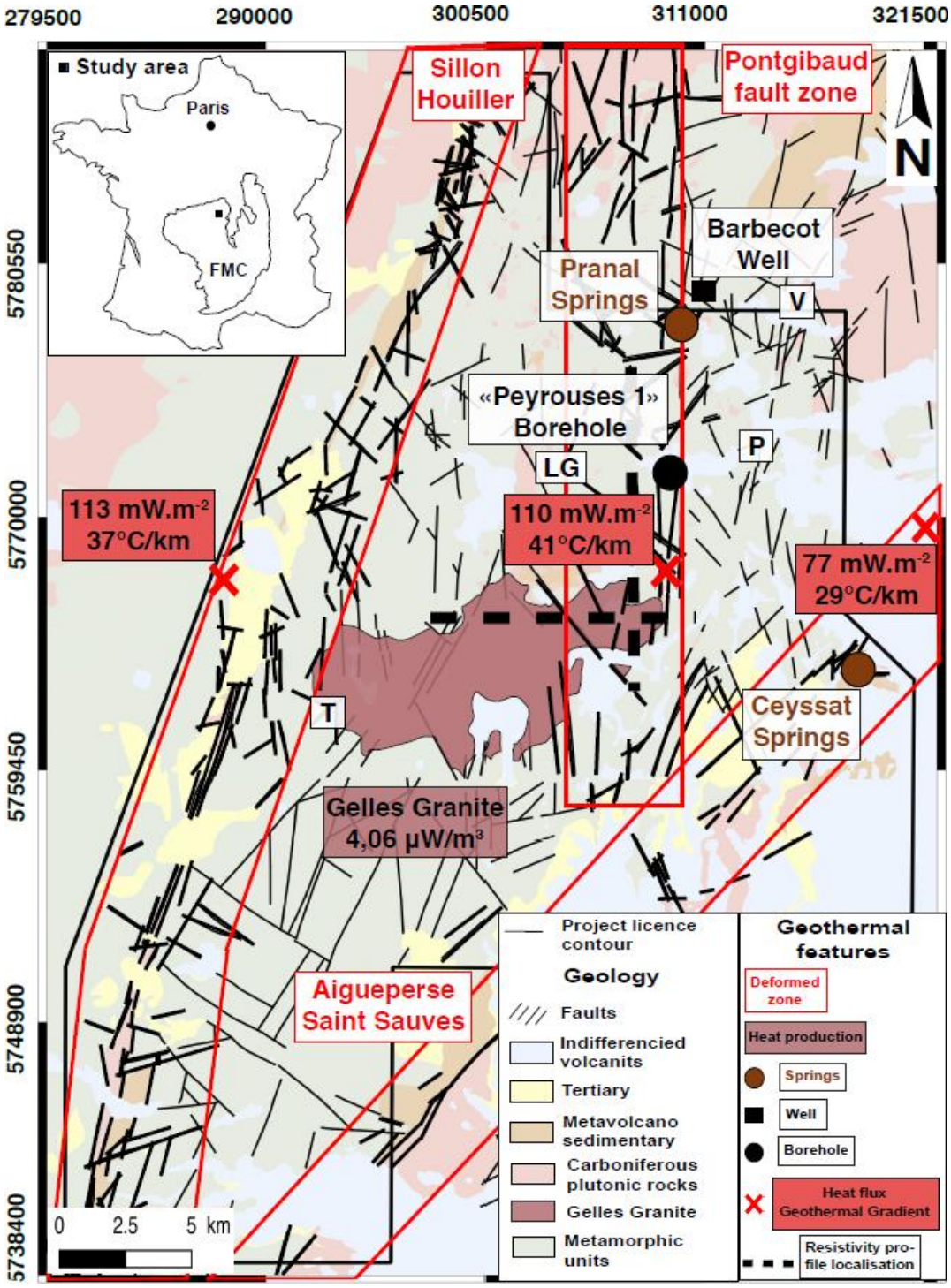

Figure 41 : Geological and geothermal features in the "La Sioule" licence area (black contour). FMC: French Massif Central. Heat flux and geothermal gradient (red crosses (Lucazeau and Vasseur, 1989; Vasseur et al. 1991), International Heat Flow Commission). Heat production (Lucazeau, 1981) and resistivity profile (black dashed line (Ars et al. 2019)). P: Pontgibaud; LG: La Goutelle; V: Villelongue; T: Tortebesse. Coordinate system: WGS84 Pseudo-Mercator EPSG:3857 (after the 1/50,000th geological map published by BRGM (Hottin et al. 2000)).

Magmatic and hydrothermal veins are widely represented. Covering a large part of the mapped region, metamorphic formations (green in Fig 41) can be separated into different lithologies. Biotite and sillimanite paragneiss extend southwards near the Miouze River and northeastwards to the Villelongue region. Orthogneiss associated with biotite and sillimanite paragneiss are present sporadically. Cordierite gneisses are more widely represented, but it is difficult to assign a cartographic boundary. Rare amphibolitic levels are interspersed in the cordierite gneisses. As an intrusive in metamorphic series, the porphyroid granite of Gelles (red in Fig 41) extends southwest of Pontgibaud, between the Sioule Valley to the East and the village of Tortebesse to the West. To the North, the last granitic points appear immediately to the west of La Goutelle.

1.2 Structural setting

In order to understand the spatial organization of potential drains of some geological structure, it is necessary to first consider the tectonic evolution of the study area (Fig 42). In the previous chapter, we have seen an effect of a tectonic stress and its orientation on a CFZ. We will then investigate the effects of the direction of the principal stress on fluid flow in preexisting fractures.

1.2.1 Famennian to late Namurian (365 Ma-315 Ma)

From Famennian to the early Visean, the maximum main horizontal stress axis is rotated 40° clockwise from NNW-SSE to NNW-SSW (Fig 42). During the Visean, the maximum main stress axis spatially varied from the vertical (extension, detachment of Argentat) to the horizontal (strike-slip, sinistral kinematic of the “Sillon Houiller”). Then, during the late Namurian, the maximum main horizontal stress shortening axis continued to rotate clockwise until it reached a NE-SW direction (Fig 42).

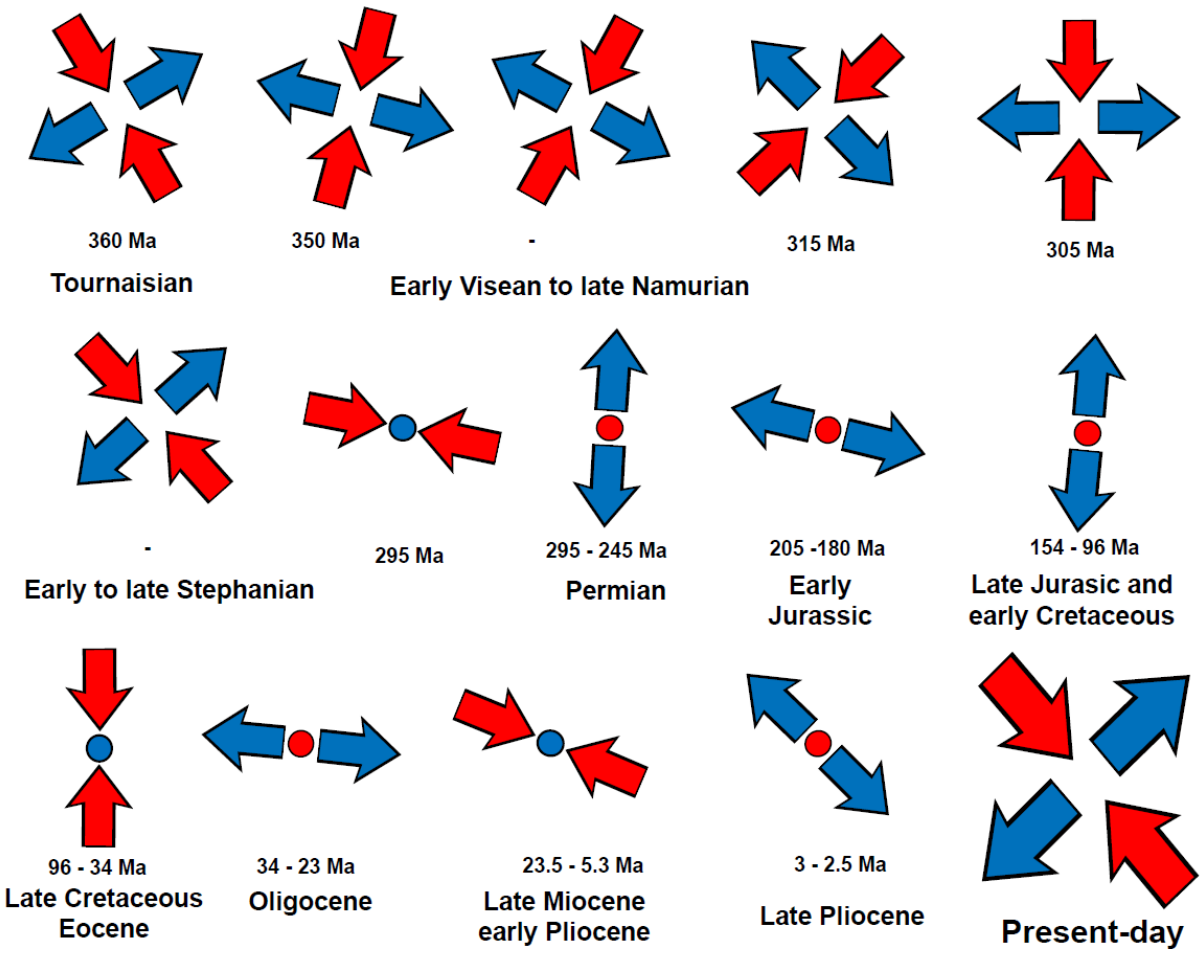

Figure 42 : Paleostress orientation in the "La Sioule" licence since the Tournaisian (360 Ma). Blue arrows indicate the extensional direction. Red arrows indicate the compressional direction (modified after Jébrak, 1978; Blès et al. 1989; Bellanger et al. 2019).

1.2.2 Early to late Stephanian (305-295 Ma)

During the lower and middle Stephanian, N-S compression created a system of conjugated N140° - 170° E sinistral and N10° -50° E dextral with N80° 120° E reverse faults. This deformation episode was responsible for the NE-SW sinistral fault of the "Sillon Houiller." During the transition from the middle to the upper Stephanian, the axis of rotation of the compression changed from N-S to NW-SE (Fig 42).

This rotation activated or reactivated dextral conjugated faults N 120° E and sinistral N160- 180° E. During the late Stephanian, the compression became E-W and resulted in a strong folding of coal deposits along the Sillon Houiller fault (Blès et al. 1989).

1.2.3 Permian to Jurassic (295-205 Ma)

Following Stephanian compression, the N-S/NE-SW Permo-Triassic extension is represented in the basement by normal faults, tension cracks, and veins (Blès et al. 1989; Bonijoly; 1981; Blès and Blès, 1982). On the Cévennes border, this N-S extension followed NW-SE directions inherited from the Stephanian, forming NE faults such as the Cévennes fault (Blès et al. 1989, Bonijoly and Germain; 1984). At the Trias-Lias border, a major metallogenic event occurred in the Massif Central, with the formation of a large number of veins and stratiform deposits, whose age was determined at about 194 Ma (Baubron, 1980).

1.2.4 Cretaceous to late Pliocene (96-2.5 Ma)

The establishment of a rift characterizes the Cenozoic in Europe: the European Cenozoic Rift System (ECRIS). This large rift system (about 1,000 km) is associated with a series of transect faults throughout the Variscan massif. This produced a radical change in the stress regime throughout the Massif Central (Figure 42). After a long period of Permian-Mesozoic extension, a N-S compressive tectonic regime was established, the effects of which were visible from England to Bohemia (Mattauer and Mercier; 1980; Letouzey and Trémolières, 1980; Bergerat, 1985; Ziegler, 1987). In the Massif Central and its borders, the Late Eocene Oligocene extension generated basins, grabens, and half-grabens bounded by normal faults, in which several hundred to thousand meters of continental sediments were deposited. The faults limiting these basins are generally N-S oriented but some NE-

SW and NW-SE trends also exist. While the extension affected the entire Massif Central and its border, the deformation was concentrated near the regional fractures inherited from the Variscan orogeny. During the Oligocene, the Western European plate was affected by a system of N-S-trending grabens forming the Western European Rift. This continental rift can be divided into several sections linked by transforming regional faults with a NE direction (Bergerat, 1985; Gélard, 1978). Calcagno et al. (2014) built a 3D geological and thermal model of the Limagne half-graben, 15 km east of the PFZ. According to their conductive model, the half-graben would host 160°C at 3 km depth.

1.2.5 Present-day stress regime

Several seismological stress-state evaluations were performed around the studied area. Mazabraud et al. (2005) have determined five focal mechanisms from regional records below the Pulvérières and St. Gervais granites, located 20 km north of the PFZ. They exhibit reverse, normal, and strike-slip mechanisms. The maximum horizontal stress axis is oriented close to NW-SE. More recently, local stress states were evaluated during the exploration of the geothermal licence based on the seismological records acquired between 2015 and 2016 by TLS-Geothermics using 11 triaxial broadband seismometers CMG40 (see Ars et al. 2019 for more details about this geophysical acquisition). Data were processed in 2018 by MAGNITUDE (a Baker Hughes company) to (i) identify microearthquake events, (ii) perform a focal mechanism analysis, and (iii) evaluate the stress state. 25 microearthquake events were identified and localized (mainly to the north of the studied area), and 14 focal mechanisms were determined (between -2 and -12 km asl). Confidence is very good for six Focal Mechanism Solutions (FMS) (good amplitudes fit at each station and focal spheres are well constrained), is good for three FMS, and is more uncertain for five FMS. They exhibit reverse (three FMS), normal (two FMS), and strike-slip regimes (nine FMS). The strike-slip regime occurred for all FMS with a high degree of confidence, for 2/3 of FMS with a good degree of confidence, and for 1/5

of FMS with a low degree of confidence. The nature of the stress tensor for each FMS quality set (see Mazabraud et al. 2005) was then estimated by assuming that the following hypotheses are true: (i) the stress field is uniform within the studied area and (ii) the tangential traction on the fault plane is parallel to the slip direction. In each of the three cases, they obtain a strike-slip regime (i.e., with a subvertical intermediary stress axis and subhorizontal maximum and minimum stress axes). Directions of the maximum stress axis are bracketed between N135° and N150° for the high-quality set and between N120° and N135° for the other two cases (Figure 42).

1.3 Structure favorable features for fluid circulation in the «La Sioule» licence

1.3.1 The Sillon Houiller fault zone

This fault zone, generally oriented N 20°, is located to the west of the area (Fig 41) and is continuous at a scale of 400 km with a sinistral motion (Faure et al. 1993; Joly et al. 2008). Evidence in various volcanic deposits highlights the high permeability of this structure since the Permian. At both sides of the Sillon Houiller, P-wave velocity anomalies indicate that this structure affects the entire lithosphere (Granet et al. 1995a). Such a large-scale structure, if permeable enough, would promote the ascent of hot hydrothermal fluids from the base of crust to the surface. According to Sobolev et al. (1997), temperature varies between the different sides of the fault at 30 km depth, from 700 to 925°C. In addition, surface heat flux equals 113 $mW.m^{-2}$ near the Sillon Houiller (Fig 41) (Lucazeau et al. 1984; Lucazeau and Vasseur, 1989). This abnormally high value is thought to be related to a relatively high mantle heat flow (Lucazeau et al. 1984), which could be related to a supposed mantle plume (Granet et al. 1995b) or past subduction-related hot upwelling (Király et al. 2017; Roche et al. 2018a, b).

1.3.2 The Aigueperse-Saint-Sauves fault zone

This NE–SW fault system is more than 300 km long (Faure et al. 1993) and crosses the southeast corner of the licence (Fig 41). It comprises a fault network, several hundred meters thick, and shifts the Sillon Houiller fault zone over a 31-km-long dextral-slip motion. The Puy de la Nugère and Puy Chopine monogenic volcanoes of the quaternary Chaîne des Puys (CdP) volcanic field (located 10 km to the east of La Sioule licence area) are emplaced on the Aigueperse–Saint-Sauves fault zone. The presence of Ceyssat, Châtelguyon, Gimaux, Saint Myon or Montpensier springs characterizes this structure as a potentially open and efficient pathway for present-day hydrothermal fluids.

1.3.3 The Pontgibaud Fault Zone

The N–S fault zone of Pontgibaud is parallel to the CdP. The CdP is a fissural volcanic field that hosts about eighty basaltic to trachytic volcanoes that erupted between 100 and 7 ka. The PFZ (Fig 41), more than 40 km long, is pinched between the Sillon Houiller and the Aigueperse–St-Sauves fault zones. In the studied area, it bounds the Viseo-Serpukhovian Gelles granite (Fernandez, 1969; Négroni, 1981). Some N–S faults of the Pontgibaud fault zone are filled by microgranite. Moreover, this N–S network is affected by As–Au, Pb–Ag and Ba–F mineralization, reflecting the ability of the system to transmit hydrothermal fluids during the Variscan. Some dating on mineralized bodies obtained on phengite and illite suggest Permian to Jurassic ages (Bril et al.1991), which reflects late hydrothermal fluid circulation related to the opening of the Alpine Tethys and the Atlantic Ocean. This mineralization is attributed to a medium temperature phase (200–400°C) subcontemporary to the end of the crystallization of the Gelles granite (Marcoux and

Picot, 1985). If evidence for hydrothermal fluid circulation exists during the Carboniferous, but also from the Permian to Jurassic, current fluid circulation along this fault zone seems also very likely. Indeed, springs can be found along the present-day fault at several locations (see details below).

1.4 Geothermal setting of the Pontgibaud area

1.4.1 Spring and magma chamber

Present-day fluid flow occurs within the Pontgibaud fault zone (Fig 41). In addition, at the time of mining activities, the galleries were regularly flooded (Lebocey, 2013). Due to cessation of mining activities in the 20th century, the mining wells were abandoned. Some wells, such as the one at Sainte-Barbe in Barbecot (4 km north of Pontgibaud), are marked by ion-rich and extremely CO2-charged flows. In addition, the Pranal spring (Fig 41) comes from a deep reservoir with estimated temperatures between 150 and 175°C (estimated using Na/K geothermometer; Verney 2005).
At a deeper level, thermo-barometric experiments on the CdP trachytes estimated the storage pressure and temperature conditions of magmas (Martel et al. 2013). For temperatures ranging from 700 to 825°C, the results of Martel et al. (2013) indicate pressures between 3 and 3.5 kbar (i.e., between 11 and 13 km deep, respectively). The thermal relaxation time calculated for these reservoirs estimate that cooling started about 15,000 years ago (Martel et al. 2013). This means that they are still potentially hot (500–600 °C), if not partially melted.

1.4.2 Surface heat flux and heat production

Part of the Pontgibaud fault zone was intersected by core drilling undertaken by the BRGM (French Geological Survey) in the 1970s. The purpose of these drillings was to characterize the mining potential of these structures. As part of this study, one of these boreholes (Peyrouses 1, location in Fig 41) remains accessible and has been used in this study. In the past, temperature measurements have been carried out between 55 and 120 m. From these measurements, a geothermal gradient of 41 C.km^{-1} has been inferred and a heat flux of 110 mW.m^{-2} was estimated (IHFC database; http://www.datapages.com/gis-map-publishing-program/gis-open-files/global-framework/global-heat-flow-database).

This relatively high heat flux value can be explained by an elevated mantle heat flow and/or a large crustal heat production. The analysis of 660 rock samples taken from granitic units in the FMC (Lucazeau, 1981) revealed an average heat production of 4.06 µW.m^{-3}. Considering an average granite thickness of 7 km (Vigneresse et al. 1999), the heat production of this granitic upper crust can only explain 26% of the heat flow measured in the Pontgibaud fault zone. The analysis of 112 samples taken from metamorphic units revealed an average heat production of 2.27 µW.m^{-3}. If this average value is representative for the remaining 22 km of crust (considering the crustal thickness in this area is 29 km, Zeyen et al. 1997), the mantle heat flow would be close to 32 mW.m^{-2}, twice as large as for a thermally stable Archean crust.

1.4.3 Magnetotelluric data

Magnetotelluric (MT) campaigns were carried out in the Pontgibaud fault zone area by TLS-Geothermics and IMAGIR between 2015 and 2017 (Ars et al. 2019). From

their 3D model of electrical resistivity produced in 2016 by IMAGIR, the profile corresponding to our geological cross-section was extracted (Fig 41). The interest of this passive electromagnetic method is its sensitivity to geometries and its ability to image conductive objects in three dimensions. Results show that the obtained conductive bodies in the upper crust could be related to the Pontgibaud fault zone.

Mining work on the Pontgibaud fault zone has highlighted structures with a dip of 70° E (Bouladon et al. 1961), but more recent data favors dips of ~ 60°, as detailed later. This steep dip is consistent with the structures that are visible on the MT image (Fig 43). The obtained resistivity model makes it possible to identify highly conductive bodies, one of which is located between a depth of 10 and 20 km (Fig 43). Petrological observations on trachytes suggest that the conductivity anomaly located at a depth between 10 and 20 km could reflect the presence of silicate melt (Martel et al. 2013).

At a depth of 8 and 3 km, two other anomalies located in the brittle crust could be linked to the presence of magmas, clays (smectites) and/or hydrothermal fluids. Whatever their nature, these two anomalies appear to be related to the Pontgibaud fault zone. This fault zone, which could be interpreted as a listric fault zone, seems to join the Aigueperse–Saint-Sauves fault system at a depth of 10 to 15 km (Ars et al. 2019). Isotopic analyses of CO_2 from the Ceyssat and Pranal resurgences at $\delta^{13}C$ (see location in Fig 41) indicate a mantle origin (Verney, 2005), which is in agreement with isotopical results from the whole French Massif Central (Bräuer et al. 2017). Indeed, the presence of CO_2 at the surface could be explained by the connectivity of the Pontgibaud and Aigueperse–Saint-Sauves structures to magmatic activity. It also highlights that these two fault zones could serve as pathways for hydrothermal fluid flow.

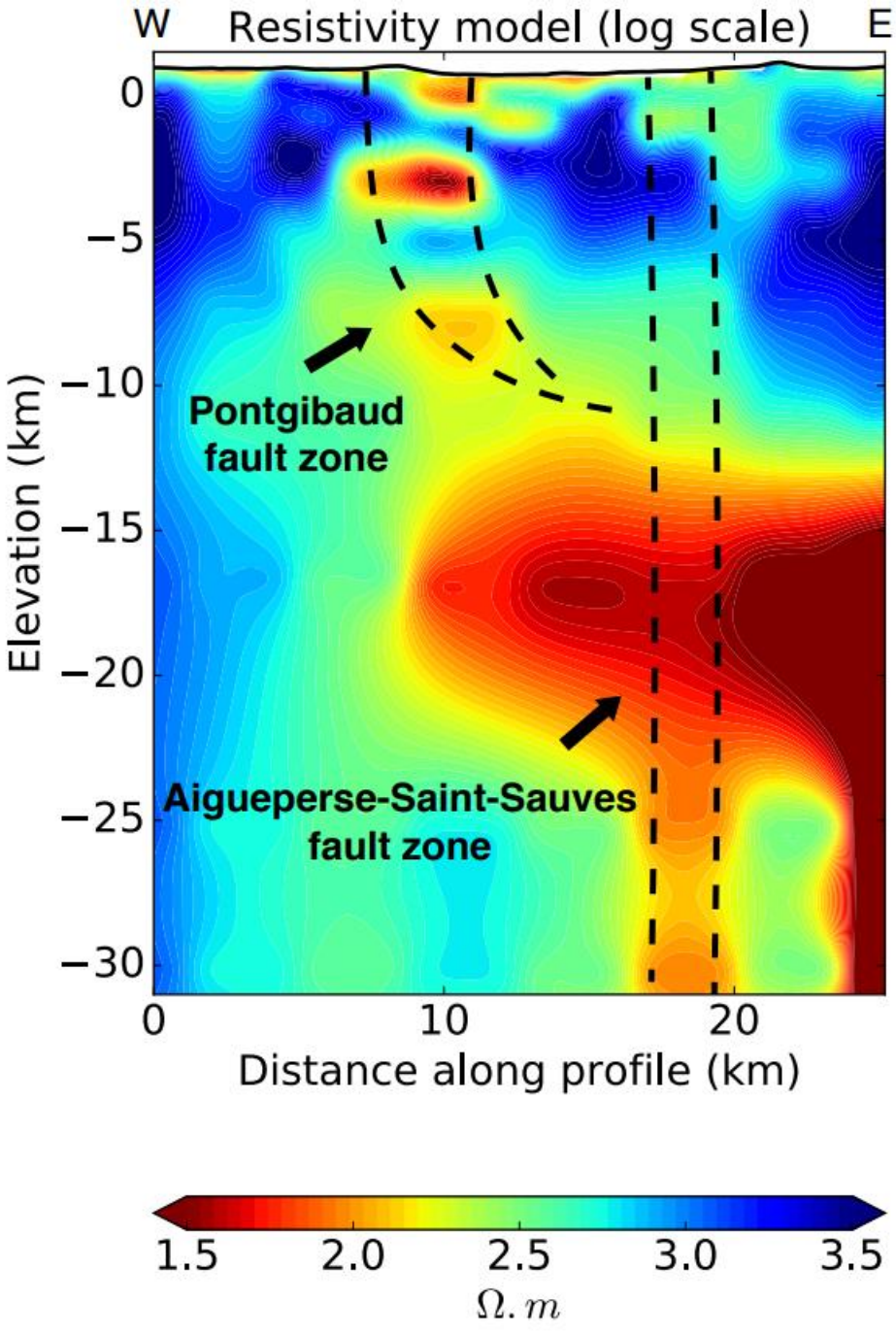

Figure 43 : 2D resistivity profile. The dashed lines represent the hypothetical tracing of the deep structures, constrained by surface signatures (fault orientation and dips). Modified after Ars et al. (2019).

2 Materials and methods

The multidisciplinary approach used here corresponds to a method widely used in oil and uranium exploration, CO_2 capture and storage studies, and reservoir engineering. It combines a field approach (structural measurements and sampling of the Peyrouses 1 borehole), a laboratory approach (2D and 3D observations and measurements of permeability and connected porosity), and, finally, numerical modelling.

2.1 Field, structural observations, and Peyrouses 1 borehole sampling

The structural measurements, performed in the field, make it possible to better characterize the intensity of the deformation in and around the Pontgibaud fault zone and also to put the geometry and architecture flow pathways into a 2D and 3D perspective. Sampling of the Peyrouses 1 borehole (Fig 44) located within the Pontgibaud fault system (see location Fig 41) provides a better understanding of the spatial distribution of pores and permeable fractures in this hydrothermal system, through thin-section observations and X-ray microtomography.

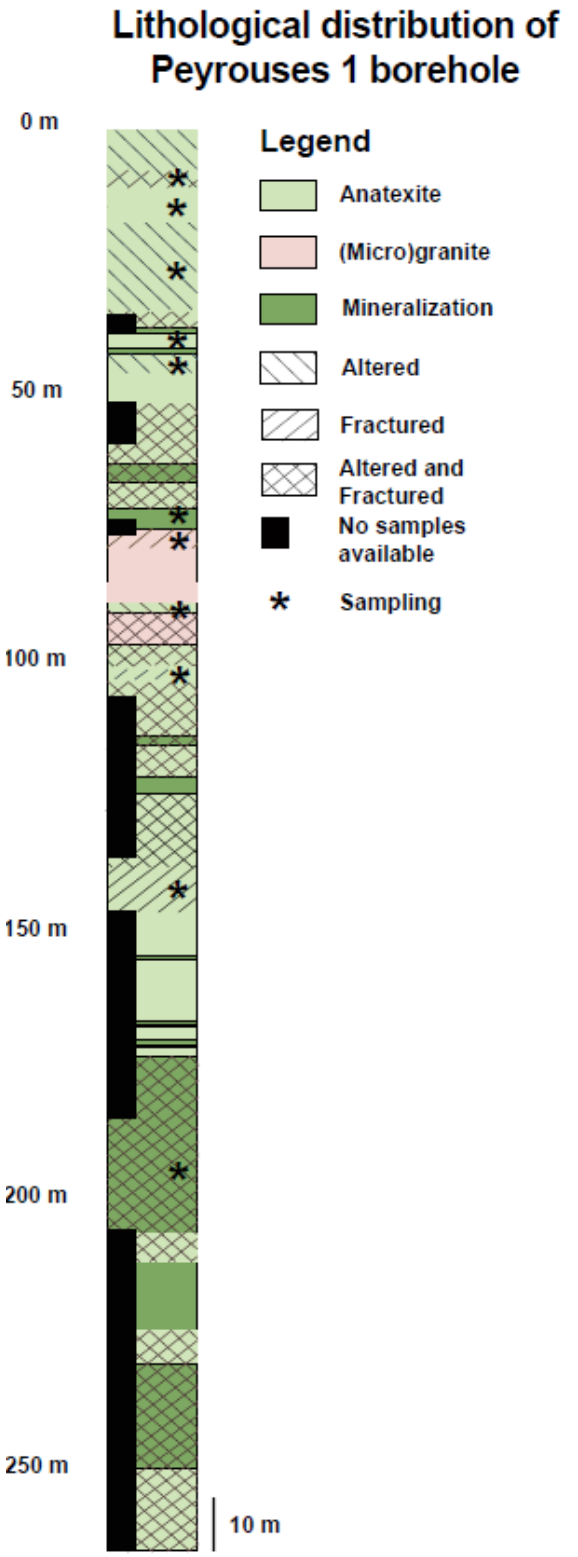

Figure 44 : Distribution of lithologies and location of the various samples taken from the Peyrouses 1 borehole. Mineralization consists of mispickel, pyrite, tourmaline, pyromorphite and galena. For the missing samples (in black on the figure), the description of the drilling done by BRGM in 1981 was used.

2.2 Laboratory observations and measurements

The samples used for laboratory measurements and observations were recovered from the Peyrouses 1 borehole (Fig 44), located within the PFZ (see Fig 41). These samples represent different facies: altered, fractured, altered and fractured, and intact facies (anatexite and microgranite). Thin-section observations on samples with different degrees of fracturing and alteration and at different scales help to characterize the petrology of the Pontgibaud hydrothermal system. 3D observations using a Phoenix nanotom microtomograph have been used at the Institut des Sciences de la Terre d'Orléans (ISTO). X-ray microtomography is a high-resolution, nondestructive 3D imaging technique (see Appendix 5). The samples were placed between a tungsten filament and a detector. During acquisition, the sample rotated 360° and the tungsten filament emitted X-rays onto the sample (using a voltage and current of 110 kV and 85 µA, respectively). The detector measured the attenuation of the emitted signal. A series of 2D images were produced, with pixel values dependent on the intensity of the emitted radiation and on the attenuation recorded by the detector. This attenuation is a function of the density and atomic number of the material through which the rays pass (Ketcham and Carlson, 2011). A 3D reconstruction of this object has been done, and each voxel reflects the average attenuation of the traversed material. However, the density contrast between two mineral phases may bias the information. A Beam-Hardening Correction (BHC) limits the loss of this information. After the reconstruction, the 3D volume was processed with the Volume Graphics VG Studio Max visualization software. This imaging technique provides high-resolution images (2.5 to 10 µm) and allows to understand how fluids can flow in these heterogeneous materials. X-ray microtomography is a common method used to characterize oil (Iglauer et al. 2013), uranium (Bonnetti et al. 2015), and geothermal reservoirs (Ohtani et al. 2000).

In order to quantify the heterogeneity of the system, permeability measurements have been performed at the Institute of Earth and Environment in Strasbourg (France) (ITES). For this purpose, 11 cylindrical samples (with a diameter of 25 mm

and length between 25 and 40 mm) were prepared from an intact sample, an altered sample, a fractured sample, and an altered and fractured sample. The crystal size of these samples was small when compared to their diameter, as is recommended for samples used for measurements of permeability (Heap, 2019). These samples were first oven dried under a vacuum at 40°C. Their connected porosities were calculated using the connected volume measured by a helium pycnometer (Micromeritics AccuPyc II 1340) and the bulk sample volume measured using digital calipers. Gas permeability was measured using a benchtop nitrogen parameter (see the schematic diagram in Appendix 6 (Farquharson et al. 2016; Heap and Kennedy, 2016)). All measurements were performed under a confining pressure of 1 MPa (samples were first left for 1 h at this pressure for microstructural equilibration) using the steady-state method. Volumetric flow rates were measured (using a Bronkhorst gas flowmeter) for six pressure differentials (measured using a Keller pressure transducer) to calculate permeability using Darcy's law and to check whether the Forchheimer and/or Klinkenberg corrections are required (for more details on this protocol, see (Heap et al. 2017; Kushnir et al. 2018). The 2D and 3D numerical modelling discussed below will use these laboratory data.

2.3 Numerical modelling approach

In order to understand the processes locating potential positive temperature anomalies and to estimate the position of the 150°C isotherm, numerical modelling of crustal scales has been performed. These models incorporate a set of field and laboratory data. This numerical approach is organized in two successive stages. The first stage is dedicated to 2D TH coupling numerical modelling. The second stage concerns the numerical modelling of the Pontgibaud hydrothermal system in 3D with THM coupling. Finally, the obtained results, and in particular the geothermal gradient and surface heat flux, were compared with field data, including resistivity data from Ars et al. (2019), which were not considered to build our numerical model.

2.3.1 Meshing geometry and boundary conditions of 2D TH Pontgibaud large-scale numerical modelling

For the 2D TH numerical modelling of the Pontgibaud large-scale numerical simulation, the mesh consists of 52,798 triangles with a size not larger than 25 m in the high-permeability zones and not smaller than 300 m in the low-permeability zones (Fig 45).

The average temperature at the surface was fixed at 10°C. According to regional data (see “Geothermal setting of the Pontgibaud area” section), a constant heat flux of 35 $mW.m^{-2}$ was imposed at the base of the model. The lateral borders of the model were thermally insulated. The use of such boundary conditions will be discussed in Chapter VI (Part 2). In addition, the use of flat topography will also be discussed in Chapter VI (Part 3).

The initial conditions of the model were defined from the stationary state obtained for the pure thermal conduction regime. At $t = 0$, the permeability were assigned to the different compartments, and the fluid flow was initiated. Considering the thermal relaxation time of the magmatic chambers (see above, Martel et al. 2013) calculations were performed up to a time of t_0 + 15,000 years.

For Darcy’s law, a no flow condition was imposed at the bottom and on both sides of the model, a surface pressure equivalent to atmospheric pressure ($P = 10^5$ Pa) was imposed at the surface and a positive pressure evolution with depth was adopted as the initial condition.

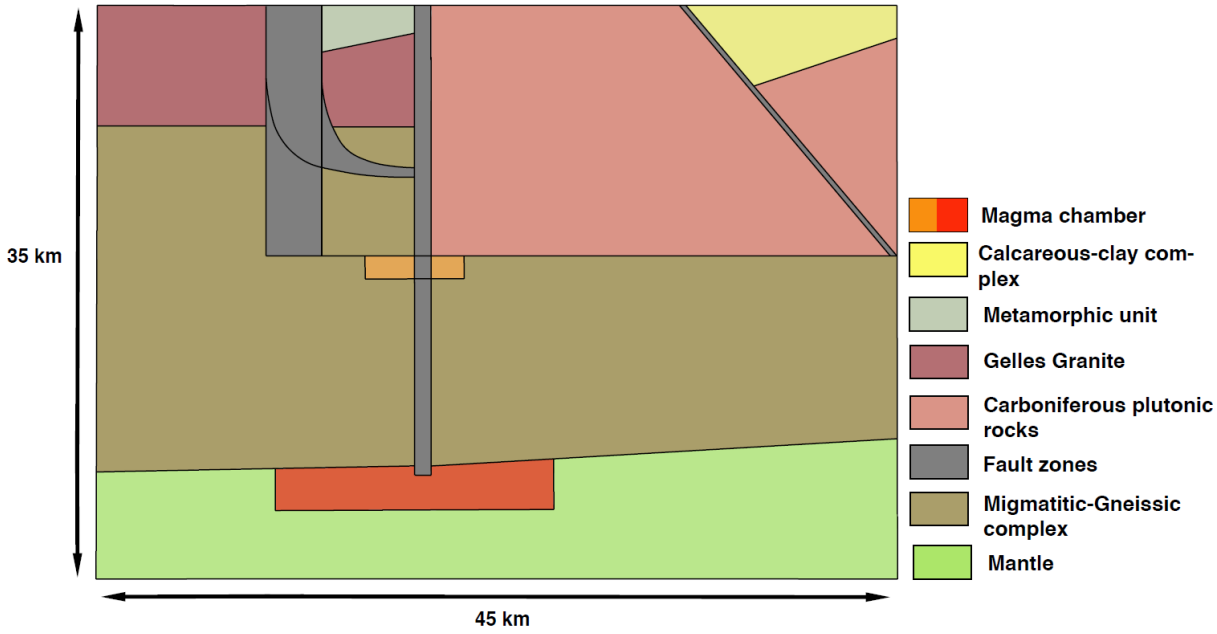

Figure 45 : Geometry studied by 2D TH numerical modelling. This simplified crustal scale geometry containing essential structural elements derived from field and geophysical data.

2.3.2 Meshing geometry and boundary conditions of 3D THM Pontgibaud large-scale numerical modelling

For the 3D THM numerical modelling of the Pontgibaud large scale numerical simulation, the mesh consists of 244,475 tetrahedra, with a maximum size of 200 m and a maximum size of 10 m in most permeable zones (Fig 46). The mesh is refined for the highest permeable zones as well as for fault and lithology intersections. Like the 2D TH models, calculation was performed up to a time of t_0 + 15,000 years, by considering the thermal relaxation of magmatic chambers (Martel et al. 2013).

One of the critical points in setting up regionally scaled mechanical models are the boundary conditions (Gunzburger and Magnenet, 2014; Reiter and Heidbach, 2014) that result from the far-field stresses. The overall stress orientation is often hinted from the integration of several measurements in a given region (such as well tests and GPS measurement). In our case, the present-day stress orientation in the

surroundings of the Pontgibaud CFZ is approximately N145° (see section « structural setting » above). As far as magnitudes are concerned, few or no indications usually exist, and our case is no exception. In most cases, numerical models include the boundary magnitudes as unknowns which are estimated through sensitivity analyses (Buchmann and Connolly, 2007) or inversion studies (Gunzburger and Magnenet, 2014). In our case, we propose to take advantage of in situ measurements from the Chassoles borehole located at 60 km south-east of Pontgibaud (Cornet and Burlet, 1992). This well was drilled for the "*Géologie Profonde de la France*" research program. The stress field has been determined by hydraulic testing. The well encountered only orthogneiss and intersected several subvertical fault zones at depths of 180 and 630 m. A total of 22 tests were run, nine between 340 and 470 m and 13 between 734 and 853 m. Many tests yielded fractures. At Chassoles, down to 7 km, the maximum stress is vertical but nearly equal to σ_H.

This stress profile has been implemented as boundary conditions for the 3D model of the Pontgibaud CFZ. The heterogeneities in rock properties and structural features affect the stress distributions (Yale, 2003), and the extrapolation of measurements to other locations and/or depths appears to be a strong assumption. Still, regarding the high number of unknowns and parameters in our model, we decided to keep these observations as inputs in our first computations for the sake of simplicity.

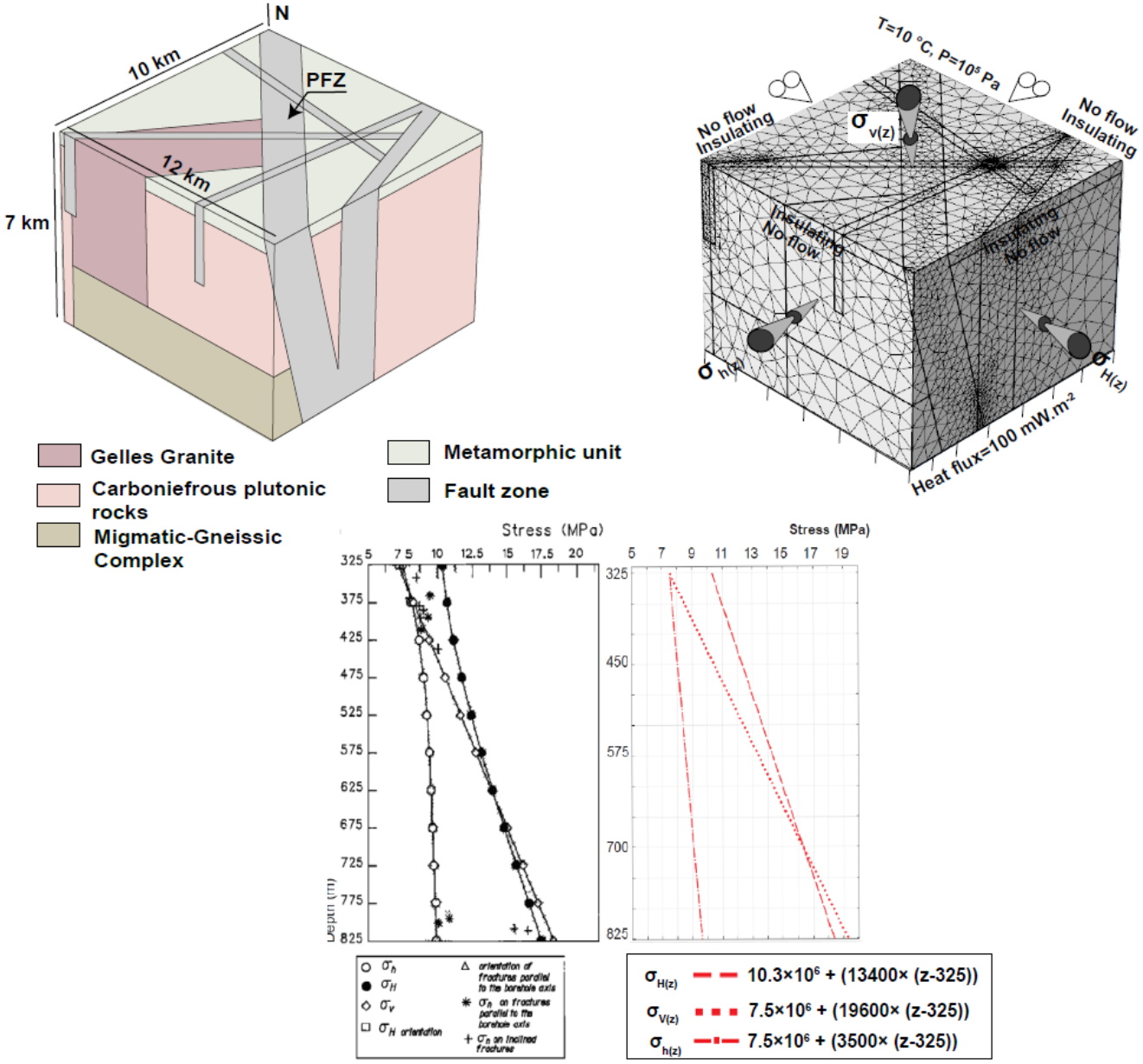

Figure 46 : Geometry, meshing, and boundary conditions for the 3D THM numerical modelling of the Pontgibaud CFZ. Stress profile of the Chassoles borehole (45.38°N, 3.09°E), from Cornet and Burlet, (1992).

3 Results

3.1 Structure characterization of the « La Sioule » licence

The « La Sioule » licence is widely affected by fracturing (see « Structural setting » section), and some episodes are directly attributable to mineralized structures. These first field observation aim to characterize the intensity of the deformation and the overall geometry of the structure present first at the Pontgibaud study area, and then within the Pontgibaud CFZ.

The North-South structures (Figure 48, A C, D, and H) represent fairly clear topographic boundaries (Fig 47 overview) and underline the axis of Pb-Zn mineralized veins. These N-S structures shift the topography by 300 m (see Appendix 7). The alignment of this axis is often interrrupted by transverse structures and masked by alluvium of the Sioule Valley, these North-South structures (Fig 48, C and D) underline a homogeneous alignment over 40 km. The dips of these structures vary between 60 and 90°.

E-W structures also mark the topography (Fig 48, E and K). With a dip between 60 and 90°, field observations and the geological map show an occurrence of these structures every 10 km in the southern part of the FMC and near the Sillon Houiller. The NW-SE (Fig 48, G, I and J) structures are quite frequent and often overlap the E-W faults without inducing significant offset.

NE-SW structural orientations are also present (Fig 48). The NE-SW (Figure 48, B, D, and F) structures can be seen widely on the geological map from the west of the Sillon Houiller to Limagne (Fig 48). They are particularly well expressed on the

Gelles granite. Mapping observations show that these faults are not too affected by N-S faults. The dip of these fault planes are mostly vertical.

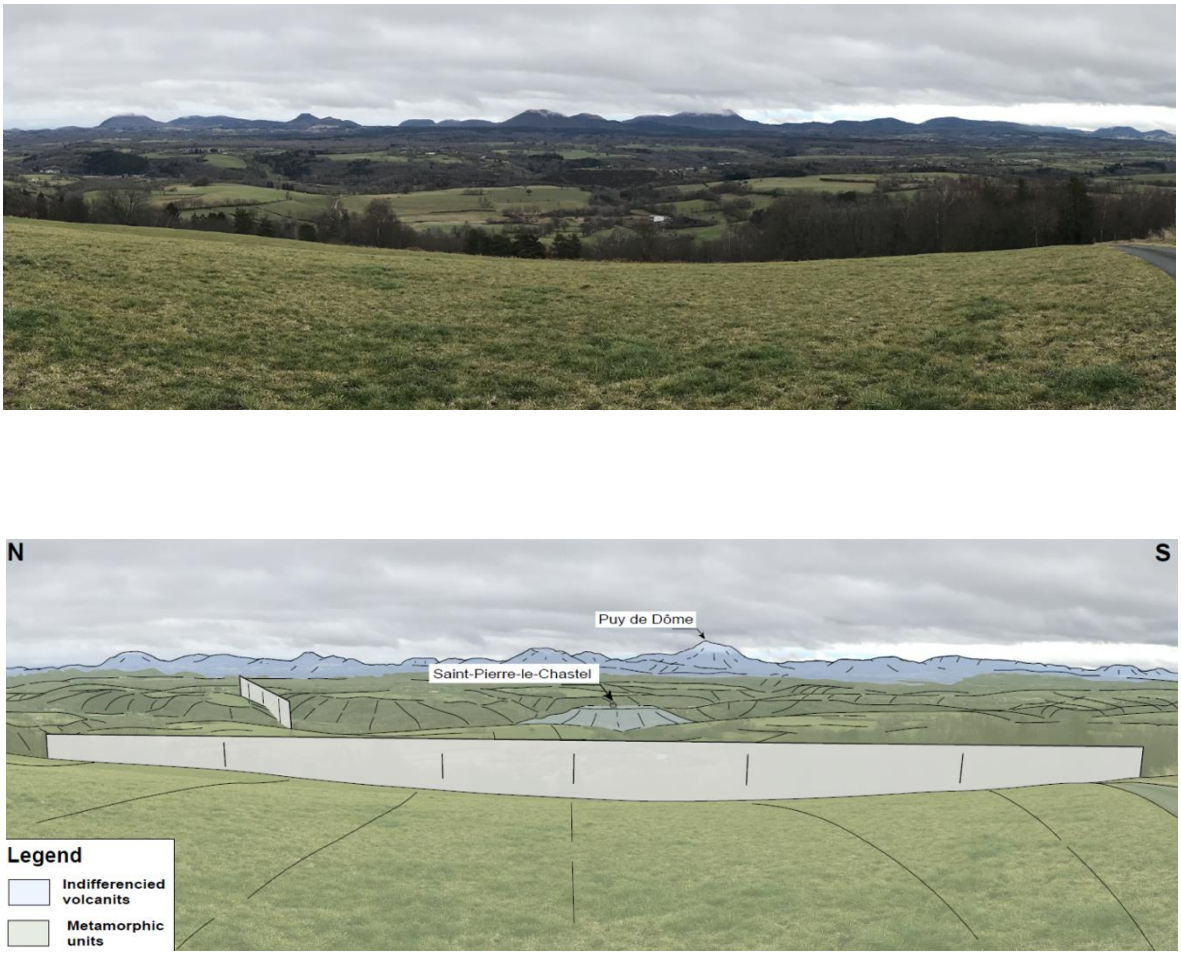

Figure 47 : Overview 1 (with and without interpretation) from the topographic tops of the Pontgibaud CFZ (see location Fig 48). The topographic offset is 300 m. N-S and NE-SW structures mark the topography. The Sioule River flows below the village of Saint Pierre-le-Chastel along a N-S axis. Metamorphic units are widely present in this area, and are partially covered by indifferenciated volcanics.

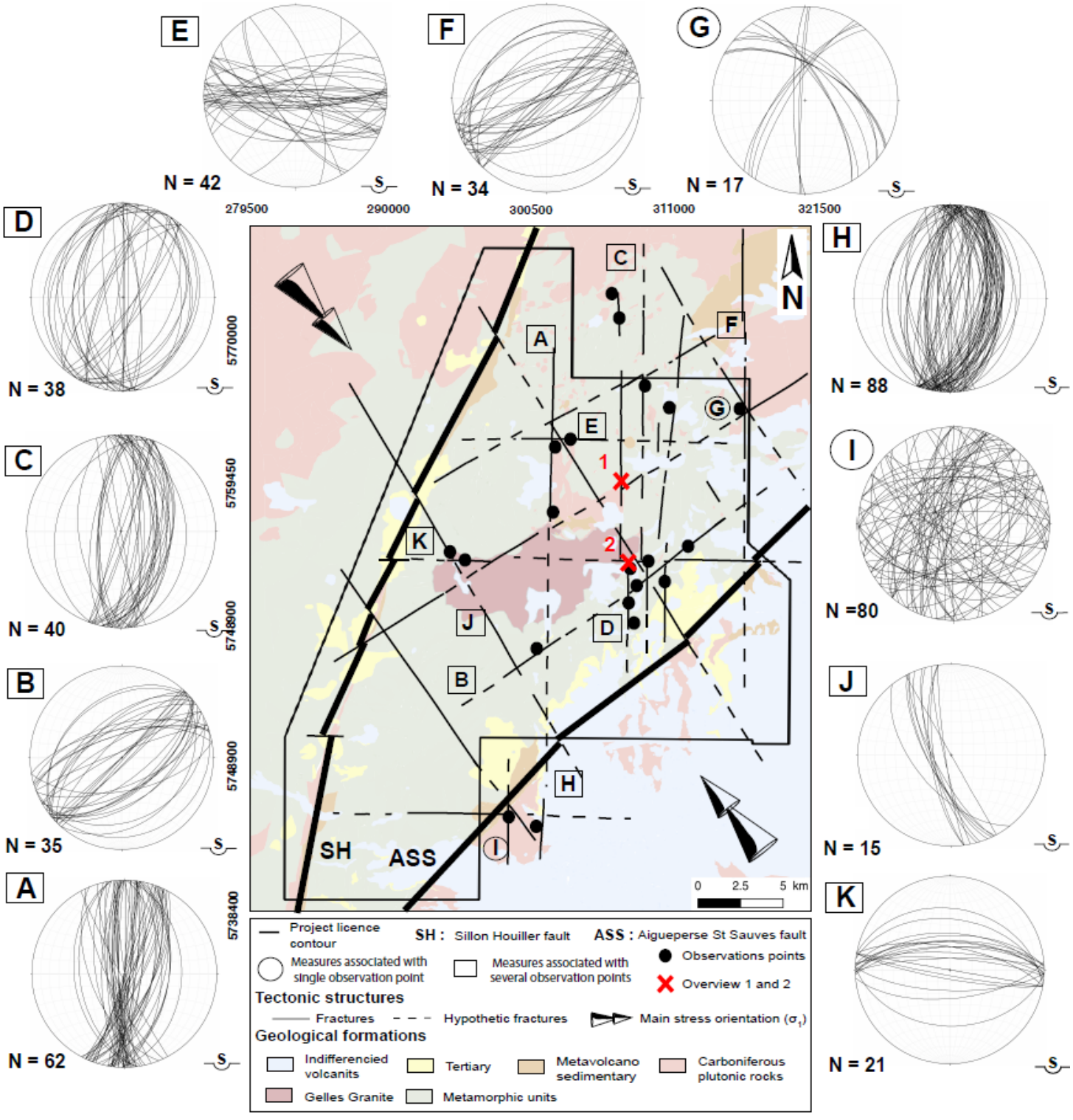

Figure 48 : Simplified structural map, showing the main and hypothetical fractures present in the « La Sioule » licence, in consistency with the Pontgibaud geological map (Hottin et al. 2000). The principal regional stress orientation are shown (Schmidt's projection on the lower hemisphere). Coordinate system: WGS84 Pseudo-Mercator EPSG: 3857.

E-W structures can be observed on the eastern part of the Gelles granite (see Fig 49). The Gelles granite is oriented E-W and is clearly intrusive in a metamorphic rock, mainly composed of gneisses and migmatites. At the outcrop, on the eastern edge, at the intersection between E-W and N-S faults, variations of intact and altered facies can be observed (Fig 49). Macroscopically, the intact areas of the Gelles granite have a distinctly coarse-grained texture.

Figure 49 : Overview 2. At the intersection between N-S and E-W structures, the Gelles granite presents succession of altered and intact facies. On this outcrop facies changes are observed every 20 m. Pictures and descriptions of these facies are detailed below

The intact zones are characterized by the presence of mega-crystals of feldspars, giving the rock a porphyroid texture (Fig 50). In the outcrop, the feldspars seem to have a clear planar orientation. Quartz, biotite and more rarely muscovite can also be seen. Cordierite and tourmaline have also been observed.

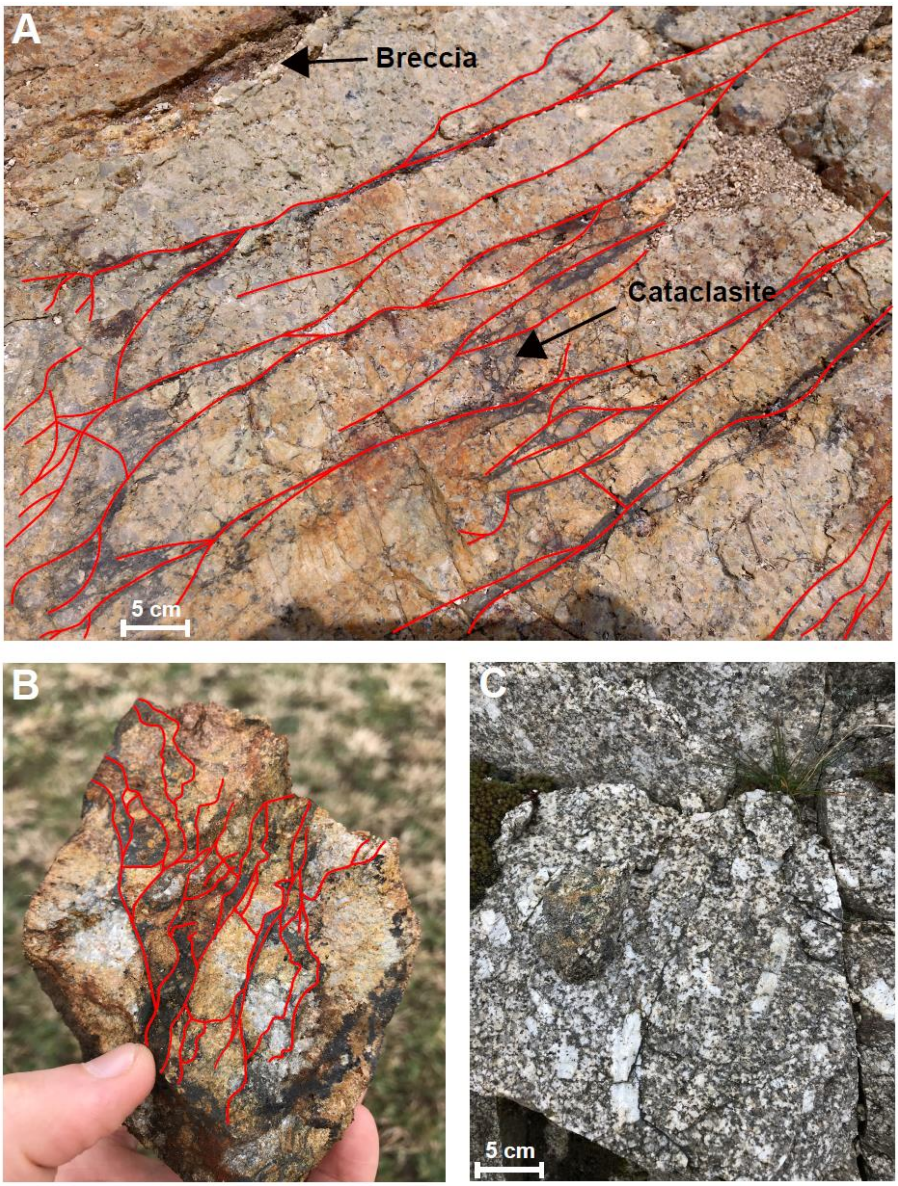

Figure 50 : Macroscopic observations of altered and intact facies at outcrop. The altered zones show breccias and catalists. Intact areas show coarse grains and mega feldspar crystals giving the rock a prophyroid texture (see text for more details).

The altered zones are crumbling, biotites are much less abundant and the feldpath crystals are dull and powdery (Fig 50A, 50B). Within these altered zones, mineralized and sealed cataclasites are observed. Observations with a binocular glass showed mineralized phases such as galena, pyrite, quartz-filled cavities (white quartz and smoky quartz), arsenopyrite. Rare cerussite and pyromorphite crystals were also observed. Marked in red in Figure 50B, the mineralizations appear to trace a dendritic network. Thin-section observations will allow us to define these networks at smaller scales, and to have a first overview of the voids that may be present. Before that, we will focus on the structures present within the Pontgibaud deformation zone.

3.2 Structure characterization of the Pontgibaud Fault Zone

Focusing on the Pontgibaud deformation zone, 126 new measurements of fault dips and orientations have been done. Three faults families have been identified. The first family comprises 67° ESE dipping normal N 10° trending vein beam faults (Fig 51a). With a surface thickness of 3 km, this normal fault zone has lowered the topography by 300 m eastwards. In addition, over the study area, the Sioule River surprisingly flows North-South over more than 10 km (appendix 7), and partly borders the vein network, before becoming meandering again. This north–south direction is also consistent with the main direction of the Limagne fault, which is located a little further east. Due to field data and geophysical arguments (see “Magnetotelluric data” section), the general geometry of the Pontgibaud fault zone could be regarded as a listric type. However, this hypothesis could be verified by coupling gravimetric, magnetotelluric and magnetic methods. The second and third fault families, both steep, intersect the Pontgibaud fault zone. The second family is formed of mainly dextral N 30° trending faults (Fig 51b), while the third family consists of sinistral faults that trend N 115° (Fig 51c).

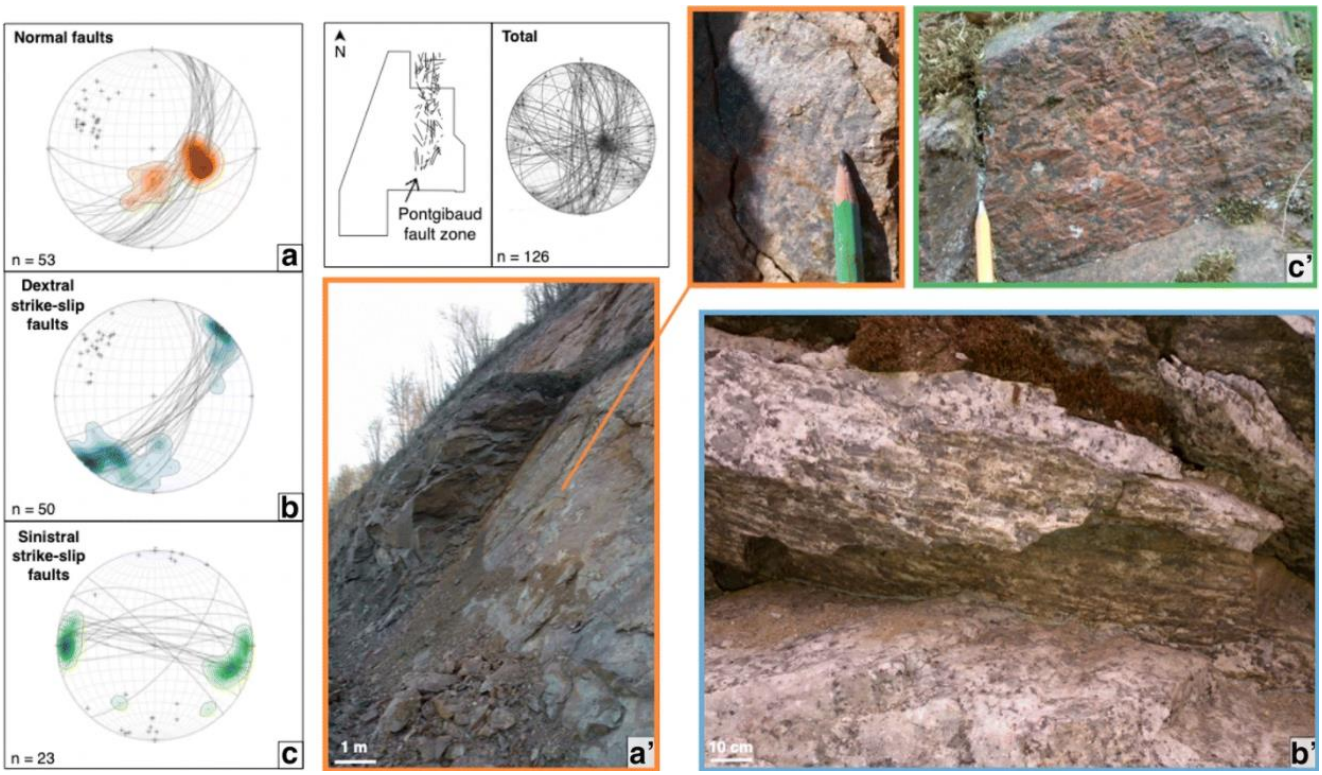

Figure 51 : Observation of the different lithologies and fault families present in the study area. a', c', Metamorphic series. b' Granite. Schmidt's projection on the lower hemisphere (a-c). Isodensity obtained with Stereonet.

3.3 Synthesis of fields observations and measurements

To summarize all field observations and data from the literature, a synthetic geological cross-section is shown in Fig 52. Its location corresponds to the geophysical profile (Fig 41) and it crosses the villages of Prondines, Ceyssat, and ends at the Limagne basin. This cross-section illustrates all the geological and geophysical fea-

tures detailed in the previous sections. Thus, the proposed listric geometry of Pontgibaud fault zone is associated with two other vertical fault families. The presence of springs within these structures is an indicator of present-day fluid circulation.

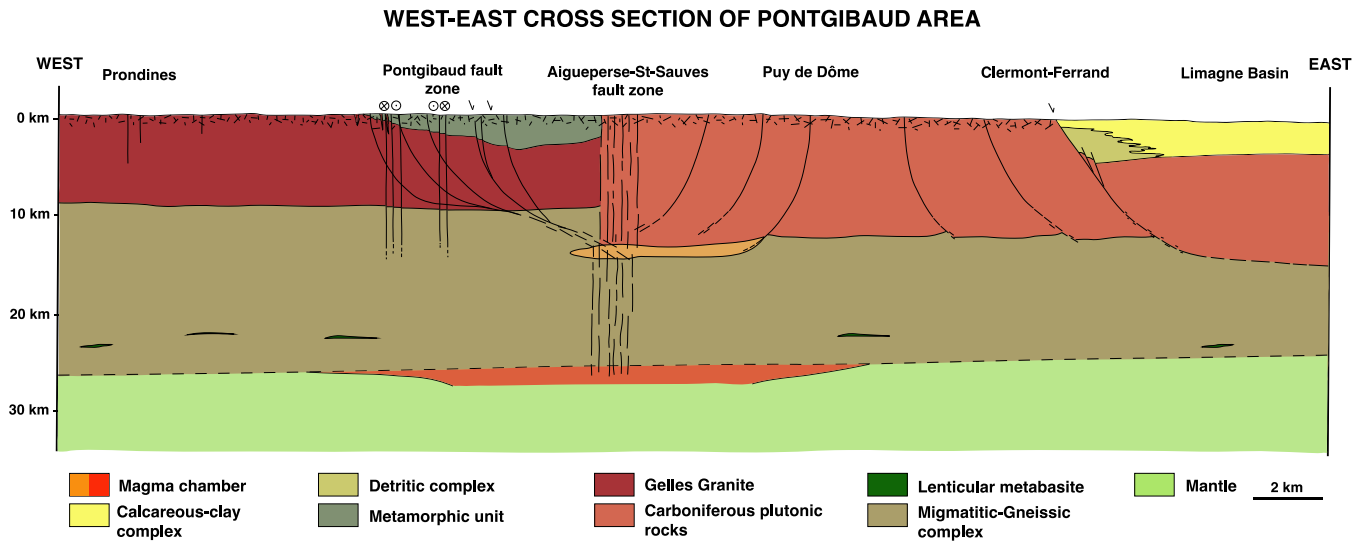

Figure 52 : Synthetic and simplified geological cross-section of the Pontgibaud area.

To sum up, the Pontgibaud CFZ is a large deformation zone (>3 km) extending over 40 km, mainly characterized by north-south structures, and crossed by E-W, NE-SW, NW-SE, and some other NNE-SSW structures.

Considering a first 3D drawing, the schematic representation of the architecture of the different structure's families could be the following – Figure 53.
Even if this figure is not to scale, it allows to represent, on a first drawing, the global architecture that will have to be considered in 3D numerical modelling. On the surface, we can see that this set is characterized by 4 families of structures having different directions and intersecting at shallow depth. Considering this fault intersection is an important element in geothermal exploration (Person et al. 2012). This aspect will be discussed in Chapter VI (Part 3). Moreover, in 3D, we will have to consider the general distribution of the different lithology present in our case study.

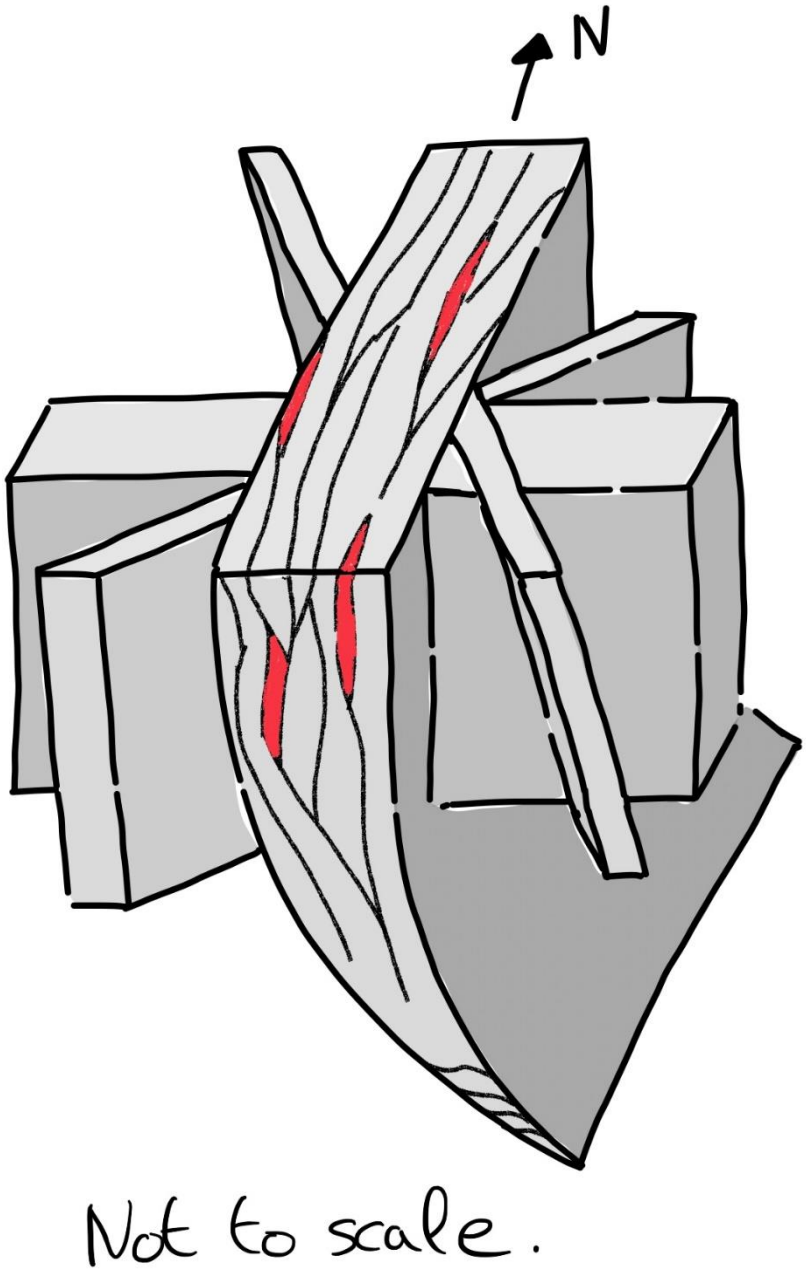

Figure 53 : First 3D drawing simplifying the architecture of the Pontgibaud fault network. All of these structures should be integrated into large-scale 3D numerical modelling.

As a whole, and represented with the different lithology, we find in addition to the Pontgibaud fault zone, 3 other structures familes. An E-W (in blue), a NE-SW family (in purple) and a NW-SE family (in green) (Fig 54). Geophysical and field data show that this rather vertical structure takes a root at depths of up to 10 km.

These field observations have been used to determine the 2D and 3D geometry of our Pontgibaud large-scale numerical model. Before that, we will visualize and quantify the permeability distribution of the Pontgibaud Fault Zone.

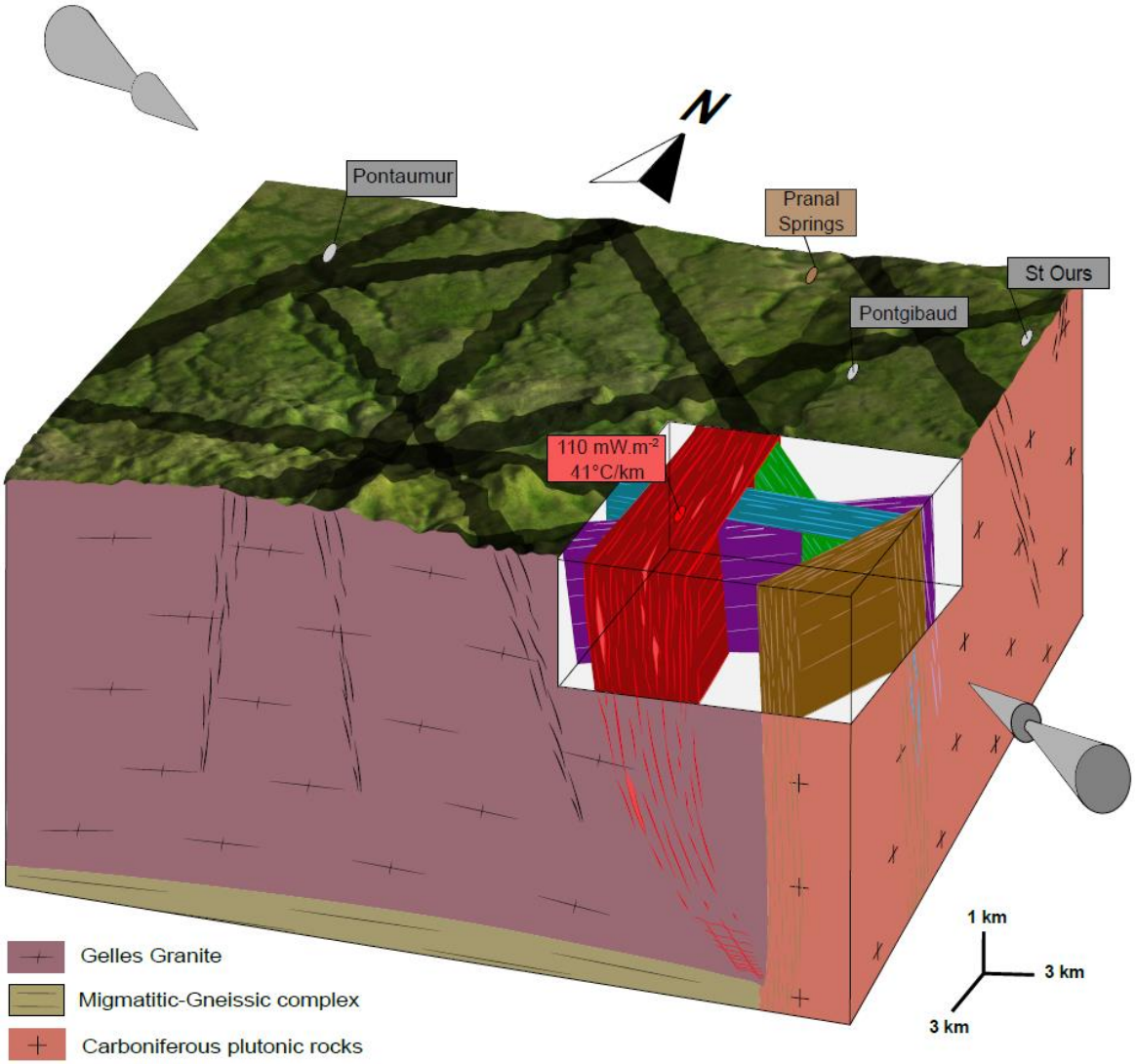

Figure 54 : Synthetic and simplified 3D diagram bloc, based on previous field observation and measurements.

3.4 Laboratory observation

3.4.1 Thin-section observations (2D observations)

The following section summarizes the main lihtologies present as well as the void space arrangement, for different scales of 2D observations. In order to make sure that the voids present are not caused by thin-section manufacture, we have highlighted the voids where secondary mineral phases have precipitated.

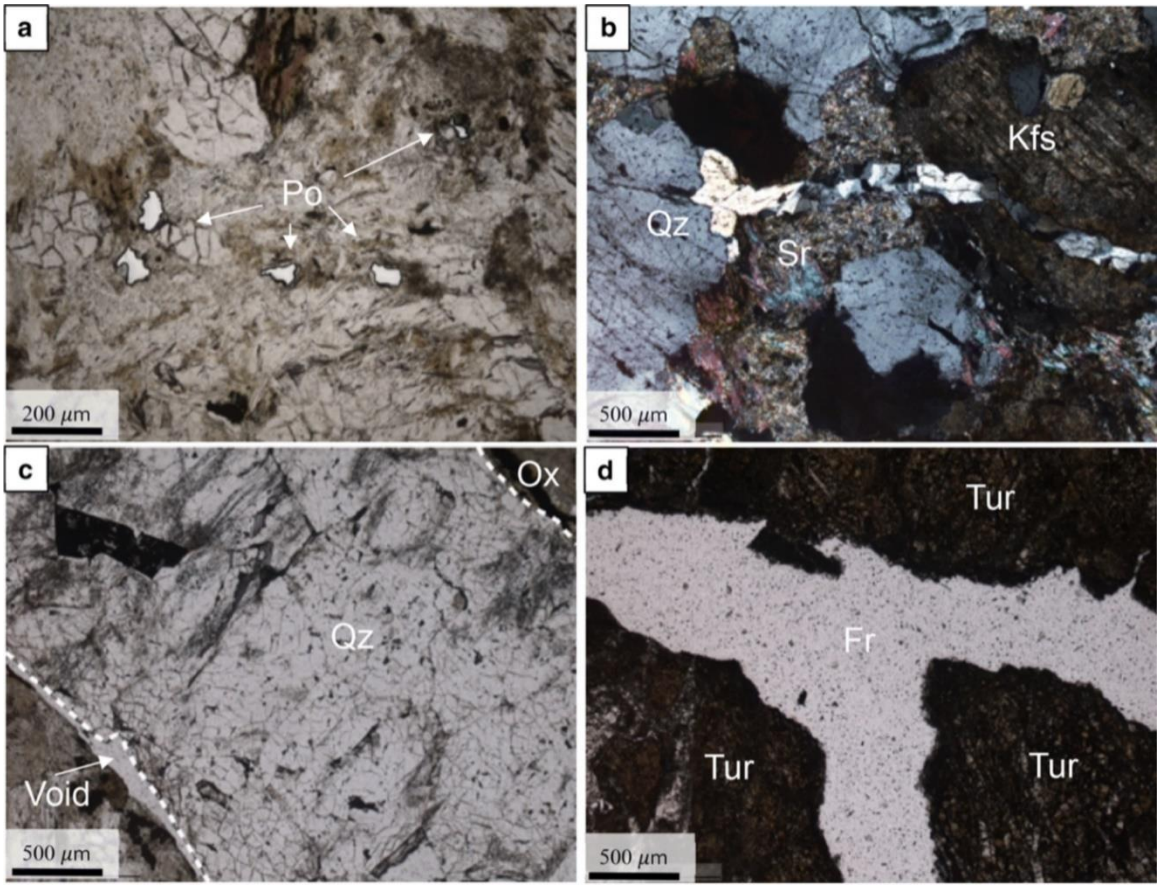

Figure 55 : Microscopic observations of thin section from the hydrothermalized zone. (a) Anatexite rich in veins. (b) Fractured anatexite. (c) Mineralized breach. (d) Prous breach. (Po) Porosity. (Qz) Quartz. (Void) Void. (Fr) Fracture. (Tur) Tourmaline. (Ox) Oxide. (Sr) Sericites (Kfs) Potassic feldspar.

First thin-section observations show fracture-rich and highly altered facies (Fig 55). These fractures are mainly filled with quartz, feldspar, phyllosilicates, ferriferous, pyrite and oxide minerals. If at the heart of these fractures the circulation of fluids appears difficult, the walls seem to be favorable for the circulation of fluids (Fig 55c). Fluid circulation within the fractures promoted the crystallization of secondary mineral phases. Tourmaline (Fig 55d), is observed in large quantities in all thin-sections. Fluid circulation also caused significant mineral dissolution (Fig 55b). This dissolution may be accompanied by a volumetric change (Launay, 2018). The volumetric change caused by alteration reactions can be calculated by considering each mineral phase and its stoichiometric coefficient.

$$\Delta V = 100.\frac{(\sum X_i^p.V_i - \sum X_i^p.V_i)}{(\sum X_i^r.V)} \qquad \text{Eq 28}$$

With ΔV (%), X_i^p and X_i^r the stoichiometric coefficients of the products and reactants of the phases present and V_i the molar volume of these phases. The calculation of the volume change was performed from the SUPCRTBL thermodynamic database (Zimmer et al. 2016) at 1 kbar and 450°C. The results of these volume changes per alteration are:

Table 2 : Some alteration reactions can favour the formation of available spaces for the circulation of fluids.

Alteration reaction	ΔV (%)
3 Feldspar-K + $2H^+$ = Muscovite + 6 Quartz + $2K^+$	-15.2
3 Albites + $2H^+$ + K^+ = Muscovite + 6 Quartz + 3 Na^+	-7.5
3 Biotites + $0.65O_2$ + 12.6 H^+ = 2 Muscovites + 3 Quartz + K^+ + $4.8Fe^{2+}$ + Mg^{2+} + $7.3H_2O$	-8.9

Mineralogical reactions are inextricably linked to changes in the chemical composition of rocks during deformation. The vast majority of mineral transformations that take place in deformed areas consume water. It is out of place here to detail the hydration reactions that depend on the composition of the protolith and the fluids present and on the pressure and temperature conditions.

The destabilization of potassium feldpaths, albite and biotite in favor of muscovites and quartz is the cause of volume loss (Table 2). These transformations can have consequences on the rheology of the materials, but especially on the capacity of the medium to let fluids circulate. These volume losses are sometimes directly visible in thin-section.

These first observations show that the fractures linked to the tectonic history drain the (paleo)fluids and produce alteration haloes at the edges of the mineralization. These aureoles are subject to significant mineral dissolution resulting in the formation of microporosity. Fractures and microporosity are available space favorable to the circulation of fluids.

Second thin-section observations show predominantly fractured and altered (Figures 56(b), 56(c), 56(d), and 56(f)). Quartz, feldspars, biotites, and muscovites are mainly found. There are also secondary mineral phases (such as tourmaline, pyrite, arsenopyrite, scorodite, and sericite) and accessory minerals (such as apatite and zircon). The least altered and unfractured sample is shown in Figure 56 (a) (LPA view). Quartz is most often xenomorphic and can form clusters of small crystals or develop over a wide range with an automorphic tendency, giving the rock a porphyritic texture. Biotite is also observed and generally automorphic and shows an onset of chloritization. We also observe the polysynthetic macle of plagioclase in Figure 56 (a) (LPA view).

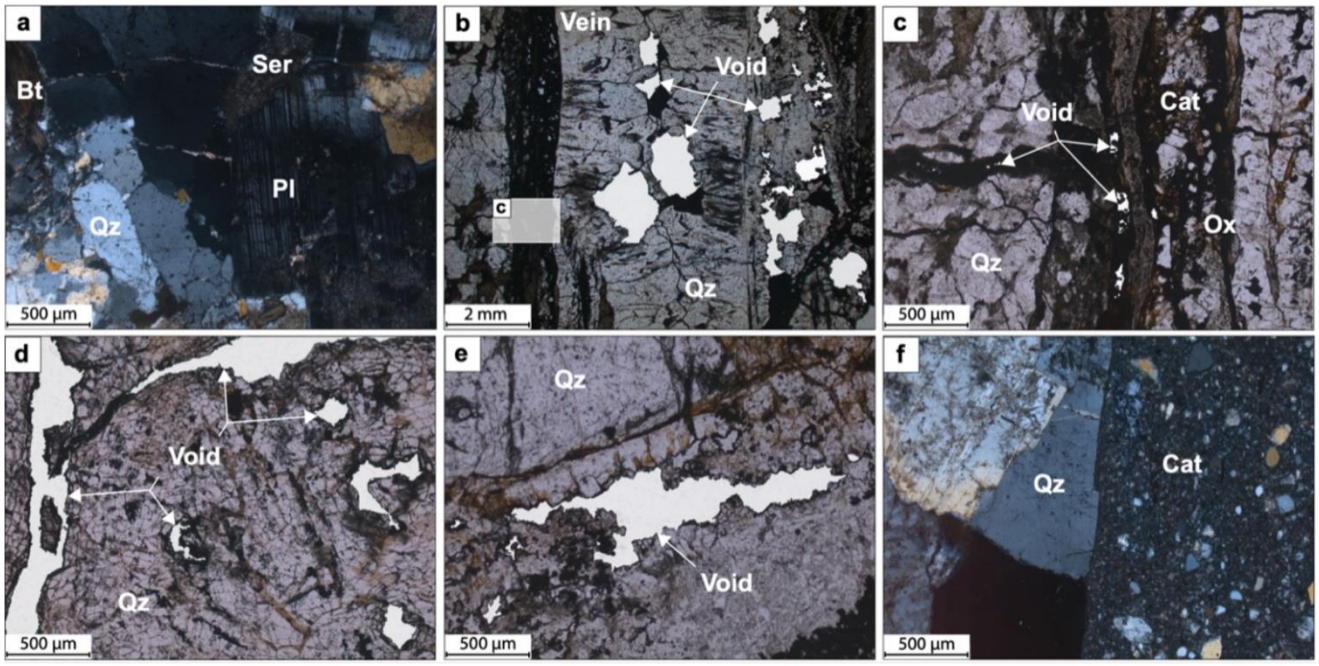

Figure 56 : Facies, textures, and composition details of the Pontgibaud hydrothermal system. (a) LPA thin-section view of least altered and unfractured samples. Others (b–e) show altered and fractured facies which are much more present in the samples. (c) is a zoom of a part of (b) and shows voids present at smaller scales. (f) Crosspolar thin-section view of cataclasite. Abbreviations from Whitney and Evans, 2009: Pl: plagioclase; Bt: biotite; Qz: quartz; Ser: sericite. Other abbreviations: Cat: cataclasite; Ox: oxyde. The thin section come from samples retrieved from the Peyrouses 1 borehole, located within the Pontgibaud CFZ (see location in Fig 41).

Within these altered and fractured facies, voids are present within cores of quartz mineralization (Figure 56(b)) but also at the walls of these mineralizations (Figures 56(b) and 56(c)). While some fractures have voids through which fluids can flow (Figure 56, (d) and (e)), other fractures are completely filled with clays, secondary mineral phases, and/or oxides. In addition, fractures can also be cemented by cataclasites (Figure 56(f)). These cataclasites consist of angular quartz clasts, plagioclase, sericite clays, and some calcites. Due to their similar petrological properties, most of these angular clasts should originate from the basement.

Most voids and secondary mineral phases appear to be associated with the development of fractures and cracks. Their interconnection could serve as potential drains for fluid circulation. The architecture of this interconnection at different scales could have a key role on the ability of the system to allow fluids to circulate.

Figures 57(a)–57(d) show images of the same sample but at progressively smaller scales (from 2 mm to 50 µm). These zoomed images are focused at the core of a fracture network in order to understand the spatial distribution of voids in the central part of the fracture network. Figures 57(e)– 57(h) again represent the same sample but at progressively smaller scales (from 500 µm to 50 µm). These zoomed images are focused at the extremities of a fracture network in order to see how fractures and pores spread to the extremities of these networks.

At a scale of 2 mm, Figure 57(a) shows macroscopic voids. They are distributed within the quartz vein and also at the walls of this mineralization. The secondary minerals and other smaller voids appear to form a network of fractures (red line) that extend away from the quartz vein, forming a dendritic network. At a scale of 500 µm (Figure 57(b)), other voids can be seen, still marked by secondary mineralization, which also follows the dendritic fracture network. By increasing the zoom again, we observe voids (Figure 57(c)) that we could not distinguish in Figure 57(b). These voids are still present within this dendritic network and are still marked by secondary mineralization. By increasing the zoom again, up to 50 µm, we still notice voids that we could not distinguish at the previous scale. These voids also follow a dendritic pattern. We find an interconnection of fractures at different scales, which form a dendritic fracture network. The precipitation of secondary mineral phases inside this dendritic fracture network shows that fluids have circulated.

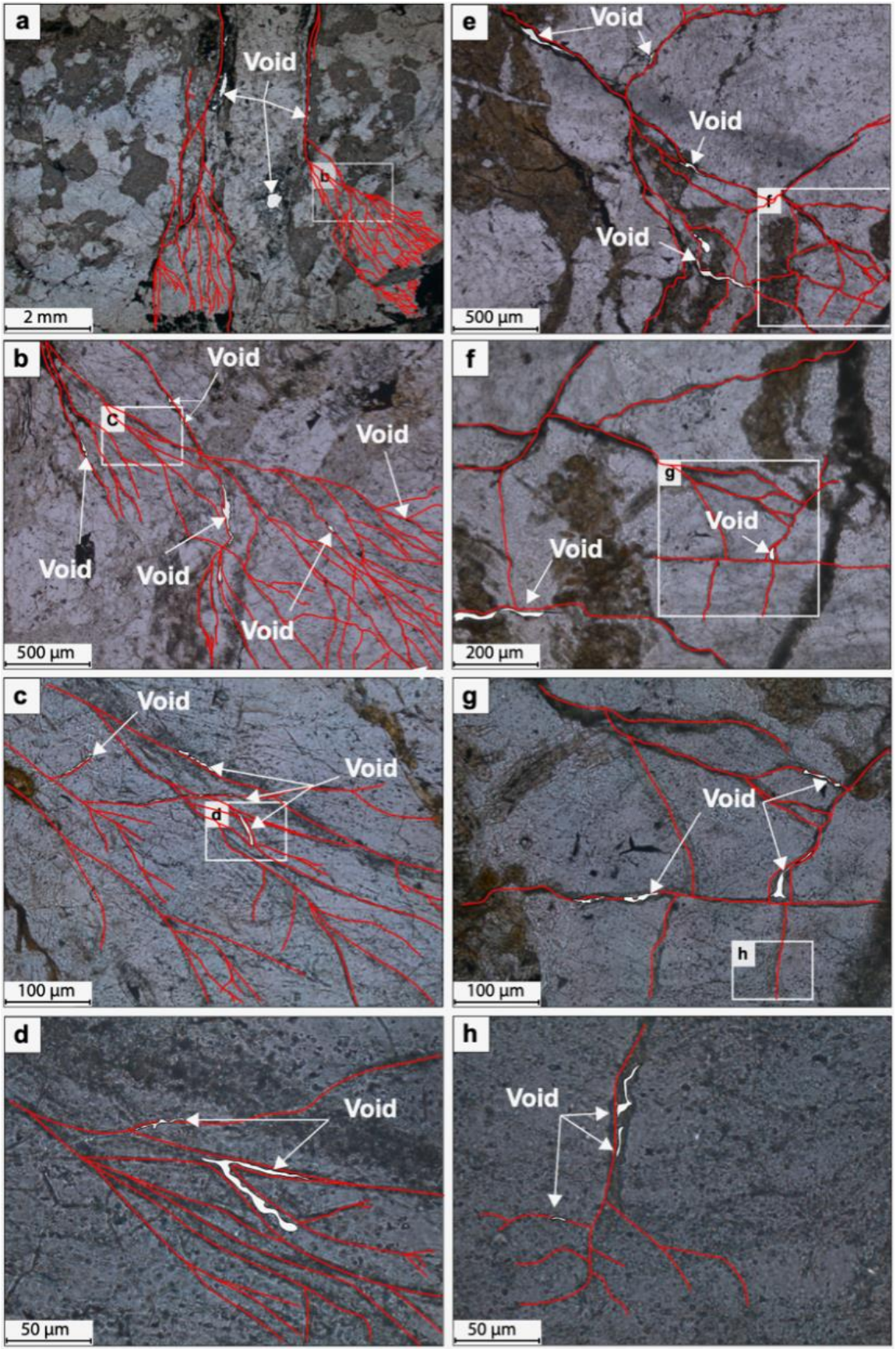

Figure 57 : Fracture design for two samples ((a–d) and (e–h), respectively) and for smaller observation scales. Fractures underlined by red lines are marked by secondary mineral phases (mainly tourmaline and oxyde) and voids.

Figure 57(e) shows another sample with a fracture network organization identical to Figure 57(a). Fractures marked by secondary mineralization, or by the presence of voids, appear to propagate spatially. By zooming in on Figure 57(e), we find voids that we could not distinguish previously (Figure 57(f)). These voids seem to follow the fractures and are also marked by the presence of late mineralization. Zooming in again on Figure 57(h), we now see a distribution of fractures that was not visible in Figure 57(g) and with an architecture not yet observed. This propagation of fractures across the box is in the form of rectangular drainage patterns (Figure 57(h)). These flow patterns are widely present in natural drainage systems. These observations give us an overview of the spatial representation of the fractures and voids. However, the ability of fluids to flow through the hydrothermal system depend on the connectivity of these fracture and micro-porosity. Three-dimensional imaging is required to qualitatively estimate the connectivity of these microstructural element. We will now see if these structures are connected in 3D.

3.4.2 X-Ray Microtomography Observations (3D observations)

The reconstruction and image processing of fractured and 3D voids in sample taken from the Pontgibaud CFZ (see location Fig 41) are shown in the following two figures. The first results (Fig 58) show the full sample with a voxel resolution of 25 µm. It is characterized by a matrix (grey in Fig 58a) and by fractures (yellow and red in Fig 58a). Two phases are present within these fractures. The red phase characterizes the mineralization of the fracture. Thin-section observations on this sample showed that this fracture is filled with lead sulphides.

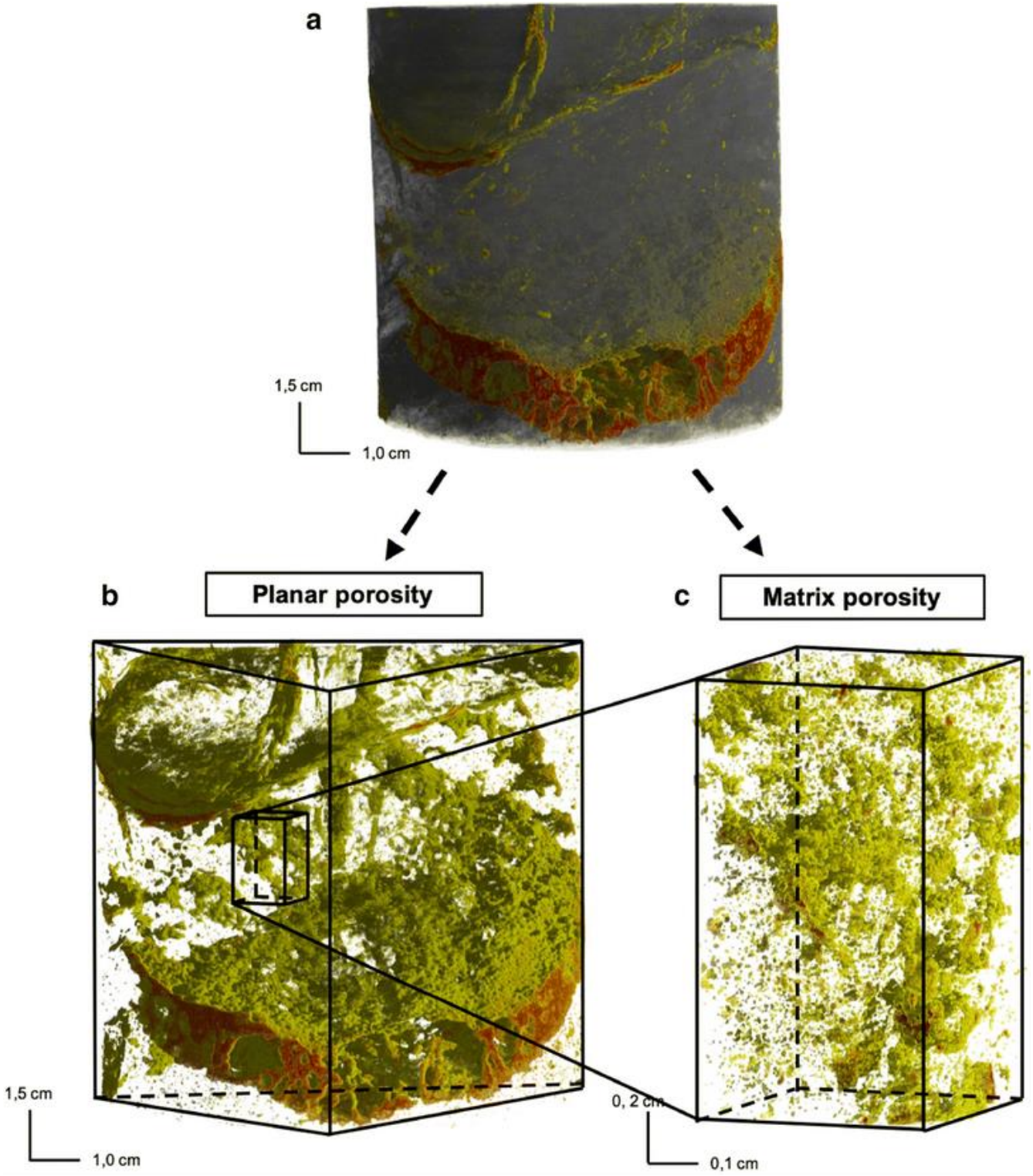

Figure 58 : Three-dimensional observations of the planar and matrix porosity of one sample taken from the Pont-gibaud fault zone. The red color of figures (a), (b), corresponds to mineralization (lead sulphides). The yellow color of figures (a), (b) corresponds to the planar porosity located on the fracture walls. The yellow color of figure (c) could correspond to the matrix porosity. The resolution of figures (a)-(c) is, respectively, 25, 25 and 4 µm.

The yellow phase represents the planar porosity (i.e., fractures). The processing of this image (Fig 58a) made it possible to isolate these fractures (Fig 58b) and qualitatively characterize the connectivity of the planar porosity. The three-dimensional visualization (Fig 58b) shows a high density of fractures. These fractures are distributed heterogeneously in space. This three-dimensional arrangement promotes connectivity of the pores located at the fracture walls (yellow in Fig 58b). Because a visualization of the matrix porosity (Fig 58b) was not possible at this resolution, due to the characteristic pore size, a smaller volume of this sample was analyzed with a resolution of 4 µm in an attempt to detect and segment the potentially connected pores. The result of the analysis and processing of the sample is given in Fig 58c. Coupling thin-section (2D) and micro-tomography (3D) observations highlight altered planar (i.e., fractures) and matrix (i.e., pores) porosities partially filled with secondary minerals.

The second results show a sample characterized by a fractured part as well as matrix part (Fig 59). Samples were cored at the edge between the fracture and the matrix (Fig 59b), as well as in the matrix (Fig 59c, Fig 59d)
The fractures are shown in red (Fig 59 (b)), and the voids are shown in yellow (Figures 59b–59d). The fractures extend over the entire length of the sample and are heterogeneously distributed (Figures 59b–59d) in space. With a resolution of 10 µm, this 3D illustration of a complex architecture of the fracture network shows an interconnection of the voids present in these fractures (Figure 59b) that could facilitate the circulation of fluids.

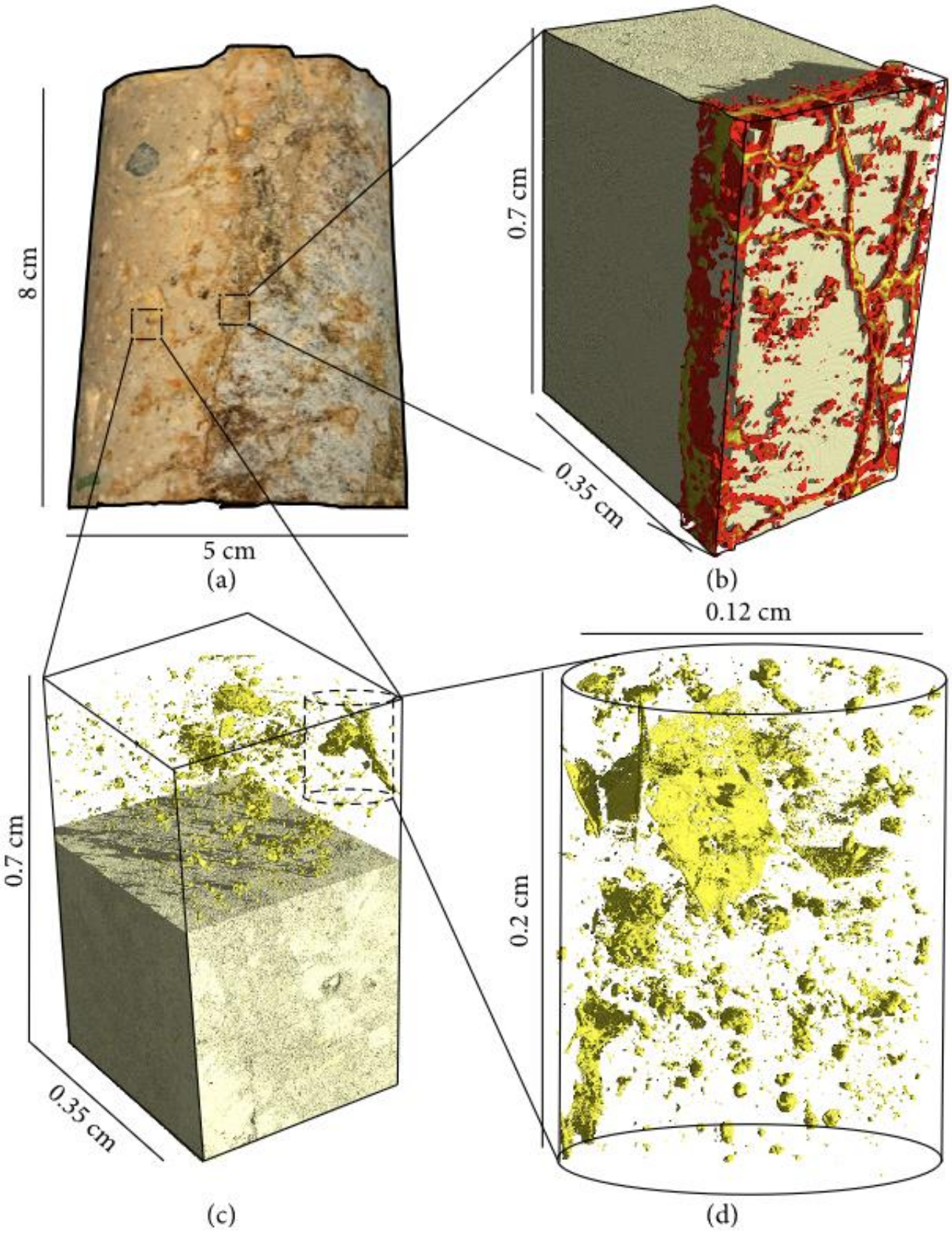

Figure 59 : 3D reconstruction of the matrix and fractures of a sample from the Peyrouses 1 borehole (a), (b), (c), (d). Fractures are shown in red and voids in yellow. The resolution of these images is 10, 10, and 2.5 µm ((b–d), respectively).

The 3D visualization of the matrix (Figure 59c) highlights the voids with a resolution of 10 µm. At this resolution, one observes globular clusters that appear to be interconnected. With a finer resolution of 2.5 µm, we can see more pores present in the matrix (Figure 59d). This resolution allows us to confirm the presence of voids that form a planar structure.

Thin-section (2D) and X-ray microtomography (3D) observations allow us to observe the 2D and 3D architecture of the fracture networks and the distribution of pores at different scales both within the fracture networks and in the matrix. The porous flow structures of the Pontgibaud hydrothermal system have multiple scales and a nonuniform distribution of the space available for fluid circulation. The anisotropic nature of the distribution of permeability in the different dimensions of space has thus been quantified by measurements of permeabilities and connected porosities.

3.5 Laboratory measurements

3.5.1 Porosity and Permeability measurements

The data show that there is a general trend of increasing permeability as a function of increasing porosity (Figure 60). Connected porosity values range from 6 to 22% (Figure 60). In most cases, the altered samples (with and without fractures) have the highest connected porosity values (around 20%), and the intact samples have the lowest porosities (between 6 and 8%). Permeability values range from 2×10^{-18} to 1×10^{-12} m^2. Altered samples with fractures have the highest permeability values (between 10^{-13} m^2 and 10^{-12} m^2). Samples that are either altered or contain a fracture are characterized by intermediate permeability, between 10^{-16} m^2 and 10^{-14} m^2.

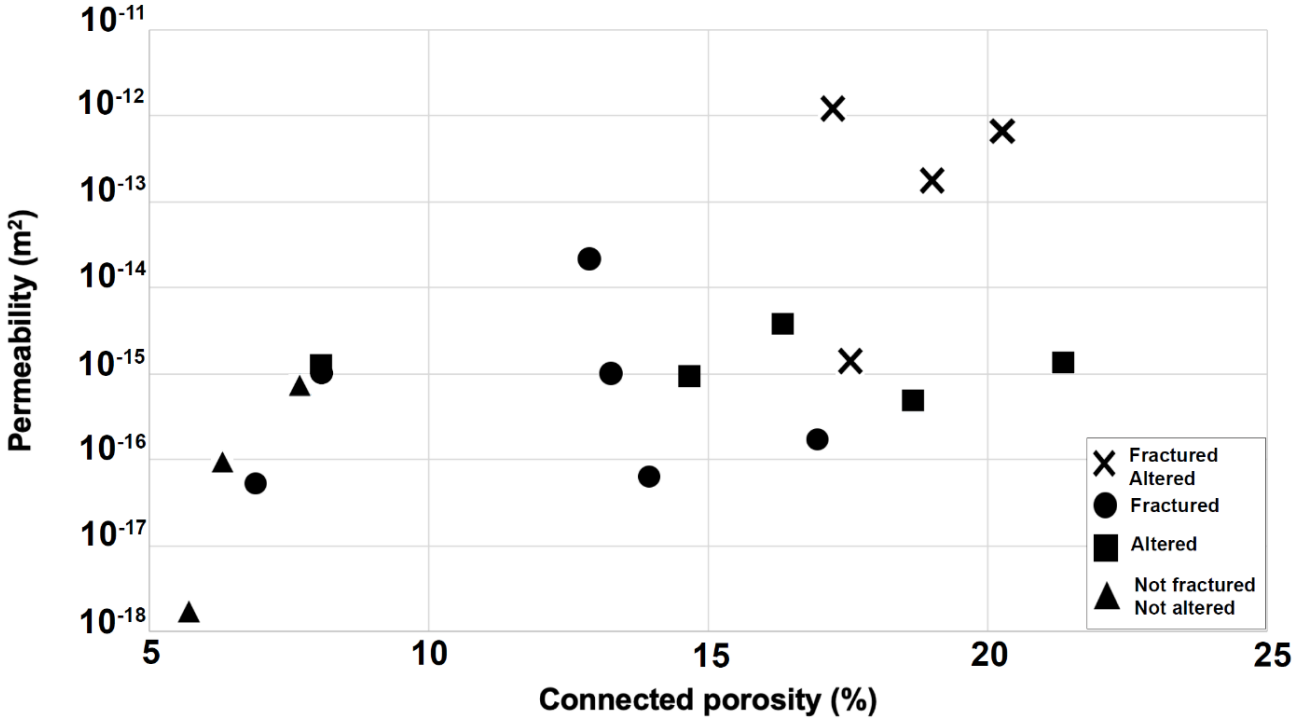

Figure 60 : Connected porosity and permeability measurements on samples taken from the Peyrouse 1 borehole (identical to those used for 2D and 3D observations). The intact samples have the lowest permeability and connected porosity value. Conversely, the altered and fractured sample has the highest value of permeability and connected porosity. These purely qualitative degrees of alteration and fracturation are based on macroscopic and microscopic observations and three-dimensional visualization by X-Ray micro-tomography analysis. (Protocol Heap and Kennedy, 2016. For more details, see Chap V, part 2 "Materials and Methods").

To summarize the three laboratory above-described results suggest that the permeability is increased by the presence of system-lengthscale fractures and alteration (Fig 60). The relatively high permeability of the measured samples (the permeability of granite can beas low as 10^{-22} m^2; Meredith et al. 2012), suggest that fluid flow within the matrix could also be significant, alongside large-scale fractures and fracture network.

3.6 Synthesis of field and laboratory observations and measurements: an introduction to large-scale numerical modelling

The aim of these field and laboratory approaches was to provide additional information for understanding a hydrothermal system in a fractured basement context. Geophysical data and structural measurements suggest that the Pontgibaud fault system is connected to the Aigueperse-Saint-Sauves fault system. The Pontgibaud fault system, associated with sub-vertical faults, concentrates a high density of fracturing and markers of (paleo)fluid flow.

All the observations have allowed the characterization of fractured, altered and intact lithologies. These observations defined a permeability that varies in the space of a crustal fault zone. These variations are found at different scales. At the outcrop scale, variations in intact and altered facies occur every 20 m. At the sample scale (5 cm), altered facies show breccias and cataclasites and mineralizations draw dendritic networks, in which voids are observable. Dendritic networks are also found in samples observed in thin sections (2 mm - 50 µm) and by X-ray micro-tomography (10 µm - 2.5 µm). The permeability and connected porosity were quantified and the ranges obtained are respectively from 2×10^{-18} to 1×10^{-12} m^2 and from 6 to 22%.

These measurements tend to confirm the ability of the system to allow fluids to flow. However, the results from the permeability measurements vary by six orders of magnitude. These variations will have a direct influence on the capacity of the system to let fluids circulate, and therefore on the thermal redistribution within the crust. Consequently, the integration of results from field observations, laboratory measurements and thermo-barometric data into numerical modelling will make it possible to test the influence of permeability on the circulation of fluids in this fault system.

In addition, the influence of previously identified control factors (dip, stress intensity, stress direction) on fluid flow in the same system can be tested.
We will attempt to synthesize these previous results, and to incorporate permeability variations into the numerical modelling. We will then proceed to large-scale numerical modelling.

3.6.1 Field, thin-section and X-Ray microtomography observations for permeability spatial variation (X, Y)

When examining different outcrops of the Pontgibaud Crustal Fault Zone, all lithologies show a large range of facies from unaltered and undeformed rocks to altered and/or fractured rocks. Breccia, fractured zones, cataclasites and mineralized veins are noteworthy (see Figure 61). These mineralizations are markers of the paleo-circulation of fluids. Samples were acquired from the "Peyrouses 1" borehole located within the Pontgibaud fault system (see Figure 61). Microstructural observations made on thin sections of these samples mainly show fractured and altered facies. Voids are located within the fracture networks (present in red, Figure 61). Some of these fractures are totally sealed, and therefore may provide barriers to fluid flow, while others show voids, thus conferring a potential permeability to the system. We therefore observed evidence for potentially high- and low-permeability zones within the fault system.

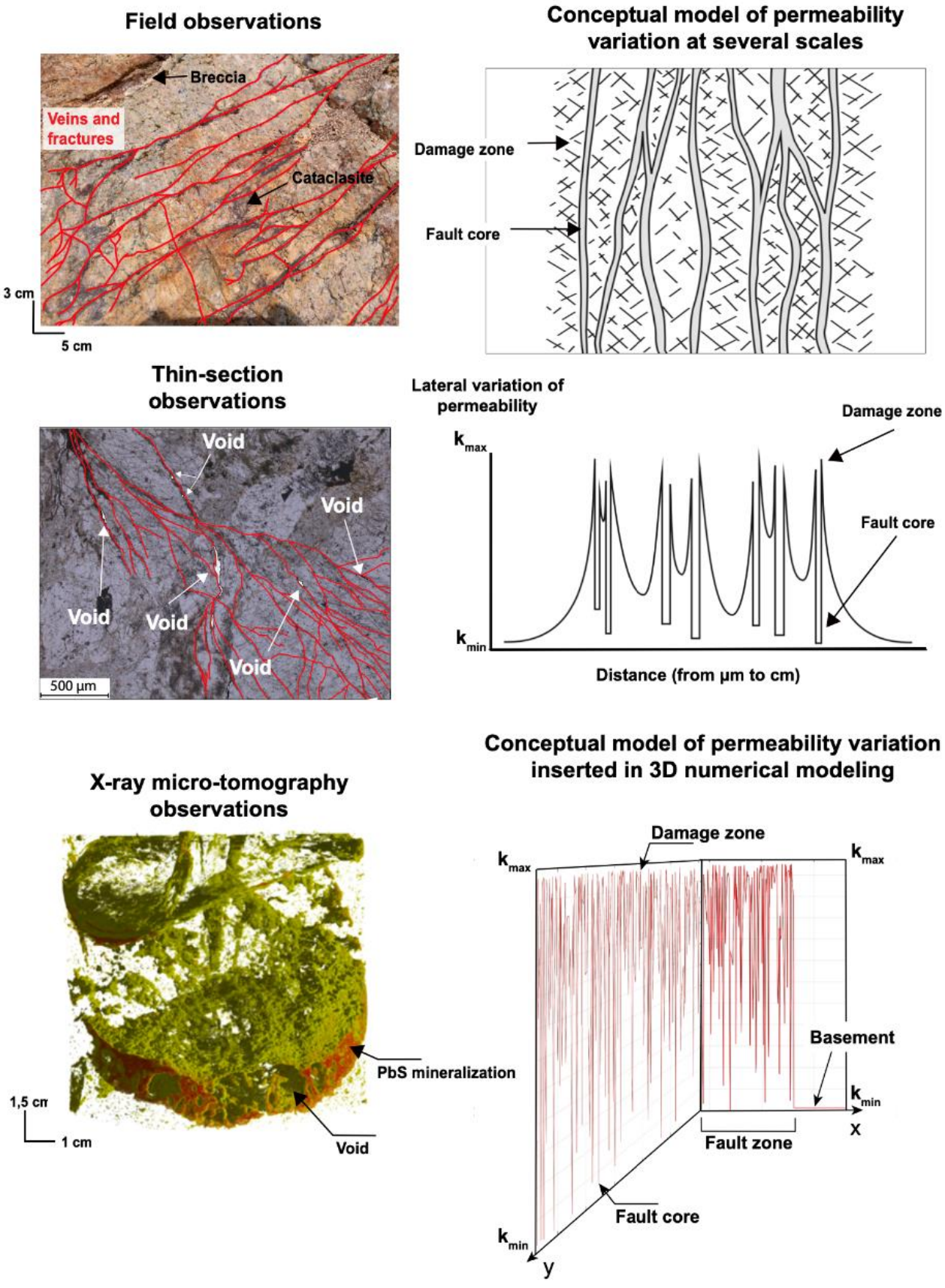

Figure 61 : Field and laboratory observation (left). Incorporation of the multiple fault core conceptual model (Faulkner et al. 2003; 2010) within numerical modelling done with Comsol Multiphysics™ (right). The resolution of the X-ray micro-tomographic image is 10 µm.

Secondary mineralization is present at the borders of voids, thus ruling out the possibility of an anthropogenic origin of these voids during the manufacturing process of the thin sections. At this scale of observation, all the fractures seem to form a dendritic network. This type of network is largely detailed in the literature (Reis, 2006; Lorenzini et al., 2011) and would be present in systems with intense fluid circulation (Bejan and Lorente, 2006).

In order for fluids to circulate, it is necessary that these voids are connected in the three dimensions of space. In order to verify this, the same samples were scanned and analyzed by X-Ray computed tomography at the Institute of Earth Sciences in Orleans (ISTO). The 3D observations (see bottom left in Figure 50) show, in yellow, the walls of mineralization in which some voids are taken into account and in red the mineralization (here galena (PbS)). The presence of voids is marked at the heart of some mineralization and at the levels of the mineralization walls. Moreover, these planes seem to be connected in the three dimensions, thus potentially facilitating the fluid circulation.

The conceptual model of Faulkner et al. (2003) describes damage zones (high permeability zone) and fault cores (low permeability zone). Considering the close correspondence between the variations in potential permeability of the different observations made with the conceptual model of Faulkner et al. (2003), we propose to integrate this permeability variation into our numerical models along the two horizontal axes, x and y (see Figure 61). Equations 24 (Chapter III) include a lateral variation of permeability within the fault zone in order to virtually reproduce the high permeability zones (damage zones) and low permeability zones (fault cores). While this model appears consistent with the model of Faulkner et al. (2003), other conceptual models of permeability variations in a fault zone may exist (Mitchell and Faulkner, 2012). The latter seems to be better suited to our field data. If the variations along the x and y axes could be constrained, variation along the z-axis and

quantification of this range of permeability variation would provide additional qualitative and quantitative information.

3.6.2 Borehole observations and permeability measurements for permeability spatial variations (X, Z)

Sampling was made on different lithological facies present in the "Peyrouses 1" borehole. The averages values of the permeability on intact, fractured, altered, fractured and altered facies are of 2.8×10^{-16}, 3.9×10^{-15}, 1.5×10^{-15}, 3.1×10^{-13} m^2, respectively. In order to observe these permeability variations according to the different facies and depth, we have transcribed these average values into a permeability/depth profile (Figure 62). This profile provides additional constraints on the variation of permeability from 0 to 250 m. We can then try to incorporate these permeability variations into our numerical model.

Depth-dependence of permeability follows the equation of Garibaldi et al. (2010). This equation makes it possible to consider the effect of compaction on permeability. Local variations in permeability are additionally given by equation 26 (Chapter IV). By zooming in on the first 250 meters, permeability variations in the order of 10^{-16} to 10^{-13} m^2 can be observed (Figure 62). This variation is of the same order of magnitude as the one measured in the laboratory. It is not surprising that the permeability variation of the numerical models does not exactly follow the variation present in the borehole. Moreover, the figures do not exactly reflect the exact values, since we have inserted the averages of these measured values. Nevertheless, we will keep the assumption that general trends are respected.

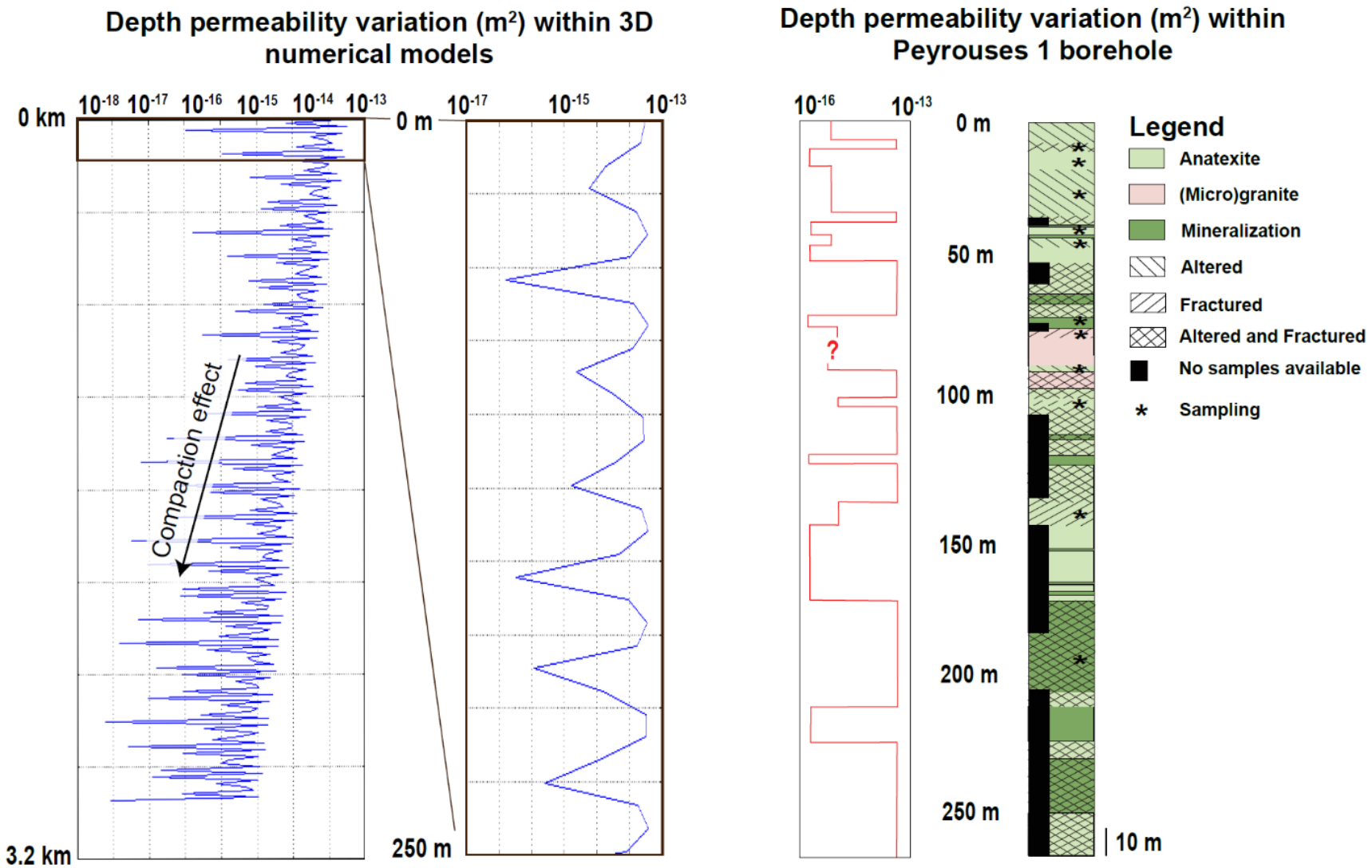

Figure 62 : Permeability variation along the x and z axes and comparison with the average permeability value of samples representing different facies taken from the Peyrouses 1 borehole (see location on Fig 41).

3.7 Numerical Approach

3.7.1 Rayleigh number analysis

Using the Pontgibaud fault zone parameters (*H = 15,000 m and h = 3000 m*) and Eq 5), the critical Rayleigh number *Rcf/4* equals *21.3*. The measured permeability varies from 10^{-18} to 10^{-12} m^2 (Fig 60), implying a variation of the Rayleigh number (Eq 3) from 0.018 to 18000. We can deduce the critical fault permeability above which thermal convection can occur:

$$K_{fc} = \frac{\left(\frac{Rcf}{4}\right).D.\nu}{g.\alpha.\Delta T.H} = 1.2 \times 10^{-15}\, m^2 \qquad \text{Eq 29}$$

Where $\alpha = 2 \times 10^{-4}\,(K^{-1})$, $\Delta T = 450\,°C$, $\mathrm{D} = 0.76 \times 10^{-6}\, m^2.s^{-1}$, and $\nu = 10^{-6}\, m^2.s^{-1}$. Thus, considering the selected parameters, it seems reasonable to consider a convective thermal regime within the Pontgibaud fault zone, at least in the case when the permeability is greater than 1.2×10^{-15} m^2. This threshold value must however be considered with caution since the fluid properties considered here correspond to those for room temperature conditions.

3.7.2 2D TH numerical modelling of the Pontgibaud Crustal Fault Zone

The geometry of the numerical model for Pontgibaud (Fig 63) is directly based on the geological model (Fig 52) and is therefore constrained by a detailed set of geological data and observations. The physical properties, integrated into the numerical models, are summarized in Appendix 1. In accordance with the thermal relaxation time of the magmatic chambers calculated on the basis of a thermo-barometric

study (Martel et al. 2013), the results of our numerical simulations are shown up to time t_0 + 15,000 years.

Figure 63 presents the results of the numerical simulations with the temperature field (colors) and isotherms in white. The stable temperature pattern shown in Fig 62 a is obtained for $K_{f_{max}}$ value up to 1.4×10^{-15} m^2. For these $K_{f_{max}}$ values, the isotherms are not deformed, but are disturbed around the cooling magma chambers. At time t_0 + 15,000 years, the cooling of the magma chambers does not disturb any isotherm in the Pontgibaud fault zone. Figure 63b represents the permeability field centered on the red box of Fig 62a. The deformed isotherms shown in Fig 63c, d are located at the intersection between the Pontgibaud listric geometry and the vertical faults (see black box, Fig 63a). For $K_{f_{max}}$ values between 1.6×10^{-15} and 1.6×10^{-14} m^2, the deformation of the isotherms can be observed (Fig 63c). In the terms previously used, the morphology of the isotherm's changes from areas of weak convection of unicellular type (blue box, $K_{f_{max}} = 1.6 \times 10^{-15}$ m^2) to areas of strong convection of bicellular type (red box, $K_{f_{max}} = 1.6 \times 10^{-14}$ m^2). This representation therefore shows that, when permeability is increased within the Pontgibaud fault zone, isotherms show an increasing disturbance.

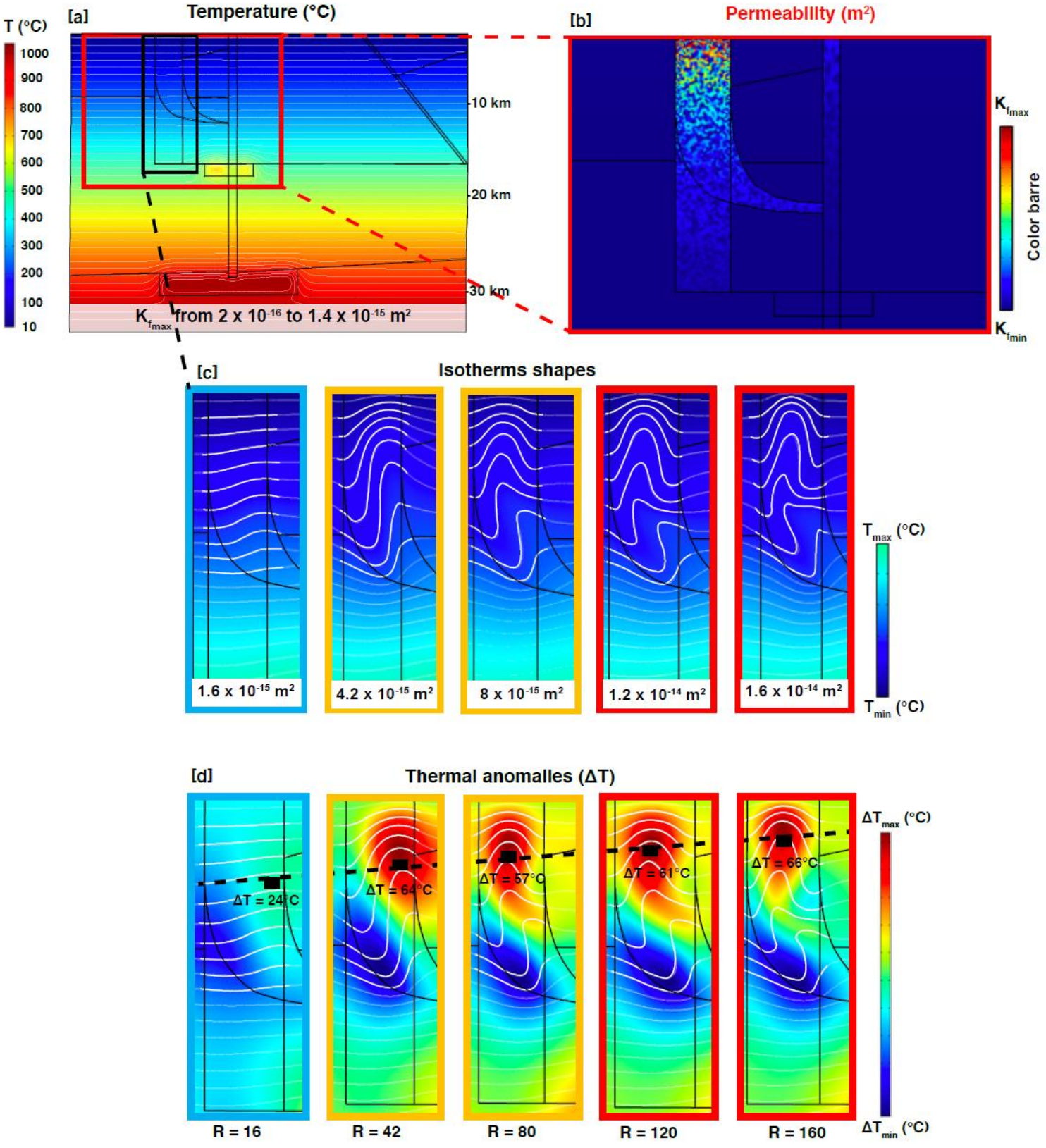

Figure 63 : Maps of temperature (a), permeabilities (b), isotherm (c) and thermal anomalies (d) of the Pontgibaud regime (at time t_0 +15,000 years). In accordance with Fig 34, color of boxes contours corresponds to one convective regimes: blues boxes correspond to areas of unicellular weak-type convection zone, oranges boxes correspond to unicellular medium type convection zone, and reds boxes correspond to bicellular strong-type convection zone.

Figure 63d shows the amplitudes and locations of the obtained thermal anomalies. These anomalies are represented as a function of R ratio, the value of the maximum temperature anomaly ($\Delta Tmax$) and its depth. As it can be seen in Fig 63d, positive and negative thermal anomalies are present in the Pontgibaud system. Positive thermal anomalies are located at the top of the fault zone, while negative thermal anomalies are located at the base of the fault zone. The depth of the positive thermal anomaly decreases for an increasing R ratio (see dashed line in Fig 63d). This latter observation is consistent with the parametric study (Figs 33, 34, Chap IV). For R ratios between 42 and 160, the value of the thermal anomaly does not show significant variation. Overall, these anomalies are between 57 and 66°C. On the other hand, when R = 16, the value of the thermal anomaly is only 24°C.

This lower value can be explained by a low deformation of the isotherms. At R = 42 and above, the isotherms show an increasing deformation up to R = 160. Considering isotherms with a relatively large deformation, the value of the positive thermal anomaly no longer varies significantly. Thus, the results of numerical simulations carried out within the Pontgibaud hydrothermal system show that the deformation of the isotherms is significant from a $K_{f_{max}}$ value of 1.6×10^{-15} m^2 (in accordance with the previous Rayleigh number analysis) and a R ratio of 16.

3.7.21 Finding the right R and K_f combination for Pontgibaud Crustal Fault Zone

The comparison of the results obtained by modelling with the data measured in the field makes it possible to assess the consistency of the obtained results. Within the Pontgibaud fault zone, the surface heat flux is 110 mW.m^{-2} and the geothermal gradient is 41°C.km^{-1} (Vasseur et al. 1991, International Heat Flow Commission). This comparison will make it possible to estimate the permeability value for which the field measurements and simulation results are consistent. Among the numerous tested models, it turns out that only some combinations precisely reproduced the

above-described thermal features. The result for the simulation with a $K_{f_{max}}$ = 1.6 × 10^{-14} m^2, show a surface heat flux of 115 mW.m^{-2} and a geothermal gradient of 39 °C.km^{-1}. Thus, for $K_{f_{max}}$ = 1.6 × 10^{-14} m^2, the results of the numerical models reproduce the heat flux and geothermal gradient values measured near the surface. The numerical models show that at a time t_0 + 10,000 years the heat flux and the geothermal gradient are 105 mW.m^{-2} and 33°C/km, respectively. At t_0 + 20,000 years we obtained 127 mW.m^{-2} and 41°C/km, respectively.

3.7.22 Combining geophysical data and numerical results

Figure 64a, b and c compare the temperature anomaly map of the Pontgibaud region with the measured resistivity profile extracted at the exact coordinates of the geological cross-section.

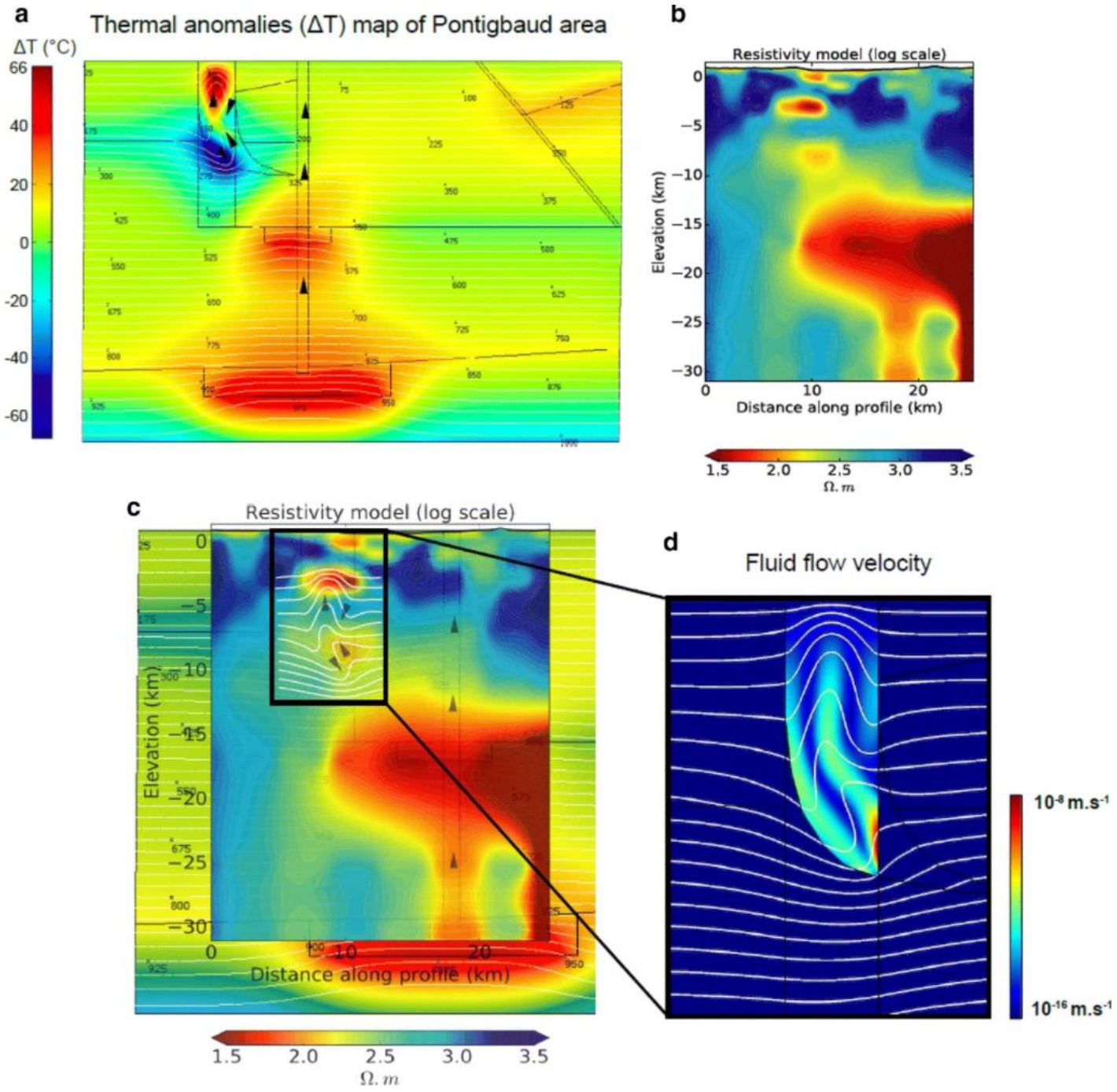

Figure 64 : (a) Thermal anomalies maps of Pontgibaud area. The black arrows represent the direction of fluid flow. (b) Resistivity model previously described (Fig 43). (c) Comparison of the numerical simulation result affecting a K_{fmax} permeability of 1.6×10^{-14} m^2 at the Pontgibaud fault zone, with the resistivity profile. (d) Fluid flow velocity within the Pontgibaud Crustal fault Zone.

The map (Fig 64a) shows positive thermal anomalies within the Pontgibaud fault zone, at the magma chambers and at the base of the sedimentary infill of the Limagne basin (right part of the model). A negative thermal anomaly is also present at the base of the Pontgibaud fault zone. The MT image shows various anomalies of low resistivity at 3, 8 and 15 km depth (Fig 64b). By superimposing the two images (Fig 64a, b), we can see that the temperature anomalies located at 3, 8 and 15 km depth are superimposed on the low-resistivity anomalies located at 3, 8 and 15 km depth. At 15 km depth, the thermobarometric study by Martel et al. (2013) shows the presence of a magma chamber. At 3 and 8 km depth, Fig 64c shows that anomalies of low resistivity are located in areas where fluids could circulate. Thus, the numerical simulation imposing a permeability $K_{f_{max}}$ = 1.6 × 10^{-14} m^2 at the Pontgibaud fault zone shows a striking consistency with the resistivity profile, even if the link between resistivity and temperature may not be so obvious. Nevertheless, isotherms deformation is correlated with high fluid flow velocity (Fig 64d).
Our 2D TH numerical results estimate a thermal anomaly of 66°C witin the Pontgibaud Crustal Fault Zone at a depth of 1.8 km (Fig 65). In 2D with a TH coupling, the results of the numerical models are comparable to the temperature data, and the geophysical profile, however, the complex nature of the interaction between Thermal (T), Hydraulical (H), Mechanical (M) and Chemical (C) coupling affect the behavior of the geothermal reservoir under natural conditions. For example, in chapter IV we were able to highlight poro-elastic effects on the setting time and spatial extent of the positive temperature anomaly.

Additionally, considering 3D numerical models will allow a better discussion of this spatial extent. Here, the 2D results (Figure 65) show that the positive temperature anomaly extends beyond the deformation zone. Indeed, an anomaly of +40°C is present at the boundary between the fault and the metamorphic series.

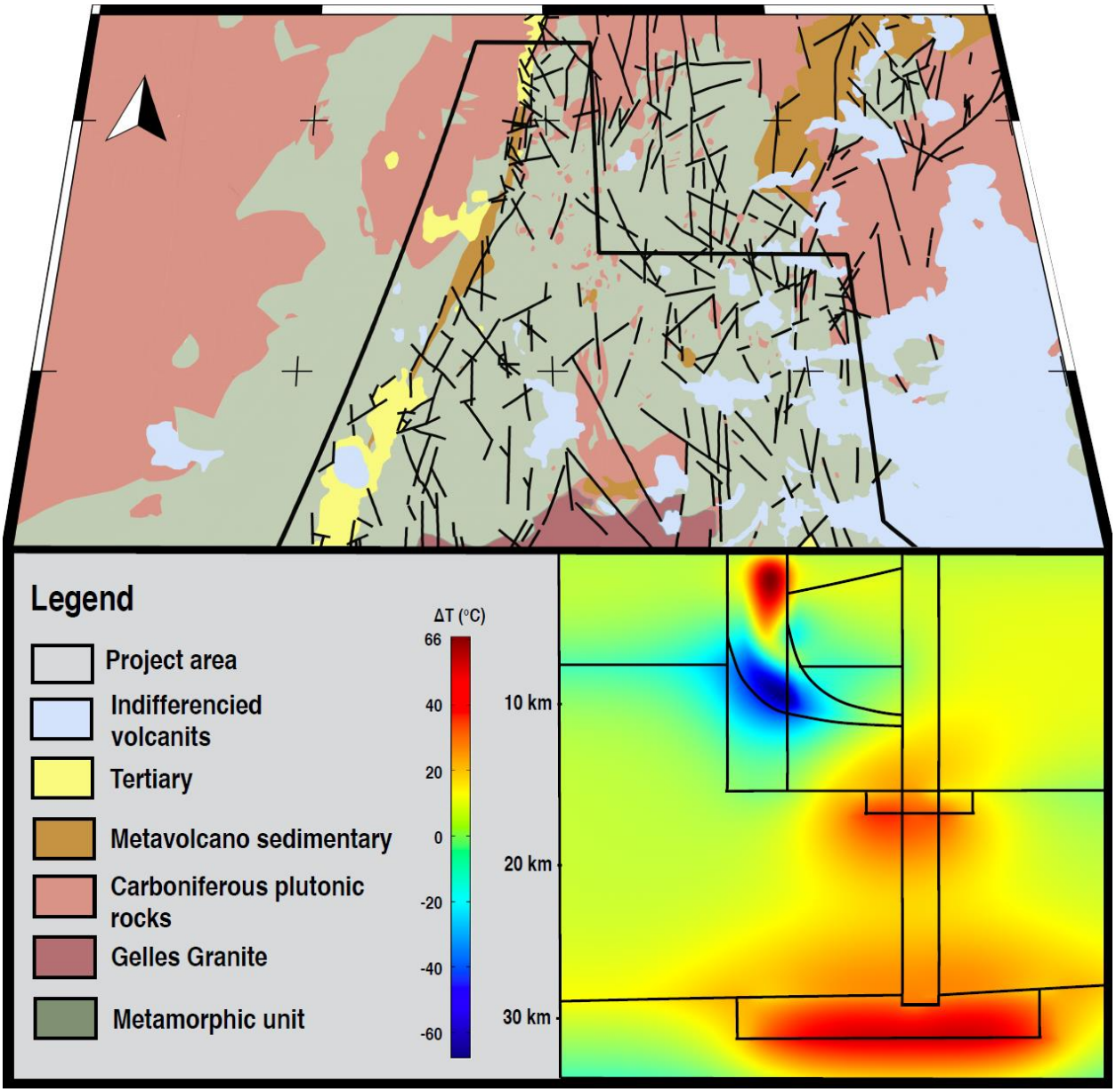

Figure 65 : 2D TH numerical simulation results for a maximum permeability imposed on the Pontgibaud Crustal Fault Zone of 1.6 × 10⁻¹⁴ m².

3.7.3 3D THM numerical modelling of the Pontgibaud Crustal Fault Zone

The results of the numerical modelling show that for a maximum permeability imposed on the Pontgibaud deformation zone of 10^{-14} m^2, the geothermal gradient would be 41.5°C/km (Figure 66(a)) and the heat flux would be 110 $mW.m^{-2}$ (Figure 66(b)), at the location (Figure 41) where the measured and estimated field data are 41°C/km and 110 $mW.m^{-2}$.

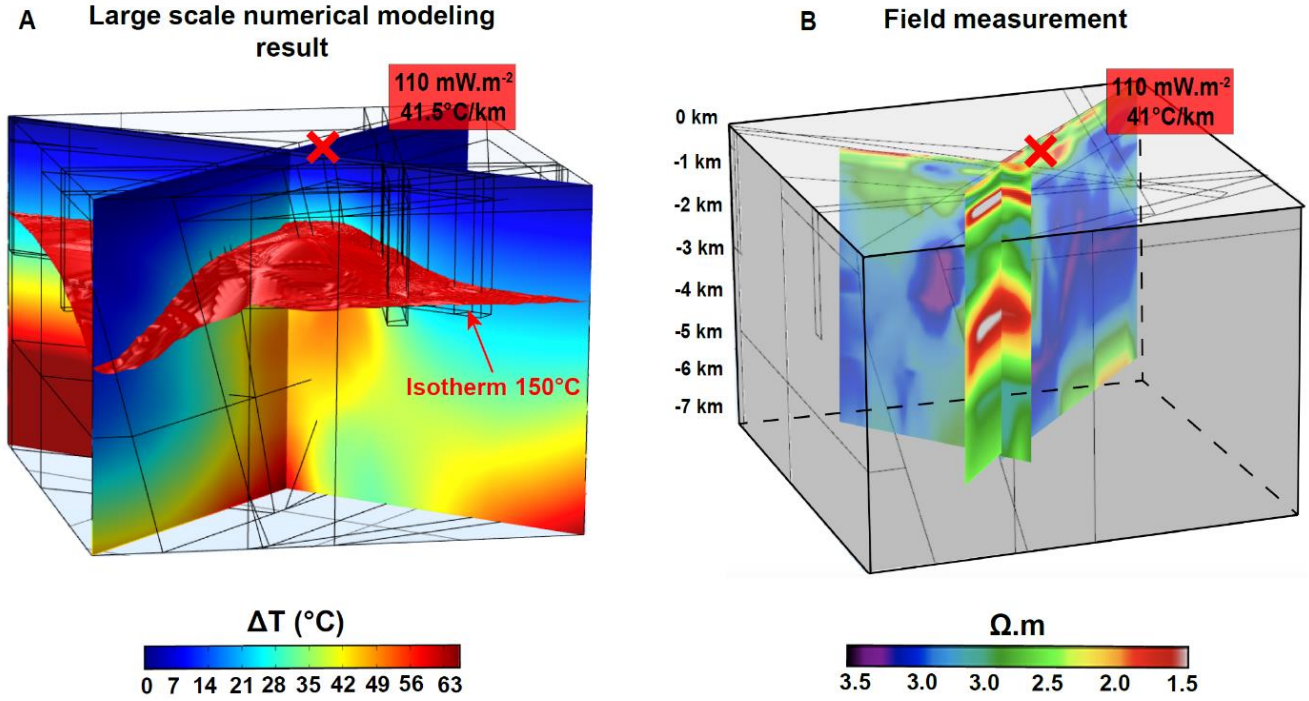

Figure 66 : 3D THM Pontgibaud large-scale numerical simulation results. (a) for a maximum permeability imposed on the Pontgibaud CFZ of 1 × 10^{-14} m^2 (b) are compared with the resistivity profiles, the geothermal gradient and heat flux. Fluid velocity vary from 10^{-8} to 10^{-10} $m.s^{-1}$.

The resistivity profiles show a low resistivity anomaly at a depth of 1 km (Figure 66(b)) and a larger low resistivity anomaly at a depth of 3-4 km. If the origin of this resistivity may be discussed, the comparison between the resistivity profiles and

the temperature anomalies shows that the temperature anomaly within the Pontgibaud deformation zone is between 2 and 3 km deep. In the middle part of the Pontgibaud deformation zone and at the intersections of the different fault families (N-S, NE-SW, NW-SE, and E-W), the 150°C isotherm (in red on Figure 66(a)) would occur at a depth of 2.3 km.

4 Discussions

4.1 Origin and effects of heterogeneities

Thin-sections observations (Fig 55, 56 and 57) revealed open fractures and fractures completely sealed by mineral precipitation. A fault can thus behave as a pathway for, or as a barrier to, fluid circulation (Bense et al. 2013). Quartz, feldspar and alteration products such as sericite are well known to form around hydrothermal sites and near faults (Bruhn et al. 1994; Sausse 1998; Caine et al. 2010). Filling fractures with cement or alteration products can reduce their permeability (e.g., Griffiths et al. 2016; Mordensky et al. 2018). When fractures transmit fluids, their immediate surroundings can be subject to significant mineral dissolution (potassic feldspar, biotite, plagioclases), forming matrix porosity around these fractures. If the minerals likely to be altered are initially connected in space, then their alterations will produce connected pores that can promote the circulation of fluids (e.g., Farquharson et al. 2019). Direct connected porosity measurements on our samples with no apparent fractures (at the lengthscale of the 40 mm-long sample) showed values between 6 and 22%. Indeed, the permeability of the altered samples was higher than that of the unaltered samples (Fig 60). The porosity values measured here are consistent with the study by Sardini et al. (1997) who quantified the connectivity of the minerals likely to be altered. Mercury porosity between 6 and 20%

was measured on samples of altered, non-fractured granite. Considering the capacity of fluids to circulate through fractures but also within the matrix itself, it is thus possible to consider Pontgibaud hydrothermal system as a reservoir with double matrix-fracture permeability. This kind of reservoir has already been observed in the altered granite of the Soultz-Sous-Forêts geothermal reservoir (Genter, 1989; Ledésert, 1993).

Thin-section (2D) and X-ray microtomography (3D) observations have revealed spatially propagating fracture networks in which fluids can flow through pores at different scales, from 2.5 µm to 2 mm (Figures 55, 56, 57, 58 and 59). This fracture propagation has been studied on mineralized systems (St. Salvy, France, and Jebel Aouam, Morocco) and in which tectonic comminution processes have been identified (Cassard et al. 1994; Jébrak, 1984; 1997). Microscopic scale pores have also been observed in the walls of some mineralization. The most frequent process in the brittle part of the crust is hydrofracturing. This process depends on the temporal variation of the fluid pressure (Phillips, 1972; Jébrak, 1992; Hagemann et al. 1992), causing a “break up” which may be at the origin of some voids. This process has been studied on sites with F (El Hammam-Morocco), Ba (Dreislar, Germany), and Ag and Au (Creede, Colorado, USA) mineralization (Jébrak, 1984). Fluid circulation can also cause the dissolution of mineral phases in the basement. Dissolution may be accompanied by a loss of volume and thus cause the formation of pores within the matrix (Launay, 2018). While the consequences of these processes can be observed in 2D and 3D, other processes can cause the opening or closing of the voids (such as volume reduction, volume expansion, and pore collapse), thus influencing the capacity of the system to allow fluids to circulate (Figure 56).

According to Bejan and Lorente (2011), architectures at different scales and arranged in a hierarchical pattern would promote fluid flow. These natural drainage systems (Figures 50, 55, 56 and 57) may have lower flow resistance than a similarly

porous volume. The constructal theory (Bejan and Lorente, 2006) allows us to describe the natural tendency of flow systems to generate multiscale shapes and structures favoring fluid flow. It has also been shown that the transition between heat transfer at the nanoscale and more conventional scales is governed by the smallest dimensions and by their spatial heterogeneities (Gosselin and Bejan, 2004). The origin of these heterogeneities could be the stress (with tectonic comminution) and the water (with fluid pressure). Finally, with knowledge of current parameters, the geometry of the Pontgibaud CFZ might correspond to an optimal one, which facilitates efficiency of convective flow.

4.2 Controlling fluid flow factors within the Pontgibaud Crustal Fault Zone

Putative structures sufficiently permeable to allow fluid circulation are commonly described for hydrothermal systems (Forster and Evans 1991; Bruhn et al. 1994; Belgrano et al. 2016) and are used in many numerical models (Forster and Smith 1989; Mckenna and Blackwell 2004; Garibaldi et al. 2010; Guillou-Frottier et al. 2013; Magri et al. 2016; Taillefer et al. 2018a, b). The results of the parametric study presented in chapter IV, and their comparison with the Pontgibaud natural system, show that when the fault zone is vertical, the value of thermal anomaly will be high and at shallow depth. This depth is also controlled by the ratio between the fault permeability and the basement permeability: when the R ratio is high, thermal anomaly will be at a shallower depth.

Measurements of permeability and connected porosities from samples from Pontgibaud show ranges of values between 2×10^{-18} m^2 and 2×10^{-12} m^2 and 6 and 22%, respectively (Fig 60). These values are within known ranges of permeability for rocks in a basement context (Achtziger-Zupančič et al. 2017), but the results show values relatively high compared to laboratory measurements on intact granite

samples (e.g., Brace et al. 1968; Kranz et al. 1979; Meredith et al. 2012). The maximum permeability value for the basement has been 10^{-16} m^2. This value is compatible with permeability values extracted from the laws of permeability decrease proposed by Ingebritsen and Appold (2012), Ingebritsen and Manning (2010).

Our data also highlight the heterogeneities of the permeability of a hydrothermal system, which could be caused by the processes of tectonic comminution, hydrofracturing, and mineral phase dissolution, processes that can form structures and pores at different scales. The permeability of a rock mass will be very much controlled by the fracture density and, importantly for hydrothermal systems, the proportion of open fractures (Heap and Kennedy, 2016; Kushnir et al. 2018; Nara et al. 2011; Eggertsson et al. 2020). Our permeability data also show that alteration can increase permeability (Figure 60). Previous studies on volcanic hydrothermal systems have also shown that hydrothermal alteration can greatly influence matrix permeability (Sruoga et al. 2020; Heap et al. 2017; Cant et al. 2018; Heap et al. 2019; Heap et al. 2020). For these natural hydrothermal systems, permeability should not be approximated to a single value but should rather be represented as pipes or channels embedded in the neighbouring system (Elder, 1981). The discussion about the permeability representation will be developed in Chapter VI (Part 4).

4.3 Positive temperature anomaly on the Pontgibaud CFZ

Figures 66(a) and 67(c) show a positive temperature anomaly that extends widely on both sides of the Pontgibaud CFZ. The origin of this anomaly would be a blob-like convective pattern. Both blob-like and finger-like convective patterns are found for low permeability ratios (see Figure 38 Chap IV). Finger-like convective patterns are characterized by isotherms covering a smaller space than blob-like convective patterns. Consequently, the volume of the temperature anomaly will be lower in a finger-like convective pattern than in a blob-like one.

As shown in Figure 67, the results of Pontgibaud large-scale numerical modelling compared with heat flux, geothermal gradient, and resistivity data show that the 150°C isotherm could be located at a depth of 2.3 km within the Pontgibaud CFZ. This upwelling of the 150°C isotherm is the result of fluid circulation through a blob-like convective pattern. This will produce a temperature anomaly within the Pontgibaud hydrothermal system, but lateral thermal diffusion is observed within the fault zone itself, thus defining a larger geothermal reservoir. Indeed, considering a simplified 3D geometry, this lateral temperature diffusion has been highlighted in recent numerical models of fluid flow around faulted zones (Guillou-Frottier et al. 2020).

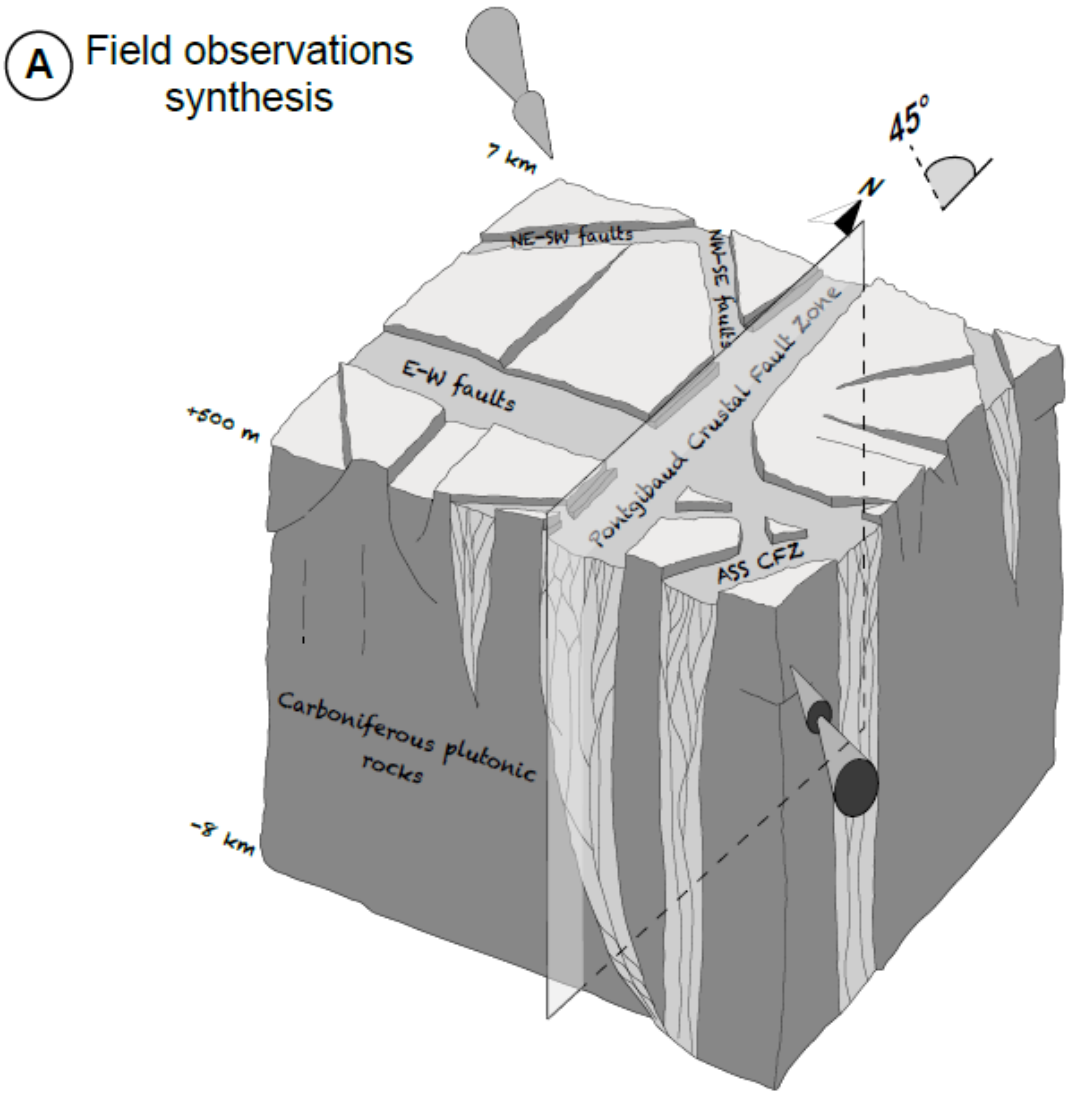
A Field observations synthesis
7 km
45°
N
NE-SW faults
NW-SE faults
E-W faults
Pontgibaud Crustal Fault Zone
ASS CFZ
+500 m
Carboniferous plutonic rocks
-8 km

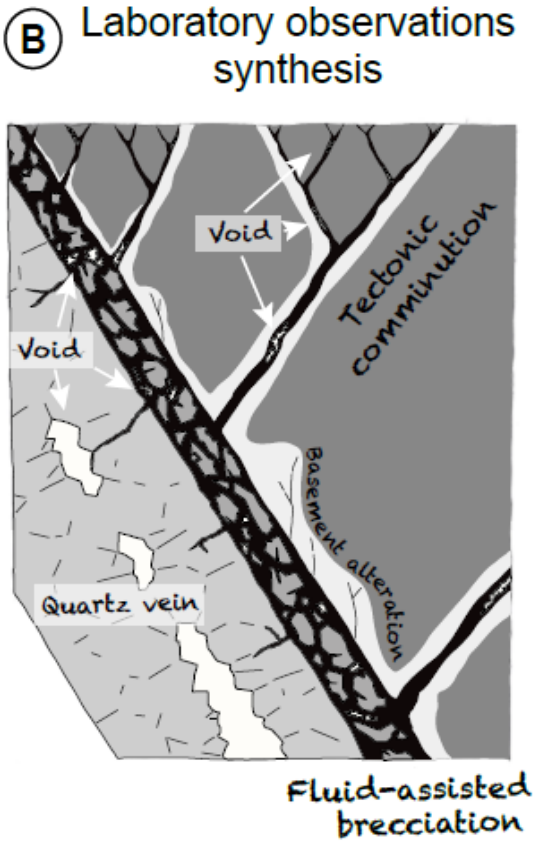
B Laboratory observations synthesis
Void
Void
Tectonic comminution
Basement alteration
Quartz vein
Fluid-assisted brecciation

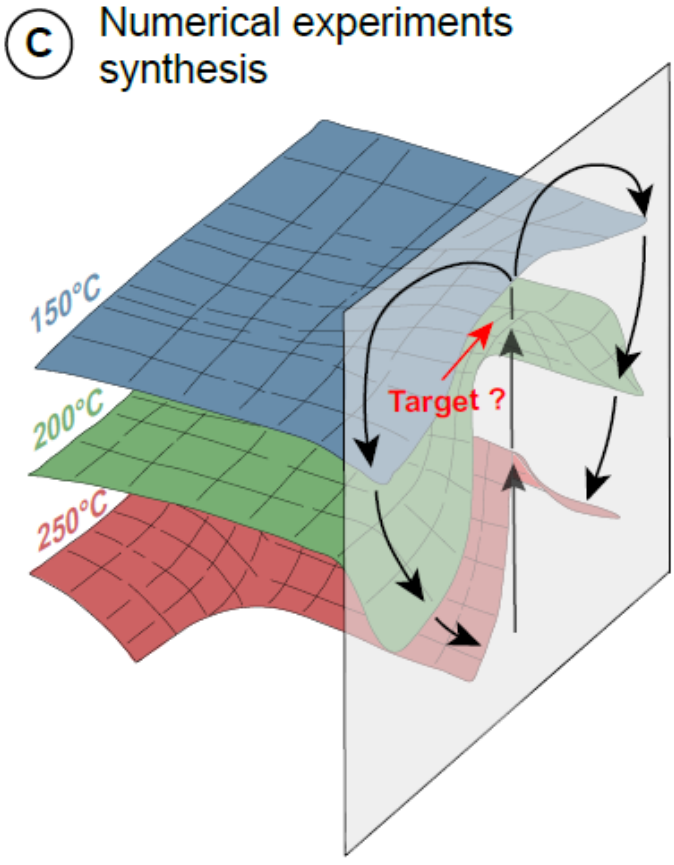
C Numerical experiments synthesis
150°C
200°C
250°C
Target ?

Figure 67 : (a) Three-dimensional conceptual model of the Pontgibaud CFZ as a potential geothermal reservoir. Details of the voids present at different scales and in which fluids can flow. (b) The processes that may be at the origin of these voids (tectonic comminution, fluid-assisted brecciation, and basement alteration) are illustrated. (c) Comparison of the large-scale modelling results with field data shows that fluid could flow through a blob-like pattern and locate the 150°C isotherm at 2.3 km depth.

Chapter VI : General discussion, limitations and perspectives

Geosciences are emerging as a key element in an effective transition from fossil fuels to low-carbon energy. The potential of geothermal energy as a supplier of energy, heating or electricity worldwide is huge. The development of deep geothermal energy must include the discovery of new geological systems for electricity generation.

In the Basin and Range (USA), it has been shown that geothermal systems without surface expression (hot springs, fumaroles) exist (Coolbaugh et al. 2006). These 'blind' systems could account for 75% of the geothermal potential of the area (Faulds and Hinz, 2015). The state of knowledge about the controlling factors of geothermal reservoirs shows that the amount of High Temperature (HT) geothermal reservoirs on a global scale is often underestimated. In 2021, in France, 14 HT (>150°C) geothermal licences have been assigned, but most of them concern collapse troughs where temperature anomalies are present at shallow depths (Rhine Grabens, Limagne, Vistrenque, Valence). The new concept behind this study is to focus on highly permeable zones in the crust, which allow hot fluids to flow at economically interesting depths. It would then be possible to focus not only on anomalously hot areas, but also on anomalously permeable areas, such as CFZs.

1 A multidisciplinary approach

The overall understanding of an outcropping fault system integrates many parameters that can be studied using a multidisciplinary approach. The multidisciplinary approach used here corresponds to a method widely used in oil and uranium exploration, CO_2 capture storage studies, and reservoir engineering (Wilson et al. 2010; Alcalde et al. 2014; Ma and Holditch, 2015). It combines a field approach (structural measurements and sampling of the Peyrouses 1 borehole), a laboratory

approach (2D and 3D observations and measurements of permeability and connected porosity), and numerical modelling.

The interest of this approach is that it makes it possible to cross-check the results of the different methods. However, it has the inconvenience of not reaching the limits of the different methods used. For example, the permeability and connected porosity measurements were performed at room temperature and under a confining pressure of 1 MPa. With this method, it is possible to obtain a range of permeability and connected porosity quite quickly. It was also possible to quantify the heterogeneity of the Pontgibaud hydrothermal system. However, this pressure and temperature does not represent in-situ conditions. High temperature and high-pressure permeability measurements (< 300°C; 50-300 MPa) can be performed in a Paterson apparatus at ISTO by using argon or water (Coelho et al. 2015). These experiments can be performed up to 3 kbar to provide more realistic data to better constrain numerical models of the natural system.

It would then be possible to image the 3D pore network and permeable structures on the same Nanotom used in this study. In our case, the density contrast between the different mineralized phases, such as galena or quartz, did not provide a better resolution than 2.5 μm. The use of a synchrotron such as the Stanford Synchrotron Radiation Lightsource (SSRL) could potentially provide a resolution of 0.15 μm on these same samples. It would then be possible to see whether dendritic networks are found at this scale, or perhaps to gain further insight into the permeability geometry.

The fluids circulation in these dendritic networks cause mineral reactions. For example, due to their swelling properties, smectites can strongly reduce the rock permeability. In order to determine the proportion of smectite, the clay fractions can be directly extracted from the mineral matrix. A nitrogen adsorption-desorption experiment at 77K could be performed to obtain information on the specific surface of the clay fractions. This characterization could be repeated after HP-HT treatments (<330°C; 50-300 MPa) in the Paterson press on a standard smectite to characterize

the Illite/smectite transition at depth and in the specific lithology (granite and migmatites) of the Pontgibaud Crustal Fault Zone.

Considering these few elements, we can easily consider that in this study, we have only scratched the surface of some of the possibilities for a more thorough understanding of the characteristics of the potential reservoir of the Pontgibaud CFZ. In this context, the GERESFAULT project (ANR-19-CE05-0043) proposes to explore the geothermal potential of CFZ by combination of field studies, experimental petrophysics, geophysics and numerical modelling. The new data and the results of this consortium (9 public and private partners) will considerably refine the elements acquired in the framework of this thesis, which can be considered as a first approach. At the scale of this thesis, the multidisciplinary approach employed has allowed a correlation between field studies, petrophysical data and numerical modelling which should allow the improvement of the geothermal exploration of CFZ.

2 Why use numerical modelling?

In engineering, modeled systems are relatively well understood and numerical modelling is used as a predictive tool. This is not necessarily the case for geological or biological problems. In this study, the construction of a numerical model forced us to think about the geometry and processes that might influence the final result. The whole methodology leads to new research questions, treated in parallel with field and laboratory observations and measurements, whose impacts can be measured and quantified by a company.

Once a model becomes consistent with the problem at hand, a tool is obtained that offers an unmatched degree of control in the field or in the laboratory. It then becomes possible to test and isolate parameters and processes that may impact on

the formation of High Temperature Geothermal Reservoirs in CFZ. In these terms we can see numerical modelling as a tool to support reflection.

Thus, in a first step we have promoted a numerical methodology to understand some limiting factors controlling the fluid circulation, the intensity of the temperature anomalies and their depths, within CFZ. To do so, we considered idealized geometries with realistic physical properties. Boundary conditions have been chosen and this choice could influence the final results.

2.1 Choice of boundary conditions

In general, different boundary conditions exist and can be imposed on numerical models. In our case, for the heat equation, we considered a Dirichlet condition (fixed surface temperature, 10°C) throughout the simulation. On the lower surface, a Neumann condition (heat flux) is applied. However, Cauchy type boundary conditions, where both temperature and heat flux are not imposed, might have been more appropriate to the problems.

The vast majority of large-scale numerical models in the Earth Sciences consider a Dirichlet condition. The atmosphere regulates the variations and the average temperature remains constant over thousands of years. In the case of geothermal systems, the presence of hot springs shows that the temperature is not constant over a whole area. In this case, the use of mixed conditions seems more appropriate. As used by Magri et al. (2016), the Cauchy condition relationship is written as :

$$Q = h(\mathrm{T}_0 - T) \qquad \text{Eq 30}$$

Where Q (W.m^{-2}) is the surface heat flux, h (W.m^{-2}.K^{-1}) a coefficient of heat transfer and T_0 (°C) the reference temperature at the surface.

In the case of the Têt fault (Pyrenees, France), Taillefer et al. (2018) find by applying a Cauchy condition on the surface (see Eq 30) the springs temperatures, whose values are between 29.1°C and 73°C. In the case of the numerical modelling of the Pontgibaud CFZ, the temperature for the Ceyssat and Pranal springs (see location Fig 41) are respectively 11.5°C and 18°C throughout the year. We have assumed that the temperature values of these resurgences do not seem to require Cauchy type boundary conditions at the surface. Nevertheless, one of the perspectives could be to consider this boundary condition and to compare the results with each other.

3 Control and limiting factors on fluid flow within CFZ in basement domain

3.1 Structural dip effect on fluid flow within CFZ

The results of the 2D parametric study with TH coupling show that the dip of the structures influences the fluid flow. These trends are also observed in 3D modelling with TH coupling (Guillou-Frottier et al. 2020). The origin of this control could be the temperature difference between the base and the top of the geological structure. Considering a constant structure length, the temperatures at the base are higher at high dips than at low dips. This difference between the base and the top of the permeable structure has a direct influence on the formation of convection cells. Physically characterising the convection cells, the Rayleigh number includes in its parameters the temperature difference between the upper and lower boundary of the system considered (see Eq 3). Therefore, by fixing the permeability, a large temperature difference between the upper and lower boundary of a faulted system may favor the formation of convection cells.

3.2 Permeability ratio effect on fluid flow within CFZ

Several authors (López and Smith, 1995; Baietto et al. 2008) showed that thermal regime is directly related to the permeability contrast between the fault and the basement. In a recent compilation of measured of inferred permeability values, Scibeck (2020) indicates, when available, the permeability ratio between the fault and the basement. We suggest a regime diagram for different 2D and 3D convective patterns as a function of permeability ratios. However, permeability ratio is probably also depth-dependent (Guillou-Frottier et al. 2020). The question whether fault zone permeability remains elevated at depth is crucial, since it may involve upwellings of deep hot fluids at shallow depths. According to Achtziger-Zupančič et al. 2017, that might be the case for dense network of overlapping fault damage zones.

3.3 Effect of topography on fluid flow within CFZ

Figure 68, shows the results of the numerical simulations with the temperature field (colors) and the isotherms in white. The maximum permeability imposed is $K_{fmax} = 2 \times 10^{-14}$ m^2. Different topography elevations were tested, from 0 m to 1000 m, with a step of 200 m.

The equations are described in part 1.1.1 of Chapter IV, the physical properties used, as well as the boundary conditions are the same as those used in the 2D TH parametric study in section 2.1 of Chapter IV. The imposed permeability will decrease with depth in the basement and will vary in the fault in such a way as to approximate a multiple fault-core conceptual model permeability variation. (see Eq 16, Fig 32).

At a topography elevation = 0 m, the isotherms within the CFZ are largely deformed. The areas where the isotherms are contracted, others where the isotherms are dilated, will result in concentrations of positive and negative temperature anomalies. The black arrows show that the fluid circulation is controlled by two small-wavelength convection cells. We have described this convection pattern as bicellular strong-type convection zone (Chapter IV).

With a flat topography and no poroelastic effect, fluid circulation occurs by free convection. The maximum temperature reached is 517.1°C. Increasing the topography to 200 m, 400 m and 600 m, the same bicellular strong-type convection zone is observed.

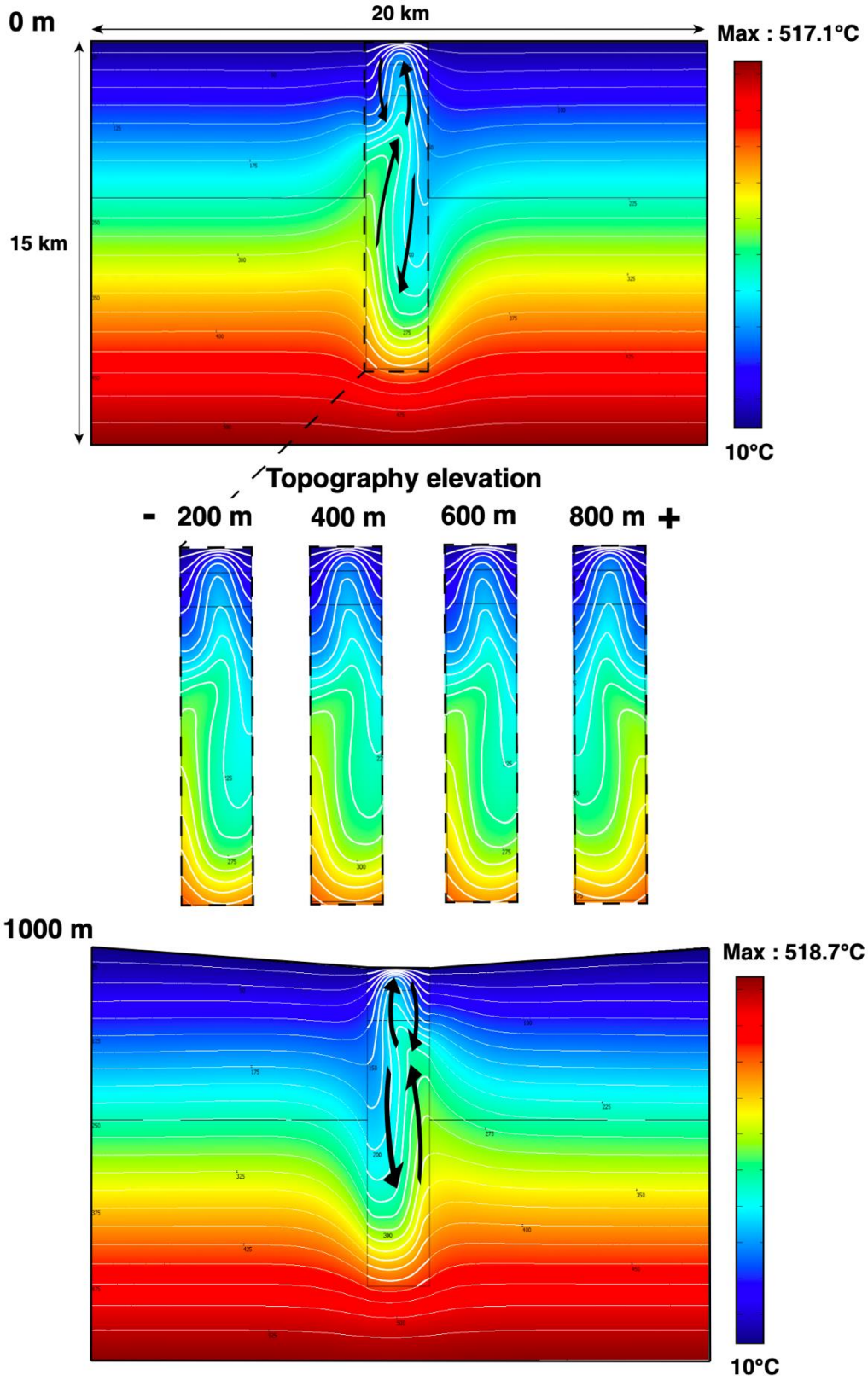

Figure 68 : Topography effect (up to 1000 m) on the isotherm distribution within a CFZ. The physical properties, geometrical parameters, mesh size and boundary conditions are the same as those presented in section 2.1 of chapter IV. All results are given in steady-state.

From 800 m onwards, the circulation of the fluids takes place in the bicellular strong-type convection zone, but the sense of the convective loops is reversed. With a topography of 1000 m, the deformation of the isotherms is identical to the previous case (800 m). The maximum temperature reached is 518.7 °C.

Thus, the fluid circulation in reverse direction for 800 and 1000 m, which could be related to the variation of the topography affects slightly the thermal distribution of the system. The different direction of fluid circulation observed from 800 m could be related to the topography, but could also be related to numerical instabilities.

3.4 What effect(s) have fault intersections on fluid flow within CFZ's?

Evidence of mineralization and fluid circulation is documented in several studies (Craw, 2000; Mickletwaite and Cox 2006, Person et al. 2012). For example, in the Basin and Range, Carlin-type gold mineralisation occurs at fault intersections (Hofstra and Cline, 2000; Faulds et al. 2004; Coolbaugh et al. 2005). Numerical modelling of the Pontgibaud fault zone shows that the 150°C isotherm rises through upward movement at the intersection of several fault families.
Person et al. 2012 have shown that fault intersections locate significant vertical velocities of fluid flow. As tectonic deformation is considered to be a force influencing fluid flow (Ord and Oliver, 1997b; Cox, 1999; Rowland and Sibson, 2004). It might then be appropriate to look at the effects of tectonic stresses, fault intersections, on fluid flow and to see the consequences on the thermicity of the medium. The general geometry of this study could be (Fig 69):

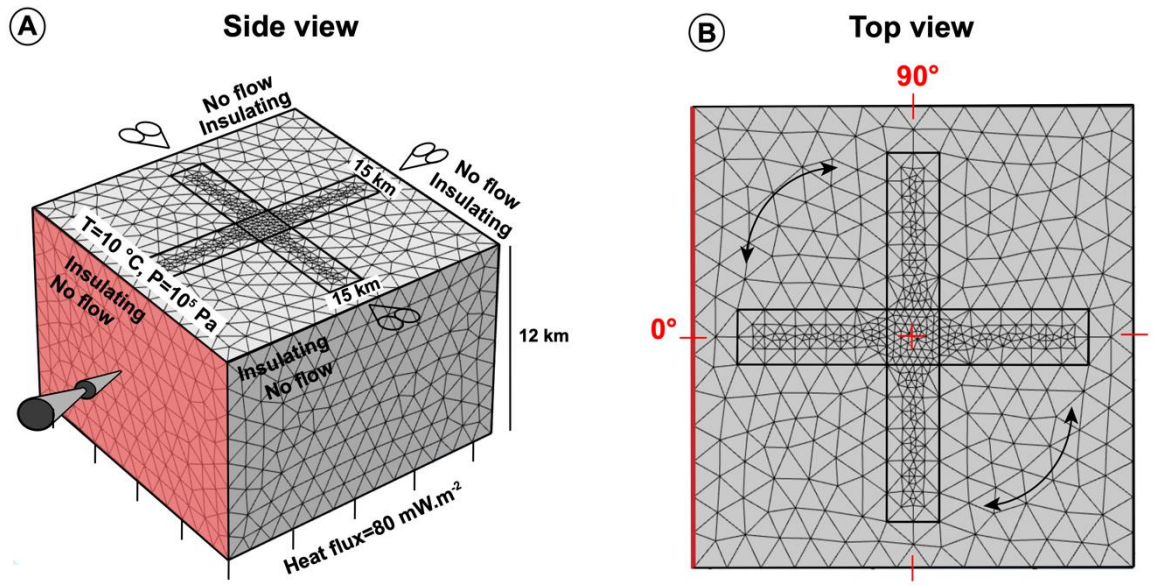

Figure 69 : A way to explore the role of stress orientation and fault intersection, on fluid flow within a CFZ. Hypothetical geometry, mesh and boundary conditions.

It would then be possible to consider the both effects of buoyancy and poroelasticity on fluid flow at fault intersections. From these results, it would be possible to identify fault intersection angles for which temperature anomalies and their depths would be more suitable.

3.5 Comparison of the numerical parametric study results with large-scale numerical modelling

3.5.1 2D study with a TH coupling

In 2D TH coupling, we observed the establishment of a thermal anomaly of 150°C at 2.5 km. According to the large-scale numerical simulation, and the convective

regime diagram, the fluid flow circulates in the bicellular strong type convection regime.

Moreover, for a fault zone permeability value of 1.6×10^{-14} m^2, R equals 160, and then confirm the quantitative approach expressed by the convective regime diagram (Fig 70). Although the 2D models give precious information on the physical mechanisms involved, it cannot capture the complexity in heat redistribution arising from the 3D configuration of the natural fault network.

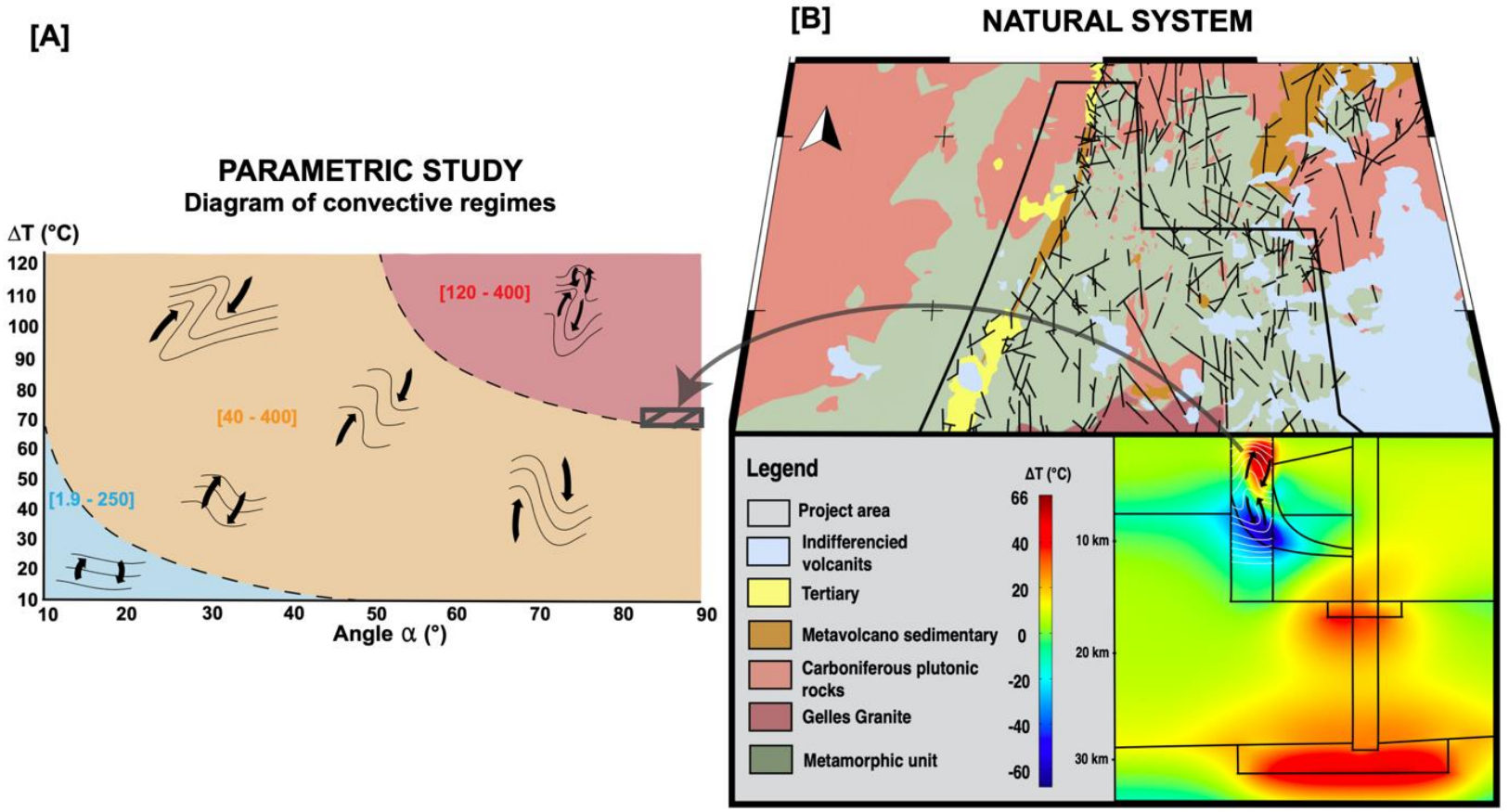

Figure 70 : [A] Diagram of convective regimes. Black lines represent isotherm morphology. The dashed black line separate three areas. In blue, the area of unicellular weak type convection zone. In orange, the area of unicellular medium-type convection zone. In red the area of bicellular strong-type convection zone. [B] Numerical simulation results for a maximum permeability imposed on the Pontgibaud fault zone of 1.6×10^{-14} m^2 at time t_0+ 15,000 yrs. See Duwiquet et al., (2019) for more details.

3.5.2 3D study with a THM coupling

The results of the 3D THM shows that other parameters can influence the fluid circulation within a CFZ: the R ratio, the stress intensity and the stress direction. By considering simplified boundary conditions, the vertical deformation zones, with an angle of 30 and 70°, with respect to the boundary stress, will concentrate the highest temperature anomalies at the lowest depths. A possible explanation for this trend is detailed below.

After considering more realistic mechanical boundary conditions, we found that when the principal stress is oriented at 30° to the fault, the poroelastic effects are less significant than when the principal stress is oriented at 90° to the vertical deformation zone.
Indeed, the fluid pressure difference, which is greater when the principal stress is perpendicular to the fault, focuses the fluid circulation on a smaller volume than when the principal stress is parallel to the fault. These poroelastic effects could explain that for given permeability ratios, a difference in the spatial volume of the temperature anomaly is observable between the blob-like convective pattern and the finger-like pattern (Fig 71). These differences in fluid flow could help to explain the differences in temperature depending on the orientation of the stress.
The Pontgibaud CFZ is located at 45° to the main regional stress (Fig 67). In this direction, the convective regime diagram (Fig 60) predicts blob-like convective pattern fluid flows for R ratio [1-200], as well as for stress intensities below 40 MPa. In view of these parameters, the result of the convective regime diagram seems to be consistent with the validation of the large-scale numerical model of the Pontgibaud CFZ in which blob-like convective pattern fluid flows would be present.
If the consistency between general concepts from very simplified numerical modelling is effectively validated by natural system results, then it would be possible to

use the convective pattern diagram in order to characterize convection regimes of a natural system according to a tectonic regime.

As we have seen, the parameters influencing the formation of these both convective patterns are the intensity and the direction of the stress (Fig 38 and 66). Thus, in a geothermal exploration context, in geological settings where the permeability is quite low, it would be advantageous to target areas where the intensity of the stress is quite low and where the direction of the stress is less than 50° with respect to the deformation zone. In this case, there will be more widespread temperature anomalies.

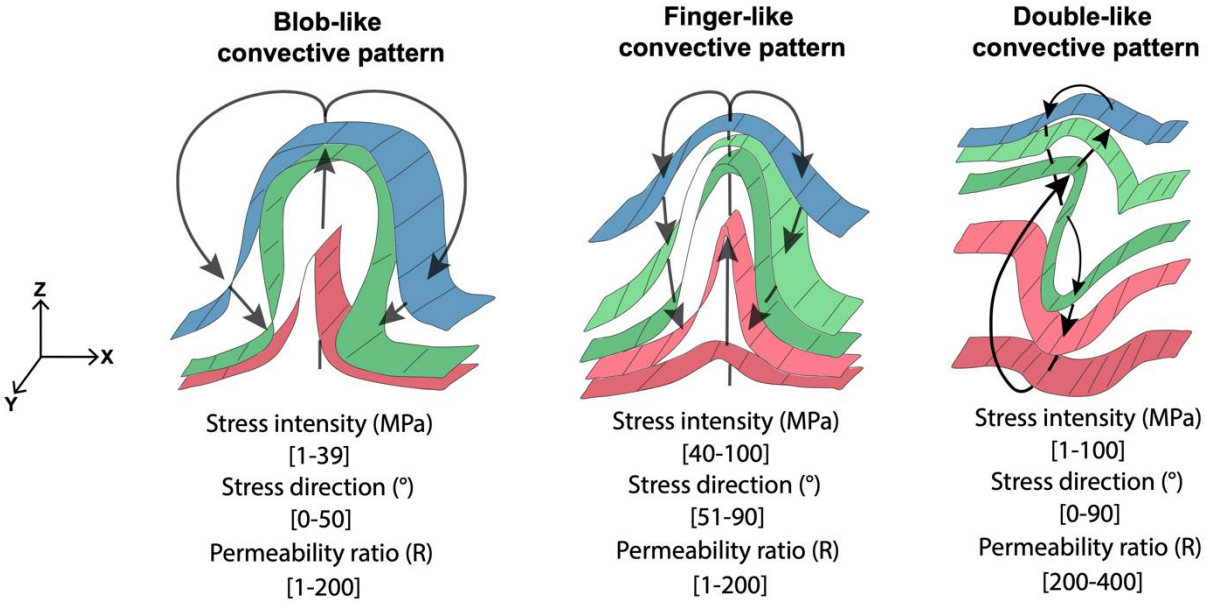

Figure 71 : Results of the 3D THM parametric study. On the whole of the calculations made (n > 2,700) three convective patterns are observable: the blob-like, the finger-like and the double-like patterns. These three patterns depend on parameters such as permeability ratio, direction and intensity of the stress. The volume of the temperature anomaly is different for each convective pattern.

For high permeability zones, the intensity and direction of the stress are no longer parameters influencing the convective regime under thermoporoelastic conditions. The double-convective pattern gives higher temperature anomalies than the two

patterns previously described ($\Delta T>87°C$). Although the temperature anomaly is more intense, the deformation of the isotherms is more restricted than for blob-like convective patterns. Thus, in areas of high permeability, the temperature anomaly will be the most intense, but the volume covered will be less than for blob-like convective patterns.

The 3D parametric studies were realized by considering the faults as vertical,. However, considering a THM coupling, it would be interesting to be able to consider the dip of the structures. It would then be possible to highlight stress directions, permeability ratios, stress intensity, and dips as favorable targets for high temperature geothermal energy. In general, geothermal exploration must consider the stress intensity, the stress direction of the stress, and the variability of permeability.

Finally, all these results are only applicable for large deformation zones in which temperature anomalies are induced by buoyancy-driven flow and with poroelastic effect. Moreover, we only consider the fluid phase (liquid water). If we were to consider two phases, liquid and gas, the poroelastic effects on the compressibility of the gas could be an important process (Brown and Korringa, 1975). If the compressibility of the fluid can also influence the elastoplastic behaviour (Runesson et al. 1996), the thermal dependence of compressibility might change the thermal distribution of the system (Motra and Stutz, 2018).

4 Darcy’s law limits and representative permeability of CFZ

4.1 Darcy’s law limits

When a fluid penetrates a porous rock, the actual path of an individual fluid particle cannot be followed analytically, but the flow can be represented by a macroscopic relationship discovered by Darcy (1856).

Darcy's law expresses the conservation of momentum in describing the flow of a viscous fluid through porous media. This law provides the scientific basis for the concept of permeability. Darcy's law and permeability were originally developed for cases where inertial forces are negligible. However, when inertial forces are strong, the ratio of flow to pressure gradient may vary. Fundamentally Johnson et al. 1987 define a transition from viscous to inertia dominated fluid momentum in a porous medium. Considering a collision-propagation scheme, Lattice-Boltzmann simulations can be used to simulate mass and heat transfers on a macroscopic scale. This method could make it possible to get rid of this problem. The fluid is then no longer considered as a continuous matter, but rather a discrete set of particles that interact with each other. However, in heterogeneous environments, resonance phenomena occur, making it difficult to understand the results of some numerical models (Hubert and Su, 2015).
Laboratory experiments (Medina et al. 2015), have shown another limitation of Darcy's law. The presence of solid suspensions in the fluid (3% is sufficient) destabilizes the linear relationship between the flow and the pressure gradient. Heterogeneous velocity fields then appear in the fractures.

4.2 Representative permeability of CFZ

According to recent studies on different geological systems, it seems that permeability around $10^{-14}\,m^2$ could represent a typical value for which geological data can be reproduced.

For example, in the case of the 300 m wide Têt fault system, French Pyrenees, Taillefer et al. (2018) reproduced the locations and temperatures of the 29 thermal springs with a permeability value of $10^{-14}\,m^2$. In a 3D model of the Lower Yarmouk Gorge, at the border between Israel, Jordan, and Syria, Magri et al. (2016) also reproduced clusters of thermal springs with realistic temperatures, with a fault permeability of $2.3\times10^{-14}\,m^2$. Roche et al. (2018) qualitatively reproduced temperature profiles measured within fault-related geothermal systems in western Turkey when permeability of detachments (low-angle normal faults, 200–400 m wide) equals $10^{-14}\,m^2$. In the case of the Pontgibaud CFZ (French Massif Central), in 2D, we reproduced the present-day surface heat flow and temperature gradient for a maximum permeability of $1.6\times10^{-14}\,m^2$. In 3D, we reproduced the present-day surface heat flow and temperature gradient for a maximum permeability of $1\times10^{-14}\,m^2$. This raises the question of how to define a permeability representative of a fractured hydrothermal system.

In the case of Pontgibaud CFZ, the permeability value is of the same order of magnitude as the others (Magri et al. 2016; Taillefer et al. 2018; Roche et al. 2018). However, the thickness of the deformation zone considered is greater than one kilometer, which is different from the other systems modeled. In addition, to match the field and laboratory observations, which have shown us at different scales of observation structures and channels, the permeability varies with depth, but also laterally. Even if we find field data for a similar permeability value as other studies, nevertheless, the geometry, permeability variation and dimensions of the system considered are not equivalent.

Using the example of the Têt fault, the size of the porous structure considered, of the order of a hundred meters, is compatible with a permeability fixed at 10^{-14} m^2. This means that the length of the porous structure is compatible with this fixed permeability value. But it would not be compatible with a kilometer-scale fractured structure. Therefore, in this case, setting a permeability of 10^{-14} m^2 is no longer a suitable approximation. In a hydrothermal medium, located within a large deformation zone, the medium presents different channels, at different scales and of varying length. By retrieving field data (heat flux, geothermal gradient, and resistivity profiles), considering permeability variations, as outlined by the multiple fault core conceptual model (Faulkner et al. 2003) would appear to be representative of the Pontgibaud fault system. Finally, we might think that when one wishes to model a natural system, the choice of the representativeness of the permeability must depend on the dimensions of the model: if the dimensions are greater than the cumulative length of the fractures considered by a fixed value of permeability, then the approximation becomes unsuitable. In this case, we believe that a representative permeability must be able, by its geometry, or by processes, to consider a set of channels embedded in a more or less permeable medium.

At this point, to aim a permeability representative of a natural system such as a CFZ, we have suggested to consider the permeability variation according to the multiple fault core conceptual model. However, considering the system in its final state does not allow to consider all the processes that lead to this final variation, and above all to be able to see these effects on fluid circulation. In other words, considering this permeability variation can be representative of the natural system, but does not allow to consider all the THMC processes that can lead to this final permeability variation. In order to focus on the processes, we considered a dynamic permeability, but whose final variation is more homogeneous (Fig 6, Part 5, Chap IV) than what is observed in the field (Fig 60, 61, 62). If considering a dynamic permeability allowed to isolate the poroelasticity driven force, it would seem unwise

at this stage to insert it in a model where the objective is to consider a representative permeability of a natural system. On the other hand, for further studies, it could be conceivable to consider this 3D permeability variation, as a result to be achieved by considering a set of THMC processes.

5 Geothermal potential of CFZ

Modern civilization could not have been what it is today without this energy transition from biomass to fossil fuels. Today's estimates of the total available fossil resources are too fuzzy, but show an inevitably limited supply of fossil resources. Considering a high threshold and at the current extraction rate, the end of fossil fuels is estimated at 500 years (Smil, 2021), i.e., 0.00001% of the time since the formation of the Earth. In this sense, low-carbon energies can be a real alternative and if developed in a suitable way, geothermal energy could play a key role in this new energy transition.

We must specify here that a geothermal reservoir is not only defined for an intensity and depth of temperature anomaly. Indeed, according to Börsing et al. (2017) and Niederau et al. (2019) enthalpy or entropy production could be more appropriate to to define the economicity of a geothermal reservoir. Futhermore, many other parameters such as the price of the steel involved in drilling, cost of drilling and feed in tariffs supporting the development of geothermal energy must then be taken into account to evaluate the feasibility and viability of the project

In this study we have scratched the surface of understanding a naturally permeable hydrothermal system as a whole and looked at some of the factors that may influence the fluid flow, the depth and the intensity of temperature anomalies. We considered CFZ to be naturally permeable zones, which would not require the use of hydrofracturing and/or hydroshearing processes, and therefore would limit the risk

of induced seismicity. In this work we have not dealt with these aspects, assuming that these large, naturally permeable deformation zones do not require such processes. However, permeability is not the only parameter to be taken into account when talking about induced seismicity.

Changes in pore pressures, changes in temperature, as well as faults and fractures can influence these processes in different ways. By comparing a 3D multi-fractured system and a single fault section under a given stress regime, Bruhn et al. 2015 showed that fracture heterogeneity plays a critical role on the magnitude of an induced seismic event. These authors demonstrate that the development of shear is controlled by pressure diffusion and that the contrasting properties of the different structures have a role on the mechanical processes. Furthermore, if the nearby structures have low natural hydraulic diffusivity, or are locked by other fault segments, the risk of inducing a significant event is higher as it can be pressurized over a large area.

These authors mention the effects of fracture heterogeneity. But it might be important to differentiate fracture density and distribution, and account for this on wave propagation. In any case, we can recommend, as Bruhn et al. 2015 do, geophysical studies of potentially sliding faults hundreds of meters from the injection wells before the process begins. Futhermore, since 2020, the United Downs Deep Geothermal Project (UDDGP) has been attempting to target a naturally fractured reservoir within the Cornish granite (heat producer) (Ledingham et al. 2019; Paulillo et al. 2020). Drilling in the Porthtowan subvertical strike-slip fault zone caused an earthquake of magnitude M = 1.5 (www.inducedearthquakes.org), too small to be felt by the local population. In our opinion, two things are interesting here: firstly, that the structure is subvertical, in strike-slip tectonic regime (two elements that have been highlighted in this these), and secondly, further driven by our optimism, that the seismicity induced in this kind of operation is limited.

Conclusion générale (version française)

L'objectif de cette thèse est d'augmenter la quantité d'énergie extraite du sous-sol en explorant de nouvelles cibles pour la géothermie de Haute-Température (T>150°C). De par leur nature perméable et profonde, les Zones de Failles Crustales constituent des cibles géologiques intéressantes en domaine de socle. Dans ces zones, la circulation de fluides par convection dépend d'un ensemble d'éléments. Au travers de modélisations numériques aux géométries simplifiées, et aux propriétés physiques réalistes, nous avons mis en avant que différents régimes convectifs existent et dépendent de paramètres comme :

(i) le pendage des zones de déformation géologiques

(ii) le rapport de la perméabilité entre les zones de déformation et l'encaissant

(iii) l'intensité et la direction d'une contrainte mécanique

(iv) le régime tectonique en place

Par les résultats de ces études paramétriques, des tendances générales peuvent être utilisées en phase exploratoire :

(v) les zones de déformations verticales concentrent les anomalies positives de température les plus intenses aux plus faibles profondeurs

(vi) les zones de déformation soumises à un régime tectonique décrochant concentrent les anomalies de températures les plus intenses avec une importante étendue spatiale

Ces résultats, génériques, ont pu être comparés et appliqués à un système naturel. D'après des données géologiques et géophysiques, la zone de faille de Pontgibaud

(Massif central, France) est une Zone de Faille Crustale abritant un système hydrothermal à quelques kilomètres de profondeur. En considérant une approche multidisciplinaire (observations de terrain, observations microscopiques, et analyses de laboratoire) la Zone de Failles Crustales de Pontgibaud est caractérisée par une large zone de déformation, sub-verticale, orientée N-S et intersectée par différentes familles de failles NE-SW, NW-SE et E-W. Ce réseau de failles présente les caractéristiques d'un potentiel réservoir à double perméabilité matrice-fracture. Les observations effectuées à différentes échelles (2.5 µm - 2 mm) montrent des structures drainantes suivant une géométrie dendritique. La théorie constructale suggère que cette géométrie, en limitant la résistance à l'écoulement, faciliterait la circulation des fluides. La circulation des fluides a pu être caractérisée en intégrant des données de terrain, des observations et mesures de laboratoires dans des modélisations numériques d'échelle crustale. Les dynamiques convectives de ces résultats sont comparables aux résultats des études paramétriques. De plus, la comparaison des résultats des modélisations numériques grande échelle avec des données de terrains (température, flux de chaleur, profil de résistivité) permettent d'estimer la profondeur de l'isotherme 150 °C à 2.3 km au niveau de la zone de faille crustale de Pontgibaud.

Finalement, en se basant sur une approche multidisciplinaire, nous émettons l'hypothèse que les Zones de Failles Crustales représentent de potentiels réservoirs pour des exploitations géothermiques de Haute-Température. Ces résultats seront plus approfondis dans de futurs travaux, et pourront considérer, par exemple, des modèles plus contraints (avec d'autres analyses de sensibilité). Ces tendances doivent également être confirmées par des forages réalisés par l'opérateur. Si ce potentiel est avéré, ce concept pourrait alors être utilisé sur d'autres zones d'études : Badenweiler-Lenzkirch Sutur (Allemagne), la zone de faille de Longmen Shan (Chine), la zone de faille de Pasmajärvi (Finlande), la faille de Keumwang (Corée du Sud), … Cette géoressource, pourrait donc accentuer son rôle dans la nouvelle transition énergétique, écologique.

General conclusion (english version)

The goal of this thesis is to increase the amount of energy extracted from the subsurface by exploring new targets for High-Temperature (T>150°C) geothermal energy. Due to their permeable and deep nature, Crustal Fault Zones are interesting geological targets in the basement domain. In these zones, the fluid circulation, by convection, depends on a set of elements. Through numerical modelling with simplified geometries and realistic physical properties, we have highlighted that different convective regime exist and depend on parameters such as:

(i) The dip of the geological deformation zones

(ii) The permeability ratio between the deformation zones and the basement

(iii) The intensity and direction of a mechanical stress

(iv) The tectonic regime at work

From the results of these parametric studies general trends can be used in the exploratory phase:

(v) Vertical deformation zones concentrate the highest temperature anomalies at the shallowest depths

(vi) Deformation zones subject to a strike-slip tectonic regime concentrate the most intense temperature anomalies with a large spatial extent

These generic results could be compared and applied to a natural system. According to geological and geophysical data, the Pontgibaud Fault Zone (Massif Central, France) is a Crustal Fault Zone hosting a hydrothermal system at a few kilometers depth. Considering a multidisciplinary approach (field observations, microscopic

observations, and laboratory analyses) the Pontgibaud Crustal Fault Zone is characterized by a large, sub-vertical, N-S oriented deformation zone intersected by different fault families NE-SW, NW-SE and E-W. This fault network has the characteristics of a dual matrix-fracture permeability. Observations at different scales (2.5 µm - 2 mm) show draining structures following a dendritic geometry. Constructal theory suggests that this geometry, by limiting resistance to flow, would facilitate fluid flow. Fluid circulation has been characterized by integrating field data, laboratory observations and measurements into crustal-scale numerical modelling. The convective dynamics of these results are comparable to the results of parametric studies. Moreover, comparison of the results of large-scale numerical modelling with field data (temperature, heat flux, resistivity profile) allowed to estimate the depth of the 150 °C isotherm at 2.3 km in the Pontgibaud crustal fault zone.

Finally, based on a multidisciplinary approach, we hypothesise that Crustal Fault Zones represent potential reservoirs for High Temperature geothermal exploitation. These results will be further investigated in future work, and may consider, for example, more constrained models (with further sensitivity analyses). These trends also need to be confirmed by operator drilling. If this potential is confirmed, then this concept could be used in other study areas: Badenweiler-Lenzkirch Sutur (Germany), the Longmen Shan fault zone (China), the Pasmajärvi fault zone (Finland), the Keumwang fault (South Korea), etc. This georesource could then accentuate its role in the new energy and ecological transition.

References

1 Publications and scientific communications associated with this thesis

1.1 Publication in peer-reviewed scientific journal

Duwiquet, H., Arbaret, L., Guillou-Frottier, L., Heap, M. J., & Bellanger, M.. On the geothermal potential of crustal fault zones: a case study from the Pontgibaud area (French Massif Central, France). *Geothermal Energy*, 2019, 7(1), 1-29. https://doi.org/10.1186/s40517-019-0150-7

Guillou-Frottier, L., **Duwiquet, H**., Launay, G., Taillefer, A., Roche, V., & Link, G.. On the morphology and amplitude of 2D and 3D thermal anomalies induced by buoyancy-driven flow within and around fault zones. *Solid Earth*, 2020, 11(4), 1571-1595. https://doi.org/10.5194/se-11-1571-2020

Duwiquet, H., Guillou-Frottier, L., Arbaret, L., Bellanger, M., Guillon, T., & Heap, M. J. Crustal Fault Zones (CFZ) as Geothermal Power Systems: A Preliminary 3D THM Model Constrained by a Multidisciplinary Approach. *Geofluids*, 2021. https://doi.org/10.1155/2021/8855632

Duwiquet, H., Magri, F., Lopez, S., Guillon, T., Arbaret, L., Bellanger, M., Guillou-Frottier, L. Tectonic regime as a control factor for Crustal Fault Zone (CFZ) geothermal reservoir in an amagmatic system. *Manuscrit to be submitted.*

Duwiquet *et al. Geotherm Energy* (2019) 7:33
https://doi.org/10.1186/s40517-019-0150-7

Geothermal Energy

RESEARCH Open Access

On the geothermal potential of crustal fault zones: a case study from the Pontgibaud area (French Massif Central, France)

Hugo Duwiquet[1,2,3,4*], Laurent Arbaret[1,3], Laurent Guillou-Frottier[2,3], Michael J. Heap[5] and Mathieu Bellanger[4]

*Correspondence:
hugo.duwiquet@gmail.com
[4] TLS-Geothermics, 92 Chemin de Gabardie, 31200 Toulouse, France
Full list of author information is available at the end of the article

Abstract

The present study aims to understand the potential of a new and novel type of geothermal play system for high temperature and electricity production: crustal fault zones (CFZ). According to geological and geophysical data, the Pontgibaud fault zone (French Massif Central) is suspected to host an active hydrothermal system at a depth of a few kilometers. The deep geometry of the fault zone and the permeability distribution are the main unknown parameters that are required to assess the geothermal potential of the Pontgibaud site. Structural and thin-section observations, laboratory permeability and connected porosity measurements and X-ray micro-tomography observations suggest that the hydrothermal system behaves like a double matrix-fracture permeability reservoir. Numerical modeling in which we varied the fault dip and the ratio between the fault zone permeability and host rock, *R*, was performed. Results indicate that three main convective regimes can be identified (weak convection, single cellular-type convection and bicellular convection). For a sufficiently high fault zone permeability ($> 1 \times 10^{-15}$ m^2), buoyancy-driven flow creates a positive thermal anomaly of several tens of °C at a depth of 2–5 km. For a vertical fault zone, the thermal anomaly is larger for higher *R* values. Numerical models, then applied to the geologically constrained Pontgibaud fault zone, show that a temperature of 150 °C at a depth of 2500 m can be obtained for a fault zone permeability of 1.6×10^{-14} m^2. Based on a multi-disciplinary approach, this work establishes a potential predictive tool for future high-temperature geothermal operations within basement rocks hosting large-scale fault systems.

Keywords: Crustal fault zones, Permeability, High-temperature geothermal system, Numerical modeling, Pontgibaud, French-Massif Central

Introduction

Exploring new geothermal targets requires the understanding of the factors affecting fluid circulation and heat transfer (Rowland and Sibson 2004; Fairley 2009). Understanding the distribution of permeability in the crust remains an essential component for the general comprehension of a geothermal model in the crustal domain, and therefore for the success of a geothermal prospect (Moeck 2014). Nowadays in France, most geothermal exploration licences are located in sedimentary basin areas or within graben structures. The Paris and Aquitaine basins, characterized by simple sedimentary structures, allow geothermal exploitation from low (30 °C) to medium (110 °C) temperature systems.

Figure 72 : Front cover of the publication (rank A) Duwiquet et al. 2019. In this study, field and laboratory data were integrated and tested in 2D numerical modelling with TH coupling. We highlighted the fact that vertical fault zones are privileged targets in the exploration phase. The role of the permeability ratio on the fluid flow was also investigated. Permeability is considered static, and heterogeneous in 2D. However, 3D and mechanical effects are not considered yet.

Solid Earth, 11, 1571–1595, 2020
https://doi.org/10.5194/se-11-1571-2020

Solid Earth Open Access EGU

On the morphology and amplitude of 2D and 3D thermal anomalies induced by buoyancy-driven flow within and around fault zones

Laurent Guillou-Frottier[1,2], Hugo Duwiquet[1,2,3], Gaëtan Launay[4], Audrey Taillefer[5], Vincent Roche[6], and Gaétan Link[7]

[1]BRGM, Georesources Division, 45060, Orléans, France
[2]ISTO, UMR7327, Université d'Orléans, CNRS, BRGM, 45071, Orléans, France
[3]TLS-Geothermics, 31200, Toulouse, France
[4]Harquail School of Earth Sciences, Laurentian University, P3E2C6, Sudbury, Canada
[5]CFG Services, 45060, Orléans, France
[6]ISTEP, UMR7193, Sorbonne Université, CNRS-INSU, 75005, Paris, France
[7]GET, UMR 5563, Université Toulouse III-Paul Sabatier, CNRS, IRD, CNES, 31400, Toulouse, France

Correspondence: Laurent Guillou-Frottier (l.guillou-frottier@brgm.fr)

Received: 10 April 2020 – Discussion started: 29 April 2020
Revised: 24 June 2020 – Accepted: 23 July 2020 – Published: 26 August 2020

Abstract. In the first kilometers of the subsurface, temperature anomalies due to heat conduction processes rarely exceed 20–30 °C. When fault zones are sufficiently permeable, fluid flow may lead to much larger thermal anomalies, as evidenced by the emergence of thermal springs or by fault-related geothermal reservoirs. Hydrothermal convection triggered by buoyancy effects creates thermal anomalies whose morphology and amplitude are not well known, especially when depth- and time-dependent permeability is considered. Exploitation of shallow thermal anomalies for heat and power production partly depends on the volume and temperature of the hydrothermal reservoir. This study presents a non-exhaustive numerical investigation of fluid flow models within and around simplified fault zones, wherein realistic fluid and rock properties are accounted for, as are appropriate boundary conditions. 2D simplified models point out relevant physical mechanisms for geological problems, such as "thermal inheritance" or pulsating plumes. When permeability is increased, the classic "finger-like" upwellings evolve towards a "bulb-like" geometry, resulting in a large volume of hot fluid at shallow depth. In simplified 3D models wherein the fault zone dip angle and fault zone thickness are varied, the anomalously hot reservoir exhibits a kilometer-sized "hot air balloon" morphology or, when permeability is depth-dependent, a "funnel-shaped" geometry. For thick faults, the number of thermal anomalies increases but not the amplitude. The largest amplitude (up to 80–90 °C) is obtained for vertical fault zones. At the top of a vertical, 100 m wide fault zone, temperature anomalies greater than 30 °C may extend laterally over more than 1 km from the fault boundary. These preliminary results should motivate further geothermal investigations of more elaborated models wherein topography and fault intersections would be accounted for.

1 Introduction

In the shallow crust, several geological systems meet the necessary conditions for the occurrence of significant deep fluid circulation. Tectonically active systems, ash-flow calderas, sedimentary basins, and especially crustal fault zones correspond to dynamic systems that are sufficiently porous and permeable to host fluid circulation (e.g., Simms and Garven, 2004; Hutnak et al., 2009; Lopez et al., 2016; Patterson et al., 2018a; Duwiquet et al., 2019). As soon as rock permeability is large enough, meteoric, metamorphic, or magmatic fluids can flow along kilometer-scale pathways at velocities reaching up to several meters per year (e.g., Forster and Smith, 1989; López and Smith, 1995). When fluid velocity is sufficiently large, heat can be advected with the fluid to shallow crustal levels (e.g., Ague, 2014), leading to the development of hydrothermal reservoirs and thus to exploitable ther-

Published by Copernicus Publications on behalf of the European Geosciences Union.

Figure 73 : Front cover of the publication (rank A) Guillou-Frottier et al. 2020. In this study, 2D and 3D numerical modelling with TH coupling was performed. Thermal inheritance effects were highlighted.Temperature anomalies can be concentrated in a fault zone but can also extend into the basement. The effects of time-varying permeability on fluid flow were tested. In 3D, the trend is confirmed: vertical fault zones concentrate the most intense temperature anomalies. However, mechanical effects are not considered yet.

Hindawi
Geofluids
Volume 2021, Article ID 8855632, 24 pages
https://doi.org/10.1155/2021/8855632

WILEY | Hindawi

Research Article

Crustal Fault Zones (CFZ) as Geothermal Power Systems: A Preliminary 3D THM Model Constrained by a Multidisciplinary Approach

Hugo Duwiquet,[1,2,3] **Laurent Guillou-Frottier**,[1,2] **Laurent Arbaret**,[2] **Mathieu Bellanger**,[3] **Théophile Guillon**,[1] **and Michael J. Heap**[4]

[1]*BRGM, Georesources Division, Av. C. Guillemin, BP 36009, F-45060 Orléans Cedex 2, France*
[2]*ISTO, UMR 7327, University of Orléans, CNRS, BRGM, 1A Rue de la Férollerie, 45071, Orléans, France*
[3]*TLS-Geothermics, 91 Chemin de Gabardie, 31200 Toulouse, France*
[4]*University of Strasbourg, CNRS, ENGEES, Institut Terre et Environnement de Strasbourg (ITES), UMR 7063, 5 Rue Descartes, Strasbourg F-67084, France*

Correspondence should be addressed to Hugo Duwiquet; hugo.duwiquet@cnrs-orleans.fr

Received 18 September 2020; Revised 7 December 2020; Accepted 16 December 2020; Published 4 February 2021

Academic Editor: Hang Lin

The Pontgibaud crustal fault zone (CFZ) in the French Massif Central provides an opportunity to evaluate the high-temperature geothermal potential of these naturally permeable zones. Previous 2D modeling of heat and mass transfer in a fault zone highlighted that a subvertical CFZ concentrates the highest temperature anomalies at shallow depths. By comparing the results of these large-scale 2D numerical models with field data, the depth of the 150°C isotherm was estimated to be at a depth of 2.5 km. However, these results did not consider 3D effects and interactions between fluids, deformation, and temperature. Here, field measurements are used to control the 3D geometry of the geological structures. New 2D (thin-section) and 3D (X-ray microtomography) observations point to a well-defined spatial propagation of fractures and voids, exhibiting the same fracture architecture at different scales (2.5 μm to 2 mm). Moreover, new measurements on porosity and permeability confirm that the highly fractured and altered samples are characterized by large permeability values, one of them reaching 10^{-12} m^2. Based on a thermoporoelastic hypothesis, a preliminary 3D THM numerical model is presented. A first parametric study highlights the role of permeability, stress direction, and intensity on fluid flow. In particular, three different convective patterns have been identified (finger-like, blob-like, and double-like convective patterns). The results suggest that vertical deformation zones oriented at 30 and 70° with respect to the maximum horizontal stress direction would correspond to the potential target for high-temperature anomalies. Finally, a large-scale 3D numerical model of the Pontgibaud CFZ, based on THM coupling and the comparison with field data (temperature, heat flux, and electrical resistivity), allows us to explore the spatial geometry of the 150°C isotherm. Although simplified hypotheses have been used, 3D field data have been reproduced.

1. Introduction

As potential geothermal reservoirs, crustal fault zones (CFZ) are still largely unexplored and unexploited (e.g., South Erzgebirge deep fault zone, Germany [1]; Gravberg, Sweden [2, 3]; Badenweiler-Lenzkirch Sutur, Germany [4]; Dewey's Fault Zone, Canada [5]; Longmen Shan Fault Zone, China [6, 7]; Pasmajärvi Fault Zone, Finland [8]; and Luchlompal fault, Russia [9]). The cost-effectiveness of a reservoir depends on permeability, heat, and fluid flow. These conditions are often related to a specific geodynamic context and the physical conditions of heat transport.

A CFZ is generally not a simple plane but rather has a complex geometry defined by a succession of fault and fracture intersections reflecting intense deformation [10–12]. CFZ are manifestations of strain localization and modify the

Figure 74 : Front cover of the publication (rank A) Duwiquet et al. 2021. A more refined multidisciplinary approach was considered. The 3D architecture of the fault networks could be integrated into 3D models with THM coupling. The permeability is considered static and heterogeneous in 3D. Based on a poroelastic hypothesis, some mechanical parameters were tested on the fluid flow. Some stress orientations are favourable to the emergence of a temperature anomaly. But we have not been able to identify any process that could explain these phenomena. Considering permeability as a dynamic parameter and more realistic mechanical boundary conditions could allow to isolate and understand such a process.

Tectonic regime as a control factor for Crustal Fault Zone (CFZ) geothermal reservoir in an amagmatic system

H. Duwiquet, F. Magri, S. Lopez, T. Guillon, L. Arbaret, M. Bellanger, L. Guillou-*Frottier*

Abstract

The Crustal Fault Zones provides an interesting geological target for high temperature geothermal energy source in naturally deep-fractured basement areas. Field and laboratory studies have already shown the ability of these systems to let fluid flow down to Brittle-Ductile-Transition. However, several key questions about exploration still exist, in particular the fundamental effect of tectonic regimes on fluid flow in fractured basement domains. Based on poroelasticity assumption, we considered an idealized 3D geometry and realistic physical properties. We examined a model with no tectonic regime (benchmark experiment) and a model with different tectonic regimes applied. Compared to the benchmark experiment, the results suggest that different tectonic regimes cause pressure changes in the fault/basement system. The tectonic-induced pressure changes affect fluid patterns, onset of convection as well as the spatial extent of thermal plumes and the intensity of the temperature anomalies.

Figure 75 : Front cover of a manuscript to be submitted to a rank A publication. 3D numerical modelling with THM coupling was performed. The permeability is considered to be dynamic and adapted to fractured media. We were able to test the effect of different tectonic regimes on fluid flow, and to see the effects on temperature anomalies. Poroelastic driven forces were used to explain the observed differences. It appears that the strike-slip systems are favourable to the development of a large temperature anomaly. These effects should be considered when studies are undertaken on natural systems. However, the complexity of these systems may reduce or increase the impact of these effects.

1.2 Scientific publications in international conference proceedings

Duwiquet, H., Arbaret, L., Bellanger, M., Guillou-Frottier, L., & Heap, M. Are Crustal Fault Zones viable geothermal resources? Insights from the Pontgibaud Fault in French Massif Central. *European Geothermal Congress 11-14 June, 2019 - Den Haag, The Netherlands. Oral Session.*

Duwiquet, H., Guillou-Frottier, L., Arbaret, L., Guillon, T., Bellanger, M., & Heap, M. (2020, February). Crustal Fault Zone: New geothermal reservoir? Structural dataset and preliminary 3D TH (M) modelling of the Pontgibaud fault zone (French Massif Central). *In 45th Workshop on Geothermal Reservoir Engineering, Stanford University-USA. Oral Session.*

Duwiquet, H., Guillou-Frottier, L., Arbaret, L., Guillon, T., Heap, M., & Bellanger, M. (2020, November). Characterization of Crustal Fault Zones as Geothermal Reservoirs: A Multidisciplinary Approach. *In 1st Geoscience & Engineering in Energy Transition Conference (Vol. 2020, No. 1, pp. 1-4). European Association of Geoscientists & Engineers, Strasbourg-France. Oral Session.*

Duwiquet, H., Guillou-Frottier, L., Arbaret, L., Bellanger, M., Guillon, T., & Heap, M. (2021, February). Crustal Fault Zones (CFZ) as Geothermal Power Systems: 3D Variation of Permeability and Related Processes. *In 46th Workshop on Geothermal Reservoir Engineering, Stanford University-USA. Oral Session.*

Duwiquet, H., Guillou-Frottier, L., Arbaret, L., Magri, F., Guillon, T., Bellanger, M., Lopez, S.,& Heap, M. (2022, February). Crustal Fault Zones as Underexploited Geothermal Resources: Contribution of Numerical Modelling and Comparison with Natural Systems. *In 47th Workshop on Geothermal Reservoir Engineering, Stanford University-USA. Oral Session.*

European Geothermal Congress 2019
Den Haag, The Netherlands, 11-14 June 2019

Are Crustal Fault Zones viable geothermal resources? Insights from the Pontgibaud Fault in French Massif Central

Hugo Duwiquet[1,2,3], Laurent Arbaret[1], Mathieu Bellanger[3], Laurent Guillou-Frottier[1,2], Michael J. Heap[4].

[1] ISTO, UMR 7327, Université d'Orléans, CNRS, BRGM, 1A rue de la Férollerie, 45071, Orléans, France

[2] BRGM, 3 av. C. Guillemin, BP39009, 45060, Orléans, Cedex 2, France

[3] TLS-Geothermics, 14bis chemin de l'Enguille, 31180, St Genies-Bellevue, France

[4]Institut de Physique de Globe de Strasbourg, UMR 7516 CNRS, Université de Strasbourg/EOST, 5 rue René Descartes, 67084, Strasbourg cedex, France

hugo.duwiquet@gmail.com

Keywords: Permeability, porosity, high-temperature geothermal system, numerical modelling, Pontgibaud, French Massif Central.

ABSTRACT

Numerous recent studies indicate that crustal-scale fault zones represent efficient conduits for meteoric fluid to flow down to mid-crustal depths (Haines et al., 2016), in particular near the brittle-ductile transition where temperature are around 350-450°C (Violay et al., 2016). The present study aims to understand the potential of a new and novel type of geothermal system for high temperature and electricity production: the Crustal Fault Zones (CFZ). The geothermal potential estimation in a basement context requires combination of geological, geophysical and thermal data. The Pontgibaud fault zone (Puy-de-Dôme, French Massif Central) includes an intensive multivariate dataset.

1. STRUCTURES AND FAVOURABLE FEATURES FOR FLUID CIRCULATION IN THE "LA SIOULE" LICENCE

Since 2014, TLS-Geothermics, a French company involved in geothermal exploration (http://www.tls-geothermics.fr/), have been keen to demonstrate the viability of CFZ's as a play for economic power generation. The demonstration of the potential of CFZ's is underway at a site in the French Massif Central (FMC) using an exploration licence named "La Sioule". Several geological observations and geophysical data, some of which being detailed in Figure 1, represent good indicators for high temperature geothermal exploitation (temperatures > 150°C for a depth lower than 3,500 m).

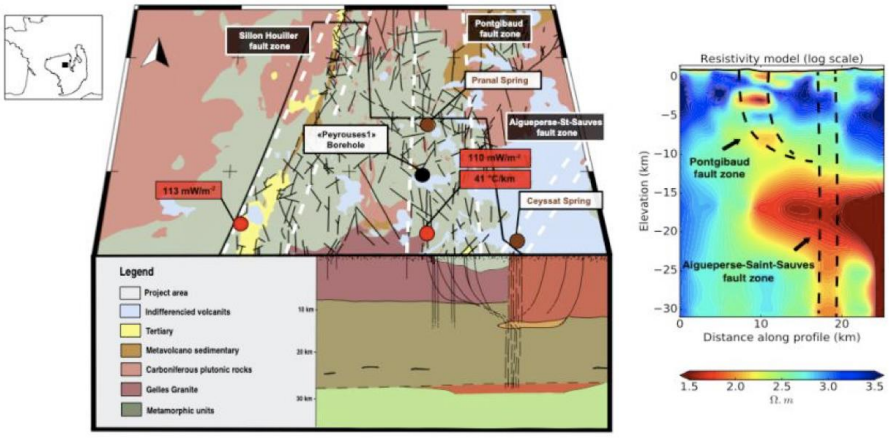

Figure 1 : Synthesis of critical available data on the "La Sioule" licence. Three principal fault zone are delineated by dashed white lines.

1

Figure 76 : Front cover of the rank B publication Duwiquet et al. 2019. This publication synthesizes the rank A publication which was published in the same year.

PROCEEDINGS, 45th Workshop on Geothermal Reservoir Engineering
Stanford University, Stanford, California, February 10-12, 2020
SGP-TR-216

Crustal Fault Zone: New geothermal reservoir? Structural dataset and preliminary 3D TH(M) modelling of the Pontgibaud fault zone (French Massif Central)

Hugo Duwiquet[1,2,3*], Laurent Guillou-Frottier[2], Laurent Arbaret[1], Théophile Guillon[2], Mathieu Bellanger[3], and Michael J. Heap[4]

[1] ISTO, UMR 7327, Université d'Orléans, CNRS, BRGM, 1A rue de la Férollerie, 45071, Orléans, France
[2] BRGM, 3 av. C. Guillemin, BP39009, 45060, Orléans, Cedex 2, France
[3] TLS-Geothermics, 91 Chemin de Gabardie, 31200, Toulouse, France
[4]Institut de Physique de Globe de Strasbourg, UMR 7516 CNRS, Université de Strasbourg/EOST, 5 rue René Descartes, 67084, Strasbourg cedex, France

*hugo.duwiquet@tls-geothermics.fr

Keywords: Crustal Fault Zone, high-temperature geothermal system, structural geology, 2D and 3D numerical modelling, TH, THM, French Massif Central.

ABSTRACT

Numerous recent studies indicate that crustal-scale fault zones represent efficient conduits for meteoric fluids to flow down to mid-crustal depths (Haines et al., 2016). The present study aims to understand the potential of a new and novel type of geothermal system for high temperature and electricity production: Crustal Fault Zones (CFZ). One such example is the Pontgibaud fault zone (French Massif Central), a 30 km-long and 3 km-wide mineralized fault zone. The Pontgibaud fault zone is also characterized by numerous CO_2-rich-thermo-mineral springs. Moreover, this area is also defined by local and regional surface heat flow values of 110 mW/m^2 (International Heat Flow Commission database) involving temperature gradients between 37 and 41 °C/km. The Pontgibaud fault zone has been well studied in the last few years (Bellanger et al., 2017), electrical conductivity anomalies have been identified (Ars et al., 2019) and the temperature anomaly has been estimated (Duwiquet et al., 2019). Estimation of the geothermal resource have been established by 2D geological numerical modelling, with Thermal-Hydraulic (TH) coupling. Here we propose to integrate structural field observation into 3D geological numerical modelling with Thermal-Hydraulic-(Mechanical) (TH(M)) coupling. We then evaluate the various applications for high-temperature geothermal exploitation.

1. INTRODUCTION

CFZ can be defined as crustal-scale heterogeneities, which localize the deformation and thus modify the mechanical properties of the crust down to Brittle-Ductile Transition (BDT). These CFZ can be found worldwide, e.g. Liquine-Ofqui fault zone, Chile (Lahsen et al., 2010) Badeweiler-Lenzkirch Sutur, Germany (Brockamp et al., 2015). Among the first studies on fluid circulation within a fault, Murphy (1979) highlighted vertical thermal instabilities linked to convection cells, and then localized positives and negatives thermal anomalies. While fault often host hydrothermal systems (Faulds et al., 2010), the permeability of these networks depends on a multitude of parameters. A parametric study was able to show that the greater the permeability ratio between the fault and its host, the shallower the temperature anomaly will be. Moreover, vertical faults will concentrate the strongest temperature anomalies at shallower depths (Duwiquet et al., 2019). Additional one parameters appears to be the relationships between fault geometry and stress field (Barton et al., 1995; Siler et al., 2019).

Consequently, it is worth using a multidisciplinary approach to strongly constrain fluid flow models in hydrothermal systems (Oda, 1986; Faulkner et al., 2010; Bense et al., 2013). As an example, the recent study by Edel et al., (2018) predicts using a combination of magnetic gravity, seimic and geological data, a temperature of 150 °C at a depth of 2500m in the northern Vosges area (France). With an improved numerical modelling approach, Guillou-Frottier et al., (2013) reproduced and predicted temperatures at geothermal sites of Soultz-sous-Forêts and Rittershoffen.

Since 2014, TLS Geothermics, a French company involved in geothermal exploration has been keen to demonstrate the viability of CFZ as a geothermal exploration play for economic power generation. The Pontgibaud fault zone, located in the "La Sioule" licence (figure 1) corresponds to well-suited case study since numerous data are available (lithology, topography, springs geochemistry, thermal properties, magnetotellurics, gravimetry...) (Bellanger 2017). Thanks to this complete dataset, a multidisciplinary approach (including field, laboratory and numerical modelling study), has been performed and trend to confirm the high-temperature geothermal potential of CFZ (Duwiquet et al., 2019). However, a better understanding of the 3-dimensional spatial distribution of the 150°C economic isotherm requires 3D numerical simulation. These 3D modelling would make it possible to consider geological units not as plans but as volumes (Magri et al., 2016; Person et al., 2012; Patterson et al., 2018). Furthermore, the integration of the THM coupling will make it possible to see the effects on permeability, fluid flow and consequently to target the intensity and depth of positive thermal anomaly.

Figure 77 : Front cover of the publication (rank B) Duwiquet et al. 2020. This study shows the first results in 3D with a THM coupling.

GET2020 EAGE

Introduction

As potential geothermal reservoirs, Crustal Fault Zones are still largely unexplored and unexploited (e.g. South Erzebirge deep fault zone, Germany (Achtziger-Zupančič, 2017), Gravberg, Sweden (Juhlin and Sandstedt 1989, Lund and Zoback 1999)). A multi-disciplinary approach has made it possible to estimate the position of the 150 °C isotherm at 2.5 km depth at the Pontgibaud Crustal Fault Zone (French Massif Central), highlighting its geothermal potential (Duwiquet et al., 2019). Although consistent with field data, this estimate did not take the 3D distribution of permeability, the 3D geometry of fault networks, and the poroelastic effects on fluid flow, and the intensity and depth of temperature anomalies into account. With more measurements, observations, and 3D modeling based on thermo-hydro-mechanical (THM) coupling, this study proposes to better characterize the geothermal reservoir potential of the Pontgibaud Crustal Fault Zone.

Favourable structure for fluid circulation: the Pontgibaud Crustal Fault Zone

The Pontgibaud Crustal Fault Zone is N-S fault zone that runs parallel to the Chaîne des Puys. The Pontgibaud Crustal Fault Zone has length of over 40 km, and is pinched between the Sillon Houiller and the Aigueperse-St-Sauve fault zones. This fault zone is affected by As-Au, Pb-Zn, and Ba-F mineralization. If evidence for paleo-fluid circulation exists, current fluid circulation along this fault zone is also very likely. Indeed, the resurgence of Pranal is in the middle of the Pontgibaud Crustal Fault Zone. Temperature measurements have been carried out between depths of 55 and 120 m. From these measurements, a geothermal gradient of 41 °C/km has been inferred and a heat flux of 100 $mW.m^{-2}$ was estimated (IHFC database; http://ihfc-iugg.org/). Magnetotelluric campaigns have been conducted in the Pontgibaud Crustal Fault Zone between 2015 and 2017. Two anomalies located at depths of 3 and 8 km in the brittle crust and could be linked to the presence of magma, clays (smectites), and/or hydrothermal fluids (Ars et al., 2019). These two anomalies appear to be related to the Pontgibaud Crustal Fault Zone.

Methods

The multidisciplinary approach used here is a method widely used in oil and uranium exploration, CO_2 capture and storage studies, and reservoir engineering. It combines a field approach (structural measurements and sampling of the Peyrouses 1 borehole), a laboratory approach (thin section and X-Ray micro-tomography observations, measurements of permeability and connected porosities (the measurements were made according to the protocol of Heap and Kennedy (2016)), and numerical modelling. The modelling component will integrate the laboratory measurements and field observations into 3D numerical modelling based on THM coupling using the Comsol Multiphysics™ software. A particular intention will be brought to the 3D representation of permeability with the knowledge of field and laboratory observations and measurements.

Results and discussion

Field observations and measurements show sub-vertical N-S structures along the Pb-Zn veins over several tens of kilometres. These N-S structures form a large deformation zone (>3 km) that is intersected by other faults with E-W, NE-SW, NW-SE directions (Figure 1). These other fault families are more widely observed around the Pontgibaud Crustal Fault Zone. Geophysical and field data show that this near-vertical structure takes root at a depth of up to 8 km (Duwiquet et al., 2020).

Thin-section and X-ray micro-tomography observations show highly altered and fractured facies. Voids are present at different observation scales from 2.5 µm to 2 mm and are connected in 3D (Figure 1). These pores are found in the cores of secondary mineralization, but also in fracture networks distributed beyond the veins. These fracture networks follow a dendritic network and disperse smaller and smaller pores within the basement. This particular fracture geometry in a heterogeneous and porous system could facilitate fluid flow (Bejan and Lorente, 2007).

The measured permeability values varied between 2×10^{-18} and 7×10^{-13} m^2, while the connected porosity values varied between 6 and 22%. The highest porosity and permeability were measured for

1st Geoscience & Engineering in Energy Transition Conference
16 – 18 November 2020, Strasbourg, France

Figure 78 : Front cover of the publication (rank B) Duwiquet et al. 2020. This publication summarizes the results that will be published in early 2021 in Geofluids. These results consider a THM coupling with 3D geometries. The permeability remains static, although heterogeneous in the three spatial dimensions.

PROCEEDINGS, 46th Workshop on Geothermal Reservoir Engineering
Stanford University, Stanford, California, February 15-17, 2021
SGP-TR-218

Crustal Fault Zones (CFZ) as Geothermal Power Systems: 3D Variation of Permeability and Related Processes

Hugo Duwiquet[1,2,3*], Laurent Guillou-Frottier[1,2], Laurent Arbaret[2], Mathieu Bellanger[3], Théophile Guillon[1], Michael J. Heap[4]

[1] BRGM, av. C. Guillemin, BP 36009, F-45060 Orléans Cedex 2, France.
[2] Univ. Orléans, CNRS, BRGM, ISTO, UMR7327 F-45071 Orléans, France.
[3] TLS-Geothermics, 91 chemin de Gabardie, 31200, Toulouse, France.
[4] Université de Strasbourg, CNRS, ENGEES, Institut Terre et Environnement de Strasbourg (ITES), UMR 7063, 5 rue Descartes, Strasbourg F-67084, France.

*hugo.duwiquet@gmail.com

Keywords: 3D permeability variations, THM numerical modeling, high-temperature geothermal energy, Crustal Fault Zone (CFZ).

ABSTRACT

The Pontgibaud Crustal Fault Zone (CFZ) in the French Massif Central provides an opportunity to evaluate the high-temperature geothermal potential of these naturally permeable zones. Previous 2D modeling of heat and mass transfer in a fault zone highlighted that a subvertical CFZ concentrates the highest temperature anomalies at shallow depths. By comparing the results of these large-scale 2D numerical models with field data, the depth of the 150°C isotherm was estimated to be at a depth of 2.5 km. However, these results did not consider 3D effects and interactions between fluids, deformation and temperature. A combined multidisciplinary approach makes it possible to better constrain the variation of permeability in 3D. This variation is then integrated into 3D numerical modeling. Based on a thermo-poroelastic assumption, a preliminary 3D THM numerical model is presented. A first parametric study highlights the role of permeability, stress direction and stress intensity on fluid flow. In particular, three different convective patterns have been identified: finger-like, blob-like and double-like convective patterns. Finally, a large-scale 3D numerical model of the Pontgibaud CFZ, based on THM coupling and the comparison with field data (temperature, heat flux, electrical resistivity), allows us to observe the convective pattern at the origin of the rise of the 150°C isotherm to economically exploitable depths. This result is obtained for values of permeability, intensity and direction of stresses comparable to the parametric study. Although simplified hypotheses have been used, 3D field data have been reproduced. Finally, we tried to understand the observed effects of poroelasticity on fluid flow.

1. INTRODUCTION

As potential renewable and economical resources, Crustal Fault Zones (CFZ) remain largely unexplored and therefore unexploited. Widely present on Earth (Scibeck, 2020), these naturally permeable zones have all the characteristics of a potential reservoir for high-temperature geothermal energy and therefore offer significant energy potential over the world. Moreover, these naturally permeable and deep zones would limit the use of hydrofracturing and/or hydroshearing that could induce seismic events that have disrupted geothermal projects or suspended operations (Deichmann and Giardini 2009, Evans et al., 2005). Since 2014, TLS-Geothermics, a French company involved in geothermal exploration, has been keen to demonstrate the viability of CFZ as a geothermal exploration play for economic power generation.

This kind of reservoir is currently poorly constrained, probably due to a lack of understanding of the primary geological factors controlling the occurrence of this type of geothermal play. In order to facilitate exploration, it seems necessary to be able to dissociate the key parameters favoring the ascent of hot fluid to economically attractive depths. Previous studies have shown that vertical deep deformation zones, could concentrate the most important temperature anomalies at the lowest depths (Duwiquet et al., 2019; Guillou-Frottier et al., 2020). Our recent results suggest that vertical deformation zones oriented at 30 and 70° relative to maximum horizontal stress could correspond to potential targets for high-temperature geothermal energy (Duwiquet et al., 2021). Permeability variation in crustal domain has been widely discussed since the 1990s (Martel, 1990). Overall, the permeability variation of CFZ is primarily controlled by the coupling between Thermal (T), Hydraulic (H), Mechanical (M), and Chemical (C) processes (Horne, 1979; Parry et al., 1988; Barton et al., 1995). Permeability can be considered as a static and isotropic parameter in space. Different studies have reproduced field data by considering fixed fault permeabilities around 10^{-14} m^2 (Guillou-Frottier et al., 2013; Magri et al., 2016). For large-deformation fault zones field data from the Pontgibaud CFZ have been reproduced by considering a static but variable permeability in different space dimensions. (Duwiquet et al., 2019; 2020; 2021). However, permeability has been recognized as a dynamic parameter evolving in time and space as a result of the various geological processes (Sibson et al., 1988; Ingebritsen and Gleeson, 2015).

In this study, we first propose additional field observations to better constrain permeability variation in the three dimensions. This variation in permeability will be integrated into a 3D coupled THM numerical modeling where a thermo-poroelastic hypothesis is assumed. These results will be compared with field data. Our multidisciplinary approach will facilitate the understanding of how fluids can circulate within a naturel system. Finally, a 3D numerical study with THM coupling and dynamic permeability will attempt to approach the different processes that can control the fluids circulation within a fault.

1

Figure 79 : Front cover of the publication (rank B) Duwiquet et al. 2021. Considering permeability as a dynamic parameter adapted to fractured media could help to understand the effect of mechanical processes having an impact on fluid flow.

PROCEEDINGS, 47th Workshop on Geothermal Reservoir Engineering
Stanford University, Stanford, California, February 7-9, 2022
SGP-TR-223

Crustal Fault Zones as underexploited geothermal resources: Contribution of numerical modelling and comparison with natural systems

Hugo Duwiquet[1,2,3*], Laurent Guillou-Frottier[1,2], Laurent Arbaret[2], Fabien Magri[4,5], Theophile Guillon[1], Mathieu Bellanger[3], Simon Lopez[1] and Michael J. Heap[6]

[1]BRGM, av. C. Guillemin, BP 36009, Orléans Cedex 2 F-45060, France. [2]Univ. Orléans, CNRS, BRGM, ISTO, UMR7327 F-45071 Orléans, France. [3]TLS-Geothermics, 91 chemin de Gabardie, 31200, Toulouse, France. [4]Department of Environmental Informatics (ENVINF), Helmotz Centre for Environmental Research (UFZ), Leipzig, Germany. [5]Freie Universität Berlin, Department of Hydrogeology, Berlin, Germany.[6]Univ. Strasbourg, CNRS, ENGEES, ITES, UMR 7063, 5 rue Descartes, Strasbourg.

*hugo.duwiquet@gmail.com

Keywords: Crustal Fault Zone, Exploration, High-Temperature Geothermal Systems, Multidisciplinary Approach, Multiphysics Modelling.

ABSTRACT

Crustal Fault Zones (CFZ) are an interesting geological target for high-temperature geothermal resources in naturally fractured and deep basement zones. Field and laboratory studies have already shown the ability of these systems to favor fluid flow down to brittle-ductile-transition. However, several key questions about exploration still exist, in particular the role of structural dip, permeability, and the effect of mechanical stress and more broadly the fundamental role of tectonic regimes on fluid flow in naturally fractured basement domains.

Considering 2D and 3D numerical modelling, with TH and THM couplings, two trends can be identified and integrated for the exploration of these targets (i) vertical faults concentrate the highest temperature anomalies at the shallowest depths (ii) strike-slip systems favor the largest temperature anomalies.

Geological and geophysical data suggest that, the Pontgibaud fault zone (French Massif Central) is a CFZ that host an active hydrothermal system at a depth of a few kilometers. We conducted an integrated study to assess its high temperature geothermal potential. Field measurements are used to control the 3D geometry of the geological structures. 2D (thin-section) and 3D (X-ray microtomography) observations point to a well-defined spatial propagation of fractures and voids, exhibiting the same fracture architecture on different scales (2.5 µm to 2 mm). Moreover, measurements of porosity and permeability confirm that the highly fractured and altered samples are characterized by high permeability values, with one sample characterized by a permeability as high as 10^{-12} m^2. Finally, a large-scale 3D numerical model of the Pontgibaud CFZ, based on THM coupling and the comparison with field data (temperature, heat flux, and electrical resistivity), allowed to explore the spatial extent of the 150°C isotherm, which rises up to a depth of 2.3 km. Though based on simplified hypotheses, our model reproduces field data. A multi-disciplinary integrative approach based on coupled 3D modeling proved to be an efficient way to assess the geothermal potential of CFZ and predict temperature distributions. It can be used as a predictive tool to develop high-temperature geothermal operations within basement rocks hosting large-scale fault systems.

Figure 80 : Front cover of the publication (rank B) Duwiquet et al. 2022. This study will synthesise all the methods and results acquired in the framework of this thesis. It will also highlight the limitations and perspectives of this work.

1.3 Participation in national and international conferences

Strasbourg Geothermal Workshop, 10-11 October 2018, Strasbourg, France. Posters session.

European Geosciences Union, 7-12 April 2019, Vienne, Autriche. Posters session.

European Geothermal Congress, 11-14 June 2019, La Haye, Pays-Bas. Oral session.

Stanford Geothermal Workshop, 10-12 February 2020, Stanford, USA. Oral session.

Geoscience and engineering in Energy Transition, 16-18 November 2020, Strasbourg, France, Oral session.

Stanford Geothermal Workshop, 15-17 February 2021, Stanford, USA. Oral session.

European Geothermal Workshop, 23-24 September 2021, Karlsruhe, Allemagne. Oral session.

Réunion de Sciences de la Terre, 01-05 November 2021, Lyon, France. Oral session.

Stanford Geothermal Workshop, 7-9 February 2022, Stanford, USA. Oral session.

2 General References

A

Achtziger-Zupančič, P., Loew, S., & Hiller, A. (2017). Factors controlling the permeability distribution in fault vein zones surrounding granitic intrusions (Ore Mountains/Germany). *Journal of Geophysical Research: Solid Earth*, 122(3), 1876-1899.

Alaskar, M., Ames, M., Connor, S., Liu, C., Cui, Y., Li, K., & Horne, R. (2012). Nanoparticle and microparticle flow in porous and fractured media—an experimental study. *Spe Journal*, 17(04), 1160-1171.

Alcalde, J., Marzán, I., Saura, E., Martí, D., Ayarza, P., Juhlin, C., ... & Carbonell, R. (2014). 3D geological characterization of the Hontomín CO_2 storage site, Spain: Multidisciplinary approach from seismic, well-log and regional data. *Tectonophysics*, 627, 6-25.

Altmann, J. B., Heidbach, O., & Gritto, R. Relative importance of processes leading to stress changes in the Geysers geothermal area. In Proceedings of thirty-eighth workshop on geothermal reservoir engineering, (2013).

American Geological Institute. Global GIS: volcanoes of the world; volcano basic data. EarthWorks, Stanford University https://earthworks.stanford.edu/catalog/harvard-glb-volc (2020).

Anderson EM (1934) Earth contraction and mountain building. *Gerlands Beiträge zur Geophisik* 42:133–159, 43:1–18.

Anderson, E. M. (1905). The dynamics of faulting. *Transactions of the Edinburgh Geological Society*. 8(3), 387- 402.

Anovitz, L. M., & Cole, D. R. (2015). Characterization and analysis of porosity and pore structures. *Reviews in Mineralogy and geochemistry*, 80(1), 61-164.

Armandine Les Landes, A., Guillon, T., Peter-Borie, M., Blaisonneau, A., Rachez, X., & Gentier, S. (2019). Locating geothermal resources: insights from 3D stress and flow models at the upper Rhine Graben scale. *Geofluids*, 2019.

Arnórsson, S. (1995). Geothermal systems in Iceland: structure and conceptual models—I. High-temperature areas. *Geothermics*, 24(5-6), 561-602.

Ars, J. M., Tarits, P., Hautot, S., Bellanger, M., Coutant, O., & Maia, M. (2019). Joint inversion of gravity and surface wave data constrained by magnetotelluric: application to deep geothermal exploration of crustal fault zone in felsic basement. *Geothermics*, 80, 56-68.

Ashwell, P. A., Kendrick, J. E., Lavallée, Y., Kennedy, B. M., Hess, K. U., von Aulock, F. W., ... & Dingwell, D. B. (2015). Permeability of compacting porous lavas. *Journal of Geophysical Research: Solid Earth*, 120(3), 1605-1622.

Axelsson, G. (1985). Hydrology and thermomechanics of liquid-dominated hydrothermal systems in Iceland.

B

Baietto, A., Cadoppi, P., Martinotti, G., Perello, P., Perrochet, P., & Vuataz, F. D. (2008). Assessment of thermal circulations in strike-slip fault systems: the Terme di

Valdieri case (Italian western Alps). *Geological Society, London, Special Publications*, 299(1), 317-339.

Barton, C. A., Zoback, M. D., & Moos, D. (1995). Fluid flow along potentially active faults in crystalline rock. *Geology*, 23(8), 683-686.

Ballas, G., Soliva, R., Sizun, J. P., Benedicto, A., Cavailhes, T., & Raynaud, S. (2012). The importance of the degree of cataclasis in shear bands for fluid flow in porous sandstone, Provence, France. *AAPG bulletin*, 96(11), 2167-2186.

Baubron, J. C., & JC, B. (1980). Nouvelles datations K/Ar sur des filons à quartz et fluorine du Massif Central français.

Baubron, J.C ; Cantagrel, J.M. (1980) Les deux volcans des Monts-Dores (Massif Central Français). *Comptes-rendus de l'Académie des Sciences Paris, sér. D.* 290, 1409-1412.

Bealieu, S. E. & Szafranski, K. (2020) InterRidge Global Database of Active Submarine Hydrothermal Vent Fields, Version 3.4. http://vents-data.interridge.org. 2019 GEMS.

Becquerel H (1896) Sur les radiations émises par phosphorescence. *Comptes rendus de l'Académie des Sciences*, Paris 122:420–421 (in French).

Bejan, A. (1997). Constructal-theory network of conducting paths for cooling a heat generating volume*. International Journal of Heat and Mass Transfer*, 40(4), 799-816.

Bejan, A. (2000). From heat transfer principles to shape and structure in nature: constructal theory. *J. Heat Transfer*, 122(3), 430-449.

Bejan, A., & Lorente, S. (2006). Constructal theory of generation of configuration in nature and engineering. *Journal of applied physics*, 100(4), 5.

Bejan, A., & Lorente, S. (2008). Design with constructal theory.

Bejan, A., & Lorente, S. (2011).The constructal law and the evolution of design in nature. *Physics of life Reviews*, 8(3), 209-240.

Bense, V. F., & Person, M. A. (2006). Faults as conduit-barrier systems to fluid flow in siliciclastic sedimentary aquifers. *Water Resources Research*, 42(5).

Bense, V. F., Person, M. A., Chaudhary, K., You, Y., Cremer, N., & Simon, S. (2008). Thermal anomalies indicate preferential flow along faults in unconsolidated sedimentary aquifers. *Geophysical Research Letters*, 35(24).

Bense, V. F., Gleeson, T., Loveless, S. E., Bour, O., & Scibek, J. (2013). Fault zone hydrogeology. *Earth-Science Reviews*, *127*, 171-192.

Ben-Zion, Y., & Rovelli, A. (2014). Properties and Processes of Crustal Fault Zones: Volume I. *Pure and Applied Geophysics*, 171(11), 2863-2865.

Belgrano, T. M., Herwegh, M., & Berger, A. (2016). Inherited structural controls on fault geometry, architecture and hydrothermal activity: an example from Grimsel Pass, Switzerland. *Swiss journal of geosciences*, 109(3), 345-364.

Bellanger, M. (2017, June). High temperature geothermal resources of crustal fault zones: a dedicated approach. In 79th EAGE Conference and Exhibition 2017-Workshops (pp. cp-519). European Association of Geoscientists & Engineers.

Bertrand, L. (2017). Étude des réservoirs géothermiques développés dans le socle et à l'interface avec les formations sédimentaires (Doctoral dissertation, Université de Lorraine).

Bernabé, Y., Li, M., & Maineult, A. (2010). Permeability and pore connectivity: a new model based on network simulations. *Journal of Geophysical Research: Solid Earth*, 115(B10).

F. Bergerat, Déformations cassantes et champs de contraintes tertiaires dans la plate-forme européenne, p. 315, 1985.

Bethke, C. M. (1985). A numerical model of compaction-driven groundwater flow and heat transfer and its application to the paleohydrology of intracratonic sedimentary basins. *Journal of Geophysical Research: Solid Earth*, 90(B8), 6817-6828.

Blès, J. L., Bonijoly, D., Castaing, C., & Gros, Y. (1989). Successive post-Variscan stress fields in the French Massif Central and its borders (Western European plate): comparison with geodynamic data. *Tectonophysics*, 169(1-3), 79-111.

Blès, J. L., & Bles, J. L. (1982). Apport de l'analyse structurale à la connaissance des gîtes filoniens.

Bodvarsson, G. (1982). Terrestrial energy currents and transfer in Iceland. *Continental and oceanic rifts*, 8, 271-282.

Bonnetti, C., Cuney, M., Malartre, F., Michels, R., Liu, X., & Peng, Y. (2015). The Nuheting deposit, Erlian Basin, NE China: synsedimentary to diagenetic uranium mineralization. *Ore Geology Reviews*, 69, 118-139.

Bonijoly, D. (1981). Étude structurale et minéralisations d'une plateforme carbonatée, le Quercy, Université d'Orléans.

Bonijoly, D., & Germain, H. (1984). Histoire tectonique post-hercynienne du bassin d'Alès (Gard), chronologie des déformations et contrôle structural des minéralisations barytiques. *Documents-BRGM*, (76).

Börsing, N., Wellmann, J. F., Niederau, J., & Regenauer-Lieb, K. (2017). Entropy production in a box: Analysis of instabilities in confined hydrothermal systems. *Water Resources Research*, 53(9), 7716-7739.

Bouladon, J. P., Picot, J. J., & Sainfeld, P. (1961). Le faisceau filonien de Pontgibaud. *Bull BRGM*, 1, 1-41.

Brace, W., Walsh, J. B., & Frangos, W. T. (1968). Permeability of granite under high pressure. *Journal of Geophysical research*, 73(6), 2225-2236.

Branquet, Y., Boulvais, P., Mercadier, J., Ledru, P., & Khairallah, C. (2019, August). Methaniferous active faults and seismic cycle in the genesis of the Athabasca giant U deposits: conceptual and numerical investigation. In *Proceedings of the 15th Biennial SGA Meeting* (pp. 52-55).

Brooks Hanson, R. (1995). The hydrodynamics of contact metamorphism. *Geological Society of America Bulletin*, 107(5), 595-611.

Brogi, A., & Fulignati, P. (2012). Tectonic control on hydrothermal circulation and fluid evolution in the Pietratonda–Poggio Peloso (southern Tuscany, Italy) carbonate-hosted Sb-mineralization. *Ore Geology Reviews*, 44, 158-171.

Bruhn, R. L., Parry, W. T., Yonkee, W. A., & Thompson, T. (1994). Fracturing and hydrothermal alteration in normal fault zones. *Pure and applied geophysics*, 142(3), 609-644.

Bruhn, D., Huenges, E., Agustsson, K., Zang, A., Rachez, X., Wiemer, S., ... & Calcagno, P. (2015). Summary of the European GEISER Project (Geothermal Engineering Integrating Mitigation of Induced Seismicity in Reservoirs). *In World Geothermal Congress*.

Bohnsack, D., Potten, M., Pfrang, D., Wolpert, P., & Zosseder, K. (2020). Porosity–permeability relationship derived from Upper Jurassic carbonate rock cores to assess the regional hydraulic matrix properties of the Malm reservoir in the South German Molasse Basin. *Geothermal Energy*, 8(1), 1-47.

Bräuer, K., Kämpf, H., Niedermann, S., & Wetzel, H. U. (2017). Regional distribution pattern of carbon and helium isotopes from different volcanic fields in the French Massif Central: Evidence for active mantle degassing and water transport. *Chemical Geology*, 469, 4-18.

Bril, H., Bonhomme, M. G., Marcoux, E., & Baubron, J. C. (1991). Ages K/Ar des minéralisations de Brioude-Massiac (W-Au-As-Sb; Pb-Zn), Pontgibaud (Pb-Ag; Sn), et Labessette (As-Pb-Sb-Au): Place de ces districts dans l'évolution géotectonique du Massif central français. *Mineralium Deposita*, 26(3), 189-198.

Brogi, A., & Fulignati, P. (2012). Tectonic control on hydrothermal circulation and fluid evolution in the Pietratonda–Poggio Peloso (southern Tuscany, Italy) carbonate-hosted Sb-mineralization. *Ore Geology Reviews*, 44, 158-171.

Brown, S. R., & Bruhn, R. L. (1998). Fluid permeability of deformable fracture networks. *Journal of Geophysical Research: Solid Earth*, 103(B2), 2489-2500.

Brown, D. W., Duchane, D. V., Heiken, G., & Hriscu, V. T. (2012). Mining the earth's heat: hot dry rock geothermal energy. *Springer Science & Business Media*.

Bruhn, R. L., Parry, W. T., Yonkee, W. A., & Thompson, T. (1994). Fracturing and hydrothermal alteration in normal fault zones. *Pure and applied geophysics*, 142(3), 609-644.

Bucher, K., & Stober, I. (2010). Fluids in the upper continental crust. *Geofluids*, 10(1-2), 241-253.

Buchmann, T. J., & Connolly, P. T. (2007). Contemporary kinematics of the Upper Rhine Graben: a 3D finite element approach. *Global and Planetary Change*, 58(1-4), 287-309.

de Buffon G-L (1778) Les époques de la nature. In: Histoire naturelle, vol XII. De L'Imprimerie Royale, À Paris (in French).

C

Cappa, F., & Rutqvist, J. (2011). Impact of CO2 geological sequestration on the nucleation of earthquakes. *Geophysical Research Letters*. 38(17).

Carman, P. C. (1937). Fluid flow through granular beds. *Trans. Inst. Chem. Eng*., 15, 150-166.

Carman, P. C (1956). The flow of gases through porous media; *Academic Press: New York*.

Caine, J. S., Evans, J. P., & Forster, C. B. (1996). Fault zone architecture and permeability structure. *Geology*, 24(11), 1025-1028.

Caine, J. S., Bruhn, R. L., & Forster, C. B. (2010). Internal structure, fault rocks, and inferences regarding deformation, fluid flow, and mineralization in the seismogenic Stillwater normal fault, Dixie Valley, Nevada. *Journal of Structural Geology*, 32(11), 1576-1589.

Cai, J., Luo, L., Ye, R., Zeng, X., & Hu, X. (2015). Recent advances on fractal modeling of permeability for fibrous porous media. *Fractals*, 23(01), 1540006.

Calcagno, P., Baujard, C., Guillou-Frottier, L., Dagallier, A., & Genter, A. (2014). Estimation of the deep geothermal potential within the Tertiary Limagne basin (French Massif Central): an integrated 3D geological and thermal approach. *Geothermics*, 51, 496-508.

Cant, J. L., Siratovich, P. A., Cole, J. W., Villeneuve, M. C., & Kennedy, B. M. (2018). Matrix permeability of reservoir rocks, Ngatamariki geothermal field, Taupo Volcanic Zone, New Zealand. *Geothermal Energy*, 6(1), 1-28.

Cao, S., & Neubauer, F. (2016). Deep crustal expressions of exhumed strike-slip fault systems: Shear zone initiation on rheological boundaries. *Earth-Science Reviews*. 162, 155-176.

Cassard, D., Chabod, J. C., Marcoux, E., Bourgine, B., & Castaing, C. (1994). Mise en place et origine des minéralisations du gisement filonien à Zn, Ge, Ag,(Pb, Cd) de Noailhac-Saint-Salvy (Tarn, France). *Chronique de la recherche minière*, (514), 3-37.

Cermak, V. (1993). Lithospheric thermal regimes in Europe. *Physics of the Earth and Planetary Interiors*, 79(1-2), 179-193.

Chester, F. M., & Logan, J. M. (1986). Implications for mechanical properties of brittle faults from observations of the Punchbowl fault zone, California. Pure and applied geophysics, 124(1), 79-106.

Chester, F. M., Evans, J. P., & Biegel, R. L. (1993). Internal structure and weakening mechanisms of the San Andreas fault. *Journal of Geophysical Research: Solid Earth*, 98(B1), 771-786.

Chester, F. M., & Chester, J. S. (1998). Ultracataclasite structure and friction processes of the Punchbowl fault, San Andreas system, California. *Tectonophysics*, 295(1-2), 199-221.

Clavaud, J. B., Maineult, A., Zamora, M., Rasolofosaon, P., & Schlitter, C. (2008). Permeability anisotropy and its relations with porous medium structure. *Journal of Geophysical Research: Solid Earth*, 113(B1).

Cloetingh, S. A. P. L., van Wees, J. D., Ziegler, P. A., Lenkey, L., Beekman, F., Tesauro, M., ... & Worum, G. (2010). Lithosphere tectonics and thermo-mechanical properties: an integrated modelling approach for Enhanced Geothermal Systems exploration in Europe. *Earth-Science Reviews*, 102(3-4), 159-206.

Coelho, G., Branquet, Y., Sizaret, S., Arbaret, L., Champallier, R., & Rozenbaum, O. (2015). Permeability of sheeted dykes beneath oceanic ridges: Strain experiments coupled with 3D numerical modeling of the Troodos Ophiolite, Cyprus. *Tectonophysics*, 644, 138-150.

Coolbaugh, M. F., Arehart, G. B., Faulds, J. E., Garside, L. J., Rhoden, H. N., Steininger, R. C., & Vikre, P. G. (2005). Geothermal systems in the Great Basin, western United States: Modern analogues to the roles of magmatism, structure, and regional tectonics in the formation of gold deposits. *In Geological Society of Nevada Symposium* (pp. 1063-1081).

Coolbaugh, M. F., Raines, G. L., Zehner, R. E., Shevenell, L., & Williams, C. F. (2006). Prediction and discovery of new geothermal resources in the Great Basin: Multiple evidence of a large undiscovered resource base. In *GRC 2006 Annual Meeting: Geothermal Resources-Securing Our Energy Future* (Vol. 30, pp. 867-873).

Coolbaugh, M. F., Sladek, C., Faulds, J.E., Zehner, R. E., Oppliger, G. L. (2007) Use of rapid temperature measurements at a 2-meter depth to augment deeper temperature gradient drilling. In: *Proceedings, thirty-second workshop on geothermal reservoir engineering, Stanford University, vol. 8.*

Connolly, J. A. D. (1997). Devolatilization-generated fluid pressure and deformation-propagated fluid flow during prograde regional metamorphism. *Journal of Geophysical Research: Solid Earth*, 102(B8), 18149-18173.

Coussy, O. (2004). Poromechanics. *John Wiley & Sons*.

Cordier PLA (1827) Essai sur la température de l'intérieur de la terre. In: *Mémoires de l'Académie des Sciences*, pp 473–556 (in French).

Cornet, F. H., & Burlet, D. (1992). Stress field determinations in France by hydraulic tests in boreholes. *Journal of Geophysical Research: Solid Earth*. 97(B8), 11829-11849.

Cox, S. F. (1999). Deformational controls on the dynamics of fluid flow in mesothermal gold systems. *Geological Society, London, Special Publications*, 155(1), 123-140.

Cox, S. (2005). Coupling between deformation, fluid pressures, and fluid flow in ore-producing hydrothermal systems at depth in the crust.

Cox, S. C., Menzies, C. D., Sutherland, R., Denys, P. H., Chamberlain, C., & Teagle, D. A. (2015). Changes in hot spring temperature and hydrogeology of the Alpine Fault hanging wall, New Zealand, induced by distal South Island earthquakes. *Geofluids*, 15(1-2), 216-239.

Craw, D. (2000). Fluid flow at fault intersections in an active oblique collision zone, Southern Alps, New Zealand. *Journal of Geochemical Exploration*, 69, 523-526.

Cui, T., Yang, J., & Samson, I. M. (2012). Tectonic deformation and fluid flow: implications for the formation of unconformity-related uranium deposits. *Economic Geology*, 107(1), 147-163.

Curewitz, D., & Karson, J. A. (1997). Structural settings of hydrothermal outflow: Fracture permeability maintained by fault propagation and interaction. *Journal of Volcanology and Geothermal Research*, 79(3-4), 149-168.

D

Darcy, H. P. G. (1856). Les fontaines publiques de la ville de Dijon. Delmont, Paris.

Darcy, H. (1857). Recherches expérimentales relatives au mouvement de l'eau dans les tuyaux (Vol. 1). Mallet-Bachelier.

Daffos C. (2018) Contrôle structural du Volcanisme Plio-quarternaire des Monts Dore. Rapport Master 2. Université d'Orléans, Institut des Sciences de la Terre d'Orléans.

Deichmann, N., & Giardini, D. (2009). Earthquakes induced by the stimulation of an enhanced geothermal system below Basel (Switzerland). *Seismological Research Letters*, 80(5), 784-798.

Descartes, R. (1644). Principia Philosophiae, Amsterdam.

Dezayes, C., Genter, A., & Valley, B. (2010). Structure of the low permeable naturally fractured geothermal reservoir at Soultz. *Comptes Rendus Geoscience*, 342(7-8), 517-530.

Dèzes, P., Schmid, S. M., & Ziegler, P. A. (2004). Evolution of the European Cenozoic Rift System: interaction of the Alpine and Pyrenean orogens with their foreland lithosphere. *Tectonophysics*, 389(1-2), 1-33.

Dickson, M. H., & Fanelli, M. (2013). Geothermal energy: utilization and technology.

Dini, A., Gianelli, G., Puxeddu, M., & Ruggieri, G. (2005). Origin and evolution of Pliocene–Pleistocene granites from the Larderello geothermal field (Tuscan Magmatic Province, Italy). *Lithos*, 81(1-4), 1-31.

Dobson, P. F., Kneafsey, T. J., Hulen, J., & Simmons, A. (2003). Porosity, permeability, and fluid flow in the Yellowstone geothermal system, Wyoming. *Journal of Volcanology and Geothermal Research*, 123(3-4), 313-324.

Donzé, F. V., Richefeu, V., & Magnier, S. A. (2009). Advances in discrete element method applied to soil, rock and concrete mechanics. *Electronic Journal of Geotechnical Engineering*, 8(1), 44.

Driesner, T. (2007). The system H2O–NaCl. Part II: Correlations for molar volume, enthalpy, and isobaric heat capacity from 0 to 1000 C, 1 to 5000 bar, and 0 to 1 XNaCl. *Geochimica et Cosmochimica Acta*. 71(20), 4902-4919.

Duan, Q., Yang, X., & Chen, J. (2017). Hydraulic properties of a low permeable rupture zone on the Yingxiu-Beichuan Fault activated during the Wenchuan earthquake, China: Implications for fluid conduction, fault sealing, and dynamic weakening mechanisms. *Tectonophysics*, 721, 123-142.

Duwiquet, H. et *al*. (2019). On the geothermal potential of crustal fault zones: a case study from the Pontgibaud area (French Massif Central, France). *Geothermal Energy*. 7(1), 1-29.

Duwiquet, H et *al*. (2021) Crustal Fault Zones (CFZ) as Geothermal Power Systems: A Preliminary 3D THM Model Constrained by a Multidisciplinary Approach. *Geofluids*. 2021.

Duwiquet, H. et *al*. (2021) Crustal Fault Zones (CFZ) as Geothermal Power Systems: 3D Variation of Permeability and Related Processes. *In Stanford Geothermal Workshop*.

E

Edel, J. B., Maurer, V., Dalmais, E., Genter, A., Richard, A., Letourneau, O., & Hehn, R. (2018). Structure and nature of the Palaeozoic basement based on magnetic, gravimetric and seismic investigations in the central Upper Rhinegraben. *Geothermal Energy*, 6(1), 1-25.

Eggertsson, G. H., Lavallée, Y., Kendrick, J. E., & Markússon, S. H. (2020). Improving fluid flow in geothermal reservoirs by thermal and mechanical stimulation: The case of Krafla volcano, Iceland. *Journal of Volcanology and Geothermal Research*, 391, 106351.

Ehlers, Todd A., and David S. Chapman. (1999). "Normal fault thermal regimes: conductive and hydrothermal heat transfer surrounding the Wasatch fault, Utah." *Tectonophysics* 312.2-4, 217-234.

Elder, J. W. (1965). Physical processes in geothermal areas. Terrestrial heat flow, 8, 211-239.

J. Elder, Geothermal systems, *Academic Press, London*, 1981.

Eldursi, K., Chi, G., Bethune, K., Li, Z., Ledru, P., & Quirt, D. (2020). New insights from 2-and 3-D numerical modelling on fluid flow mechanisms and geological factors responsible for the formation of the world-class Cigar Lake uranium deposit, eastern Athabasca Basin, Canada. *Mineralium Deposita*, 1-24.

Ercan, A. (2002). Petroleum and geothermal model of Aegean Sea and western Anatolia. In Turkey*: Second Balkan Geophysical Congress and Exhibition* (pp. 158-159).

Evans, J. P., Forster, C. B., & Goddard, J. V. (1997). Permeability of fault-related rocks, and implications for hydraulic structure of fault zones. *Journal of structural Geology*, 19(11), 1393-1404.

F

Fairley, J. P. (2009). Modeling fluid flow in a heterogeneous, fault-controlled hydrothermal system. *Geofluids*, 9(2), 153-166.

Famin, V., Philippot, P., Jolivet, L., & Agard, P. (2004). Evolution of hydrothermal regime along a crustal shear zone, Tinos Island, Greece. *Tectonics*, 23(5).

Farquharson, J. I., Heap, M. J., Lavallee, Y., Varley, N. R., & Baud, P. (2016). Evidence for the development of permeability anisotropy in lava domes and volcanic conduits. *Journal of Volcanology and Geothermal Research*, 323, 163-185.

Farquharson, J. I., Wild, B., Kushnir, A. R., Heap, M. J., Baud, P., & Kennedy, B. (2019). Acid-induced dissolution of andesite: evolution of permeability and strength. *Journal of Geophysical Research: Solid Earth*, 124(1), 257-273.

Faulkner, D. R., Lewis, A. C., & Rutter, E. H. (2003). On the internal structure and mechanics of large strike-slip fault zones: field observations of the Carboneras fault in southeastern Spain. *Tectonophysics*, 367(3-4), 235-251.

Faulkner, D. R., Jackson, C. A. L., Lunn, R. J., Schlische, R. W., Shipton, Z. K., Wibberley, C. A. J., & Withjack, M. O. (2010). A review of recent developments concerning the structure, mechanics and fluid flow properties of fault zones. *Journal of Structural Geology*, *32*(11), 1557-1575.

Faulds, J. E., Coolbaugh, M., Blewitt, G., & Henry, C. D. (2004). Why is Nevada in hot water? Structural controls and tectonic model of geothermal systems in the northwestern Great Basin. *Geothermal Resources Council Transactions*, 28, 649-654.

Faulds, J. E., Coolbaugh, M. F., Vice, G. S., & Edwards, M. L. (2006). Characterizing structural controls of geothermal fields in the northwestern Great Basin: A progress report. *Geothermal Resources Council Transactions*, 30, 69-76.

Faulds, J., Coolbaugh, M., Bouchot, V., Moek, I., & Oguz, K. (2010, April). Characterizing structural controls of geothermal reservoirs in the Great Basin, USA, and Western Turkey: developing successful exploration strategies in extended terranes. In *World Geothermal Congress* (pp. 11-p).

Faulds, J. E., Hinz, N. H., Coolbaugh, M. F., Cashman, P. H., Kratt, C., Dering, G., ... & McLachlan, H. (2011). Assessment of favorable structural settings of geothermal systems in the Great Basin, western USA. *Geothermal Resources Council Transactions*, 35, 777-783.

Faulds, J., & Hinz, N. (2015, April). Favorable tectonic and structural settings of geothermal systems in the Great Basin region, western USA: Proxies for discovering blind geothermal systems. In *Proceedings World Geothermal Congress*, Melbourne, Australia.

Faulkner, D. R., Jackson, C. A. L., Lunn, R. J., Schlische, R. W., Shipton, Z. K., Wibberley, C. A. J., & Withjack, M. O. (2010). A review of recent developments concerning the structure, mechanics and fluid flow properties of fault zones. *Journal of Structural Geology*, 32(11), 1557-1575.

Faure, M., Grolier, J., & Pons, J. (1993). Extensional ductile tectonics of the Sioule metamorphic series (Variscan French Massif Central). *Geologische Rundschau*, 82(3), 461-474.

Faure, M. (1995). Late orogenic carboniferous extensions in the Variscan French Massif Central. *Tectonics*, 14(1), 132-153.

Faure, M., Lardeaux, J. M., & Ledru, P. (2009). A review of the pre-Permian geology of the Variscan French Massif Central. *Comptes rendus géoscience*, 341(2-3), 202-213.

Fernandez, A. (1969). La série cristallophyllienne et les granites de la région de Pontgibaud (Puy de Dôme) Massif Central Français (Doctoral Dissertation, Université de Clermont Ferrand).

Fourier J (1824) Remarques Générales Sur Les Températures Du Globe Terrestre Et Des Espaces Planétaires. *Ann Chim Phys* 27:136–167.

Forster, C., & Smith, L. (1989). The influence of groundwater flow on thermal regimes in mountainous terrain: A model study. *Journal of Geophysical Research: Solid Earth*, 94(B7), 9439-9451.

Forster, C. B., & Evans, J. P. (1991). Hydrogeology of thrust faults and crystalline thrust sheets: Results of combined field and modeling studies. *Geophysical Research Letters*, 18(5), 979-982.

Forster, P. M., Forster, H. I., Evans, M. J., Gidden, M. J., Jones, C. D., Keller, C. A., ... & Turnock, S. T. (2020). Current and future global climate impacts resulting from COVID-19. *Nature Climate Change*, 10(10), 913-919.

Förster, A., & Förster, H. J. (2000). Crustal composition and mantle heat flow: Implications from surface heat flow and radiogenic heat production in the Variscan Erzgebirge (Germany). *Journal of Geophysical Research: Solid Earth*, 105(B12), 27917-27938.

Freeze, R. A. (1979). J. A. Cherry, Groundwater.

G

Garibaldi, C., Guillou-Frottier, L., Lardeaux, J. M., Bonté, D., Lopez, S., Bouchot, V., & Ledru, P. (2010). Thermal anomalies and geological structures in the Provence basin: Implications for hydrothermal circulations at depth. *Bulletin de la Société Géologique de France*, 181(4), 363-376.

Gaucher, E., Schoenball, M., Heidbach, O., Zang, A., Fokker, P. A., van Wees, J. D., & Kohl, T. (2015). Induced seismicity in geothermal reservoirs: A review of forecasting approaches. *Renewable and Sustainable Energy Reviews*, 52, 1473-1490

Gaunt, H. E., Sammonds, P. R., Meredith, P. G., Smith, R., & Pallister, J. S. (2014). Pathways for degassing during the lava dome eruption of Mount St. Helens 2004–2008. *Geology*, 42(11), 947-950.

GEBCO Compilation Group. GEBCO 2020 Grid. British Oceanographic Data Centre https://doi.org/10.5285/a29c5465-b138-234d-e053-6c86abc040b9 (2020).

Gelard, J. P. (1978). La fracturation de la Bourgogne méridionale, essai d'interprétation et implications tectoniques régionales*. Revue de géographie physique et de géologie dynamique Paris*, 20(1), 5-27.

Genter, A. (1989). Géothermie roches chaudes sèches: le granite de Soultz-sous-Forêts (Bas-Rhin, France): fracturation naturelle, altérations hydrothermales et interaction eau-roche (Doctoral dissertation, Orléans).

Genter, A., Goerke, X., Graff, J. J., Cuenot, N., Krall, G., Schindler, M., & Ravier, G. (2010, April). Current status of the EGS Soultz geothermal project (France). *In world geothermal congress*, WGC2010, Bali, Indonesia (pp. 25-29).

Genter, A., Evans, K., Cuenot, N., Fritsch, D., Sanjuan, B. (2010). Contribution of the exploration of deep crystalline fractured reservoir of Soultz to the knowledge of enhanced geothermal systems (EGS). *Comptes Rendus Geoscience*. 342(7-8), 502-516.

Gerdes, M. L., Baumgartner, L. P., & Person, M. (1998). Convective fluid flow through heterogeneous country rocks during contact metamorphism. *Journal of Geophysical Research: Solid Earth*, 103(B10), 23983-24003.

Ghanbarian, B., Hunt, A. G., Ewing, R. P., & Sahimi, M. (2013). Tortuosity in porous media: a critical review. *Soil science society of America journal*, 77(5), 1461-1477.

Ghanbarian, B., Hunt, A. G., Ewing, R. P., & Skinner, T. E. (2014). Universal scaling of the formation factor in porous media derived by combining percolation and effective medium theories. *Geophysical Research Letters*, 41(11), 3884-3890.

Gleeson, T., & Ingebritsen, S. (Eds.). (2016). Crustal permeability. John Wiley & Sons.

Goldemberg, J. (ed.) (2000): World energy assesment: energy and the challenge of sustainability. United Nations Development Programme, United Nations Department of Economic and Social Affairs, World Energy Council.

Gosselin, L., & Bejan, A. (2004). Constructal heat trees at micro and nanoscales. *Journal of applied physics*, 96(10), 5852-5859.

Gomila, R. et *al*. (2021). Quantitative anisotropies of palaeopermeability in a strike-slip fault damage zone: Insights from micro-CT analysis and numerical simulations. *Tectonophysics*, 228873.

Goutorbe, B., Lucazeau, F., & Bonneville, A. (2007). Comparison of several BHT correction methods: a case study on an Australian data set. *Geophysical Journal International*, 170(2), 913-922.

Gleeson, T., & Ingebritsen, S. (Eds.). (2016). Crustal permeability. *John Wiley & Sons*.

Glover, P. W. J., Matsuki, K., Hikima, R., & Hayashi, K. (1998) Fluid flow in synthetic rough fractures and application to the Hachimantai geothermal hot dry rock test site. *Journal of Geophysical Research: Solid Earth*. 103(B5), 9621-9635.

Grasby, S. E., & Hutcheon, I. (2001). Controls on the distribution of thermal springs in the southern Canadian Cordillera. *Canadian Journal of Earth Sciences*, 38(3), 427-440.

Granet, M., Stoll, G., Dorel, J., Achauer, U., Poupinet, G., & Fuchs, K. (1995). Massif Central (France): new constraints on the geodynamical evolution from teleseismic tomography. *Geophysical Journal International*, 121(1), 33-48.

Granet, M., Wilson, M., & Achauer, U. (1995). Imaging a mantle plume beneath the French Massif Central. *Earth and Planetary Science Letters*, 136(3-4), 281-296.

Grawinkel, A., & Stöckhert, B. (1997). Hydrostatic pore fluid pressure to 9 km depth-Fluid inclusion evidence from the KTB deep drill hole. *Geophysical Research Letters*, 24(24), 3273-3276.

Grübler, A. (2003). Technology and global change. Cambridge university press.

Griffiths, L., Heap, M. J., Wang, F., Daval, D., Gilg, H. A., Baud, P., ... & Genter, A. (2016). Geothermal implications for fracture-filling hydrothermal precipitation. *Geothermics*, 64, 235-245.

Gudmundsson, A. (2000). Active fault zones and groundwater flow. *Geophysical Research Letters*, 27(18), 2993-2996.

Gueguen, Y., & Dienes, J. (1989). Transport properties of rocks from statistics and percolation. *Mathematical geology*, 21(1), 1-13.

Guillou, L., Mareschal, J. C., Jaupart, C., Gariépy, C., Bienfait, G., & Lapointe, R. (1994). Heat flow, gravity and structure of the Abitibi belt, Superior Province, Canada: Implications for mantle heat flow. *Earth and Planetary Science Letters*, 122(1-2), 103-123.

Guillou-Frottier, L., Carrė, C., Bourgine, B., Bouchot, V., & Genter, A. (2013). Structure of hydrothermal convection in the Upper Rhine Graben as inferred from corrected temperature data and basin-scale numerical models. *Journal of Volcanology and Geothermal Research*, 256, 29-49.

Guillou-Frottier, L., Duwiquet, H., Launay, G., Taillefer, A., Roche, V., & Link, G. (2020). On the morphology and amplitude of 2D and 3D thermal anomalies induced by buoyancy-driven flow within and around fault zones. *Solid Earth*, 11(4), 1571-1595.

Gunzburger, Y., & Magnenet, V. (2014). Stress inversion and basement-cover stress transmission across weak layers in the Paris basin, France. *Tectonophysics*, 617, 44-57.

Guo, T., Zhang, S., Ge, H., Wang, X., Lei, X., & Xiao, B. (2015). A new method for evaluation of fracture network formation capacity of rock. *Fuel*, 140, 778-787.

H

Haenel, R., Stegena, L., & Rybach, L. (Eds.). (1988). Handbook of terrestrial heat-flow density determination: with guidelines and recommendations of the International Heat Flow Commission (Vol. 4). *Springer Science & Business Media*.

Haines, S., Lynch, E., Mulch, A., Valley, J. W., & van der Pluijm, B. (2016). Meteoric fluid infiltration in crustal-scale normal fault systems as indicated by δ18O and δ2H geochemistry and 40Ar/39Ar dating of neoformed clays in brittle fault rocks. *Lithosphere*, 8(6), 587-600.

Häfele, W., & Sassin, W. (1977). The global energy system. *Annual Review of Energy*, 2(1), 1-30.

Hagemann, S. G., Groves, D. I., Ridley, J. R., & Vearncombe, J. R. (1992). The Archean lode gold deposits at Wiluna, Western Australia; high-level brittle-style mineralization in a strike-slip regime. *Economic Geology*, 87(4), 1022-1053.

Harcouët-Menou, V., Guillou-Frottier, L., Bonneville, A., Adler, P. M., & Mourzenko, V. (2009). Hydrothermal convection in and around mineralized fault zones: insights from two-and three-dimensional numerical modeling applied to the Ashanti belt, Ghana. *Geofluids*, 9(2), 116-137.

Hasterok, D., & Webb, J. (2017). On the radiogenic heat production of igneous rocks. *Geoscience Frontiers*, 8(5), 919-940.

Heap, M. J., & Kennedy, B. M. (2016). Exploring the scale-dependent permeability of fractured andesite. *Earth and Planetary Science Letters*, 447, 139-150.

Heap, M. J., Kushnir, A. R., Gilg, H. A., Wadsworth, F. B., Reuschlé, T., & Baud, P. (2017). Microstructural and petrophysical properties of the Permo-Triassic sandstones (Buntsandstein) from the Soultz-sous-Forêts geothermal site (France). *Geothermal Energy*, 5(1), 1-37.

Heap, M. J. (2019). The influence of sample geometry on the permeability of a porous sandstone. *Geoscientific Instrumentation, Methods and Data Systems*, 8(1), 55-61.

Heap, M. J. et *al*. (2020). Towards more realistic values of elastic moduli for volcano modelling. *Journal of Volcanology and Geothermal Research*. 390, 10668.

Huber, C., & Su, Y. (2015). A pore-scale investigation of the dynamic response of saturated porous media to transient stresses. *Geofluids*, 15(1-2), 11-23.

Huenges, E., & Ledru, P. (Eds.). (2011). Geothermal energy systems: exploration, development, and utilization. *John Wiley & Sons*.

Huismans, R. S., Podladchikov, Y. Y., & Cloetingh, S. (2001). Dynamic modeling of the transition from passive to active rifting, application to the Pannonian basin. *Tectonics*, 20(6), 1021-1039.

Hurtig, E., Cermak, V., Haenel, R., & Zui, V. (1992). Geothermal atlas of Europe.

Hurter, S., & Haenel, R. (2002). Atlas of geothermal resources in Europe.

Huttrer, G. W. (2020, April). Geothermal power generation in the world 2015-2020 update report. In *Proceedings World Geothermal Congress* (p. 17).

von Humboldt, A. (1817) Des lignes isothermes et de la distribution de la chaleur sur le globe. *Mémoires de Physique et de Chimie de la Société d'Arcueil* 3:462–602.

Hofstra, A. H. (2000). Characteristics and models for Carlin-type gold deposits*. Rev. Econ. Geol*., 13, 163-220.

Holmes, A. (1930) Radioactivity and geology. *Trans Edinb Geol Soc,* 12:281–283.

Holmes, A. (1931) Radioactivity and earth movements. *Nature,* 128:49.

Horton, C. W., & Rogers Jr, F. T. (1945). Convection currents in a porous medium. *Journal of Applied Physics*. 16(6), 367-370.

Horne, R. N. (1979). Three-dimensional natural convection in a confined porous medium heated from below. *Journal of Fluid Mechanics*. 92(4), 751-766.

Hottin, A. M., Camus, G., Michaeli, B., Marchand, J., Perichaud, J. J., D'arcy, D. (2000). Carte géologique de Pontgibaud à 1/50 000. Editions BRGM.

Howald, T., Person, M., Campbell, A., Lueth, V., Hofstra, A., Sweetkind, D., ... & Phillips, F. M. (2015). Evidence for long timescale (> 103 years) changes in hydrothermal activity induced by seismic events. *Geofluids*, 15(1-2), 252-268.

I

Iglauer, S., Paluszny, A., & Blunt, M. J. (2013). Simultaneous oil recovery and residual gas storage: A pore-level analysis using in situ X-ray micro-tomography. *Fuel*, 103, 905-914.

Ito, T., & Zoback, M. D. (2000). Fracture permeability and in situ stress to 7 km depth in the KTB scientific drillhole. *Geophysical Research Letters*, 27(7), 1045-1048.

Ingebritsen, S. E., & Appold, M. S. (2012). The physical hydrogeology of ore deposits. *Economic Geology*, 107(4), 559-584.

Ingebritsen, S. E., & Manning, C. E. (2010). Permeability of the continental crust: dynamic variations inferred from seismicity and metamorphism. *Geofluids*, 10(1-2), 193-205.

Ingebritson, S. E., & Gleeson, T. (2014). Crustal permeability: Introduction to the special issue.

J

Jaupart, C., Mareschal, J. C., & Watts, A. B. (2007). Heat flow and thermal structure of the lithosphere. *Treatise on geophysics*, 6, 217-252.

Jamtveit, B., Putnis, C. V., & Malthe-Sørenssen, A. (2009). Reaction induced fracturing during replacement processes. *Contributions to Mineralogy and Petrology*, 157(1), 127-133.

Jebrak, M. (1980). Le filon des farges et les minéralisations à barythine, fluorine et galène du district d'Ussel (Massif Central Français).

Jébrak, M. (1984). Contribution à l'histoire naturelle des filons (F, BA) du domaine varisque: essai de caractérisation structurale et géochimique des filons en extension et en décrochement dans les massifs centraux français et marocains (Doctoral dissertation).

Jébrak, M. (1997). Hydrothermal breccias in vein-type ore deposits: a review of mechanisms, morphology and size distribution. *Ore geology reviews*, 12(3), 111-134.

Jenkins, B. (1993). Properties of Biomass, Appendix to Biomass Energy Fundamentals. Palo Alto, CA: EPRI.

Johnson, D. L., Koplik, J., & Dashen, R. (1987). Theory of dynamic permeability and tortuosity in fluid-saturated porous media. *Journal of fluid mechanics*, 176, 379-402.

Jolie, E, Klinkmueller, M, Moeck, I. (2015). Diffuse surface emanations as indicator of structural permeability in fault-controlled geothermal systems. *J Volcanol Geotherm Res*.; 290:97–113.

Jolie, E., Scott, S., Faulds, J., Chambefort, I., Axelsson, G., Gutiérrez-Negrín, L. C., ... & Zemedkun, M. T. (2021). Geological controls on geothermal resources for power generation. *Nature Reviews Earth & Environment,* 2(5), 324-339.

Joly, J. (1909) Radioactivity and geology: an account of the influence of radioactive energy on terrestrial history. *Archibald Constable & Co., Ltd, London*.

Joly, A., Martelet, G., Chen, Y., & Faure, M. (2008). A multidisciplinary study of a syntectonic pluton close to a major lithospheric-scale fault—Relationships between the Montmarault granitic massif and the Sillon Houiller Fault in the Variscan French

Massif Central: 2. Gravity, aeromagnetic investigations, and 3-D geologic modeling. *Journal of Geophysical Research: Solid Earth*, 113(B1).

Juhlin, C., & Sandstedt, H. (1989). Storage of nuclear waste in very deep boreholes: Feasibility study and assessment of economic potential. Pt. 1 and 2 (No. SKB-TR--89-39). *Swedish Nuclear Fuel and Waste Management Co*..

Juliusson, E., & Horne, R. N. (2010, February). Characterization of fractures in Geothermal Reservoirs. In *World Geothermal Congress*. Bali.

Jupp, T., & Schultz, A. (2000). A thermodynamic explanation for black smoker temperatures. *Nature*, 403(6772), 880-883.

K

Katto, Y., & Masuoka, T. (1967). Criterion for the onset of convective flow in a fluid in a porous medium*. International Journal of Heat and Mass Transfer*. 10(3), 297-309.

Kendrick, J. E., Lavallée, Y., Hess, K. U., Heap, M. J., Gaunt, H. E., Meredith, P. G., & Dingwell, D. B. (2013). Tracking the permeable porous network during strain-dependent magmatic flow. *Journal of Volcanology and Geothermal Research*, 260, 117-126.

Ketcham, R. A., & Carlson, W. D. (2001). Acquisition, optimization and interpretation of X-ray computed tomographic imagery: applications to the geosciences. *Computers & Geosciences*, 27(4), 381-400.

Király, Á., Capitanio, F. A., Funiciello, F., & Faccenna, C. (2017). Subduction induced mantle flow: Length-scales and orientation of the toroidal cell. *Earth and Planetary Science Letters*, 479, 284-297.

Klug, C., & Cashman, K. V. (1996). Permeability development in vesiculating magmas: implications for fragmentation. *Bulletin of Volcanology*, 58(2), 87-100.

Korvin, G. (1992). Fractal models in the earth sciences (Vol. 396). Amsterdam: *elsevier*.

Kozeny, J. (1927). S.B. Akad. Wiss. Wien, 136 a, 271.

Kozlovsky, Y. A. (1984). The world's deepest well. *Scientific American*, 251(6), 98-105.

Kozlovsky, Y. A. (1987). Hydrogeological essay. In The superdeep well of the Kola Peninsula (pp. 271-287). *Springer*, Berlin, Heidelberg.

Kukkonen, I. T., & Peltonen, P. (1999). Xenolith-controlled geotherm for the central Fennoscandian Shield: implications for lithosphere–asthenosphere relations. *Tectonophysics*, 304(4), 301-315.

Kushnir, A. R., Martel, C., Bourdier, J. L., Heap, M. J., Reuschlé, T., Erdmann, S., ... & Cholik, N. (2016). Probing permeability and microstructure: unravelling the role of a low-permeability dome on the explosivity of Merapi (Indonesia). *Journal of Volcanology and Geothermal Research*, 316, 56-71.

Kushnir, A. R., Heap, M. J., & Baud, P. (2018). Assessing the role of fractures on the permeability of the Permo-Triassic sandstones at the Soultz-sous-Forêts (France) geothermal site. *Geothermics*, 74, 181-189.

Kranz, R. L. (1979, February). Crack growth and development during creep of Barre granite. In *International Journal of Rock Mechanics and Mining Sciences & Geomechanics* Abstracts (Vol. 16, No. 1, pp. 23-35). Pergamon.

Kwiatek, G., et *al*. Microseismicity induced during fluid-injection: A case study from the geothermal site at Groß Schönebeck, North German Basin. *Acta Geophysica*. 58(6), 995-1020 (2010).

L

Lahsen, A., Muñoz, N., & Parada, M. A. (2010, April). Geothermal development in Chile. In *Proceedings world geothermal congress*, Bali, Indonesia (pp. 25-29).

Lapwood, E. R.: Convection of a fluid in a porous medium, *Math. Proc*. Cambridge, 44, 508–521, 1948.

Lamur, A., Kendrick, J. E., Eggertsson, G. H., Wall, R. J., Ashworth, J. D., & Lavallée, Y. (2017). The permeability of fractured rocks in pressurised volcanic and geothermal systems. Scientific reports, 7(1), 1-9.

Launay, G. (2018). Hydrodynamique des systèmes minéralisés péri-granitiques: étude du gisement à W-Sn-(Cu) de Panasqueira (Portugal) (Doctoral dissertation, Université d'Orléans).

Launay, G., Sizaret, S., Guillou-Frottier, L., Fauguerolles, C., Champallier, R., & Gloaguen, E. (2019). Dynamic permeability related to greisenization reactions in Sn-W ore deposits: Quantitative petrophysical and experimental evidence. *Geofluids*, 2019.

Laumonier, M., Arbaret, L., Burgisser, A., & Champallier, R. (2011). Porosity redistribution enhanced by strain localization in crystal-rich magmas. *Geology*, 39(8), 715-718.

Lavallée, Y., Benson, P. M., Heap, M. J., Flaws, A., Hess, K. U., & Dingwell, D. B. (2012). Volcanic conduit failure as a trigger to magma fragmentation. *Bulletin of Volcanology*, 74(1), 11-13.

Lavallée, Y., Benson, P. M., Heap, M. J., Hess, K. U., Flaws, A., Schillinger, B., ... & Dingwell, D. B. (2013). Reconstructing magma failure and the degassing network of dome-building eruptions. *Geology*, 41(4), 515-518.

Lebocey J. (2013). Géologie et gîtologie du district du Pontgibaud (Puy-de-Dôme). In: Bayle LD, De Ascençao Guedes R, Gol D, editors. *Le Règne Minéral*-hors série XIX-2013. p 35–42.

Lechler, P. J., Coolbaugh, M. F. (2007) Gaseous emissions from Steamboat Springs, Brady's Hot Springs, and Desert Peak Geothermal Systems, Nevada. *Geotherm Resour Council Trans*. 31:359–61.

Lecoq H. et Bouillet JB. (1830) Vues et coupes des formations géologiques du département du Puy-de-Dôme, Clermont-Ferrand.

Ledingham, P., Cotton, L., & Law, R. The united downs deep geothermal power project. *Proc. 44th Work. Geotherm. Reserv. Eng*, **1-11** (2019).

Ledesert, B. (1993). Fracturation et paléocirculations hydrothermales: application au granite de Soultz-Sous-Forêts (Doctoral dissertation, Poitiers).

Ledru, P.., Lardeaux, J. M., Santallier, D. Autran, A., Quenardel, J. M., Floc'h, J. P., ... & Ploquin, A. (1989). Où sont les nappes dans le Massif central français ?. Bulletin de la Société géologique de France, (3), 605-618.

Ledru, P., & Guillou-Frottier, L. (2010). Reservoir definition. Geothermal Energy Systems: Exploration, Development, and Utilization. *Wiley–VCH, Weinheim*.

Lee, S. H., Lough, M. A., & Jensen, C. L. (2001). Hierarchical modeling of flow in naturally fractured formations with multiple length scales. *Water resources research*, 37(3), 443-455.

Lefort, J. P., & Agarwal, B. N. P. (2002). Topography of the Moho undulations in France from gravity data: their age and origin. *Tectonophysics*, 350(3), 193-213.

Letouzey, J., & Tremolieres, P. (1980). Paleo-stress fields around the Mediterranean since the Mesozoic from microtectonics. Comparison with plate tectonic data. In Tectonic Stresses in the Alpine-Mediterranean Region (pp. 173-192). *Springer*, Vienna.

Loaiza, S., Fortin, J., Schubnel, A., Gueguen, Y., Vinciguerra, S., & Moreira, M. (2012). Mechanical behavior and localized failure modes in a porous basalt from the Azores*. Geophysical Research Letters*, 39(19).

López, D. L., & Smith, L. (1995). Fluid flow in fault zones: analysis of the interplay of convective circulation and topographically driven groundwater flow. *Water resources research*, 31(6), 1489-1503.

Louis, S., Luijendijk, E., Dunkl, I., & Person, M. (2019). Episodic fluid flow in an active fault. *Geology*, 47(10), 938-942.

Lorenzini, G., Moretti, S., & Conti, A. (2011). Fin shape thermal optimization using Bejan's constructal theory. *Synthesis Lectures on Engineering*, 6(1), 1-219.

Liang, X., Xu, T., Feng, B., & Jiang, Z. (2018). Optimization of heat extraction strategies in fault-controlled hydro-geothermal reservoirs. *Energy*. 164, 853-870.

Lin, G., Zhao, C., Hobbs, B. E., Ord, A., & Mühlhaus, H. B. (2003). Theoretical and numerical analyses of convective instability in porous media with temperature-dependent viscosity. *Communications in numerical methods in engineering*, 19(10), 787-799.

Linstrom, P. J., & Mallard, W. G. (2001). The NIST Chemistry WebBook: A chemical data resource on the internet. *Journal of Chemical & Engineering Data*, 46(5), 1059-1063.

Lucazeau, F. (1981). Flux de chaleur, production de chaleur et évolution géodynamique récente du Massif Central Français, Thèse de doctorat.

Lucazeau, F., Vasseur, G., & Bayer, R. (1984). Interpretation of heat flow data in the French Massif Central. *Tectonophysics*, 103(1-4), 99-119.

Lucazeau, F., & Vasseur, G. (1989). Heat flow density data from France and surrounding margins. *Tectonophysics*, 164(2-4), 251-258.

Lucazeau, F., Leroy, S., Bonneville, A., Goutorbe, B., Rolandone, F., d'Acremont, E., ... & Al-Toubi, K. (2008). Persistent thermal activity at the Eastern Gulf of Aden after continental break-up. *Nature Geoscience*, 1(12), 854-858.

Lucazeau, F. (2019). Analysis and mapping of an updated terrestrial heat flow data set. *Geochemistry, Geophysics, Geosystems*, 20(8), 4001-4024.

Lun-Tao, T., Ouyang, S., Tai-Rong, G., Ching-Ray, L., Hu, K. H., Chun-Li, L., & Chun-Jao, W. (2008). Insight into the geothermal structure in Chingshui, Ilan, Taiwan. TAO: *Terrestrial, Atmospheric and Oceanic Sciences*, 19(4), 4.

Lund, B., & Zoback, M. D. (1999). Orientation and magnitude of in situ stress to 6.5 km depth in the Baltic Shield. *International Journal of Rock Mechanics and Mining Sciences*, 36(2), 169-190.

Lund, J. W. & Toth, A. N. Direct utilization of geothermal energy 2020 worldwide review. *Geothermics* 90, 101915 (2020).

M

Ma, Y. Z., & Holditch, S. (2015). Unconventional oil and gas resources handbook: Evaluation and development. Gulf professional publishing.

Magri, F., Inbar, N., Siebert, C., Rosenthal, E., Guttman, J., & Möller, P. (2015). Transient simulations of large-scale hydrogeological processes causing temperature and salinity anomalies in the Tiberias Basin. *Journal of Hydrology*, 520, 342-355.

Magri, F., Möller, S., Inbar, N., Möller, P., Raggad, M., Rödiger, T., .. & Siebert, C. (2016). 2D and 3D coexisting modes of thermal convection in fractured hydrothermal systems-Implications for transboundary flow in the Lower Yarmouk Gorge. *Marine and Petroleum Geology*, 78, 750-758.

Magri, F., Cacace, M., Fischer, T., Kolditz, O., Wang, W., & Watanabe, N. (2017). Thermal convection of viscous fluids in a faulted system: 3D benchmark for numerical codes. *Energy Procedia*, 125, 310-317.

Mattauer, M. & Mercier, J. L. (1980) Microtectonique et grande tectonique, vol. 10, pp. 141–161.

Malkovsky, V. I., & Pek, A. A. (2004). Timescales for reaching steady-state fluid flow in systems perturbed by formation of highly permeable faults. *Geofluids* 4(4), 253-258.

Malkovsky, V. I., & Magri, F. (2016). Thermal convection of temperature-dependent viscous fluids within three-dimensional faulted geothermal systems: Estimation from linear and numerical analyses. *Water Resources Research*, 52(4), 2855-2867.

Manning, C. E., & Ingebritsen, S. E. (1999). Permeability of the continental crust: Implications of geothermal data and metamorphic systems. *Reviews of Geophysics*, 37(1), 127-150.

Mandelbrot, B. B., & Mandelbrot, B. B. (1982). The fractal geometry of nature (Vol. 1). New York: WH freeman.

Marcoux, E., & Picot, P. (1985). Les minéralisations de Pontgibaud (Puy-de-Dôme), France: Une approche complémentaire par la géochimie isotopique du plomb et les paragenèses. *Chronique de la recherche minière*, (481), 27-38.

Martel C, Champallier R, Prouteau G, Pichavant M, Arbaret L, Balcone-Boissard H, Scaillet B. Trachyte phase relations and implication for magma storage conditions in the Chaîne des Puys (French Massif Central). *J Petrol*. 2013;54(6):1071–107.

Mareschal, J. C., Jaupart, C., Gariépy, C., Cheng, L. Z., Guillou-Frottier, L., Bienfait, G., & Lapointe, R. (2000). Heat flow and deep thermal structure near the southeastern edge of the Canadian Shield. *Canadian Journal of Earth Sciences*, 37(2-3), 399-414.

Mareschal, J. C., & Jaupart, C. (2004). Variations of surface heat flow and lithospheric thermal structure beneath the North American craton. *Earth and Planetary Science Letters*, 223(1-2), 65-77.

Mazurek, M. (2000). Geological and hydraulic properties of water-conducting features in crystalline rocks. In Hydrogeology of crystalline rocks (pp. 3-26). *Springer*, Dordrecht.

Mazabraud, Y., Béthoux, N., Guilbert, J., & Bellier, O. (2005). Evidence for short-scale stress field variations within intraplate central-western France. *Geophysical Journal International*, 160(1), 161-178.

McKenna, J. R., & Blackwell, D. D. (2004). Numerical modeling of transient Basin and Range extensional geothermal systems. *Geothermics*, 33(4), 457-476.

McLellan, J. G., Oliver, N. H. S., & Schaubs, P. M. (2004). Fluid flow in extensional environments; numerical modelling with an application to Hamersley iron ores. *Journal of Structural Geology*, 26(6-7), 1157-1171.

Medina, R., Elkhoury, J. E., Morris, J. P., Prioul, R., Desroches, J., & Detwiler, R. L. (2015). Flow of concentrated suspensions through fractures: small variations in solid concentration cause significant in-plane velocity variations. *Geofluids*, 15(1-2), 24-36.

Meredith, P. G., Main, I. G., Clint, O. C., & Li, L. (2012). On the threshold of flow in a tight natural rock. *Geophysical research letters*, 39(4).

Merrill, A. L., and B. K. Watt. 1973. Energy Value of Foods: Basis and Derivation. Washington, DC: United States Department of Agriculture.

Mezri, L., Le Pourhiet, L., Wolf, S., & Burov, E. (2015). New parametric implementation of metamorphic reactions limited by water content, impact on exhumation along detachment faults. *Lithos*, 236, 287-298.

Micarelli, L., Benedicto, A., & Wibberley, C. A. J. (2006). Structural evolution and permeability of normal fault zones in highly porous carbonate rocks. *Journal of Structural Geology*, 28(7), 1214-1227.

Michon, L., & Merle, O. (2001). The evolution of the Massif Central Rift; spatio-temporal distribution of the volcanism. *Bulletin de la Société géologique de France*, 172(2), 201-211.

Micklethwaite, S., & Cox, S. F. (2006). Progressive fault triggering and fluid flow in aftershock domains: Examples from mineralized Archaean fault systems. *Earth and Planetary Science Letters*, 250(1-2), 318-330.

Mitchell, T. M., & Faulkner, D. R. (2012). Towards quantifying the matrix permeability of fault damage zones in low porosity rocks. *Earth and Planetary Science Letters*, 339, 24-31.

Moeck, I. S. (2014). Catalog of geothermal play types based on geologic controls. *Renewable and Sustainable Energy Reviews*, 37, 867-882.

Moore, J. C., & Saffer, D. (2001). Updip limit of the seismogenic zone beneath the accretionary prism of southwest Japan: An effect of diagenetic to low-grade metamorphic processes and increasing effective stress. *Geology*, 29(2), 183-186.

Mourzenko, V. V., Thovert, J. F., & Adler, P. M. (2011). Permeability of isotropic and anisotropic fracture networks, from the percolation threshold to very large densities. *Physical Review* E, 84(3), 036307.

Mordensky, S. P., Villeneuve, M. C., Kennedy, B. M., Heap, M. J., Gravley, D. M., Farquharson, J. I., & Reuschlé, T. (2018). Physical and mechanical property relationships of a shallow intrusion and volcanic host rock, Pinnacle Ridge, Mt. Ruapehu, New Zealand. *Journal of Volcanology and Geothermal Research*, 359, 1-20.

Morris, A., Ferrill, D. A., Henderson, D. B. (1996). Slip-tendency analysis and fault reactivation. *Geology*. 24(3), 275-278.

Mueller, S., Melnik, O., Spieler, O., Scheu, B., & Dingwell, D. B. (2005). Permeability and degassing of dome lavas undergoing rapid decompression: an experimental determination. *Bulletin of Volcanology*, 67(6), 526-538.

Muir-Wood, R., & King, G. C. (1993). Hydrological signatures of earthquake strain. *Journal of Geophysical Research: Solid Earth*, 98(B12), 22035-22068.

Murphy, H. D. (1979). Convective instabilities in vertical fractures and faults. *Journal of Geophysical Research: Solid Earth*, 84(B11), 6121-6130.

N

Nara, Y., Meredith, P. G., Yoneda, T., & Kaneko, K. (2011). Influence of macro-fractures and micro-fractures on permeability and elastic wave velocities in basalt at elevated pressure. *Tectonophysics*, 503(1-2), 52-59.

Negroni, J. M. (1981). Le district de Pontgibaud: cadre géologique, evolution structural et métallogénique (Doctoral dissertation).

Niederau, J., Wellmann, J. F., & Börsing, N. (2019). Analyzing the influence of correlation length in permeability on convective systems in heterogeneous aquifers using entropy production. *Geothermal Energy*, 7(1), 1-27.

Noda, H., & Shimamoto, T. (2005). Thermal pressurization and slip-weakening distance of a fault: An example of the Hanaore fault, southwest Japan. *Bulletin of the Seismological Society of America*, 95(4), 1224-1233.

Nur, A., & Walder, J. (1990). Time-dependent hydraulics of the Earth's crust. In The role of fluids in crustal processes (Vol. 113). National Academy Press Washington, DC.

Nyblade, A. A., & Pollack, H. N. (1993). A global analysis of heat flow from Precambrian terrains: implications for the thermal structure of Archean and Proterozoic lithosphere. *Journal of Geophysical Research: Solid Earth*, 98(B7), 12207-12218.

O

Oda, M. (1986). An equivalent continuum model for coupled stress and fluid flow analysis in jointed rock masses. *Water resources research*, 22(13), 1845-1856.

Olasolo, P., Juárez, M. C., Morales, M. P., & Liarte, I. A. (2016). Enhanced geothermal systems (EGS): A review. *Renewable and Sustainable Energy Reviews*, 56, 133-144.

Okumura, S., Nakamura, M., Nakano, T., Uesugi, K., & Tsuchiyama, A. (2010). Shear deformation experiments on vesicular rhyolite: Implications for brittle fracturing, degassing, and compaction of magmas in volcanic conduits. *Journal of Geophysical Research: Solid Earth*, 115(B6).

Ohtani, T., Nakashima, Y., & Muraoka, H. (2000). Three-dimensional miarolitic cavity distribution in the Kakkonda granite from borehole WD-1a using X-ray computerized tomography. *Engineering geology*, 56(1-2), 1-9.

Ord, A., & Oliver, N. H. S. (1997). Mechanical controls on fluid flow during regional metamorphism: some numerical models. *Journal of Metamorphic Geology*, 15(3), 345-359.

O'Sullivan, M. J., Pruess, K., & Lippmann, M. J. State of the art of geothermal reservoir simulation. *Geothermics*. 30(4), 395-429 (2001).

P

Pálmason, G. (1967). On heat flow in Iceland in relation to the Mid-Atlantic Ridge. In Iceland and Mid-ocean ridges (Vol. 38, pp. 111-127). *Soc. Sci. Islandica*, Reykjavik.

Parisio, F., Vilarrasa, V., Wang, W., Kolditz, O., & Nagel, T. (2019). The risks of long-term re-injection in supercritical geothermal systems. *Nature communications*, 10(1), 1-11.

Paulillo, A., Cotton, L., Law, R., Striolo, A., & Lettieri, P. (2020). Geothermal energy in the UK: The life-cycle environmental impacts of electricity production from the United Downs Deep Geothermal Power project. *Journal of Cleaner Production*, 249, 119410.

Patterson, J. W., Driesner, T., Matthai, S., & Tomlinson, R. (2018a). Heat and fluid transport induced by convective fluid circulation within a fracture or fault. *Journal of Geophysical Research: Solid Earth,* 123(4), 2658-2673.

Patterson, J. W., Driesner, T., & Matthai, S. K. (2018b). Self-organizing fluid convection patterns in an en echelon fault array. *Geophysical Research Letters*, 45(10), 4799-4808.

Patterson, J. W., & Driesner, T. (2021). Elastic and Thermoelastic Effects on Thermal Water Convection in Fracture Zones. *Journal of Geophysical Research: Solid Earth*, 126(2), e2020JB020940.

Person, M., Hofstra, A., Sweetkind, D., Stone, W., Cohen, D., Gable, C. W., & Banerjee, A. (2012). Analytical and numerical models of hydrothermal fluid flow at fault intersections. *Geofluids*, 12(4), 312-326.

Penhoët E. (2021) Potentiel géothermique haute enthalpie du bassin du Malzieu et de la faille de la Margeride (Lozère, Massif Central) : Analyse structurale et modélisation numérique. Rapport Master 1. Université d'Orléans. ENSEGID, Bordeaux.

Phillips, W. J. (1972). Hydraulic fracturing and mineralization. *Journal of the Geological Society*. 128(4), 337-359.

Pinet, C., Jaupart, C., Mareschal, J. C., Gariepy, C., Bienfait, G., & Lapointe, R. (1991). Heat flow and structure of the lithosphere in the eastern Canadian Shield. Journal of Geophysical Research: Solid Earth, 96(B12), 19941-19963.

R

Rabinowicz, M., Boulegue, J., & Genthon, P. (1998). Two-and three-dimensional modeling of hydrothermal convection in the sedimented Middle Valley segment, Juan de Fuca Ridge. *Journal of Geophysical Research: Solid Earth*, 103(B10), 24045-24065.

Radau R (1880) The interior of the earth*. Popular Sci Mon* (July):289–303.

Ranjram, M., Gleeson, T., & Luijendijk, E. (2015). Is the permeability of crystalline rock in the shallow crust related to depth, lithology or tectonic setting? *Geofluids*, 15(1-2), 106-119.

Reiter, K., & Heidbach, O. (2014). 3-D geomechanical–numerical model of the contemporary crustal stress state in the Alberta Basin (Canada). *Solid Earth*, 5(2), 1123-1149.

Reis, A. H. (2006). Constructal theory: from engineering to physics, and how flow systems develop shape and structure.

Rice, J. R., & Cleary, M. P. (1976). Some basic stress diffusion solutions for fluid-saturated elastic porous media with compressible constituents. *Reviews of Geophysics*, 14(2), 227-241.

Roche, V., Sternai, P., Guillou-Frottier, L., Menant, A., Jolivet, L., Bouchot, V., & Gerya, T. (2018). Emplacement of metamorphic core complexes and associated

geothermal systems controlled by slab dynamics. *Earth and Planetary Science Letters*, 498, 322-333.

Roche, V., Bouchot, V., Beccaletto, L., Jolivet, L., Guillou-Frottier, L., Tuduri, J., ... & Tokay, B. (2019). Structural, lithological, and geodynamic controls on geothermal activity in the Menderes geothermal Province (Western Anatolia, Turkey). *International Journal of Earth Sciences*, 108(1), 301-328.

Rowland, J. V., & Sibson, R. H. (2004). Structural controls on hydrothermal flow in a segmented rift system, Taupo Volcanic Zone, New Zealand. Geofluids, 4(4), 259-283.

Rudnicki, J. W., & Hsu, T. C. (1988). Pore pressure changes induced by slip on permeable and impermeable faults. *Journal of Geophysical Research: Solid Earth*, 93(B4), 3275-3285.

S

Saar, M. O., & Manga, M. (2004). Depth dependence of permeability in the Oregon Cascades inferred from hydrogeologic, thermal, seismic, and magmatic modeling constraints. *Journal of Geophysical Research: Solid Earth*, 109(B4).

Saevarsdottir, G., Tao, P. C., Stefansson, H., & Harvey, W. Potential use of geothermal energy sources for the production of lithium-ion batteries. *Renewable energy*. 61, 17-22 (2014).

Sardini, P., Ledésert, B., & Touchard, G. Quantification of microscopic porous networks by image analysis and measurements of permeability in the Soultz-sous-Forêts granite (Alsace, France). *In Fluid flow and Transport in rocks*. 171-189, (1997).

Saffer, D. M. (2015). The permeability of active subduction plate boundary faults. *Geofluids*, 15(1-2), 193-215.

Sammis, C. G., Rosakis, A. J., & Bhat, H. S. (2009). Effects of off-fault damage on earthquake rupture propagation: experimental studies. In Mechanics, Structure and Evolution of Fault Zones (pp. 1629-1648). *Birkhäuser Basel*.

Sandiford, M., & McLaren, S. (2006). Thermo-mechanical controls on heat production distributions and the long-term evolution of the continents.

Santouil, (1980). Tectonique et microtectonique comparée de la distension permienne et de l'évolution post-triasique dans les bassins de Lodève, Saint-Affrique et Rodez (France S. E.) Dissertation. Université Montpellier.

Sausse, J. (1998). Caractérisation et modélisation des écoulements fluides en milieu fissuré. Relation avec les altérations hydrothermales et quantification des paléo- contraintes. Dissertation, Université Henri Poincaré-Nancy I.

Scholtès, L. U. C., & Donzé, F. V. (2012). Modelling progressive failure in fractured rock masses using a 3D discrete element method. *International Journal of Rock Mechanics and Mining Sciences*, 52, 18-30.

Schmittbuhl, J., Lambotte, S., Lengliné, O., Grunberg, M., Jund, H., Vergne, J., ... & Masson, F. (2021). Induced and triggered seismicity below the city of Strasbourg, France from November 2019 to January 2021. *Comptes Rendus. Géoscience*, 353(S1), 1-24.

Schubert, G., Cassen, P., Young, R. E. (1979). Core cooling by subsolidus mantle convection. *Phys Earth Planet Int* 20:194–208.

Schulz, S. E., & Evans, J. P. (1998). Spatial variability in microscopic deformation and composition of the Punchbowl fault, southern California: implications for mechanisms, fluid–rock interaction, and fault morphology. *Tectonophysics*, 295(1-2), 223-244.

Scott, S., Driesner, T., & Weis, P. (2017). Boiling and condensation of saline geothermal fluids above magmatic intrusions. *Geophysical Research Letters*. 44(4), 1696-1705.

Scibek, J. (2020). Multidisciplinary database of permeability of fault zones and surrounding protolith rocks at world-wide sites. *Scientific data*, 7(1), 1-14.

Şengör, A. M. C., Görür, N., & Şaroğlu, F. (1985). Strike-slip faulting and related basin formation in zones of tectonic escape: Turkey as a case study.

Shi, Y., Song, X., Li, J., Wang, G., Zheng, R., & YuLong, F. (2019). Numerical investigation on heat extraction performance of a multilateral-well enhanced geothermal system with a discrete fracture network. *Fuel*, 244, 207-226.

Shields, J. K., Mader, H. M., Pistone, M., Caricchi, L., Floess, D., & Putlitz, B. (2014). Strain-induced outgassing of three-phase magmas during simple shear. *Journal of Geophysical Research: Solid Earth*, 119(9), 6936-6957.

Sibson, R. H. (1974). Frictional constraints on thrust, wrench and normal faults. *Nature*, 249(5457), 542-544.

Sibson, R. H. (1987). Earthquake rupturing as a hydrothermal mineralizing agent. *Geology*, 15(8), 701-704.

Siebenaller, L., Boiron, M. C., Vanderhaeghe, O., Hibsch, C., Jessell, M. W., Andre-Mayer, A. S., ... & Photiades, A. (2013). Fluid record of rock exhumation across the brittle–ductile transition during formation of a Metamorphic Core Complex (Naxos Island, Cyclades, Greece). *Journal of Metamorphic Geology*, 31(3), 313-338.

Siler, D. L.H et *al*. (2019). Three-dimensional geologic mapping to assess geothermal potential: examples from Nevada and Oregon. *Geothermal Energy***.** 7(1), 1-32.

Siler, D. L., Hinz, N. H.,& Faulds J. E. (2018). Stress concentrations at structural discontinuities in active fault zones in the western United States: Implications for permeability and fluid flow in geothermal fields. *Geol Soc Am Bull*.

Smil, V. (2016). Energy transitions: global and national perspectives. ABC-CLIO.

Smil, V. (2021). Grand Transitions: How the Modern World Was Made. New York: *Oxford University Press*, xi+338 pp.

Smith, L., & Chapman, D. S. (1983). On the thermal effects of groundwater flow: 1. Regional scale systems. *Journal of Geophysical Research: Solid Earth*, 88(B1), 593-608.

Sobolev, S. V., Zeyen, H., Granet, M., Achauer, U., Bauer, C., Werling, F., ... & Fuchs, K. (1997). Upper mantle temperatures and lithosphere-asthenosphere system beneath the French Massif Central constrained by seismic, gravity, petrologic and thermal observations. *Tectonophysics*, 275(1-3), 143-164.

Sruoga, P., Rubinstein, N., & Hinterwimmer, G. (2004). Porosity and permeability in volcanic rocks: a case study on the Serie Tobífera, South Patagonia, Argentina. Journal of Volcanology and Geothermal Research, 132(1), 31-43.

Sibson, R. H. (1994). Crustal stress, faulting and fluid flow. Geological Society, London, Special Publications, 78(1), 69-84.

Souque, C., Knipe, R. J., Davies, R. K., Jones, P., Welch, M. J., & Lorenz, J. (2019). Fracture corridors and fault reactivation: Example from the Chalk, Isle of Thanet, Kent, England. *Journal of Structural Geology*, 122, 11-26.

Stauffer, D., & Aharony, A. (2018). Introduction to percolation theory. Taylor & Francis.

Stober, I., & Bucher, K. (2015). Hydraulic conductivity of fractured upper crust: insights from hydraulic tests in boreholes and fluid-rock interaction in crystalline basement rocks. *Geofluids*, 15(1-2), 161-178.

Styron, R. GEMScienceTools/gem-global-active-faults: First release of 2019 (Version 2019.0). Zenodo https://doi.org/10.5281/zenodo.3376300 (2019).

Sukop, M. C., van Dijk, G. J., Perfect, E., & van Loon, W. K. (2002). Percolation thresholds in 2-dimensional prefractal models of porous media. *Transport in Porous Media*, 48(2), 187-208.

Sun, Z. X. et *al*. Numerical simulation of the heat extraction in EGS with thermal-hydraulic-mechanical coupling method based on discrete fractures model. *Energy*. 120, 20-33 (2017).

T

Taillefer, A., Soliva, R., Guillou-Frottier, L., Le Goff, E., Martin, G., & Seranne, M. (2017). Fault-related controls on upward hydrothermal flow: an integrated geological study of the Têt fault system, Eastern Pyrénées (France). *Geofluids*.

Taillefer, A., Guillou-Frottier, L., Soliva, R., Magri, F., Lopez, S., Courrioux, G., ... & Le Goff, E. (2018). Topographic and faults control of hydrothermal circulation along dormant faults in an orogen. *Geochemistry, Geophysics, Geosystems*, 19(12), 4972-4995.

Terakawa, T., Miller, S. A., & Deichmann, N. (2012). High fluid pressure and triggered earthquakes in the enhanced geothermal system in Basel, Switzerland. *Journal of Geophysical Research: Solid Earth*, 117(B7).

Tenthorey, E., & Cox, S. F. (2003). Reaction-enhanced permeability during serpentinite dehydration. *Geology*, 31(10), 921-924.

Tenthorey, E., & Gerald, J. D. F. (2006). Feedbacks between deformation, hydrothermal reaction and permeability evolution in the crust: Experimental insights. *Earth and Planetary Science Letters*, 247(1-2), 117-129.

Tester, J.W., et *al*. (2006) The Future of geothermal energy. Tech. Rep., Idaho National Laboratory, copyright by Massachussetts Institute of Technology.

Tozer, D. C. (1965) Thermal history of the Earth. *Geophys J Int* 3(2–3):95–112.

Turcotte, D. L., Torrance K. E., Hsui, A. T., (1973) Convection in the earth's mantle. *Methods Comput Phys* 13:431–454.

Turcotte, D. L., & Schubert, G. (1982) Geodynamics: applications of continuum physics to geological problems. *Wiley*, New York.

Turcotte, D. L., & Schubert, G. (2002). Geodynamics. *Cambridge university press.*

U

USDA. 2011. National Nutrient Database for Standard Reference. http://ndb.nal.usda .gov.

V

Valette, C. O. (1983). Karsts et filons à fluorine dans le faisceau synclinal du Morvan: le gisement d'Argentolle (Saône-et-Loire, France) (Doctoral dissertation).

Vallier, B., Magnenet, V., Schmittbuhl, J., & Fond, C. (2020). THM modeling of gravity anomalies related to deep hydrothermal circulation at Soultz-sous-Forêts (France). *Geothermal Energy*, 8(1), 1-21.

Vasseur, G., Gable, R., Feuga, B., & Bienfait, G. (1991). Groundwater flow and heat flow in an area of mineral springs. *Geothermics*, 20(3), 99-117.

Verney, N. (2005). Importance du contexte géologique dans la signature chimique et isotopique (Carbone 13) des sources hydrothermales. Applications aux émergences du Puy de Dôme. Université Blaise Pascal, MsC thesis.

Vigneresse, J. L., Tikoff, B., & Améglio, L. (1999). Modification of the regional stress field by magma intrusion and formation of tabular granitic plutons. *Tectonophysics*, 302(3-4), 203-224.

Violay, M., Heap, M. J., Acosta, M., & Madonna, C. (2017). Porosity evolution at the brittle-ductile transition in the continental crust: Implications for deep hydro-geothermal circulation. *Scientific reports*, 7(1), 1-10.

W

Wannamaker, P. E. (2005). Anisotropy versus heterogeneity in continental solid earth electromagnetic studies: fundamental response characteristics and implications for physicochemical state. *surveys in Geophysics*, 26(6), 733-765.

Wanner, C., Diamond, L. W., & Alt-Epping, P. Quantification of 3-D thermal anomalies from surface observations of an orogenic geothermal system (Grimsel Pass, Swiss Alps). *Journal of Geophysical Research: Solid Earth*. 124(11), 10839-10854 (2019).

Wang, Y., Li, T., Chen, Y., & Ma, G. (2019). A three-dimensional thermo-hydro-mechanical coupled model for enhanced geothermal systems (EGS) embedded with discrete fracture networks*. Computer Methods in Applied Mechanics and Engineering*, 356, 465-489.

Walder, J., & Nur, A. (1984). Porosity reduction and crustal pore pressure development. *Journal of Geophysical Research: Solid Earth*, 89(B13), 11539-11548.

Walferdin M (1837) Observation de la température du puits foré de Grenelle. *Comptes rendus de l'Académie des Sciences 4*.

Watanabe, N., Egawa, M., Sakaguchi, K., Ishibashi, T., & Tsuchiya, N. Hydraulic fracturing and permeability enhancement in granite from subcritical/brittle to supercritical/ductile conditions. *Geophysical Research Letters*. 44(11), 5468-5475 (2017).

Watanabe, N., Abe, H., Okamoto, A., Nakamura, K., & Komai, T. Formation of amorphous silica nanoparticles and its impact on permeability of fractured granite in superhot geothermal environments. *Scientific reports*. 11(1), 1-11 (2021).

Weis, P., Driesner, T., & Heinrich, C. A. (2012). Porphyry-copper ore shells form at stable pressure-temperature fronts within dynamic fluid plumes. *Science*, 338(6114), 1613-1616.

Wegener, A. (1912) Die Entstehung der Kontinente. Dr. A. Petermanns Mitteilungen aus Justus Perthes' Geographischer Anstalt 63:185–195, 253–256, 305–309.

Weis, P. (2015). The dynamic interplay between saline fluid flow and rock permeability in magmatic-hydrothermal systems. *Geofluids*, 15(1-2), 350-371.

Williams, D. L., Von Herzen, R. P., Sclater, J. G., & Anderson, R. N. (1974). The Galapagos spreading centre: lithospheric cooling and hydrothermal circulation. *Geophysical Journal International*, 38(3), 587-608.

Wilson, T., Bosman, S., Heath, P., Gouthas, G., Cowley, W., Mauger, A., ... & Delaney, G. (2010). The search for unconformity-related uranium mineralisation in the Pandurra Formation, South Australia: an international multidisciplinary collaboration. MESA Journal, 58, 9-15.

Wilson, C. J., & Rowland, J. V. (2016). The volcanic, magmatic and tectonic setting of the Taupo Volcanic Zone, New Zealand, reviewed from a geothermal perspective. *Geothermics*, 59, 168-187.

Wilson, M. P. et *al*. (2017). HiQuake: The human-induced earthquake database. *Seismological Research Letters*, 88(6), 1560-1565. Data set https://inducedearthquakes.org.

Wright, H. M., Cashman, K. V., Gottesfeld, E. H., & Roberts, J. J. (2009). Pore structure of volcanic clasts: measurements of permeability and electrical conductivity. *Earth and Planetary Science Letters*, 280(1-4), 93-104.

Y

Yale, D. P. (2003). Fault and stress magnitude controls on variations in the orientation of in situ stress. *Geological Society, London, Special Publications*, 209(1), 55-64.

Yardley, B. W. D. (1986). Fluid migration and veining in the Connemara Schists, Ireland. In Fluid—rock interactions during metamorphism (pp. 109-131). *Springer*, New York, NY.

Yang, T., Yang, X., Duan, Q., Chen, J., & Dekkers, M. J. (2016). Rock magnetic expression of fluid infiltration in the Yingxiu-Beichuan fault (Longmen Shan thrust belt, China). *Geochemistry, Geophysics, Geosystems*, 17(3), 1065-1085.

Yokoyama, T., & Takeuchi, S. (2009). Porosimetry of vesicular volcanic products by a water-expulsion method and the relationship of pore characteristics to permeability. *Journal of Geophysical Research: Solid Earth*, 114(B2).

Z

Zareidarmiyan, A., Parisio, F., Makhnenko, R. Y., Salarirad, H., & Vilarrasa, V. (2021). How equivalent are equivalent porous media? *Geophysical Research Letters*, e2020GL089163.

Zenghua, L., Guoxiang, C., Bethune, K. M., David, T., & Gerard, Z. (2017). Structural controls on fluid flow during compressional reactivation of basement faults: insights from numerical modeling for the formation of unconformity-related uranium deposits in the Athabasca Basin, Canada. *Economic Geology*, 112(2), 451-466.

Zeyen, H., Novak, O., Landes, M., Prodehl, C., Driad, L., & Hirn, A. (1997). Refraction-seismic investigations of the northern Massif Central (France). *Tectonophysics*, 275(1-3), 99-117.

Zhao, C., Hobbs, B. E., Mühlhaus, H. B., Ord, A., & Lin, G. (2003). Convective instability of 3-D fluid-saturated geological fault zones heated from below. *Geophysical Journal International*, 155(1), 213-220.

Zhao, Z., Rutqvist, J., Leung, C., Hokr, M., Liu, Q., Neretnieks, I., ... & Zimmerman, R. (2013). Impact of stress on solute transport in a fracture network: A comparison study. *Journal of Rock Mechanics and Geotechnical Engineering*, 5(2), 110-123.

Zhang, Z., Peng, S., Ghassemi, A., & Ge, X. (2016). Simulation of complex hydraulic fracture generation in reservoir stimulation. *Journal of Petroleum Science and Engineering*, 146, 272-285.

Zhang, Q., Zhu, W., Liu, W., Yue, M., & Song, H. (2020). Numerical simulation of fractured vertical well in low-permeable oil reservoir with proppant distribution in hydraulic fracture. *Journal of Petroleum Science and Engineering*, 195, 107587.

Zhou, S., Zhuang, X., & Rabczuk, T. (2018). A phase-field modeling approach of fracture propagation in poroelastic media. *Engineering Geology*, 240, 189-203.

Ziegler, P. A. (1987). Late Cretaceous and Cenozoic intra-plate compressional deformations in the Alpine foreland—a geodynamic model. *Tectonophysics*, 137(1-4), 389-420.

Zimmer, K., Zhang, Y., Lu, P., Chen, Y., Zhang, G., Dalkilic, M., & Zhu, C. (2016). SUPCRTBL: A revised and extended thermodynamic dataset and software package of SUPCRT92. *Computers & geosciences*, 90, 97-111.

Zoback et *al*. (2003). Determination of stress orientation and magnitude in deep wells. *International Journal of Rock Mechanics and Mining Sciences*. 40(7-8), 1049-1076.

Zoback, M. L. Stress field constraints on intraplate seismicity in eastern North America. *Journal of Geophysical Research: Solid Earth*. 97(B8), 11761-11782 (1992).

Appendices

Appendix 1 : Rock properties for Pontgibaud 2D TH parametric study and large-scale numerical modelling. Properties of these paramters have been recovered in the following works: Mareschal and Jaupart (2011), Lucazeau et al. (1984); Hasterok et al (2017), Taillefer (2017), Guillou-Frottier et al. (2013), Launay (2018), McKenna and Blackwell (2004), Smith and Chapman (1998), Rabinowicz et al. (1998).

Variables	Symbols	Mag-matic cham-ber	Gelles granite	Calcare-ous clay complex	Mantle	Meta-mor-phic unit	Carbonif-erous plu-tonic rocks	Migmatitic gneissic complex	Fault Zone	Units
Bulk density	ρ_s	3300	2600	2650	3300	2700	2600	3000	2600	kg/m^3
Permeability	k	variable	variable	variable	variable	variable	variable	variable	variable	m^2
Porosity	ε_p	0.1	0.05	0.1	0.02	0.05	0.05	0.05	0.1	%
Thermal con-ductivity	λ_s	2.2	3.25	2.2	3.0	2.5	2.8	2.5	2.8	W/(m.K)
Heat produc-tion	A	0.5	4.06	1.7	0.5	2.1	3.5	2	1	μW/m^3
Heat capacity	Cp_S	800	800	880	1000	800	800	800	800	J/(kg.K)

Appendix 2 : Rock properties for 3D THM parametric study. Properties of these parameters have been recovered in the following works: Smith and Chapman, 1983; Mckenna and Blackwell, 2004; Rabinowicz et al., 1998; Mareschal et al., 2012; Cappa and Rutqvist, 2011; Coussy, 2004; Hasterok and Webb, 2017; Guillou-Frottier et al., 2013; Duwiquet et al., 2019.

Variables	Symbols	Basement	Fault Zone	Units
Young's modulus	E	60	5	GPa
Poisson's ratio	ν	0.25	0.25	-
Bulk density	ρ_s	2600	2600	kg/m^3
Permeability	k	variable	variable	m^2
Porosity	ε_p	0.05	0.1	-
Biot-Willis coefficient	α_B	0.8	0.8	-
Thermal conductivity	λ_s	2.8	2.8	W/(m.K)
Heat production	A	3.5	1	μW/m^3
Heat capacity	Cp_S	800	800	J/(kg.K)

Appendix 3: Rock properties for Pontgibaud 3D THM large-scale numerical modelling. Properties of these parameters have been recovered in the following works: Smith and Chapman, 1983; Mckenna and Blackwell, 2004; Rabinowicz et al., 1998; Mareschal et al., 2012; Cappa and Rutqvist, 2011; Coussy, 2004; Hasterok and Webb, 2017; Taillefer et al., 2017, Guillou-Frottier et al., 2013; Duwiquet et al., 2019.

Variables	Symbols	Gelles granite	Metamorphic unit	Carboniferous plutonic rocks	Migmatitic gneissic complex	Fault Zone	Units
Young's modulus	E	60	60	60	60	5	GPa
Poisson's ratio	ν	0,25	0.25	0.25	0.25	0.25	-
Bulk density	ρ_s	2600	2700	2600	3000	2600	kg/m^3
Permeability	k	variable	variable	variable	variable	variable	m^2
Porosity	ε_p	0.05	0.05	0.05	0.05	0.1	-
Biot-Willis coefficient	α_B	0.8	0.8	0.8	0.8	0.8	-
Thermal conductivity	λ_s	3.25	2.5	2.8	2.5	2.8	W/(m.K)
Heat production	A	4.06	2.1	3.5	2	1	μW/m^3
Heat capacity	Cp_S	800	800	800	800	800	J/(kg.K)

Appendix 4 : Fluid properties for numerical parametric studies and for Pontgibaud large-scale numerical modelling. Properties of these parameters have been recovered in the following works: Smith and Chapman, 1983; Mckenna and Blackwell, 2004; Rabinowicz et al., 1998; Mareschal et al., 2012; Cappa and Rutqvist, 2011; Coussy, 2004; Hasterok and Webb, 2017; Taillefer et al., 2017, Guillou-Frottier et al., 2013; Duwiquet et al., 2019.

Variables	Symbols	Values	Units
bulk density	ρf	variable	Kg/m^3
Thermal conductivity	λ_f	0.6	W/m.K
Heat capacity	Cp_S	4200	J/(kg.K)
Dynamic viscosity	μ_f	variable	Pa.s^{-1}
Compressibility	χ_f	4×10^{-10}	Pa^{-1}
Fluid source term	Q_m	0	kg/m^3/s

Appendix 5 : Schematic representation of the working of an X-ray micro-tomograph.

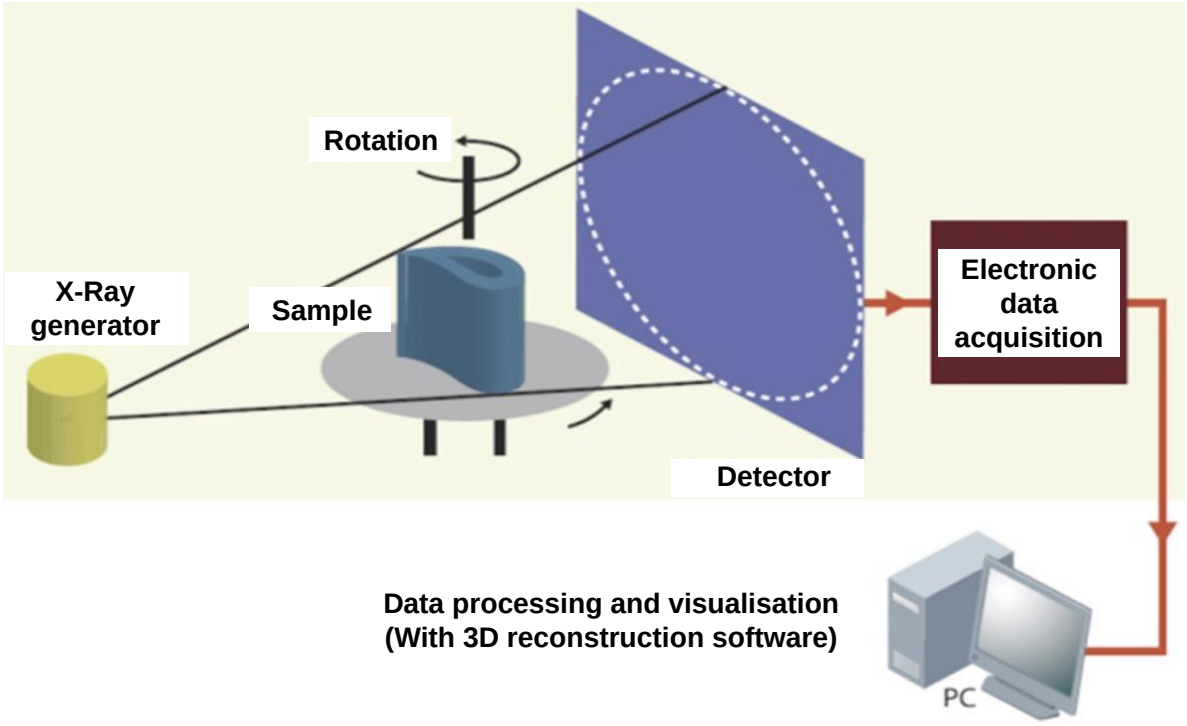

Appendix 6 : Schematics of the experimental apparatus. (a–b) Schematic diagrams (not to scale) of the bench-top permeameter. Inset in panel (b) shows a schematic of an intact sample and a fractured sample showing the geometry of the fracture plane (From Heap and Kenndy,2016).

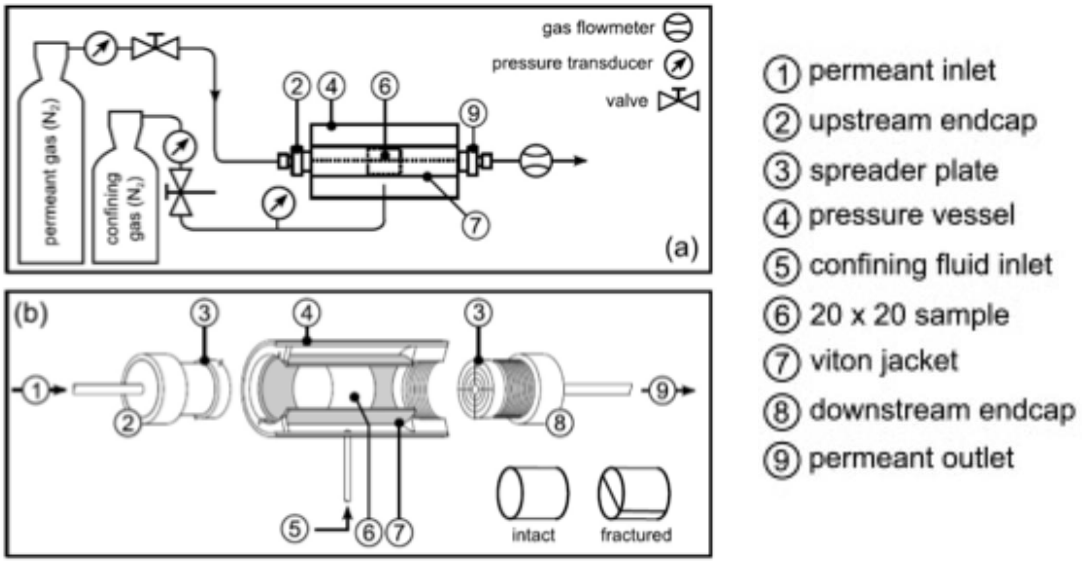

Appendix 7 : Topographic shift of 300 m at the Pontgibaud Crustal Fault Zone

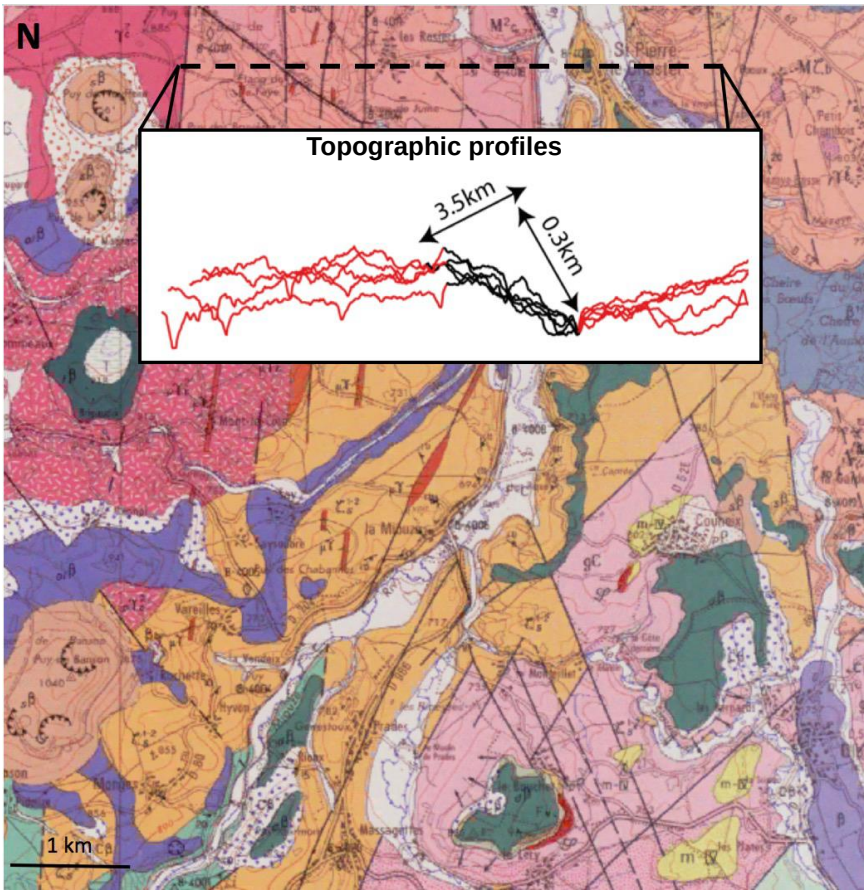

Appendix 8 : Set of properties and parameters (physical, geometrical, meshes) integrated and used within the large-scale numerical model of the Pontgibaud crustal fault zone. Raw report automatically generated by Comsol Multiphysics™.

Comsol Multiphysics Report

Contenu

1 Définitions globales

Date	Jun 23, 2021 11:18:01 PM

Réglages globaux

Nom	Ptgbd_larscle_num3D_THM
Version de COMSOL	COMSOL 5.5

Paramètres

Nom	Expression	Valeur	Description
ModYoungB	60[GPa]	60[Gpa]	Module_Young_basement
ModYoungF	5[Gpa]	5[Gpa]	Module_Young_Fault
CoefPoisson	0.25	0.25	Coefficient_Poisson

2 Composant 1

2.1 Définitions

2.1.1 Variables

Variables 1

Sélection

Niveau géométrique	Modèle entier

Nom	Expression	Unité	Description
SigH	10.3e6 + (13400*(z-325))	m	Con-trainte_H
SigV	7.5e6 + (19600*(z-325))	m	Con-trainte_V
Sigh	7.5e6 + (3500*(z-325))	m	Con-trainte_h
ViscoDyn	0.00002414*exp(570/(T+133))	$Pa.s^{-1}$	Visco-site_dy-namique
rhoPT	1006+(7.424^{e}-7*p)+(-0.3922*(T-273.15))+(-4.441^{e}-15*p^2)+(4.547^{e}-9*p*(T-273.15))+(-0.003774*(T-273.15)^2)+(1.451^{e}-23*p^3)+(-1.793^{e}-17*p^2*(T-273.15))+(7.485^{e}-12*p*(T-273.15)^2)+(2.955^{e}-6*(T-273.15)^3)+(-1.463^{e}-32*p^4)+(1.361^{e}-26*p^3*(T-273.15))+(4.018^{e}-21*(p^2)*((T-273.15)^2))+(-7.372^{e}-15*p*(T-273.15)^3)+(5.698^{e}-11*(T-273.15)^4)	$Kg.m^{3}$	Masse_volu mique_P_T
K3D	1^{e}-16*(exp((z-800)/2500)*(101 + 100*sin(2*pi*(z + x + y)/0.000001)))		Varia-tion_perm-éabilité_3D

2.1.2 Sélections

25

Type de sélection
Explicit

Sélection
Pas de domaines

2.1.3 Repères

Repère sur frontière 1

Type de système de coordonnées	Repère sur frontière
Etiquette	sys1

2.2 Géométrie 1

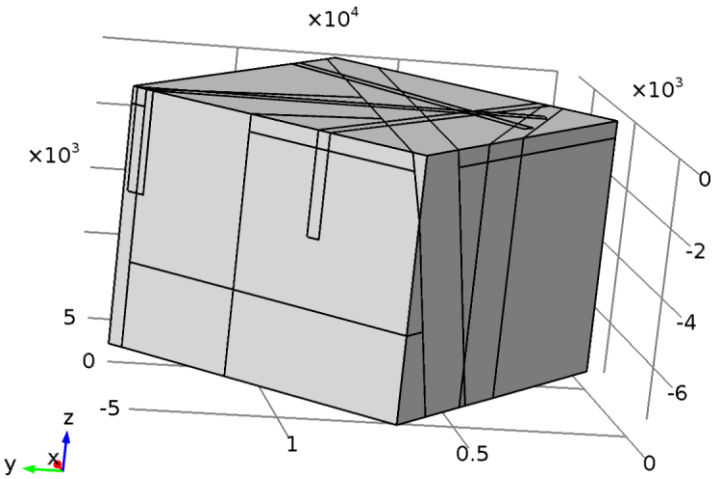

Géométrie 1

Unités

Unité de longueur	m
Unité d'angle	deg

2.3 Poroélasticité

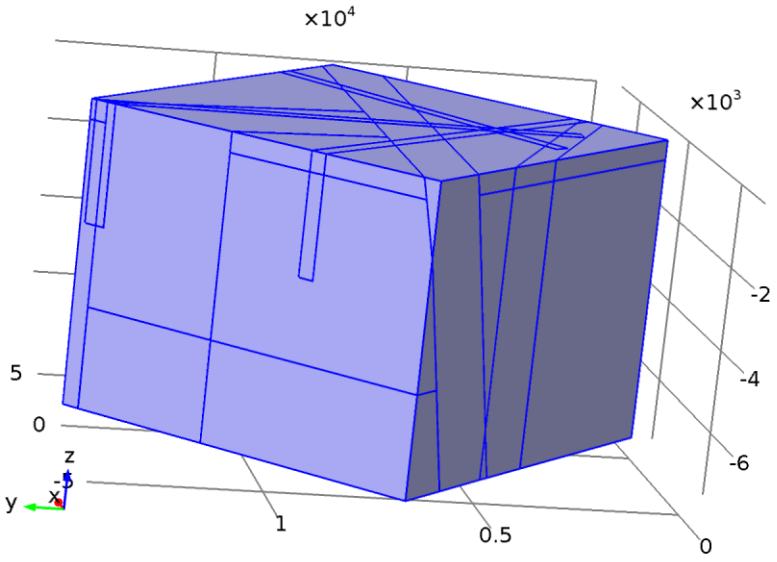

Poroélasticité

2.3.1 Matériau poroélastique

Equations

$$-\underline{\nabla : \sigma} = \mathbf{F}_V, \quad \sigma = J^{-1}\mathbf{F}\mathbf{S}\mathbf{F}^T, \quad \mathbf{F} = (\mathbf{I} + \nabla\mathbf{u}), \quad J = \det(\mathbf{F})$$

$$\mathbf{S} - \mathbf{S}_0 = \underline{\underline{\mathbf{C}} : (\epsilon - \epsilon_0 - \epsilon_{inel})} - \underline{\alpha_B p_f \mathbf{I}}$$

$$\epsilon = \frac{1}{2}\left[(\nabla\mathbf{u})^T + \nabla\mathbf{u} + (\nabla\mathbf{u})^T\nabla\mathbf{u}\right]$$

$$\underline{\rho S \frac{\partial p_f}{\partial t}} + \nabla \cdot (\rho\mathbf{u}) = Q_m - \underline{\rho\alpha_B \frac{\partial e_{vol}}{\partial t}}$$

$$\mathbf{u} = \underline{-\frac{\kappa}{\mu}(\nabla p_f + \rho g \nabla D)}$$

$$S = \epsilon_p \chi_f + \frac{(\alpha_B - \epsilon_p)(1 - \alpha_B)}{K}$$

2.4 Transfert de chaleur en milieu poreux

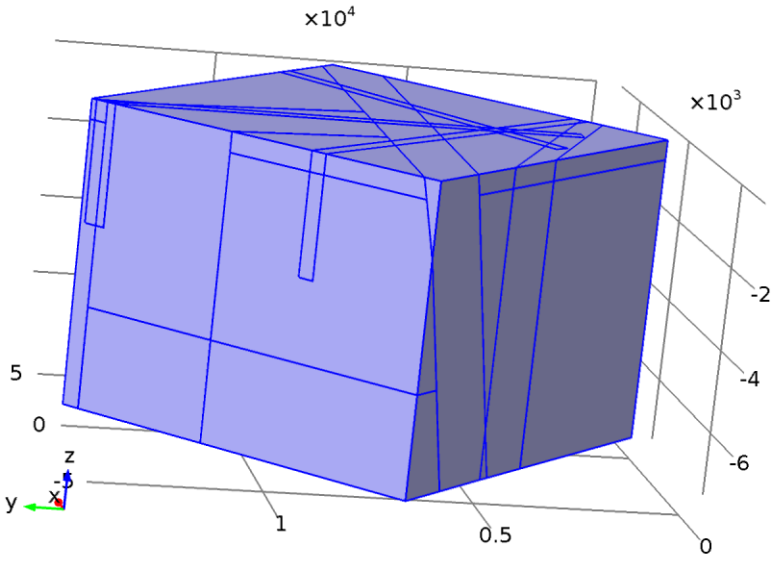

Transfert de chaleur en milieu poreux

Equations

$$(\rho C_p)_{\text{eff}}\frac{\partial T}{\partial t} + \rho C_p \mathbf{u}\cdot\nabla T + \nabla\cdot\mathbf{q} = Q + Q_{\text{vd}}$$

$$\mathbf{q} = -k_{\text{eff}}\nabla T$$

$$(\rho C_p)_{\text{eff}} = \theta_{\text{p}}\rho_{\text{p}}C_{p,\text{p}} + (1-\theta_{\text{p}})\rho C_p$$

$$k_{\text{eff}} = \theta_{\text{p}}k_{\text{p}} + (1-\theta_{\text{p}})k + k_{\text{disp}}$$

2.5 Maillage 1

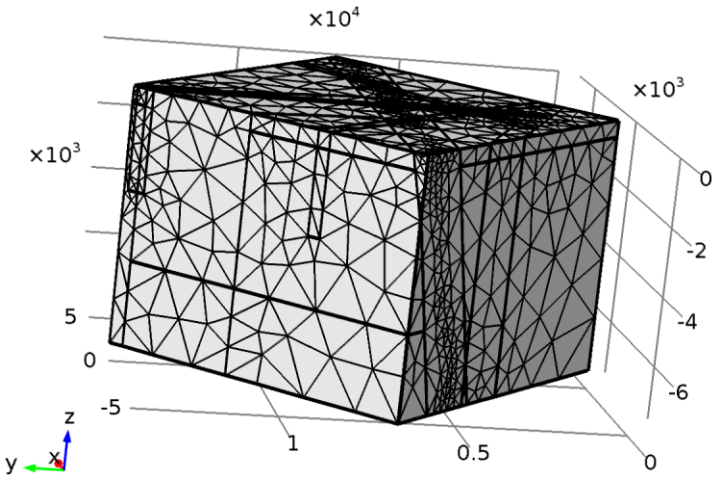

Maillage 1

3 Etude 1

Information sur le calcul

Temps de calcul	62 min 56 s
CPU	Intel(R) Core(TM) i7-8850H CPU @ 2.60GHz, 6 coeurs
Système d'exploitation	Windows 8

3.1 Temporel

Réglages de l'étude

Description	Valeur
Inclure la non-linéarité géométrique	Activé

Temps	Unité
range(0,1,10) range(10,10,100) range(100,100,1e5) range(1e5,1000,2e6)	a

Sélection du maillage

Géométrie	Maillage
Géométrie 1 (geom1)	mesh1

Hugo DUWIQUET

Les Zones de Failles Crustales comme systèmes géothermiques électrogènes. Apport des modélisations numériques et confrontation aux systèmes naturels

Les Zones de Failles Crustales (ZFC) constituent une cible géologique intéressante pour les ressources géothermiques à haute température dans les zones de socle naturellement fracturées. Des études de terrain et de laboratoire ont déjà montré la capacité de ces systèmes à faciliter l'écoulement des fluides jusqu'à la transition ductile-fragile. Cependant, plusieurs questions clés concernant l'exploration subsistent, en particulier le rôle du pendage, de la perméabilité, de l'effet des contraintes mécaniques et, plus largement, le rôle fondamental des régimes tectoniques sur l'écoulement des fluides dans les domaines de socle naturellement fracturés. En considérant des modélisations numériques 2D et 3D, avec des couplages TH et THM, deux tendances peuvent être identifiées et intégrées pour l'exploration de ces cibles : (i) les failles verticales concentrent les plus fortes anomalies de température aux plus faibles profondeurs (ii) les systèmes en décrochement favorisent les plus grandes anomalies de température. Les données géologiques et géophysiques suggèrent que la zone de faille de Pontgibaud (Massif Central français) est une ZFC qui abrite un système hydrothermal actif à une profondeur de quelques kilomètres. Une étude intégrée pour évaluer son potentiel géothermique de Haute Température a été effectuée. Les mesures de terrain permettent de contrôler la géométrie 3D des structures géologiques. Les observations 2D (lames-minces) et 3D (microtomographie à rayons X) mettent en évidence une propagation spatiale bien définie des fractures et des vides, présentant la même architecture de fracture à différentes échelles (2,5 µm à 2 mm). En outre, les mesures de la porosité et de la perméabilité confirment que les échantillons fortement fracturés et altérés sont caractérisés par des valeurs de perméabilité élevées, un échantillon étant caractérisé par une perméabilité aussi élevée que 10^{-12} m^2. Enfin, un modèle numérique 3D à grande échelle de la ZFC de Pontgibaud, basé sur le couplage THM et la comparaison avec les données de terrain (température, flux de chaleur et résistivité électrique), a permis d'explorer l'étendue spatiale de l'isotherme 150°C, qui s'élève jusqu'à une profondeur de 2,3 km. Bien que basé sur des hypothèses simplifiées, notre modèle reproduit les données de terrain. Une approche intégrée multidisciplinaire basée sur une modélisation 3D couplée s'est avérée être un moyen efficace d'évaluer le potentiel géothermique de la ZFC et de prédire les distributions de température. Elle peut être utilisée comme un outil prédictif pour développer des opérations géothermiques à haute température dans des roches du socle abritant des systèmes de failles à grande échelle.

Mots clés : Zones de Failles Crustales, Exploration, systèmes géothermaux de Haute Température, Approche multidisciplinaire, Modélisations multiphysiques.

Crustal Fault Zones as geothermal power systems. Contribution of numerical modelling and comparison with natural systems

Crustal Fault Zones (CFZ) are an interesting geological target for high-temperature geothermal resources in naturally fractured and deep basement zones. Field and laboratory studies have already shown the ability of these systems to favor fluid flow down to brittle-ductile-transition. However, several key questions about exploration still exist, in particular the role of structural dip, permeability, and the effect of mechanical stress and more broadly the fundamental role of tectonic regimes on fluid flow in naturally fractured basement domains. Considering 2D and 3D numerical modelling, with TH and THM couplings, two trends can be identified and integrated for the exploration of these targets (i) vertical faults concentrate the highest temperature anomalies at the shallowest depths (ii) strike-slip systems favor the largest temperature anomalies. Geological and geophysical data suggest that, the Pontgibaud fault zone (French Massif Central) is a CFZ that host an active hydrothermal system at a depth of a few kilometers. We conducted an integrated study to assess its high temperature geothermal potential. Field measurements are used to control the 3D geometry of the geological structures. 2D (thin-section) and 3D (X-ray microtomography) observations point to a well-defined spatial propagation of fractures and voids, exhibiting the same fracture architecture on different scales (2.5 µm to 2 mm). Moreover, measurements of porosity and permeability confirm that the highly fractured and altered samples are characterized by high permeability values, with one sample characterized by a permeability as high as 10^{-12} m^2. Finally, a large-scale 3D numerical model of the Pontgibaud CFZ, based on THM coupling and the comparison with field data (temperature, heat flux, and electrical resistivity), allowed to explore the spatial extent of the 150°C isotherm, which rises up to a depth of 2.3 km. Though based on simplified hypotheses, our model reproduces field data. A multi-disciplinary integrative approach based on coupled 3D modeling proved to be an efficient way to assess the geothermal potential of CFZ and predict temperature distributions. It can be used as a predictive tool to develop high-temperature geothermal operations within basement rocks hosting large-scale fault systems.

Keywords : Crustal Fault Zones, Exploration, High-Temperature geothermal system, Multidisciplinary approach, Multiphysics modelling.

Géosciences pour une Terre durable brgm

ISTO, 1A rue de la Ferollerie Campus Geoscience, 45100 Orléans

TLS GEOTHERMICS